SYNTHESIS, CRYSTAL GROWTH AND MAGNETIC PROPERTIES OF TWO-DIMENSIONAL SPIN SYSTEMS

Lia Šibav

Doctoral Dissertation
Jožef Stefan International Postgraduate School
Ljubljana, Slovenia

Supervisor: Asst. Prof. Mirela Dragomir, Jožef Stefan Institute, Ljubljana, Slovenia

Evaluation Board:
Prof. Darja Lisjak, Chair, Jožef Stefan Institute, Ljubljana, Slovenia
Prof. Anton Meden, Member, Faculty of Chemistry and Chemical Technology, University of Ljubljana, Ljubljana, Slovenia
Prof. J. Paul Attfield, Member, The University of Edinburgh, Edinburgh, United Kingdom

MEDNARODNA PODIPLOMSKA ŠOLA JOŽEFA STEFANA
JOŽEF STEFAN INTERNATIONAL POSTGRADUATE SCHOOL



Lia Šibav

SYNTHESIS, CRYSTAL GROWTH AND MAGNETIC PROPERTIES OF TWO-DIMENSIONAL SPIN SYSTEMS

Doctoral Dissertation

SINTEZA, GOJENJE MONOKRISTALOV IN MAGNETNE LASTNOSTI DVODIMENZIONALNIH SPINSKIH SISTEMOV

Doktorska disertacija

Supervisor: Asst. Prof. Mirela Dragomir

Ljubljana, Slovenia, April 2026

Acknowledgements

First and foremost, I would like to express my gratitude to my supervisor, Asst. Prof. Mirela Dragomir, for her invaluable guidance, support, and mentorship throughout my PhD studies. Her shared knowledge and insightful ideas have been instrumental in the completion of this work.

I am also thankful to Asst. Prof. Matic Lozinšek for conducting single-crystal X-ray diffraction on our $SrCu_2(BO_3)_2$ and $RETa_7O_{19}$ crystals, and to the entire Extreme Conditions Chemistry Lab (K2) team for their support, collaboration, and the memorable moments we have shared.

I would like to extend my gratitude to other collaborators for their contributions and assistance with structural analyses: Graham King from the Canadian Light Source, for performing synchrotron powder X-ray diffraction on our $SrCu_2(BO_3)_2$ samples and providing valuable guidance on Rietveld refinement; Bor Arah and Aleksander Učakar, for their help with SEM measurements; Edi Krajnc, for performing PXRD measurements during the early stages of my PhD work; and Maja Koblar, for her assistance with sample preparation for SEM-EDS analyses and some analyses on La-doped $SrCu_2(BO_3)_2$ crystals.

A significant part of this research comprised magnetic property measurements and analyses. I would like to thank Prof. Zvonko Jagličić from the Faculty of Civil Engineering and the Institute of Mathematics, Physics and Mechanics for performing magnetic susceptibility measurements.

The magnetic studies of $SrCu_2(BO_3)_2$ doping were conducted in collaboration with Prof. Denis Arčon from Condensed Matter Physics Department. I am very grateful for his guidance in ESR measurements and data interpretation with all the insightful discussions. I would also like to thank Tilen Knaflič for his help with ESR measurements and data fitting, interpretation of the results, and high-field ESR experiments, which were performed in collaboration with Prof. Sergei Zvyagin and Kirill Povarov from HZDR, whom I would like to acknowledge as well. Additional thanks are due to Žiga Gosar from F5 and Prof. Hiroyuki Nojiri from Tohoku University, Japan, for performing high-field susceptibility measurements on Mg-doped $SrCu_2(BO_3)_2$.

The work on $RETa_7O_{19}$ crystal growth was performed as a part of a collaboration with Assoc. Prof. Andrej Zorko and Tina Arh from Condensed Matter Physics Department, both of whom I would like to thank very much for their assistance and valuable discussions.

I would like to thank Prof. Barbara Malič for providing me with the opportunity to pursue my PhD work at the Department of Electronic Ceramics (K5), and all my department colleagues for their support and assistance throughout this journey.

To anyone who has contributed in any way, but whom I have not specifically mentioned, I offer my sincere thanks. I am deeply grateful to my family and friends for their unwavering support, encouragement, and understanding throughout this entire process. Finally, I gratefully acknowledge the financial support of the Slovenian Research and Innovation Agency, the K5 Department, and the projects listed in the publications attached to the dissertation. ChatGPT (OpenAI) was used for linguistic editing and grammar improvements.

Abstract

Low-dimensional spin systems constitute an important class of quantum materials in which reduced dimensionality and lattice geometry strongly influence magnetic interactions. From a materials science perspective, they provide model compounds for linking crystal structure, chemical composition, and emergent magnetic behavior driven by quantum effects in systems with reduced dimensionality. Despite the existence of several theoretical models, experimentally realized materials that closely match them remain scarce. To bridge the gap between theoretical predictions and their experimental implementation in two-dimensional systems, this dissertation investigates chemical doping of prototypical Shastry-Sutherland compound, $SrCu_2(BO_3)_2$, as well as single-crystal growth of rare-earth heptatantalates, $RETa_7O_{19}$, with a perfect triangular lattice. This work focuses on the synthesis, structural characterization, and magnetic behavior of these systems.

Chemical doping of $SrCu_2(BO_3)_2$ has been predicted to drive the system towards exotic magnetic states, such as superconductivity and quantum spin-liquid states. The first part of the dissertation experimentally investigates the effects of chemical substitution on the structure and magnetic properties of this system. A-site charge doping with M = La or Na is studied up to nominal $x = 0.15$ in $Sr_{1-x}M_xCu_2(BO_3)_2$, while B-site nonmagnetic doping, i. e., magnetic dilution, with Mg explores nominal concentrations up to $x = 0.10$ in $SrCu_{2-x}Mg_x(BO_3)_2$. The incorporation of dopants into the parent structure is confirmed for La- and Mg-doping, although at lower levels compared to nominal concentrations, whereas Na likely incorporates only in trace amounts. All dopants induce spin-dimer breaking, with the strongest effect observed for Mg-induced magnetic dilution. Both La and Mg substitution significantly reduce the effective spin gap, with the reduction being more pronounced for Mg. This reduction is accompanied by the development of antiferromagnetic correlations between dimer-free Cu^{2+} spins. In particular, Mg-doping gives rise to a distinct superstructure, evidenced by emergence of a high-field magnetic anomaly and the suppression of the plateau at 1/8 of the saturation magnetization.

The second part of the dissertation focuses on optimization of a flux method to grow high quality single crystals of $NdTa_7O_{19}$, the first Ising quantum spin liquid candidate on a perfect triangular lattice. With lateral sizes up to 3.5 mm and thicknesses up to 2 mm, the resulting crystals are the largest reported to date, allowing a precise characterization of the magnetic ground state. The method is further refined to grow three additional representatives of the rare-earth heptatantalate series. Two of them, $ErTa_7O_{19}$ and $DyTa_7O_{19}$, exhibit similar magnetic anisotropy to that of $NdTa_7O_{19}$, potentially hosting a disordered ground state, while $GdTa_7O_{19}$ is paramagnetic. The method could be applied to further representatives of the series.

Overall, the dissertation advances the field of two-dimensional magnetism in two complementary directions. First, the systematic study of $SrCu_2(BO_3)_2$ doping elucidates the intrinsic limitations and effects of chemical substitution on the parent lattice at both atomic and macroscopic scales. Second, the flux growth of rare-earth heptatantalates provides a new platform for exploring exotic magnetic phenomena in ideal triangular-lattice materials, including potential quantum spin-liquid states.

Povzetek

Nizkodimenzionalni spinski sistemi predstavljajo pomembno skupino kvantnih materialov, pri katerih nizka dimenzionalnost in mrežna geometrija močno vplivata na magnetne interakcije. Z vidika znanosti o materialih predstavljajo modelne sisteme za razumevanje povezave med kristalno strukturo, kemijsko sestavo in magnetnim obnašanjem, ki ga v nizkodimenzionalnih sistemih določajo kvantni efekti. Kljub številnim teoretičnem modelom eksperimentalno realizirani materiali, ki jih ti modeli opisujejo, ostajajo redki. Za premostitev razkoraka med teoretičnimi napovedmi in njihovo eksperimentalno realizacijo v dvodimenzionalnih sistemih doktorska disertacija preučuje kemijsko dopiranje prototipne Shastry–Sutherlandove spojine $SrCu_2(BO_3)_2$ ter rast monokristalov heptatantalatov redkih zemelj, $RETa_7O_{19}$, ki kristalizirajo v popolni trikotni mreži. Delo se osredotoča na sintezo, strukturno karakterizacijo in magnetno obnašanje teh sistemov.

Kemijsko dopiranje $SrCu_2(BO_3)_2$ naj bi po napovedih vodilo sistem k eksotičnim magnetnim stanjem, kot sta superprevodnost in kvantnospinska tekočina. Prvi del disertacije eksperimentalno preučuje vpliv dopiranja na strukturo in magnetne lastnosti tega sistema. Dopiranje na A-mestu z M = La oz. Na je raziskano do nominalne koncentracije $x = 0{,}15$ v $Sr_{1-x}M_xCu_2(BO_3)_2$, medtem ko študija nemagnetnega dopiranja na B-mestu z Mg, t. i. magnetnega redčenja, preučuje nominalne koncentracije do $x = 0{,}10$ v $SrCu_{2-x}Mg_x(BO_3)_2$. Vključitev dopantov v osnovno strukturo je potrjena za La in Mg, čeprav pri nižjih koncentracijah od nominalnih, medtem ko kaže, da se Na vgradi le v sledovih. Vsi trije dopanti povzročijo razpadanje spinskih dimerov bakra do prostih bakrovih spinov, pri čemer je učinek najmočnejši pri magnetnem redčenju z Mg. Dopiranje tako z La kot z Mg vodi do izrazitega zmanjšanja efektivne energijske reže spinskih vzbuditev, ki je izrazitejše pri Mg. Za ta dva dopanta se pojavijo še antiferomagnetne korelacije med prostimi bakrovimi spini. Pri dopiranju z Mg pride do nastanka izrazite superstrukture, kar se kaže v pojavu magnetne anomalije pri visokih poljih in zmanjšanju platoja na 1/8 nasičene magnetizacije.

Drugi del disertacije predstavlja optimiziran protokol gojenja visokokakovostnih monokristalov prvega kandidata za kvantno spin tekočino z Isingovimi spini na popolni trikotni mreži, $NdTa_7O_{19}$. Kristali s širinami do 3,5 mm in debelinami do 2 mm so največji vzgojeni doslej in omogočajo natančno magnetno karakterizacijo osnovnega stanja. Metoda je bila dodatno izpopolnjena za rast treh dodatnih predstavnikov serije heptatantalatov redkih zemelj. Dva, $ErTa_7O_{19}$ in $DyTa_7O_{19}$, kažeta podobno magnetno anizotropijo kot $NdTa_7O_{19}$, kar odpira možnost realizacije eksotičnih osnovnih stanj ter njihove natančne karakterizacije, $GdTa_7O_{19}$ pa je paramagneten. Metodo bi lahko v prihodnje uporabili tudi za druge predstavnike te serije.

Disertacija prispeva k napredku področja dvodimenzionalnega magnetizma v dveh smereh. Sistematična študija dopiranja $SrCu_2(BO_3)_2$ najprej pojasnjuje intrinzične omejitve in učinke kemijske substitucije na osnovno strukturo na atomski in makroskopski ravni. Gojenje monokristalov heptatantalatov redkih zemelj iz visokotemperaturne raztopine pa ponuja nove možnosti za raziskovanje eksotičnih magnetnih pojavov v materialih s pravilno trikotno mrežo, ki vključuje potencialna stanja kvantnospinske tekočine.

Contents

List of Figures **xiii**

List of Tables **xv**

Abbreviations **xvii**

Symbols **xix**

1 Introduction **1**
1.1 Introduction to Magnetism 1
1.2 Magnetic Interactions 2
1.3 Bulk Magnetic Properties 3
1.4 Low-Dimensional and Frustrated Magnetism 5
1.5 Quantum Spin Liquids 9
1.6 Solid-state Synthesis and Single-Crystal Growth of Low-Dimensional Magnets 11
1.7 Scope of the Dissertation 14
1.8 Characterization Methods 15
1.8.1 Structural Characterization 15
1.8.2 Microstructural Characterization 16
1.8.3 Magnetic Characterization 17

2 Aims and Hypotheses **19**
2.1 Aims 19
2.2 Hypotheses 19

3 Tuning the Magnetism of $SrCu_2(BO_3)_2$ by Chemical Doping **21**
3.1 Motivation 21
3.2 A-site Sr Aliovalent Substitutions in $SrCu_2(BO_3)_2$: Structural and Magnetic Effects 23
3.2.1 Influence of La-Doping on the Magnetic Properties of the Two-Dimensional Spin-Gapped System $SrCu_2(BO_3)_2$ 23
3.2.2 Effects of Na-doping on the Structure and Magnetism of $SrCu_2(BO_3)_2$ 50
3.3 B-site Cu Nonmagnetic Substitutions in $SrCu_2(BO_3)_2$: Magnetic Dilution Effects 65
3.4 Conclusions 87

4 Single-Crystal Growth of Rare-Earth Heptatantalates $RETa_7O_{19}$ with a Perfect Triangular Lattice **89**
4.1 Motivation 89
4.2 Optimized Flux Single-Crystal Growth of the Quantum Spin Liquid Candidate $NdTa_7O_{19}$ and Other Rare-Earth Heptatantalates, $ErTa_7O_{19}$ and $GdTa_7O_{19}$ 90

4.3 Synthesis and Crystal Growth of Other $RETa_7O_{19}$ Candidates, $DyTa_7O_{19}$ and $YbTa_7O_{19}$ 109
4.4 Conclusions 114

5 Conclusions and Outlook **115**

Appendix A $NdTa_7O_{19}$ Single Crystal Anisotropy Determined by ESR **119**

References **121**

Bibliography **127**

Biography **131**

List of Figures

Figure 1.1: The schematic representation of different types of magnetic ordering. 5

Figure 1.2: A schematic representation of spin dimensionality in a 2D system showing the spin orientations in a) one dimension b), two dimensions and c) three dimensions. 7

Figure 1.3: A schematic representation of magnetic frustration on different lattice units: a) triangular, b) pyrochlore and c) square with antiferromagnetic nearest-neighbor and next-nearest neighbor couplings of comparable magnitude.....8

Figure 1.4: Schematic representations of a) the VBS model, b) the RVB model, and c) the long-range RVB model. 10

Figure 3.1: The ground state of a Shastry-Sutherland system as a function of J'/J ratio. The representation of the ground states was adapted from [34], while the critical J'/J values were taken from [35]. 21

Figure 3.2: Representation of a) charge doping of $SrCu_2(BO_3)_2$ with La^{3+} or Na^+ and b) magnetic dilution of $SrCu_2(BO_3)_2$ with Mg^{2+}.....22

Figure 3.3: a) Laboratory PXRD patterns of polycrystalline $Sr_{1-x}Na_xCu_2(BO_3)_2$ with nominal $x = 0$, 0.05, 0.10, and 0.15 after solid-state reaction. b) Enlarged view of the 34°–46° 2θ range for higher clarity. c) The evolution of the unit cell parameters a and c as a function of nominal doping. d) The unit cell volume values as a function of nominal doping. 53

Figure 3.4: Profile fit of room-temperature laboratory PXRD (Cu Kα, λ = 1.5406 Å) of $Sr_{1-x}Na_xCu_2(BO_3)_2$ powders with the selected nominal concentration $x = 0.05$. The Rietveld refinement analysis was performed using the $I\bar{4}2m$ space group.....53

Figure 3.5: Representative normalized EDS point analysis spectra collected on the matrix of polycrystalline $Sr_{1-x}Na_xCu_2(BO_3)_2$ with nominal a) $x = 0.05$, b) 0.10 , and c) $x = 0.15$. 55

Figure 3.6: A representative SEM image and EDS elemental mapping analysis of polycrystalline $Sr_{1-x}Na_xCu_2(BO_3)_2$ with nominal $x = 0.15$ reveals a segregation of sodium in the intergranular regions. 56

Figure 3.7: Normalized EDS point analysis spectra collected in the vicinity of intergranular areas of polycrystalline $Sr_{1-x}Na_xCu_2(BO_3)_2$ with a) nominal $x = 0.05$ and b) $x = 0.15$....57

Figure 3.8: The magnetic susceptibility curves of undoped polycrystalline $SrCu_2(BO_3)_2$ and $Sr_{1-x}Na_xCu_2(BO_3)_2$ with nominal $x = 0.05$, 0.10, and 0.15, measured at $\mu_0 H = 1$ kG. 58

Figure 3.9: Low-temperature fits of the $1/\chi$ data to a Curie-Weiss law at $T = 2$–3.4 K for polycrystalline $Sr_{1-x}Na_xCu_2(BO_3)_2$ with nominal x = 0.05, 0.10, and 0.15, compared to the undoped system from ref. [35].....61

Figure 3.10: X-band ESR spectra of polycrystalline $Sr_{1-x}Na_xCu_2(BO_3)_2$ with nominal a) $x = 0.05$, b) 0.10 and c) 0.15, at selected temperatures 40, 90, 130, 170 and 250 K... 62

Figure 3.11: Low-temperature X-band ESR spectra of polycrystalline $Sr_{1-x}Na_xCu_2(BO_3)_2$ with nominal a) $x = 0$ at selected temperatures 11 and 20 K [35], b) 0.05, c) $x = 0.10$, and d) 0.15, at selected temperatures 5, 10 and 20 K. 63

Figure 4.1: Rietveld refinement profiles of laboratory PXRD data (Cu Kα, $T = 293$ K) of a) $DyTa_7O_{19}$ and b) $YbTa_7O_{19}$. 110

Figure 4.2: The comparison of unit cell volume of five polycrystalline $RETa_7O_{19}$ samples from Chapter 4, as determined by Rietveld refinement analysis. 111

Figure 4.3: A $DyTa_7O_{19}$ single crystal, obtained in this work. 112

Figure 4.4: a) Magnetic susceptibility of a $DyTa_7O_{19}$ single crystal. b) $M(H)$ curves for $H \perp c$ and $H \parallel c$ at 2 K. 113

Figure A.1: The angular dependence of a) g-factor and b) ESR linewidth for the $NdTa_7O_{19}$ single crystal. 120

List of Tables

Table 1.1: Possibilities of formation of long- (LRO) or short-range order (SRO) for different combinations of lattice dimensionality, N, and spin dimensionality, n. 7

Table 3.1: Structural parameters derived from the Rietveld refinement analyses of polycrystalline $Sr_{1-x}Na_xCu_2(BO_3)_2$ with $x = 0$ [35], 0.05, 0.10, and 0.15, performed in $I\bar{4}2m$ space group. 54

Table 3.2: The average semi-quantitative atomic % values of Sr, Cu, O and Na, obtained from point analyses collected on the matrix of $Sr_{1-x}Na_xCu_2(BO_3)_2$ samples with nominal $x = 0.05$, 0.10, and $x = 0.15$, together with Na/Cu, Na/Sr and Cu/Sr ratios. 56

Table 3.3: The complete results of high-temperature magnetic susceptibility data fits in the interval 100−300 K for $Sr_{1-x}Na_xCu_2(BO_3)_2$ powders ($x = 0$−0.15) using the Curie-Weiss law equation, Eq. (3.2). 58

Table 3.4: Summary of magnetic parameters derived from various fits of susceptibility data for $Sr_{1-x}Na_xCu_2(BO_3)_2$ with $x = 0.05$, 0.10 and 0.15, compared to parameters of the undoped system, $x = 0$, from ref. [35]. 59

Table 3.5: The complete results of magnetic susceptibility data fits in the temperature interval 2−6 K for different doping concentrations using Eq. (3.3). 60

Table 4.1: Detailed Rietveld refinement analysis results on polycrystalline $DyTa_7O_{19}$ and $YbTa_7O_{19}$, performed on room-temperature data collected using Cu Kα radiation ($\lambda = 1.5406$ Å). 111

Abbreviations

a. u.	...	arbitrary units
EDS	...	Energy-Dispersive X-ray Spectroscopy
EPR	...	Electron Paramagnetic Resonance
ESR	...	Electron Spin Resonance
LRO	...	long-range order
PXRD	...	Powder X-ray Diffraction
QSL	...	Quantum Spin Liquid
RE	...	rare-earth element
RVB	...	resonating valence-bond
SEM	...	Scanning Electron Microscopy
SRO	...	short-range order
VBS	...	valence-bond solid

Symbols

B	...	magnetic flux density
B_0	...	applied external magnetic field
ΔB	...	EPR (ESR) linewidth
C	...	Curie constant
χ	...	magnetic susceptibility
d	...	interplanar distance
e	...	elementary charge
E	...	energy
f	...	frustration index
g_{J}	...	Landé g-factor
$\hbar$	...	reduced Planck constant
$\hat{H}$	...	energy of interaction Hamiltonian
H	...	magnetic field strength
J	...	total angular momentum
$J_{i,j}$	...	magnetic exchange interaction
l	...	quantum number
L	...	total orbital angular momentum
λ	...	wavelength
M	...	magnetization
m_{l}	...	orbital quantum number
m_{s}	...	spin quantum number
m_e	...	electron mass
N	...	lattice dimensionality
n	...	integer number
n	...	main quantum number
n	...	spin dimensionality
μ_{i}	...	magnetic moment
μ_{B}	...	Bohr magneton
s	...	spin quantum number
S	...	total spin angular momentum
T	...	temperature
T_{C}	...	Curie temperature
T_{N}	...	Néel temperature
T_{O}	...	ordering temperature
T_{max}	...	susceptibility maximum temperature

θ	...	Weiss constant (related to Curie-Weiss law in magnetism)
θ	...	diffraction angle (related to Bragg's law in powder X-ray diffraction)
V	...	volume
ν	...	frequency

Chapter 1

Introduction

The chapter begins with an overview of the fundamental concepts of magnetism required to understand low-dimensional spin systems, followed by an introduction to low-dimensional magnetism. The studied materials exhibit frustrated magnetism, which is discussed together with the related class of quantum spin liquids. The two main research directions of this dissertation are subsequently outlined. Finally, the synthesis and characterization techniques used in this work are briefly presented, highlighting their key principles and features.

1.1 Introduction to Magnetism

Magnetism has captivated human curiosity since ancient times, with its earliest recorded observations dating back to ancient Greece and China. Naturally occurring lodestones were observed to attract iron, sparking curiosity and early attempts to understand this phenomenon [1]. The mysterious force was initially attributed to supernatural properties, guiding scholars to theorize about its origins. Over time, magnetism became a subject of scientific inquiry, influencing navigation with the development of the magnetic compass and later advancing the understanding and design of magnetic materials. Despite centuries of study, magnetism remains an active and evolving field of research, continuing to unveil new phenomena in solid materials [2].
Magnetic fields originate from electric charges in motion or the magnetic moments of electrons, which are fundamentally quantum-mechanical in nature. In condensed matter systems, magnetism is effectively described in terms of localized magnetic moments, μ_i, which arise primarily from the spin and orbital angular momentum of electrons [3]. Each electron possesses two key angular momenta: the orbital angular momentum, characterized by the quantum number l, which defines the shape of the orbital, and the spin angular momentum, often referred to only as spin, characterized by the spin quantum number s. Both angular momenta are inherently quantized. For orbital angular momentum, the quantum number l can take integer values from 0 up to $n-1$, corresponding to s, p, d, … orbitals, with $2l+1$ possible projections $m_l = -l, -l+1, \dots, l$, which determine the orientation of the orbital in space. In contrast, for electrons, the spin quantum number is fixed at $s = 1/2$. Spin is an intrinsic property of elementary particles such as electrons, protons, and neutrons, which are all fermions characterized by half-integer spin. As a result, the spin projection along any chosen axis, m_s, can take only two values, $+1/2$ or $-1/2$, corresponding to the two allowed spin orientations [3].

The orbital angular momentum results from the electron's motion around the nucleus, and is considered an extrinsic property, while the spin is an intrinsic quantum property, arising from the fundamental nature of quantum mechanics, independent of classical

motion. Therefore, the orbital and spin angular momenta are also referred to as extrinsic and intrinsic angular momenta, respectively. Together with the principal quantum number, n, the orbital quantum number l and the magnetic quantum numbers, m_l and m_s, completely define the state of an electron in an atom [3].

When considering the atom as a whole, the total spin angular momentum, $\boldsymbol{S}$, is the vector sum of the individual electron spins, while the total orbital angular momentum, $\boldsymbol{L}$, is the vector sum of the orbital angular momenta of all electrons. The total angular momentum results from the coupling of $\boldsymbol{S}$ and $\boldsymbol{L}$ via spin–orbit coupling, and is defined as:

$$\boldsymbol{J} = \boldsymbol{L} + \boldsymbol{S}. \tag{1.1}$$

The value of the magnetic moment μ can be calculated as:

$$\mu = \mu_B g_J \sqrt{J(J+1)}. \tag{1.2}$$

Here, g_J denotes a Landé g-factor, which is dimensionless, given by:

$$g_J = \tfrac{3}{2} + \tfrac{S(S+1)-L(L+1)}{2J(J+1)}, \tag{1.3}$$

and μ_B represents the Bohr magneton, the natural unit for expressing the electron magnetic moment, calculated by:

$$\mu_B = \tfrac{e\hbar}{2m_e}, \tag{1.4}$$

with e being the elementary charge, $1.6022 \cdot 10^{-19}$ A s, $\hbar$ the reduced Planck constant, $1.0546 \cdot 10^{-34}$ J s and m_e the electron mass, $9.109 \cdot 10^{-31}$ kg, yielding a final value of $9.274 \cdot 10^{-24}$ J/T [3].

An atom or ion is considered *magnetic* if it contains *d*- or *f*-block ions with partially filled d or f orbitals. For *d*-group elements, the quantum number $J \approx S$, as L is generally quenched. The quenching comes from crystal field effects from the surrounding ligands or lattice interactions, which split the degenerate orbital states, effectively "freezing" the orbital angular momentum L in a specific direction. This prevents it from freely contributing to the total angular momentum [4].

1.2 Magnetic Interactions

While individual electron spins and their associated angular momenta define the intrinsic magnetic properties of atoms, real materials consist of many interacting magnetic moments. These moments do not exist in isolation but influence one another through various fundamental interactions. The nature and strength of these interactions determine the collective magnetic behavior of a system, playing a crucial role in the emergence of macroscopic magnetic properties.

The magnetic dipolar interaction arises from the coupling between two magnetic dipoles and is present between all magnetic entities, from atomic spins to bulk magnets. However, its energy scale corresponds to temperatures of the order of ~1 K. Therefore, it cannot account for long-range magnetic ordering, such as ferromagnetism or antiferromagnetism, observed in many materials, which typically occurs at considerably higher temperatures [3].

In contrast, long-range magnetic order is predominantly governed by exchange interactions. They arise from electrostatic repulsion between electrons, where the spatial arrangement of electrons affects their overall energy. Due to the Pauli exclusion principle,

electrons with parallel spins avoid each other, reducing their electrostatic repulsion and leading to a net exchange interaction that drives magnetic ordering. The energy of interaction for a pair of electrons can be written as [3]:

$$\hat{H} = -2J\boldsymbol{S}_1 \cdot \boldsymbol{S}_2. \tag{1.5}$$

Although this equation is straightforward to derive for a pair of electrons, extending it to a system with many interacting particles is significantly more complex. However, early advances in quantum mechanics revealed that such interactions are not unique, but instead arise universally between all neighboring atoms. This recognition leads to the expansion of the interaction in terms of a many-body system, which is represented by the Hamiltonian of the Heisenberg model, given by the following equation:

$$\hat{H} = -\sum_{i,j} J_{i,j} \boldsymbol{S}_i \cdot \boldsymbol{S}_j. \tag{1.6}$$

Here, $J_{i,j}$ represents the exchange constant between the i^{th} and j^{th} spins [3]. Due to the inclusion of each pair of spins twice in the summation, the factor of 2 is omitted.

In context of materials, the magnetic exchange interaction can be direct or indirect [5]. A direct interaction refers to exchange between nearest-neighbor magnetic ions and is most efficient in the presence of sufficient overlap of the relevant d and f orbitals. Notable examples are the ferromagnetic $3d$ metals nickel, iron and cobalt. However, direct exchange is rarely the dominant mechanism governing magnetic properties. When direct overlap between orbitals of neighboring magnetic ions is weak or absent, the exchange interaction is mediated indirectly. The most common type of indirect exchange interactions for insulating materials is superexchange, which occurs between non-neighboring magnetic ions with non-magnetic ions in between them. For magnetic oxides, it occurs through the p-orbital of the oxygen atom. However, polyatomic ions such as borate or sulfate anions as well as organic molecules can also mediate superexchange interactions [6]. In case of metals, the indirect exchange, known as "RKKY exchange" (Ruderman–Kittel–Kasuya–Yosida) or "itinerant exchange", is mediated by conduction electrons [5].

1.3 Bulk Magnetic Properties

The collective behavior of magnetic moments in a material is governed by intrinsic magnetic interactions and determines its overall response to an external magnetic field. Measuring specific quantities, such as magnetization and magnetic susceptibility provides insight into the fundamental properties and behavior of a magnetic system. *Magnetization*, M, is a macroscopic quantity describing the net magnetic moment of a material and serves as a measurable parameter of its response to an external magnetic field. It is defined as the net magnetic moment per unit volume:

$$M = \frac{\sum_i \mu_i}{V}, \tag{1.7}$$

where $\sum_i \mu_i$ is the sum of all individual magnetic moments within the material, given in A m^2, and V is the volume in m^3. Magnetization is thus expressed in amperes per meter (A/m). *Magnetic susceptibility*, χ, quantifies the material's response to an applied magnetic field. At low fields, where magnetization increases proportionally with the external magnetic field H, magnetic susceptibility is defined as:

$$\chi = \frac{M}{H}, \tag{1.8}$$

and is dimensionless. Another commonly used form is molar susceptibility, which expresses the susceptibility per mole of the material and is typically reported in SI units of m^3/mol or CGS units emu/mol [3].

According to their response to an external magnetic field, materials can be broadly classified into two main categories: *paramagnetic* and *diamagnetic*. Materials containing unpaired electrons in *d* or *f* orbitals are paramagnetic. In an ideal paramagnet, the magnetic moments exhibit no static correlations in the absence of an external magnetic field, analogous to the non-interacting particles of an ideal gas, and are randomly oriented [4].

However, upon application of an external magnetic field, they tend to align parallel to the field, producing a net magnetization. In the high-temperature limit, where thermal energy exceeds the energy of magnetic exchange interaction, the magnetic susceptibility of paramagnetic materials follows the *Curie law*:

$$\chi = \frac{C}{T}, \tag{1.9}$$

where C represents the Curie constant and T the given temperature, both in K [4]. The application of a magnetic field to a paramagnetic material lifts the degeneracy of the magnetic energy levels through the *Zeeman effect* [3]. This phenomenon describes the splitting of electron energy levels in an external field, fundamentally arising from the interaction between the magnetic moment of the material and the applied external field. Classically, the energy of a magnetic moment $\boldsymbol{\mu}$ aligned with an external field $\boldsymbol{B}$ is given by [3]:

$$E = -\boldsymbol{\mu} \cdot \boldsymbol{B}, \tag{1.10}$$

where E is expressed in J and B in T. For a quantum spin system with total spin S, the energy levels split according to the spin projection quantum number m_S along the along the direction of the applied field. If the field is oriented along the z-axis, the energy eigenvalues are [3]:

$$E = g\mu_B m_S \cdot B. \tag{1.11}$$

Here, g is the Landé factor, μ_B the Bohr magneton, B the external magnetic field, and m_S assumes values in integer steps between $-S$ to S; $-S$, $-S+1$, ..., $S-1$ S, leading to $2S+1$ discrete energy levels.

The Zeeman splitting plays a crucial role in various physical effects, such as the behavior of magnetization in an applied field and the thermal population of spin states. It also provides the underlying principle for several experimental techniques, including electron spin resonance (ESR) spectroscopy, allowing a local investigation of electron correlations in magnetic solids.

Diamagnetic materials, in contrast to paramagnetic ones, do not possess unpaired electrons. They exhibit a weak repulsion to an applied magnetic field, with the induced minor magnetization oriented in the direction opposite to the external field, resulting in a small negative magnetic susceptibility. Although typically considerably weaker than paramagnetism, diamagnetism is a universal phenomenon present in all materials due to the field-induced modification of electron orbital motion [3].

In contrast to the idealized theoretical description of paramagnets, real materials exhibit weak but finite correlations between the paramagnetic moments. Upon cooling, thermal fluctuations of the magnetic moments are suppressed, and correlations between them gradually increase, ultimately leading to a phase transition into an ordered magnetic state at a critical temperature. The two basic types of long-range magnetic ordering are

ferromagnetic and *antiferromagnetic* ordering (Figure 1.1). In ferromagnetic materials, the magnetic moments align parallel to each other, which results in a large net magnetization. In real materials, however, the spins align parallel only in certain magnetic domains, while the domains themselves remain randomly oriented [7]. The ordering occurs below the *Curie temperature,* T_C. In case of antiferromagnetism, magnetic moments of equal magnitude are aligned antiparallel to each other, which results in a zero-net magnetization. The associated ordering temperature is referred to as the *Néel temperature*, T_N. Another prominent type of magnetic ordering is *ferrimagnetism*, encountered in materials with two or more magnetically inequivalent sublattices. The sublattice moments align antiparallel, which still results in an overall net magnetization due to unequal sublattice moments. In addition, several unconventional types of magnetic ordering have been identified, including canted antiferromagnetism and helimagnetic ordering (Figure 1.1) [4].

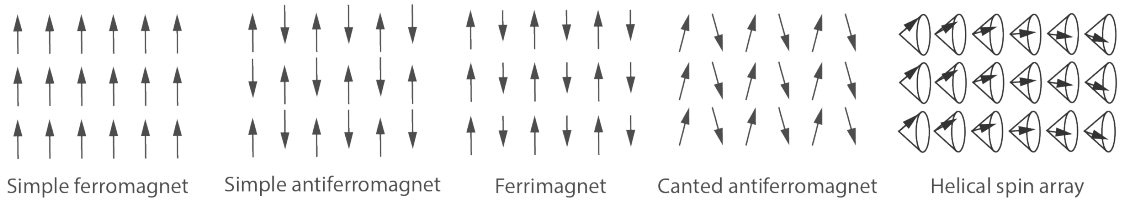


Figure 1.1: Schematic representation of different types of magnetic ordering. Adapted from [4].

To account for the interactions present in real paramagnetic materials, which become increasingly significant at lower temperatures, a correction to the Curie law is introduced in the form of the *Weiss constant*, θ, given in K, leading to the *Curie-Weiss law*:

$$\chi = \frac{C}{T - \theta}. \tag{1.12}$$

The Weiss constant reflects the strength and sign of the effective internal magnetic field arising from magnetic interactions. A positive value of θ indicates predominant ferromagnetic interactions, while a negative value suggests antiferromagnetic interactions [4].

1.4 Low-Dimensional and Frustrated Magnetism

In a classical magnet, the magnetic moments of the atoms are strongly correlated in all three spatial dimensions. If these strong correlations are reduced to two dimensions or one dimension of space, the material is defined as a *low-dimensional* magnetic material [8]. These are bulk materials which showcase pronounced magnetic anisotropies arising from the spatial arrangement of magnetic ions in the crystal lattice. In low-dimensional and frustrated magnetism, due to quenching of the orbital angular momentum for *d*-group elements (as noted in Section 1.1), the expressions *magnetic moment* and *spin* are commonly used interchangeably. This convention is adopted for the remainder of this dissertation.

A basic categorization of low-dimensional magnets divides them into two main groups: *quasi-one-dimensional* ($N = 1$) and *quasi-two-dimensional* magnets ($N = 2$), with N representing *lattice dimensionality*. The term "quasi" emphasizes that a dimensionality $N = 1$ or 2 provides the best effective description of a given material, although, due to deviations between theory and experiment, is not necessarily exact. In quasi-one-

dimensional magnets, the distances between magnetic ions are considerably shorter in one spatial direction compared to the other two, leading to a dominant magnetic exchange interaction along a single axis and much weaker interactions in the remaining directions. Such structures are commonly approximated as magnetic chains. In quasi-two-dimensional magnets, the distances between magnetic ions are comparable in two spatial directions and significantly larger in the remaining one, resulting in strong in-plane exchange interactions and a weak out-of-plane coupling. The magnetic exchange interactions therefore dominate in two spatial directions and such systems can be well described as magnetic layers [9].

Beyond one- and two-dimensional magnets, two other groups of low-dimensional magnets are frequently addressed. The cases where the structure is best approximated by spin dimers, trimers or tetramers, are referred to as magnetic clusters or zero-dimensional magnets [6]. At the crossover between one and two-dimensional systems lies a distinct subclass of low-dimensional magnets, known as spin ladders – systems of interacting antiferromagnetic chains – which exhibit characteristics intermediate between one- and two-dimensional magnets. Interest in spin ladders increased following theoretical predictions of superconductivity upon hole doping [6].

Three important crystal engineering aspects related to the synthesis of a low-dimensional magnetic material can be identified: (i) the source of spin, (ii) the bridging groups and (iii) spacers [10].

The predominantly used source of spin (i) are magnetic ions, the most frequently encountered being $3d$ metal ions, such as Cu^{2+}, V^{4+} and Co^{2+}. Less frequently, the role of spin source can be fulfilled by organic radicals [9], such as the family of κ—BEDT-TTF$_2$X, where BEDT-TTF stands for bis(ethylenedithio)tetrathiafulvalene and X is a monovalent anion, usually a Cu complex [11]. The total spin angular momentum of the magnetic ion, S, plays a key role in determining the relevance of quantum fluctuations in a magnetic system. In particular, low-spin systems such as $S = 1/2$ or $S = 1$ are strongly influenced by quantum effects, whereas higher-spin systems ($S = 3/2$) tend to approach the classical limit [3].

The role of the (ii) bridging groups is to mediate a type of magnetic exchange interaction, which determines the correlations between the magnetic moments. The most common bridging group in low-dimensional magnetism is the oxygen atom, with superexchange being the dominant mechanism (described in Section 1.2).

The basis of low-dimensional spin systems are the magnetic correlations reduced to two or one dimension of space which is readily achieved if the structure provides a greater distance between the atoms in one or two spatial dimensions. The non-magnetic atoms or molecules that provide this separation are referred to as (iii) spacers. These are usually counter non-magnetic ions such as K^+ or La^{3+}, organic ions, neutral ligands or solvent molecules [10]. The synthesis can also be completed without spacers if a compound exhibits pronounced anisotropic distortions of the coordination polyhedra due to Jahn–Teller effect, which lead to elongated metal–ligand bonds and consequently weaker magnetic exchange interactions in specific crystallographic directions [9]. The Jahn-Teller theorem asserts that a non-linear molecular system in a degenerate electronic state is unstable and will have a tendency towards lowering its energy and removing the degeneracy by undergoing a distortion, forming a system of lower symmetry [12]. This phenomenon is most frequently observed in compounds with d-block metal ions, where the geometry of the ligands surrounding the central ion is octahedral or tetrahedral. In octahedrally coordinated systems, this distortion typically manifests as an anisotropic elongation or compression of metal–ligand bonds along one coordination direction. In two-dimensional magnetism, such bond-length anisotropy can suppress magnetic exchange interactions perpendicular to the layers, effectively stabilizing magnetic layers. This is commonly observed in Cu^{2+} compounds. A compound where this is realized is $KCuF_3$ [9].

Low-dimensional magnets can be categorized according to their *spin dimensionality*, n, which denotes the number of spatial components (x, y, z) of the spin considered in the model (Figure 1.2) [9].

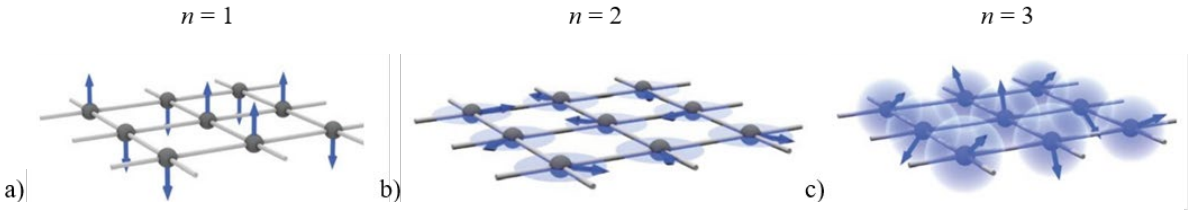


Figure 1.2: A schematic representation of spin dimensionality in a 2D system showing the spin orientations in a) one dimension b), two dimensions and c) three dimensions. Adapted from [13].

In theoretical calculations, the interactions for a given model are typically considered only between nearest-neighbor spins, with the relevant number of spin spatial components determined by n [9]. Considering all three possible spin spatial components, the mathematical description of magnetic interaction for a pair of interacting spins, given in Equation 1.5, becomes:

$$\hat{H} = -2\ [J_{xx}S_{1x}S_{2x} + J_{yy}S_{1y}S_{2y} + J_{zz}S_{1z}S_{2z}], \tag{1.13}$$

where $S = 1/2,\ 1,\ 3/2,\ 2,\ 5/2$ and so forth [9]. Based on spin dimensionality, three theoretical models are identified:

- the Heisenberg model: $n = 3$; $J_{xx} \approx J_{yy} \approx J_{zz}$.
- the XY model: $n = 2$; $J_{zz} << J_{xx} \approx J_{yy}$.
- the Ising model: $n = 1$; $J_{zz} >> J_{xx} \approx J_{yy}$ [4].

Combining the three spin dimensionalities with the three lattice dimensionalities results in nine distinct situations (Table 1.1). Long-range order (LRO) arises in all cases for the lattice dimensionality $N = 3$ and for the two-dimensional lattice, $N = 2$, with a spin dimensionality of $n = 1$, also referred to as the two-dimensional Ising case. All the remaining combinations enable short-range order (SRO), desired in low-dimensional magnetism [4].

Table 1.1: Possibilities of formation of long- (LRO) or short-range order (SRO) for different combinations of lattice dimensionality, N, and spin dimensionality, n.

		N		
		1	2	3
n	1	SRO	LRO	LRO
	2	SRO	SRO	LRO
	3	SRO	SRO	LRO

A notable phenomenon that prevents the formation of long-range order in a magnetic material is *magnetic frustration*. A simple 2D representation of *geometrical frustration* is antiferromagnetic ordering of magnetic moments on a triangular lattice (Figure 1.3 a). If two antiparallel Ising spins ($n = 1$) are projected onto the vertexes of an equilateral triangle, an addition of the third spin can never satisfy an overall antiferromagnetic ordering since the geometry of the lattice prevents it from being aligned simultaneously

antiparallel to both of the remaining spins. Consequently, apart from increasing spin correlations, the magnetic moments will have an additional constraint to remain disordered upon cooling. As each of the three given spins can adopt two possible orientations and all resulting configurations are energetically equivalent, the ground state is six-fold degenerate.

Geometrical frustration is most commonly realized on two-dimensional lattices, such as a perfect triangular lattice (Figure 1.3 a) and the Kagomé lattice (Stars of David formed by corner-sharing triangles, frequently encountered in natural minerals). In three-dimensional lattices, it is typically observed on the triangular pyrochlore lattice or a three-dimensional triangular – pyrochlore lattice (Figure 1.3 b) [14]. In terms of groups of compounds, geometrical frustration is most frequently encountered in *d*-group transition metal and rare-earth oxides [4].

In addition to lattice geometry, frustration in magnetic systems can also originate from other mechanisms, such as *competing interactions*. This type of frustration is commonly observed on hexagonal honeycomb lattices, but it can also be found on other lattice geometries such as square (Figure 1.3 c). In a square lattice, frustration arises when the nearest-neighbor and next-nearest neighbor magnetic exchange couplings are of comparable strength [6].

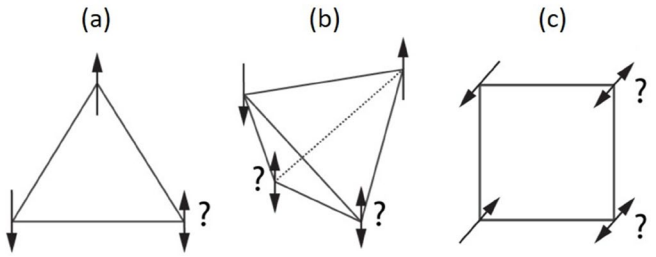


Figure 1.3: A schematic representation of magnetic frustration on different lattices: a) triangular, b) pyrochlore and c) square with antiferromagnetic nearest-neighbor and next-nearest neighbor couplings of comparable magnitude. Adapted from [4].

From a thermodynamic perspective, magnetic frustration contradicts the third law of thermodynamics, which states that as temperature approaches absolute zero, the entropy of a system should approach zero as well, with the system eventually settling into one single configuration. In conventional systems, entropy decreases as the system transitions to a long-range ordered state at a critical temperature. However, in frustrated materials, the inherent frustration compels the spins to retain their dynamic behavior at sufficiently low temperatures, even when their thermal energy would ordinarily be insufficient to maintain such motion, thereby hindering the removal of entropy. As a result, frustrated magnets exhibit a key distinction from conventional magnets: they typically transition into an ordered state at significantly lower temperatures [4].

Consequently, frustrated materials exhibit unconventional macroscopic properties, such as anomalous temperature-dependent behaviors in magnetic susceptibility and heat capacity. They typically exhibit slow transitions to ordered states and can display unusual magnetization dynamics, including slower relaxation times or atypical hysteresis behavior. Additionally, frustration can give rise to novel quantum states and quasiparticles, such as spinons and triplons, which challenge conventional understanding and provide deep insights into the complex magnetic interactions present in these materials [14].

1.5 Quantum Spin Liquids

The significantly lower ordering temperatures of frustrated materials compared to conventional magnets naturally raises an intriguing question: can spins remain disordered all the way down to absolute zero, appearing to challenge the expectations of the third law of thermodynamics? A distinctive subclass of frustrated magnets that exhibits this behavior, which has captured considerable research interest over the past two decades, are quantum spin liquids (QSLs) [15]. These systems are predicted to host a range of exotic phenomena, including excitations with fractional quantum numbers, emergent gauge fields, and potential unconventional superconductivity. The future of QSL research holds promise not only for fundamental physics but also from an applicative standpoint, as it has been linked to advances in quantum computing and memory storage.

The first model proposed to describe the ground state of quantum spin liquids was the *resonating valence bond* (RVB) model, introduced by Anderson in 1973 [16]. To build this model, he first considered constructing a lattice of the simplest basic building blocks for a non-magnetic system − a pair of $S = 1/2$ spins − which forms a spin dimer with a singlet ground state with total $S = 0$. A model considering such spin dimers, also referred to as *valence bonds*, localized on the simplest frustrated lattice – the perfect triangular lattice, was introduced as a *valence bond solid* (VBS) (Figure 1.4 a). The RVB model (Figure 1.4 b) describes the ground state of a QSL as a superposition of all possible valence-bond configurations with equal energies. In the simplest RVB model, the valence-bond formations only comprise nearest-neighbor interactions, while an extended, long-range RVB model (Figure 1.4 c) considers all the possible spin pair combinations across the whole lattice. This is a characteristic feature of QSLs known as *long-range quantum entanglement*.

These models illustrate that a QSL state, although possibly realized in magnetic materials, is essentially non-magnetic, as the spins forming each spin pair remain dynamic and strongly correlated to the zero-temperature limit. The analogy of the state's properties to the liquid state lends the name "quantum spin liquid".

The study of QSLs is driven not only by their unconventional magnetic behavior but also by their potential to unveil entirely new phases of matter, thereby expanding the landscape of quantum materials [14]. One particularly compelling prospect is the possible emergence of superconductivity in doped QSLs. In 1987, Anderson extended his original RVB theory, proposing that charge doping, i. e., introducing mobile charge carriers, allows the pre-existing spin singlets (valence bonds) to effectively act as Cooper pairs, giving rise to superconductivity without conventional electron-phonon interactions.

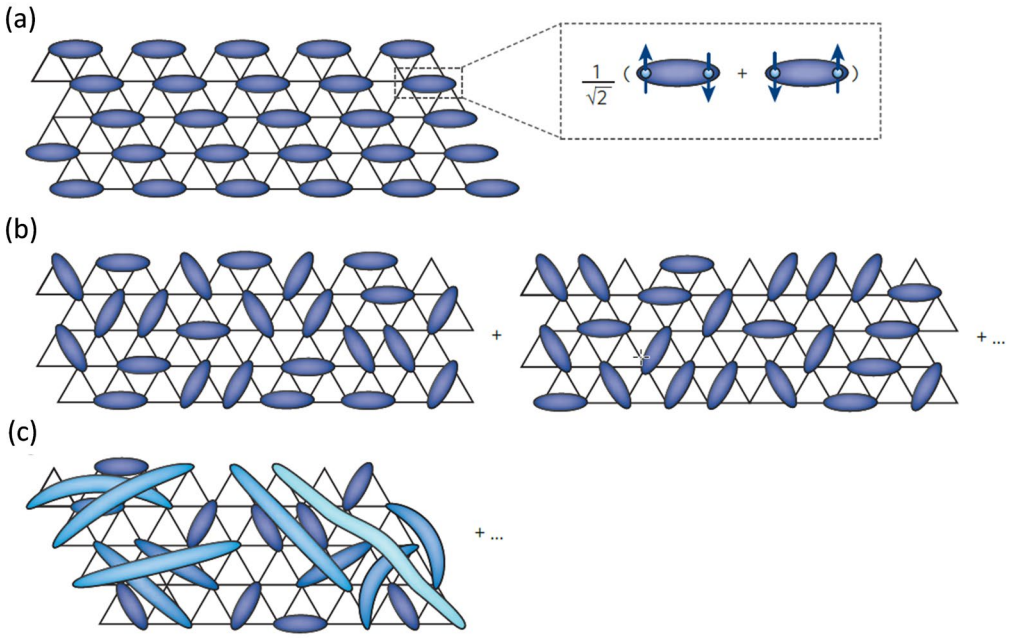


Figure 1.4: Schematic representations of a) the VBS model, with spin dimer singlets depicted as blue ellipses; b) the RVB model, representing a linear combination of all possible nearest-neighbor valence-bond formations, all of equal energy; c) the long-range RVB model, expanding the formation of spin singlets between nearest-neighbors to long-range correlations. Adapted from [15].

The concept of *RVB superconductivity* has been suggested as a possible mechanism of high-temperature superconductivity in cuprates, where parent compounds exhibit strong electronic correlations and magnetic frustration, forming a Mott-insulating state with short-range spin correlations, which resemble those described in RVB theory. Within this framework, the quantum entanglement of the spin-singlets supports coherent charge transport upon doping, leading to superconductivity [17]. This framework has since laid the foundation for numerous theoretical and experimental studies exploring the connection between frustrated magnetism, quantum entanglement, and high-temperature superconductivity, driving ongoing efforts to uncover novel superconducting materials based on frustrated magnetism.

One of the major challenges in studying QSL candidate materials is the difficulty of probing these states at the lowest temperatures. While disordered magnetic states have been observed in candidate materials down to temperatures as low as 10 mK, the possibility of eventual magnetic ordering at further lower temperatures cannot be ruled out, making a definitive identification of a QSL state elusive. Consequently, compounds that exhibit characteristics typical of QSLs—such as strong frustration and the absence of long-range magnetic order—are generally referred to as *QSL candidates*. To identify potential QSLs, several key characteristics are examined. An important first indication is the presence of lattice geometries that favor strong geometrical frustration. A quantitative measure of frustration is given by the dimensionless frustration index:

$$f = \frac{|\theta|}{T_{\mathrm{O}}}, \tag{1.14}$$

where θ represents the Weiss constant and T_{O} the ordering temperature, both in K [4]. Systems with $f > 10$ are generally considered frustrated [4], whereas higher values, $f >> 100$, are characteristic of highly frustrated magnets and are frequently encountered

in QSL candidates [15]. Further crucial indicators include the absence of magnetic ordering at the lowest temperatures, confirmed via local probes such as muon spin relaxation or nuclear magnetic resonance. The presence of fractionalized excitations, detectable through elastic and inelastic neutron scattering on single crystals, provides additional evidence, in particular the observation of spinons as excitations. Transport measurements can further reveal whether these excitations are localized or itinerant, offering deeper insight into the quantum properties of the studied system [15].

1.6 Solid-state Synthesis and Single-Crystal Growth of Low-Dimensional Magnets

The primary method used in this dissertation to synthesize polycrystalline materials is the *ceramic method*. Also known as *conventional* or *high-temperature solid-state synthesis*, it remains a widely used approach for the preparation of polycrystalline materials that exhibit low-dimensional magnetism and exotic magnetic properties [19,20]. This fundamental method consists of performing a reaction of non-volatile solid precursors at elevated temperatures (typically between 500 and 2000 °C), where diffusion at particle interfaces governs the transformation into the desired phase. The reaction mechanism is diffusion-limited, requiring optimized particle size and morphology to enhance surface contact and minimize diffusion distances, and the driving force for the reaction is the reduction of surface energy. To facilitate reaction kinetics, precursor powders are ground, homogenized, and pelletized to ensure uniform mixing [18]. Overcoming the activation energy barriers necessary for cation mobility requires high synthesis temperatures [19]. Typically, multiple sintering cycles are employed, with intermediate regrinding and repelletizing steps to expose fresh surfaces and accelerate the reaction. Given the substantial lattice energies of precursor materials, these elevated temperatures are essential to enable proper diffusion. A significant strength of this method lies in its simplicity, requiring only well-mixed reactants and a furnace.

However, this method also requires prolonged reaction times and substantial energy input due to the sustained high temperatures necessary for diffusion [18]. Moreover, these elevated temperatures give rise to several significant drawbacks. The first is the increased volatility of certain reactants, which can lead to stoichiometric deviations and phase decomposition. In addition, inhomogeneous diffusion at particle interfaces can result in chemical inhomogeneities throughout the sample. The enhanced mobility of reactant species under these conditions further contributes to the formation of defects, such as vacancies and site substitutional disorder, a factor particularly relevant in quantum spin liquid research. Finally, high-temperature synthesis inherently favors the formation of thermodynamically stable phases, often precluding access to metastable states that are crucial for exploring exotic magnetic behavior [19].

In quantum materials research, access to high-quality single crystals is of paramount importance, as they offer significant advantages over polycrystalline materials in the precise characterization of fundamental properties. Low-dimensional magnets, which exhibit strong anisotropies, require measurements along all three spatial directions, which is only achievable with single crystals, whereas polycrystalline samples provide limited information. Single crystals also enable a more accurate determination of phase transitions and, in the case of quantum spin liquids, allow for direct probing of fractionalized excitations, which is crucial for understanding their exotic quantum states.

Beyond the structural advantages, single crystals are of higher purity than polycrystalline materials, which is a critical factor given the extreme sensitivity of quantum

materials to chemical impurities and defects. Such irregularities can significantly alter the probed quantum states and hinder the studies of intrinsic physical properties. A notable example is the early development of topological insulators, where unwanted impurities in precursor materials rendered the bulk phase too conductive, masking the characteristic topologically protected surface states [20]. Consequently, advances in single-crystal growth techniques are essential, not only for refining material quality but also for ensuring accessibility, as many existing methods require sophisticated and costly equipment. Developing more efficient, scalable and reproducible growth procedures remains a key challenge in the field.

In this dissertation, the primary technique for obtaining single crystals is the *flux method* [21,22]. This technique involves the crystallization of a target compound from a high-temperature solution. The solvent, known as the flux, typically consists of one or a combination of inorganic compounds with relatively low melting points. First, a melt containing the flux and constituents of the crystal to be grown is formed at a temperature above the melting point of the flux and slightly above the saturation temperature of the compound to be grown as single crystals. Afterwards, the solution is slowly cooled for the precipitation to take place. The crystallization begins with nucleation, which usually takes place on the surface of the melt or on crucible walls. The crystallization can also be performed using a seed crystal. The crystals then precipitate from the solution, lowering its saturation temperature. This process continues to occur during the slow cooling step. The solution reaching its melting point marks the endpoint of the process. The reaction can also be stopped artificially.

A critical factor in successful flux crystal growth is the careful selection of the flux material, which must exhibit low toxicity, low volatility, and should not chemically interact with or alter the components of the crystal to be grown, nor react with the crucible material [21,22]. This ensures that no undesired chemical reactions or contaminations occur that could interfere with the growth process or degrade the final product. An optimum flux is often achieved by using a mixture of compounds, which can offer several advantages. For instance, mixtures can retain the desirable solvent properties of a volatile flux while simultaneously reducing its vapor pressure. Additionally, they can lower viscosity, reduce the crystallization temperature, and improve the size and habit of the crystals. Even a small amount of an additive—often just a few percent—can significantly influence the outcome of the growth process, although the atomic mechanism behind these effects is not fully understood [21]. In cases where the flux is composed of multiple components, the flux composition becomes particularly important. Additionally, the flux must possess the ability to dissolve a substantial amount of reagents, allowing for a high concentration of the desired material. It should possess a low melting point and show a significant change in solubility with temperature to facilitate the controlled growth of the crystal [22]. Moreover, the flux should be easily removable after the growth process, ensuring that it does not leave undesirable residues or interfere with the final product. Other desirable properties of the flux are the availability in pure form at low cost [21].

Flux growth offers several advantages over other crystal growth methods, especially for materials that present challenges when grown from the pure melt. The principal advantage of using a flux is that crystal growth occurs below the melting point of the target compound. This is essential for many materials, including those that *melt incongruently*, i.e., decompose upon heating into a different solid phase and a liquid of different composition. In such cases, direct growth from the melt leads to the formation of undesired secondary phases. Flux growth is also beneficial for *materials undergoing phase transitions*, as it enables crystal growth at temperatures below the transition, preventing severe strain or fracture. Furthermore, it is also suitable for *materials with high vapor pressures* at their melting points or those that have *volatile constituents*, which may change their chemical

composition when exposed to high temperatures. Additionally, flux growth is effective for *highly refractory materials* that require difficult or expensive techniques for crystallization from the melt.

Other advantages of flux crystal growth stem from the fact that the growing crystal is not subjected to steep temperature gradients. This allows the crystal to grow in an unconstrained manner, free from mechanical or thermal restrictions, which promotes the development of well-formed facets. Combined with the relatively low growth temperature compared to the melting point of the solute, this process often leads to improved crystal quality, including fewer point defects, lower dislocation densities, and reduced low-angle grain boundaries, compared to crystals grown directly from their own melt [23]. Flux growth also generally does not require costly equipment and thus represents a more accessible and cost-effective technique compared to many others that require highly specialized equipment [21].

Despite its advantages, flux growth faces several challenges and limitations. One of the primary difficulties is that the growth mechanism in fluxes is not well understood, largely due to the complexities involved in studying the in-situ solvent-solute interactions. This lack of understanding makes it challenging to predict and control the growth process effectively [22]. Another issue are possible flux inclusions in the crystals, which can lead to impurities that can significantly affect crystal quality [21]. The flux may become trapped within the growing crystal, introducing defects such as substitutional or interstitial incorporation of solvent ions, as well as microscopic or macroscopic inclusions of solvent or impurities. These inclusions can degrade the crystal properties. Additionally, non-uniform doping can occur, leading to inconsistencies in the material's composition. The growth process itself can be slow, and container-related issues—such as contamination from the crucible material—can further complicate the process [23]. Furthermore, growing significantly large crystals using the flux method is challenging, and the risk of contamination from both the flux and the crucible material can significantly hinder the final result. In addition, separating the grown crystals from the crucible can be challenging, with the potential for damage during the extraction process [21]. Optimizing growth parameters—such as the batch size, flux-to-material mass ratio (and, in the case of multi-component fluxes, the flux composition), as well as temperature-related factors like dwell temperature, dwell time, and cooling rate—is often a trial-and-error process [22]. Since these factors can dramatically influence the size, shape, and purity of the crystals, precise control over these parameters is difficult to achieve, requiring careful experimentation to fine-tune the conditions for optimal crystal growth.

An example of a complex and sophisticated crystal-growth technique, which requires specialized equipment, is the *optical floating zone method*. In the field of low-dimensional magnets and quantum spin liquids, it is commonly used for the growth of large single crystals suitable for neutron scattering experiments. It involves mounting two polycrystalline rods—the feed rod (above) and the seed rod (below)—with the desired crystal composition in a specialized floating-zone furnace. The material is heated until it becomes completely molten, forming the so-called *floating zone*, which acts as a liquid bridge connecting the two rods and is stabilized by surface tension. The polycrystalline material is fed into the zone, which slowly moves downwards as the growth of the single crystal gradually progresses. The technique offers two significant advantages that are crucial for maintaining crystal purity, making it particularly valuable for the synthesis of quantum materials. Firstly, it enables a crucible-free growth, eliminating a major source of extrinsic impurities. Secondly, it facilitates zone-refinement: if the equilibrium solubility of impurities is lower in the solid than in the melt, the impurities are progressively removed from the growing crystal and accumulate in the molten zone, leading to a significant purification of the material [20]. Given the large number of parameters that need to be

considered, the technique is relatively complex. Examples of these parameters are the feed rod quality, the rotational speed, the growth rate and the temperature profile of the zone. The growth process can be carried out across a broad temperature range up to 3000 °C [19]. Extremely high growth temperatures, which exceed 3000 °C, can be reached using focused laser sources [24]. The technique is not suitable for materials with high viscosity, low surface tension as well as for compounds that undergo phase transitions upon cooling, which often results in structural failure after the growth [25]. Although not employed within the scope of this dissertation, the technique was briefly presented due to its significance in the first part of the dissertation.

1.7 Scope of the Dissertation

In low-dimensional magnetism, bridging the gap between theoretical models and experimental realization presents a significant challenge. While theoretical descriptions in one-dimensional systems are relatively well understood, real materials often exhibit additional complexities, which complicate direct comparisons with idealized models. Transitioning from one to two-dimensional magnetism, the situation becomes increasingly intricate. The increased degrees of freedom and enhanced quantum fluctuations open the door to complex ground states, exotic quasiparticles, and many-body interactions, amplifying the difficulty of developing accurate theoretical models that fully capture the magnetism of these compounds.

Despite these challenges, certain compounds provide rare exact realizations of theoretical models. One notable example is $SrCu_2(BO_3)_2$, a two-dimensional frustrated antiferromagnet in which frustration arises from competing interactions on a square lattice [6]. This material constitutes the exact experimental realization of the Shastry-Sutherland model [26], which describes a set of orthogonal spin dimers on a square lattice, where the ground state is a product of dimer singlets [27]. As such, $SrCu_2(BO_3)_2$ serves as an exemplary system for comparing theory and experiment in two-dimensional magnetism.

A fundamental characteristic of certain low-dimensional antiferromagnets with a spin-singlet ground state is the presence of a *spin gap* in the excitation spectrum. This gap represents a finite energy difference between the ground state and the first excited magnetic state. Conventional antiferromagnets typically exhibit gapless excitations, allowing spin fluctuations to occur at low energies. However, in systems such as spin chains, ladders, and certain frustrated magnets, such as $SrCu_2(BO_3)_2$, quantum effects can open a spin gap, requiring a finite amount of energy to excite the system. This phenomenon is closely linked to exotic quantum states, including spin-liquid phases, dimerized states, and the Haldane phase in integer-spin chains. A spin gap suppresses low-temperature magnetic susceptibility and specific heat, distinguishing these materials from classical antiferromagnets. Chemical doping is an effective way to tune the spin gap and control the magnetic properties of a compound. Another intriguing quantum property of low-dimensional magnets, which was first observed in $SrCu_2(BO_3)_2$, is the appearance of *magnetization plateaus* in the magnetization spectrum [28]. The plateaus occur at specific fractional values of the saturation magnetization, such as 1/8, 1/4 [28] and 1/3 [29], as a consequence of magnetic frustration [14].

Importantly, the ground state of $SrCu_2(BO_3)_2$ lies in close proximity of a potential quantum critical point that could separate the singlet-dimer phase from other competing phases [30], sparking interest in tuning the ground state in order to realize novel quantum states. One promising route for such tuning is chemical substitution. In analogy with the nomenclature commonly used for oxide materials with multiple cation sublattices [18], the Sr^{2+} and Cu^{2+} crystallographic positions are referred to as the *A-site* and *B-site*,

respectively. Theoretical predictions suggest that A-site aliovalent doping, where Sr^{2+} is replaced with ions such as La^{3+} or Na^{+}, may promote the emergence of unconventional superconductivity, while B-site isovalent substitution of Cu^{2+} with nonmagnetic ions such as Mg^{2+}, also referred to as magnetic dilution, could lead to a quantum spin liquid state [31]. However, these predictions remain largely unverified.

The first part of the dissertation experimentally investigates the effects of chemical substitution on the structure and magnetic properties of the parent compound, focusing on the three dopants introduced above, namely aliovalent La^{3+} or Na^{+} replacing Sr^{2+} on the A-site and isovalent Mg^{2+} replacing Cu^{2+} on the B-site. A broad range of nominal doping concentrations is systematically explored. The studies combine bulk and local probes and provide information on the dopant incorporation into the parent structure, which remained unexplored in earlier studies. In addition, flux method is introduced as an alternative route to optical floating zone growth to obtain La-doped $SrCu_2(BO_3)_2$ single crystals.

The second part of the dissertation focuses on single-crystal growth of selected members of the rare-earth (RE) heptatantalate family, $RETa_7O_{19}$, where RE represents a rare-earth element. This is a class of two-dimensional frustrated antiferromagnets, realized on a perfect triangular lattice. Recently, $NdTa_7O_{19}$ has been identified as a new type of QSL candidate – the first experimental realization of the perfect triangular-lattice antiferromagnet with dominant Ising-like spin correlations [32]. Thus far, magnetic properties of $NdTa_7O_{19}$ have only been assessed on a polycrystalline sample. Multiple magnetic measurements indicated the absence of long-range magnetic order, suggesting a dynamical ground state [32]. However, a comprehensive understanding of such states requires investigations on high-quality single crystals, which enable precise determination of magnetic anisotropy and momentum-resolved studies of spin correlations. The dissertation focuses on the optimization of a flux-growth procedure for $NdTa_7O_{19}$, aiming to provide large, high-quality single crystals suitable for multiple magnetic measurements, allowing a detailed characterization of the ground state. The crystal growth protocol developed in this study has been extended to three other members of the rare-earth heptatantalate family, $ErTa_7O_{19}$, $GdTa_7O_{19}$ and $DyTa_7O_{19}$, laying the foundation for future detailed characterizations of magnetism in these compounds and studies of the role of the rare-earth ion in determining their magnetic behavior.

This Section summarizes the two main research directions of the dissertation. More detailed motivation and background for each subtopic are provided in Section 3.1 for chemical doping of $SrCu_2(BO_3)_2$ and Section 4.1 for single-crystal growth of $RETa_7O_{19}$ as well as in the introductions of the individual manuscripts included in each chapter.

1.8 Characterization Methods

This Section provides a brief description of the structural and magnetic characterization methods pertinent to this dissertation.

1.8.1 Structural Characterization

X-ray diffraction (XRD) is a fundamental non-destructive technique used to analyze the crystal structure of solid materials. Upon interacting with a sample, X-rays scatter according to Bragg's law:

$$n\lambda = 2d\sin\theta. \tag{1.15}$$

Here, n represents an integer, λ is the wavelength of the incident beam in nm, d is the interplanar distance in nm and θ the diffraction angle in degrees. The result of an XRD analysis is a diffraction pattern that is characteristic to the analyzed compound.

Single-crystal X-ray diffraction (SCXRD) is employed to determine the precise atomic arrangement within a crystal by analyzing its three-dimensional diffraction pattern of discrete Bragg reflections. The resulting intensity data are subsequently used for structure solution and refinement, yielding the atomic positions, bond lengths, and angles with high accuracy.

Laue X-ray diffraction (Laue XRD) involves exposing a single crystal to a polychromatic X-ray beam, generating a pattern of discrete diffraction spots corresponding to reflections from multiple crystallographic planes simultaneously. Analysis of the Laue pattern provides information on the crystal orientation, point-group symmetry, and lattice parameters, making the technique particularly valuable for aligning single crystals prior to comprehensive characterization.

Powder X-ray diffraction (**PXRD**) is a standard technique for the analysis of polycrystalline samples, primarily utilized for phase identification, allowing verification of the formation of the target phase and detection of secondary phases or impurities by comparing the resulting diffraction pattern with reference databases. The weight fractions of the present phases can also be quantified by performing a quantitative phase analysis after the data collection, typically by Rietveld refinement. From the peak positions and peak shapes, information on multiple properties of the solid material can be obtained such as the crystallite size, shape and microstrain. If single crystals are not available, the unit cell parameters of a new phase can also be determined from powder data through indexing. However, compared to single-crystal diffraction, structure solution from powder data is considerably more challenging. PXRD is therefore not a primary technique for structure determination, mainly due to the loss of directional information. This loss can be understood by considering the respective representations of reciprocal space in single-crystal and powder diffraction. In single-crystal diffraction, the periodic arrangement of atoms in the crystal lattice leads to reflections located at well-defined positions in three-dimensional reciprocal space. These reflections are observed only when the corresponding reciprocal lattice points satisfy the diffraction condition, i.e., when they intersect the Ewald sphere. Conversely, in the case of powder diffraction, the situation differs as the X-rays diffract from a large number of crystallites with random orientations. For any given set of lattice planes (hkl), there will always be a number of crystallites fulfilling the Bragg condition, resulting in a spherical distribution of intensity in reciprocal space rather than discrete points. These spherical surfaces intersect the Ewald sphere, generating Debye–Scherrer cones, which appear as rings on a two-dimensional detector. Upon radial integration, these rings are converted into a one-dimensional diffraction pattern of intensity as a function of the scattering angle (2θ). This averaging over all orientations effectively reduces the three-dimensional reciprocal space information to a one-dimensional profile, resulting in a fundamental loss of directional information. As the diffraction angles are determined solely by the interplanar spacing d, reflections originating from different sets of lattice planes that share identical d-values coincide at the same 2θ position. This results in peak overlap, which can affect phase identification or quantitative analysis. *Multiplicity overlap* appears in high-symmetry systems, such as cubic, where multiple symmetry-equivalent sets of lattice planes, such as (100), (010) and (001) or (110), (101) and (011), have identical d-spacings, and therefore overlap in the powder diffraction pattern. In contrast, lower-symmetry systems feature a larger number of structurally unrelated reflections, which may coincidentally exhibit very similar d-spacings, resulting in *accidental overlap*. Laboratory PXRD typically uses fixed-wavelength X-rays from sealed tube or rotating anode sources, while a significantly improved resolution, faster data collection,

and better detection of minor phases can be obtained using synchrotron PXRD, which provides higher intensity and tunable wavelengths [33].

1.8.2 Microstructural Characterization

Another technique that utilizes X-rays is **Energy-Dispersive X-ray Spectroscopy (EDS)** combined with **Scanning Electron Microscopy (SEM)**, which provides complementary information to PXRD by offering insights into the elemental composition and morphology of a sample [34]. High-resolution SEM imaging provides detailed insights into the surface morphology of the sample, allowing for the visualization of surface features at various scales. This is achieved by systematically scanning a focused beam of accelerated electrons across the specimen surface. The interaction of the electron beam with the sample generates several types of signals, including secondary electrons, backscattered electrons, characteristic X-rays, and photons of various energies, which originate from specific interaction volumes within the material. The most commonly used imaging signals are secondary and backscattered electrons. Secondary electrons, emitted from a shallow region near the beam impact area, provide detailed information on surface topography and produce the characteristic three-dimensional appearance of SEM images due to the large depth of field and shadowing effects. Backscattered electrons, originating from deeper regions of the sample, generate atomic-number contrast, causing heavier elements to appear brighter and lighter elements darker. SEM imaging thus enables visualization of microstructural features, including morphology and phase inhomogeneities [34]. Energy-dispersive X-ray spectroscopy (EDS) complements SEM imaging by providing elemental analysis. The primary electron beam ejects inner-shell electrons from the sample, and the resulting vacancies are filled by higher-energy electrons, emitting X-rays characteristic of each element. These X-rays are detected by a semiconductor detector, producing a spectrum that enables identification and semi-quantitative analysis of the elements. By scanning the electron beam across the sample surface, EDS can also generate elemental maps, revealing the spatial distribution of elements and detecting inhomogeneities, segregations or inclusions. This technique is thus valuable for confirming dopant incorporation in the targeted material and providing a semi-quantitative estimate of the effective doping level [34].

1.8.3 Magnetic Characterization

The DC (static) **magnetic susceptibility** (χ), as defined in Eq. (1.8), is a fundamental probe for studying bulk magnetism of low-dimensional and frustrated magnets. Experimentally obtained susceptibility values provide insight into the strength of magnetic interactions, the presence or absence of long-range order (LRO) at finite temperatures or under an applied magnetic field, and phase transitions between ordered and disordered states [19]. Additionally, magnetic susceptibility measurements can be used to determine the frustration index [4].

A high-resolution local probe that provides information on paramagnetic species in low-dimensional magnets is **electron spin resonance spectroscopy (ESR)**, also known as **electron paramagnetic resonance spectroscopy (EPR)**. The fundamental principle of ESR is based on the interaction between unpaired electron spins and an external magnetic field. In such a field, the electron magnetic moment adopts discrete orientations parallel or antiparallel to the field direction, resulting in Zeeman splitting of the spin energy levels. During an ESR experiment, a paramagnetic species—such as magnetic ions in low-dimensional magnets—is exposed to microwaves at a fixed frequency while the external magnetic field is gradually increased. When the applied field matches the energy difference

between the spin-up and spin-down states of the unpaired electrons, microwave absorption occurs, causing some spins to transition from the lower to the higher energy state. This absorption is detected as an ESR signal, which is typically displayed as the first derivative of the absorption spectrum to facilitate parameter analysis. Three key parameters are commonly derived from ESR measurements:

- ESR linewidth, ΔB or ΔB_{pp} (peak-to-peak linewidth), measured in Gauss (G) or Tesla (T): The linewidth is related to the relaxation time of the higher spin state to transition back to the ground, low-spin state. This is further correlated to the strength of magnetic interactions in the system, where stronger interactions result in a broader linewidth.
- *g*-factor (dimensionless): This parameter provides information about the local environment of the spins and the presence of internal magnetic fields in the system. Since the *g*-factor is characteristic of different paramagnetic centers, it can also aid in identifying those in the specimen. The *g*-factor value can be determined by the following equation:

$$g = \frac{h\nu}{\mu_B B_0}, \tag{1.16}$$

  where h represents the Planck constant ($\approx 6.626 \cdot 10^{-34}$ J s), ν the frequency of microwaves in Hz, μ_B the Bohr magneton ($\approx 9.274 \cdot 10^{-24}$ J/T) and B_0 the applied external magnetic field, measured in T.
- ESR intensity: The intensity is directly proportional to the number of spins which transitioned into a high-spin state, resulting in the signal, as well as to the probability of the observed transition [35].

Chapter 2

Aims and Hypotheses

2.1 Aims

The goals of this dissertation have been set as follows:
1. To experimentally verify theories which predict realizations of superconductivity for substituting Sr^{2+} ions in $SrCu_2(BO_3)_2$ with aliovalent cations, such as La^{3+} or Na^{+}, and quantum spin liquid state for substituting Cu^{2+} ions with isovalent nonmagnetic counterparts such as Mg^{2+}, i.e., magnetic dilution.
2. To determine the effect of La, Na and Mg-doping of $SrCu_2(BO_3)_2$ on the structure and magnetism of the parent compound.
3. To develop a flux method to grow doped $SrCu_2(BO_3)_2$ single crystals.
4. To develop a flux method and establish an approach to grow high-quality $NdTa_7O_{19}$ single crystals with sizes suitable for multiple measurements, allowing a full magnetic characterization of the disordered ground state.
5. To develop methods to grow other rare-earth heptatantalates, $RETa_7O_{19}$, such as RE = Er, Gd, Yb, Dy, with sizes suitable for multiple magnetic characterizations, starting from the flux method, established for the growth of $RETa_7O_{19}$ crystals.
6. To determine the magnetic ground state of the $RETa_7O_{19}$ candidates.
7. To investigate the phase relationships in RE_2O_3–Ta_2O_5 systems.

2.2 Hypotheses

The following hypotheses will be tested in the dissertation:
1. A-site charge- or hole-doped $SrCu_2(BO_3)_2$, achieved through substitutions of Sr^{2+} with aliovalent ions, can lead to unconventional superconductivity.
2. B-site doping, i.e. magnetic dilution, of $SrCu_2(BO_3)_2$, achieved through substitutions of Cu^{2+} with isovalent ions, can result in softening of the magnetic interactions in the system, a reduction of the spin gap and breaking of the Cu^{2+} spin dimers. The interactions between dimer-free Cu^{2+} ions could stabilize a novel magnetic state.
3. The nominal $SrCu_2(BO_3)_2$ doping limits can be pushed to higher values than previously reported.
4. Subtle changes in the $SrCu_2(BO_3)_2$ unit cell parameters and unit cell volume are expected upon doping.
5. $SrCu_2(BO_3)_2$ single crystals with sizes suitable for magnetic characterization of the ground state can be grown by flux method.

6. Limited or no incorporation of La^{3+} in the $SrCu_2(BO_3)_2$ structure is expected in polycrystalline samples, but the incorporation of dopants can be facilitated during single crystal growth.
7. A flux method to grow high-quality $NdTa_7O_{19}$ single crystals with sizes suitable for a full magnetic characterization of a disordered magnetic ground state can be developed.
8. The habit of the flux-grown $NdTa_7O_{19}$ single crystals is expected to be of plate-like and hexagonal morphology, which can be influenced by altering the growth parameters.
9. Based on the flux method, developed to grow $NdTa_7O_{19}$ crystals, a flux method can also be established for the growth of other rare-earth heptatantalates, $RETa_7O_{19}$ with RE = Er, Gd, Yb, Dy, with sizes suitable for multiple magnetic measurements.
10. $RETa_7O_{19}$ single crystals will allow a more precise determination of their magnetic ground state compared to the polycrystalline form.

Chapter 3

Tuning the Magnetism of $SrCu_2(BO_3)_2$ by Chemical Doping

3.1 Motivation

Strontium copper orthoborate, $SrCu_2(BO_3)_2$, is a quasi-two-dimensional frustrated antiferromagnet [28], first synthesized by Smith and Keszler [36]. Since then, it has attracted widespread attention as the first experimental realization of the Shastry–Sutherland model, providing a rare opportunity for direct comparison between a theoretical model and experimental observations. The model, introduced in 1981 [27], describes a set of orthogonal spin dimers on a square lattice (Figure 3.1), with intradimer magnetic exchange coupling J and interdimer magnetic exchange J'. A more detailed description with the corresponding Hamiltonian, the $SrCu_2(BO_3)_2$ structure and a representation of the magnetic $Cu_2(BO_3)_2^{2-}$ layer, mapped onto the Shastry-Sutherland lattice, are provided in the Journal Article in Chapter 3.3. The Hamiltonian and the model are given in Section 1 (Introduction), while the $SrCu_2(BO_3)_2$ structure is displayed in Section 3 (Results and Discussion) of the attached Journal Article.

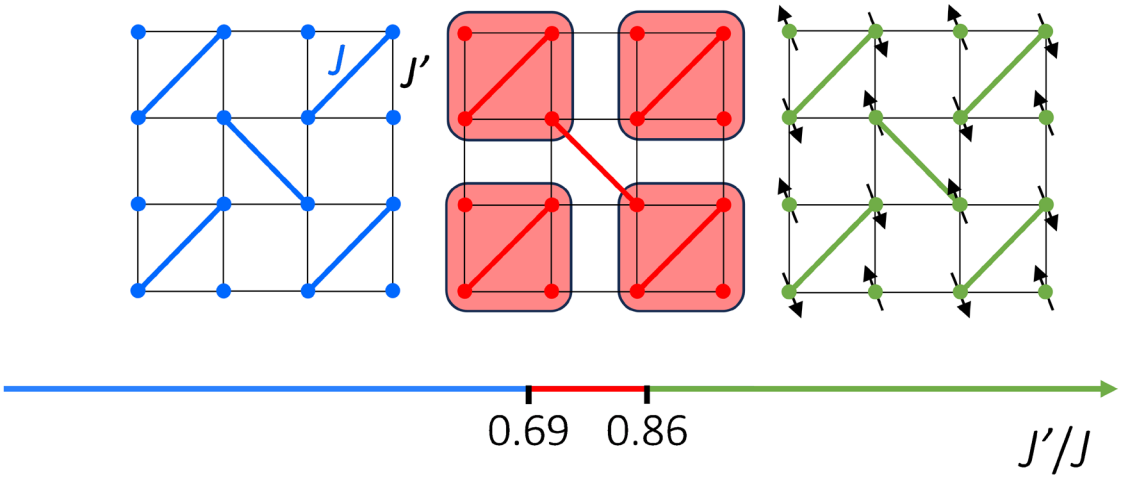


Figure 3.1: The ground state of a Shastry-Sutherland system as a function of J'/J ratio. The representation of the ground states was adapted from [37], while the critical J'/J values were taken from [38].

The ground state of a Shastry-Sutherland system is governed by the ratio J'/J. For $J'/J \lesssim 0.69$, the ground state is a dimer spin singlet. Increasing the ratio leads to a plaquette singlet state, whereas for $J'/J \gtrsim 0.86$, a Néel antiferromagnetic phase is stabilized (Figure 3.2) [30,38]. For $SrCu_2(BO_3)_2$, this ratio equals approximately 0.68 [26], placing the system in the dimer spin singlet regime, yet close to a quantum critical point that separates this state from competing magnetic phases. This proximity renders $SrCu_2(BO_3)_2$ an exceptional platform for tuning magnetic exchange couplings, aiming to reach the quantum critical point, potentially realizing novel exotic quantum states. One promising approach to achieve such tuning is chemical doping.

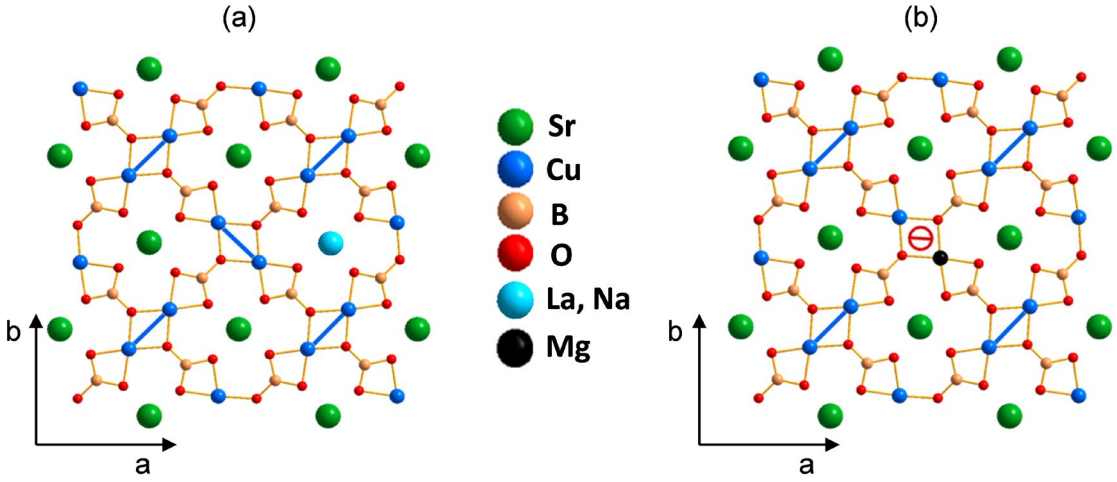


Figure 3.2: Representation of a) charge doping of $SrCu_2(BO_3)_2$ with La^{3+} or Na^+ and b) magnetic dilution through doping with Mg^{2+}.

Theoretical studies indeed predicted the emergence of exotic states upon chemical doping. A-site charge doping, where Sr^{2+} is replaced with aliovalent ions such as La^{3+} or Na^+ (Figure 3.2 a), was anticipated to induce RVB superconductivity by introducing mobile carriers in the system, enabling the localized spin pairs to become itinerant and thus analogous to Cooper pairs [31]. On the other hand, B-site magnetic dilution, i. e. substituting Cu^{2+} by isovalent nonmagnetic counterparts such as Mg^{2+} (Figure 3.2 b), was predicted to break the spin dimers, thereby liberating Cu^{2+} spins that may establish long-range correlations and quantum entanglement, potentially realizing a QSL state [31].

Despite these compelling theoretical anticipations of novel quantum states, experimental verifications remain limited. This Chapter presents systematic experimental investigations of the effects of substitutions with the aforementioned dopants on the structure and magnetic properties of $SrCu_2(BO_3)_2$. By accessing higher nominal dopant concentrations and utilizing local compositional and spectroscopic techniques such as EDS–SEM and ESR, this work expands the experimental scope beyond that of previous studies on doped $SrCu_2(BO_3)_2$. La-doping was investigated using $Sr_{1-x}La_xCu_2(BO_3)_2$ single crystals with lateral sizes up to 3 mm with nominal concentrations up to $x = 0.15$, grown by a flux method as a simpler alternative to the optical floating zone technique previously used for this doping in the literature. Meanwhile, Na- and Mg-doping is studied in polycrystalline samples, with nominal concentrations up to $x = 0.15$ in $Sr_{1-x}Na_xCu_2(BO_3)_2$ and $x = 0.10$ in $SrCu_{2-x}Mg_x(BO_3)_2$.

A detailed background and motivation for studies on doped $SrCu_2(BO_3)_2$ along with an overview of the existing literature, are provided in the Journal Article Introduction in Chapter 3.3, with further details on A-site doping in Journal Article Introduction in Chapter 3.2.1.

3.2 A-site Sr Aliovalent Substitutions in $SrCu_2(BO_3)_2$: Structural and Magnetic Effects

3.2.1 Influence of La-Doping on the Magnetic Properties of the Two-Dimensional Spin-Gapped System $SrCu_2(BO_3)_2$

This Section presents a systematic study of electron-doping effects on the structure and magnetism of $SrCu_2(BO_3)_2$, which experimentally examines theoretical predictions of possible unconventional superconductivity induced by aliovalent Sr^{2+} substitution with La. The study is conducted on single-crystalline $Sr_{1-x}La_xCu_2(BO_3)_2$ samples with nominal $x = 0.02$, 0.03, 0.04, 0.05, 0.10 and 0.15.

The optimization of a flux method for growing La-doped $SrCu_2(BO_3)_2$ single crystals, originally employed to obtain submillimeter-sized crystals for structure solution of undoped $SrCu_2(BO_3)_2$ [36], is first presented. The optimal conditions yielded blue plate-like La-doped single crystals of lateral dimensions up to 3 mm.

The samples show a subtle yet systematic decrease in unit cell volume, resulting from a partially successful substitution of Sr with La in the parent $SrCu_2(BO_3)_2$. The effective dopant incorporation increases with nominal concentration, although it remains below the nominal values.

The effective La-doping achieved by this method leads to a progressive reduction of the effective spin gap from 28.2(3) K to 20.3(4) K at nominal $x = 0.15$. This is accompanied by a subtle decrease in magnetic susceptibility maximum. Additionally, the emergence of dimer-free Cu^{2+} spins is observed at low temperatures, which seem to develop antiferromagnetic correlations below 5.5 K. The concentration of these spins progressively increases with nominal doping. It is further found that at low doping levels, the observed spin-gap reduction is primarily driven by Cu^{2+} $S = ½$ spin-dimer breaking, while the doping shows little influence on the intrinsic dimer lattice spin dynamics.

The doping thus affects the antiferromagnetic interactions, while no superconductivity is observed in the samples. Although the effective doping remains below the nominal values, this method represents an alternative to optical floating zone growth and may be applicable to other dopants. A further optimization may also allow growing crystals with a higher effective concentration of La.

This Section addresses Aims 1–3 and evaluates Hypotheses 1 and 3–6.

Published in: L. Šibav, T. Knaflič, G. King, Z. Jagličić, M. Koblar, K. Povarov, S. Zvyagin, D. Arčon and M. Dragomir, "Influence of La-doping on the magnetic properties of the two-dimensional spin-gapped system $SrCu_2(BO_3)_2$," *Inorg. Chem.*, vol. 65, no. 1, pp. 291−302, 2026, DOI: 10.1021/acs.inorgchem.5c04249 (IF = 4.7, 2024, Q1).

First author contribution: Conducted solid-state synthesis and optimized the flux method to grow La-doped $SrCu_2(BO_3)_2$ single crystals. Performed Rietveld refinement analysis of synchrotron XRD data, as well as compositional analysis and mapping using EDS-SEM on samples with nominal $x = 0.02$, 0.05, 0.10 and 0.15. Performed fitting of magnetic susceptibility data, ESR spectroscopy measurements and ESR data analysis. Prepared the sample (stacking of single crystals) for high-field ESR measurements. Co-conceived the structure of the manuscript, co-wrote the original draft, and participated in the review and editing process together with the co-authors.

Inorganic Chemistry

Open Access
This article is licensed under CC-BY 4.0

pubs.acs.org/IC Article

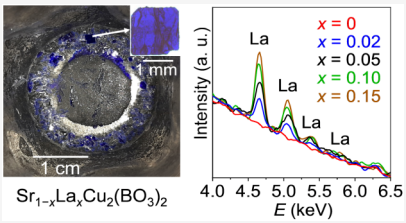
Influence of La Doping on the Magnetic Properties of the Two-Dimensional Spin-Gapped System $SrCu_2(BO_3)_2$

Lia Šibav, Tilen Knaflič, Graham King, Zvonko Jagličić, Maja Koblar, Kirill Povarov, Sergei Zvyagin, Denis Arčon, and Mirela Dragomir*

Cite This: *Inorg. Chem.* 2026, 65, 291−302 Read Online

ACCESS | Metrics & More | Article Recommendations | Supporting Information

ABSTRACT: Doping of the two-dimensional dimer antiferromagnet $SrCu_2(BO_3)_2$ has long been proposed as a potential route toward realizing resonating valence bond superconductivity in this system; however, experimental progress has remained limited. This study explores the effects of La doping on the ground state of $SrCu_2(BO_3)_2$ and reports the first flux growth of $Sr_{1-x}La_xCu_2(BO_3)_2$ single crystals with nominal doping levels up to $x = 0.15$. Powder X-ray diffraction and energy-dispersive X-ray spectroscopy confirm the successful incorporation of La on the Sr sites within the same tetragonal $I\bar{4}2m$ structure, although the effective doping was found to be <50% of the nominal concentration. La doping induces systematic changes in the magnetic properties of $SrCu_2(BO_3)_2$, with a reduction of the effective spin gap from 28.2 K for the undoped sample to 20.3 K for $x = 0.15$, as determined from the low-temperature magnetic susceptibility. The X-band electron spin resonance measurements reveal the emergence of unpaired Cu^{2+} spins, which develop antiferromagnetic correlations below ∼5.5 K. These findings corroborate the breaking of the local spin dimers in $SrCu_2(BO_3)_2$ induced by La doping. No superconductivity is observed across the entire doping range studied.



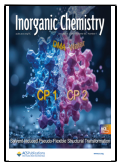
1. INTRODUCTION

In the last decades, considerable research has been devoted to low-dimensional quantum magnets, in particular, to those exhibiting a spin gap in their excitation spectra. In this context, charge-transfer insulators, such as Cu^{2+} oxides, have been extensively investigated due to their connection to cuprate superconductors. The discovery of high-T_C superconductivity in charge-doped cuprates in 1986[1] indicated the potential of chemical doping as an avenue for accessing novel exotic ground states in low-dimensional and frustrated quantum magnets.[2] This milestone spurred extensive theoretical work, proposing mechanisms for unconventional superconductivity, such as the resonating valence bond (RVB) model on the 2D frustrated spin lattice,[3,4] which predicts that upon doping, the charge-transfer gap closes. This would allow previously localized spin-singlet pairs (analogous to Cooper pairs) to propagate freely, leading to the onset of superconductivity.

While there have been several studies on gapped one-dimensional (1D) magnetic systems with spin-singlet ground states, such as spin-Peierls,[5] Haldane chains,[6] or spin ladders,[7] there are less examples of two-dimensional (2D) spin-gapped systems.[8−10] Thus, systems with a 2D spin-singlet ground state and frustrated spin configuration are of great interest. One notable representative of such systems is the frustrated antiferromagnet $SrCu_2(BO_3)_2$.[11−13] The unique structure of this material consists of Cu^{2+} ions ($S = 1/2$), which form a two-dimensional orthogonal dimer lattice that stacks along the *c*-axis. Each Cu^{2+}−Cu^{2+} pair constitutes a strongly antiferromagnetically coupled dimer within the *ab* plane, with the next-nearest exchange to the neighboring dimers comparable in strength. The resulting network maps directly onto the Shastry−Sutherland model, describing a frustrated quantum spin system characterized by competing intradimer (J) and interdimer (J') antiferromagnetic exchange interactions.[14−16] Due to the orthogonal arrangement of adjacent dimers, when the ratio J'/J is sufficiently small, i.e., $J'/J < 0.69$, the model takes an exact ground state comprising a product of singlet states on each dimer.[13] For intermediate values $0.86 > J'/J > 0.69$, a gapped plaquette singlet phase emerges.[17] For $J'/J > 0.86$, the system transitions to a Néel antiferromagnetic state,[17] with a quantum spin liquid phase possibly stabilized between the gapped plaquette-singlet and magnetically ordered regimes.[18,19]

Experimental values for $J'/J = 0.68$[17] locate $SrCu_2(BO_3)_2$ very close to the quantum phase boundaries either to a Néel ordered state or to the plaquette singlet state. Various experiments provide firm evidence for a dimer spin-singlet ground state with the gap $\Delta = 34(1)$ K.[20−22] Magnetization curves collected at temperatures well below the gap show quantized plateaus at 1/3, 1/4, or 1/8 of the Cu saturation moment due to the localized nature of excited triplets.[12,23] The

Received: September 10, 2025
Revised: December 10, 2025
Accepted: December 12, 2025
Published: December 29, 2025



ACS Publications
© 2025 The Authors. Published by American Chemical Society

https://doi.org/10.1021/acs.inorgchem.5c04249
Inorg. Chem. 2026, 65, 291−302

origin of these plateaus was attributed to the nearly localized nature of the triplet excitations.[13]

Both external pressure and chemical doping have proven effective in tuning the magnetic ground state of $SrCu_2(BO_3)_2$; pressure reduces the spin gap by modifying exchange interactions and pushing the system closer to phase boundaries,[24−29] while magnetic dilution—such as Mg substitution for Cu—suppresses the spin gap by disrupting the singlet dimer order.[30] According to theoretical predictions, a resonating valence bond superconductor might be realized as the ground state of $SrCu_2(BO_3)_2$ upon A-site electron or hole doping—specifically, by substituting the interlayer Sr^{2+} with an aliovalent ion, M^{3+} or M^{+}, respectively, resulting in $Sr_{1-x}M_xCu_2(BO_3)_2$.[31−33] However, despite its potential, A-site chemical substitution in $SrCu_2(BO_3)_2$ remains remarkably difficult. Previous studies on polycrystalline samples with various dopants, i.e., Ca, Ba, Al, La, Na, or Y, showed only subtle structural and magnetic changes, as the effective doping concentrations are consistently low. Moreover, challenges with efficient dopant incorporation and impurity phases highlighted the need for single crystals.[34,35] The optical floating zone method enabled the growth of doped single crystals with dopants such as Ba, Na, or La,[36−38] but these efforts echoed similar challenges: crystal growth was slow, highly sensitive to chemical composition and growth conditions, and often resulted in multigrain samples. Each dopant significantly altered the growth parameters, making reproducible, uniform doping difficult, even at low dopant concentrations. Similar issues were reported for B-site doping with isovalent, nonmagnetic ions,[30,39−41] emphasizing the need for further research and alternative growth methods.

Motivated by reports that La induces the most significant reduction of the spin gap among the A-site dopants,[35] this work focuses on La doping of $SrCu_2(BO_3)_2$. Previous investigations of both polycrystalline and single-crystalline samples—such as those prepared by Liu et al.[35] and Dabkowska et al.,[37] respectively—were limited in doping range, reaching only up to nominal $x = 0.10$, and hindered by complications including secondary phase formation and instabilities of the crystal growth. In this work, a flux method, previously used for the growth of submillimeter single crystals of undoped $SrCu_2(BO_3)_2$ using $LiBO_2$ as a flux,[11] was optimized to grow plate-like $Sr_{1-x}La_xCu_2(BO_3)_2$ single crystals (with $x = 0.02$, 0.03, 0.04, 0.05, 0.10, and 0.15), reaching lateral sizes up to 3 mm. La incorporation into the parent structure was unambiguously confirmed by powder X-ray diffraction (PXRD) and energy-dispersive X-ray spectroscopy (EDS). It was found that the effective doping was <50% of the nominal value. The limited incorporation of La nonetheless induced progressive changes in magnetic behavior. A gradual reduction of the effective spin gap—from 28.2 K for undoped $SrCu_2(BO_3)_2$ to 20.3 K at $x = 0.15$—was observed, accompanied by the emergence of dimer-free Cu^{2+} spins at low temperatures. X-band and high-field electron spin resonance (ESR) spectroscopy further showed evidence of antiferromagnetic exchange interactions between these spins below 5.5 K, which primarily account for the observed effective spin-gap reduction at low doping levels, while the intrinsic dimer lattice spin dynamics remain largely preserved.

2. EXPERIMENTAL SECTION

2.1. Synthesis. *2.1.1. Solid-State Synthesis.* Polycrystalline $Sr_{1-x}La_xCu_2(BO_3)_2$ samples with nominal x concentrations of 0, 0.01, 0.02, 0.03, 0.04, 0.05, 0.10, and 0.15 were first prepared using a conventional solid-state method.[30] High-purity $SrCO_3$ (Alfa Aesar, 99.994%), CuO (Aldrich, 99.99%), H_3BO_3 (Alfa Aesar, 99.9995%), and La_2O_3 (Alfa Division, 99.99%) were used as starting materials. Prior to use, La_2O_3 was preannealed in air at 1000 °C for 48 h.

The corresponding reactions can be described by the following equations:

$$SrCO_3 + 2CuO + 2H_3BO_3 \rightarrow SrCu_2(BO_3)_2 + CO_2 + 3H_2O \quad (1)$$

$$1-xSrCO_3 + 2CuO + 2H_3BO_3 + x/2\,La_2O_3 \rightarrow Sr_{1-x}La_xCu_2(BO_3)_2 + 1-xCO_2 + 3H_2O \quad (2)$$

2.1.2. Single-Crystal Growth. Single-crystal growth experiments were performed by optimizing a previously reported flux method[11] for growing undoped $SrCu_2(BO_3)_2$ for structure solution using lithium metaborate, $LiBO_2$, as the flux. Here, blue $Sr_{1-x}La_xCu_2(BO_3)_2$ powders of nominal doping concentrations $x = 0$, 0.02, 0.03, 0.04, 0.05, 0.10, and 0.15 that resulted from solid-state reactions were used as starting materials.

In a typical flux growth experiment, between 0.25 and 0.50 g of polycrystalline $Sr_{1-x}La_xCu_2(BO_3)_2$ was hand-homogenized together with the flux in an agate mortar at material-to-flux mass ratios of 2:1, 3:1, 4:1, 5:1, 7:1, or 10:1. The homogenized mixture was transferred into 20 or 30 mL platinum crucibles, covered with a platinum lid, and positioned inside an alumina crucible covered with an alumina cap. The crucible was then heated to 875 °C in a muffle furnace at a heating rate of 100 °C/h and left to dwell for 1, 2, or 3 h, followed by slow cooling to 600 °C with cooling rates of 1, 2, 3, 5, or 10 °C/h before being air-quenched to room temperature. A schematic representation of the experimental setup and the growth process is shown below (Figure 1). The resulting blue thin plate-like single crystals with lateral sizes up to 3 mm were separated from the crucible using deionized water in an ultrasonic bath.

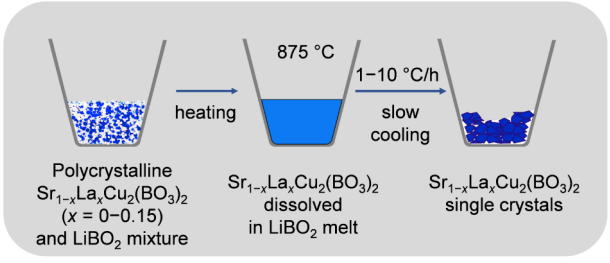


Figure 1. Schematic representation of the experimental setup and process for the $Sr_{1-x}La_xCu_2(BO_3)_2$ flux growth, illustrating three key steps: (left) preparation of the initial polycrystalline mixture of $Sr_{1-x}La_xCu_2(BO_3)_2$ and $LiBO_2$ flux, (middle) dissolution of the mixture in molten flux at a dwell temperature of 875 °C, and (right) formation of $Sr_{1-x}La_xCu_2(BO_3)_2$ single crystals during slow cooling.

2.2. Characterization. *2.2.1. Powder X-ray Diffraction (PXRD).* The phase composition of undoped and La-doped polycrystalline samples obtained after the solid-state synthesis, as well as powders from crushed single crystals, was first probed using laboratory powder X-ray diffraction (PXRD) with a Panalytical X'Pert Pro powder diffractometer and Cu−

https://doi.org/10.1021/acs.inorgchem.5c04249
Inorg. Chem. 2026, 65, 291−302

Kα1 radiation in the 20−120° 2θ range with a step size of 0.016° and a counting time of 300 s per step. Crushed single crystals were also analyzed by synchrotron PXRD; the data were collected at the Brockhouse high-energy wiggler beamline[42] at the Canadian Light Source (CLS) using an area detector and λ = 0.3502 Å radiation with Ni as a calibrant. Single crystals of each nominal doping concentration were crushed, placed into Kapton capillaries, measured in a 2θ range of 1−26° and binned into 0.01° steps.

A Rietveld least-squares method was used for structural refinements, which were performed using the program GSAS-II.[43]

2.2.2. Scanning Electron Microscopy (SEM) and Energy-Dispersive X-ray Spectroscopy (EDS). For chemical analysis and microstructural investigation, $Sr_{1-x}La_xCu_2(BO_3)_2$ single crystals were mounted on carbon tape and carbon coated by using a Balzers SCD 050 sputter coater Balzers SCD 050. The SEM imaging and EDS compositional analyses of the crystals were performed on two instruments: a Thermo Fisher Quanta 650 ESEM equipped with an energy-dispersive X-ray spectrometer (Oxford Instruments, AZtec Live, Ultim Max SDD 65 mm^2) and a field-emission-gun scanning electron microscope (FE-SEM; JEOL JSM-7600) equipped with an energy-dispersive X-ray spectrometer (EDS; INCA Oxford 350 EDS SDD) and electron backscatter diffraction (EBSD). The accelerating voltage used was 20 kV in all cases.

2.2.3. Magnetic Susceptibility. Magnetic susceptibility measurements were performed on a Quantum Design MPMS3 (undoped $SrCu_2(BO_3)_2$) and MPMS-XL-5 (La-doped $SrCu_2(BO_3)_2$) SQUID magnetometers in a temperature interval 2−300 K in a static magnetic field of 1 kG. An undoped $SrCu_2(BO_3)_2$ single crystal was fixed to a quartz holder with Apiezon-N grease and inserted into the magnetometer. The La-doped $SrCu_2(BO_3)_2$ single crystals were measured as polycrystalline samples, randomly stacked at the bottom of a Wilmad 4 mm Suprasil ESR sample tube. The temperatures corresponding to the susceptibility maxima, T_{max}, were determined by fitting the susceptibility data near the peak to a Lorentzian function.

2.2.4. Electron Spin Resonance Spectroscopy (ESR). Continuous wave (CW) electron spin resonance spectroscopy experiments were performed by using a conventional Bruker E500 spectrometer, operating in the X-band at the resonant frequency ν_L of 9.37 GHz. The spectrometer was equipped with a Varian TEM104 dual cavity resonator, an Oxford Instruments ESR900 cryostat, and an Oxford Instruments ITC503 temperature controller.

The measurements were conducted from room temperature down to 4 K with a typical modulation amplitude of 5 G, a modulation frequency between 50 and 100 kHz, and microwave power of 1−2 mW.

For each measurement, approximately 30 mg of polycrystalline undoped $SrCu_2(BO_3)_2$ and 5−30 mg of La-doped small single crystals (measured as quasi-polycrystalline samples) were placed in 4 mm Suprasil quartz ESR tubes (Wilmad). For samples with x = 0.10 and x = 0.15, the ESR spectrometer was equipped with a Bruker 4122SHQE cylindrical resonator operating at 9.4 GHz. Due to the higher sensitivity of this resonator, the latter two samples were measured using a low microwave power of 0.1 mW.

High-field ESR measurements were performed at the High Magnetic Field Laboratory (HLD), Helmholtz-Zentrum Dresden Rossendorf (HZDR) employing a transmission-type ESR spectrometer (similar to that described in ref[44]) in magnetic fields up to 16 T. Multiple crystals with a nominal La concentration of 0.03 were stacked using vacuum grease. A set of VDI microwave sources was used, allowing probe of magnetic excitations at different frequencies in the range from 140 to 495 GHz. Prior to the measurements of ESR spectra, the sample was slowly cooled to the base temperature T = 1.7−2.9 K.

3. RESULTS AND DISCUSSION

3.1. Synthesis and Crystal Growth. Solid-state synthesis of $Sr_{1-x}La_xCu_2(BO_3)_2$ with x = 0.01, 0.02, 0.03, 0.04, 0.05, 0.10, and 0.15 predominantly results in the tetragonal $SrCu_2(BO_3)_2$ phase with the $I\bar{4}2m$ space group, as confirmed by laboratory PXRD (Figure 2). A small amount of CuO is also present, consistent with previous reports on undoped polycrystalline samples.[11,45] A secondary La phase, $LaBO_3$, becomes noticeable when $x \geq 0.01$, suggesting that La does not incorporate into the parent structure but instead forms a La-rich impurity phase. A systematic increase in the concentrations of both $LaBO_3$ and CuO with increasing La content is also observed, supporting this conclusion. This is additionally substantiated by the absence of notable peak shifts in the PXRD patterns relative to the undoped sample.

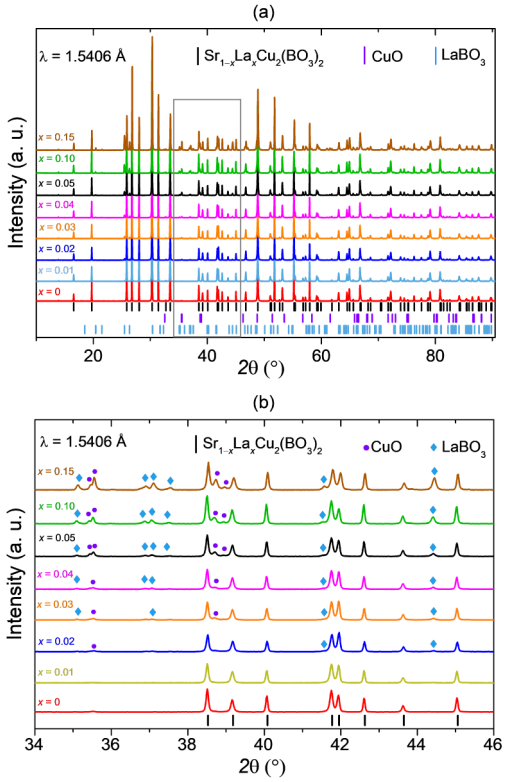


Figure 2. (**a**) Laboratory PXRD patterns of polycrystalline $Sr_{1-x}La_xCu_2(BO_3)_2$ with x = 0, 0.01, 0.02, 0.03, 0.04, 0.05, 0.10, and 0.15 as synthesized from the thermal solid-state chemistry route. All doped samples exhibit the main $SrCu_2(BO_3)_2$ phase, accompanied by minor amounts of unreacted CuO and $LaBO_3$ as secondary phases. (**b**) Enlarged view of the 34°−46° 2θ range marked with a gray rectangle in a), highlighting the reflections corresponding to the CuO and $LaBO_3$ impurities for improved clarity.

Since a direct solid-state synthesis proved ineffective for incorporating La, single-crystal growth was pursued as an

https://doi.org/10.1021/acs.inorgchem.5c04249
Inorg. Chem. 2026, 65, 291−302

alternative. Given the reported challenges associated with the optical floating zone growth,[37] the flux method emerged as a more practical and accessible approach for growing these crystals. This technique does not require highly specialized equipment and was considered likely to succeed as it had previously been used to grow crystals of the undoped phase.[11,46,47] In a previous attempt to synthesize $SrCu_2(BO_3)_2$[11] crystals intended for structure determination via single-crystal X-ray diffraction (SCXRD), $LiBO_2$ was used as flux. Two other subsequent studies reported the use of another borate flux, namely $Na_2B_4O_7$.[46,47] In the present study, both fluxes were tested in initial experiments; however, only $LiBO_2$ yielded crystals in our setup and was thus chosen for optimization and subsequent growth experiments. The starting materials for these crystal growth experiments were $Sr_{1-x}La_xCu_2(BO_3)_2$ powders prepared via solid-state synthesis.

The material-to-flux mass ratio, dwell time, dwell temperature, and cooling rate were optimized to result in blue plate-like undoped and La-doped $SrCu_2(BO_3)_2$ single crystals with lateral sizes of up to 3 mm (Figure 3 and Supporting Information, Figure S1). The optimal conditions within the tested parameters (Section 2.2), which yielded the largest crystals, are a material-to-flux mass ratio of 3:1 or 4:1, a dwell time of 2 h at 875 °C, and cooling from 875 to 600 °C at a rate of 2 °C/h, followed by air quenching to room temperature. Material-to-flux mass ratios of 5:1 or higher, as well as 2:1 or lower, result in crystals with minimal sizes. A faster cooling rate of 10 °C/h does not yield single crystals, whereas slower cooling rates of 5 or 3 °C/h produced crystals, albeit smaller compared to those formed at the optimal 2 °C/h rate. Further reduction of the cooling rate to 1 °C/h does not offer any additional benefit in crystal size. In contrast to the dwell time, which shows no notable effect, the material-to-flux mass ratio and cooling rate are identified as key factors influencing the crystal growth. We note that for undoped $SrCu_2(BO_3)_2$, the resulting crystals are significantly larger than those reported in ref[11], corroborating a successful optimization of growth conditions in this study.

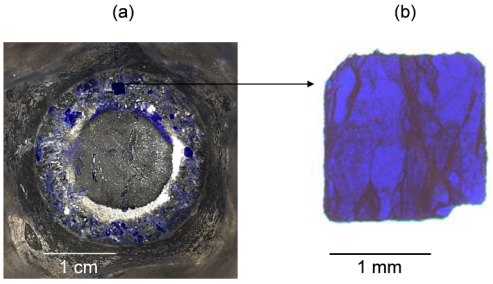


Figure 3. (**a**) Representative image of as-grown $Sr_{1-x}La_xCu_2(BO_3)_2$ single crystals on the walls of a Pt crucible immediately after air quenching. (**b**) Optical image of a selected single crystal after its separation from the flux.

The incorporation of La in the parent $SrCu_2(BO_3)_2$ structure during single-crystal growth is assessed by PXRD performed on crushed single crystals of $Sr_{1-x}La_xCu_2(BO_3)_2$ crystals with nominal x = 0−0.15 (Figure 4a). The absence of La-based secondary phases in normalized synchrotron PXRD patterns indicates a successful incorporation of lanthanum in the parent $SrCu_2(BO_3)_2$ structure upon single-crystal growth. At the highest nominal concentrations, x = 0.10 and 0.15, $LaBO_3$ reappears as a minor secondary phase, as previously detected in polycrystalline samples prepared by the thermal solid-state chemistry route. Its presence is likely due to residual unincorporated $LaBO_3$ particles remaining on the crystal surfaces, as ultrasonication—used to separate the crystals from the flux after growth—was kept brief to avoid damaging the thin, plate-like crystals. This interpretation is further supported by EDS analysis (discussed in the next section), where $LaBO_3$ particles are observed on the surface of crystals with these nominal doping concentrations. Unreacted CuO is detected in all samples, originating from the crystal surfaces, as suggested by EDS analysis and prior reports.[11]

A detailed summary of Rietveld refinement profiles and resulting structural parameters is available in the Supporting Information (Supporting Information, Figure S2 and Tables S1 and S2). Rietveld refinement analyses with the $I\bar{4}2m$ space

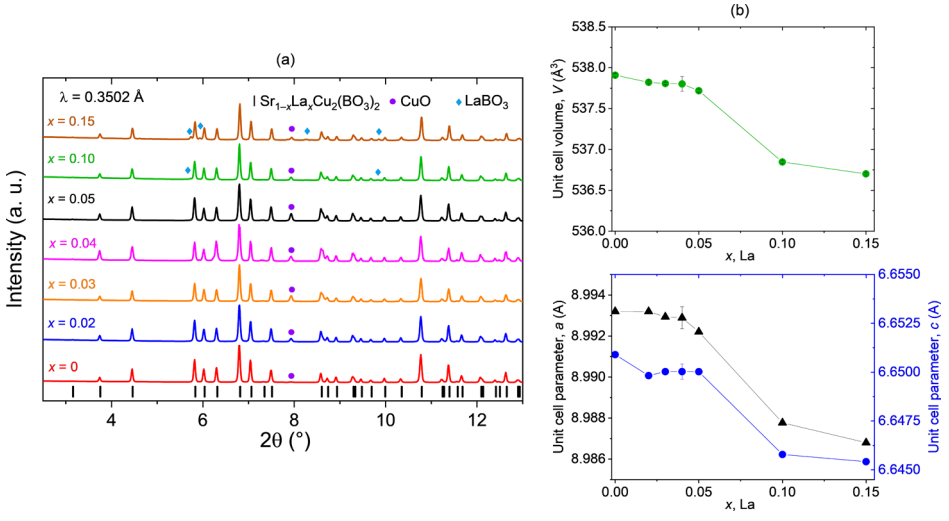


Figure 4. (**a**) Synchrotron (λ = 0.3502 Å) PXRD of $Sr_{1-x}La_xCu_2(BO_3)_2$ crushed single crystals with nominal x = 0−0.15. The presence of the main phase, $SrCu_2(BO_3)_2$, is observed along with a small fraction of unreacted CuO. A few peaks corresponding to the $LaBO_3$ secondary phase are also noticed at the highest two nominal concentrations, x = 0.10 and x = 0.15, with the former being barely detectable. (**b**) The unit cell volume decreases with increasing nominal La doping, consistent with the smaller ionic radius of La^{3+} compared to that of Sr^{2+}.

https://doi.org/10.1021/acs.inorgchem.5c04249
Inorg. Chem. 2026, 65, 291−302

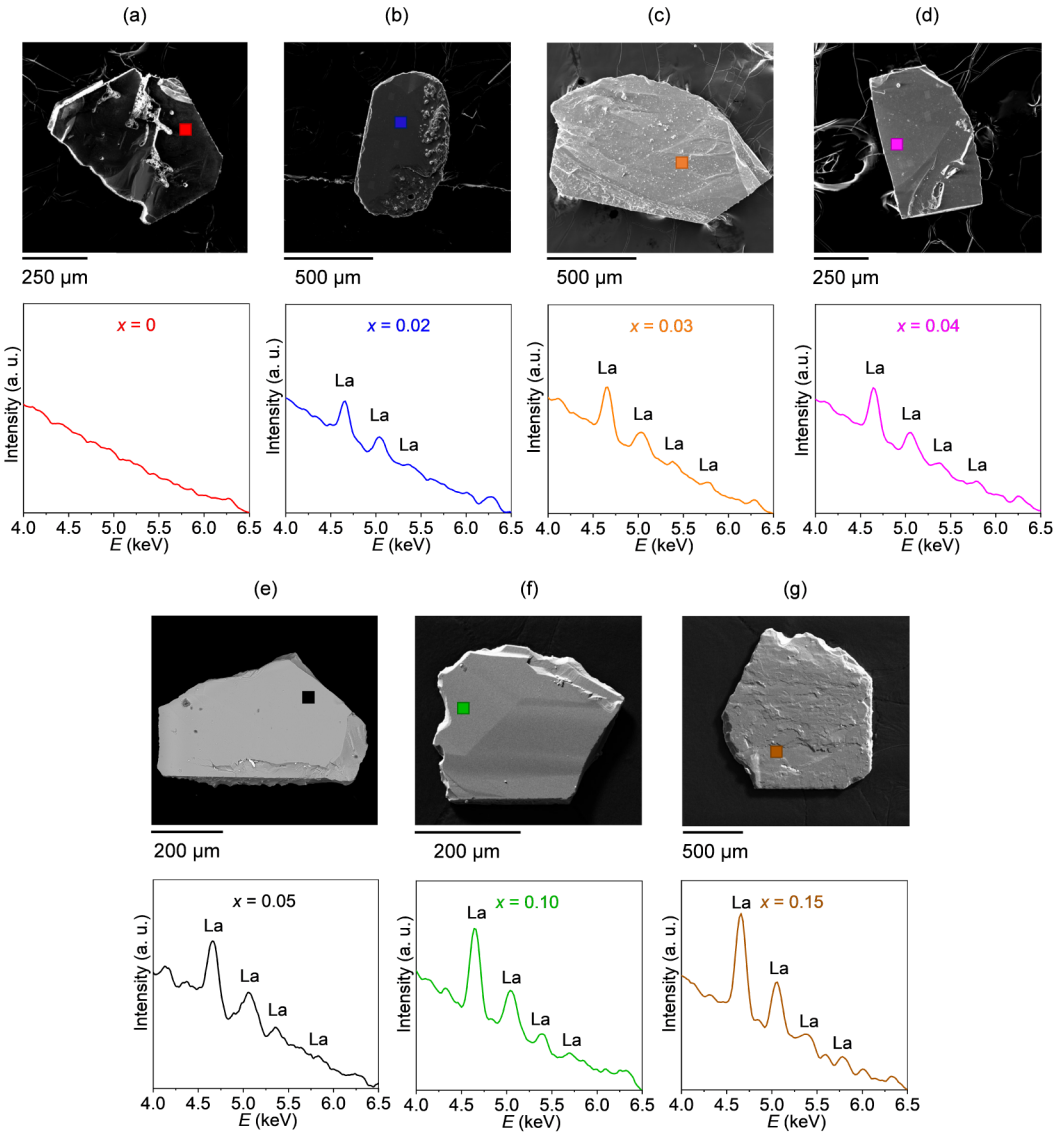


Figure 5. (a–g) Representative EDS point analysis spectra for $Sr_{1-x}La_xCu_2(BO_3)_2$ single crystals with x = 0–0.15. The corresponding SEM images for each doping concentration are displayed above the EDS spectra with squares indicating the selected regions for the point analysis.

group (Supporting Information, Table S1) reveal a decreasing trend in the unit cell parameters and volume as a function of nominal doping concentration (Figure 4b). This trend is consistent with expectations based on the ionic radii of the substituting ions, where Sr^{2+} (1.26 Å, coordination number CN = 8) is partially replaced by La^{3+} (1.16 Å, CN = 8). Specifically, the unit cell volume decreases from 537.91(2) $Å^3$ for the undoped sample to 536.70(1) $Å^3$ for the sample with nominal x = 0.15, corresponding to a slight volume reduction of 0.22%, which suggests minimal but clearly detectable structural distortion. A small decrease in the unit cell volume is observed up to x = 0.05, followed by a more pronounced reduction for x = 10 and x = 0.15. This aligns well with the trends observed in the EDS and magnetic susceptibility measurements, as well as with literature reports on doped crystals with nominal x = 0.05, grown by the optical floating zone method,[37] which also showed a decrease in unit cell volume relative to both undoped ceramics and single crystals.

3.2. Scanning Electron Microscopy (SEM) and Energy-Dispersive X-ray Spectroscopy (EDS). Previous studies on polycrystalline samples indicated that La does not incorporate in the structure during the solid-state synthesis.[48] This is also confirmed by our findings—see Section 3.1. However, SEM-EDS analyses performed on single crystals unambiguously prove the successful incorporation of La into the parent structure of $SrCu_2(BO_3)_2$ during single-crystal growth as La is consistently detected for all nominal doping concentrations (Figure 5).

The characteristic La emission peaks are clearly observed at 4.65 (Lα) and 5.04 keV (Lβ_1) in all doped samples. Although two other La peaks, the Lβ_2 emission at 5.38 keV and the La emission at 5.89 keV, are weaker than the main Lα emission line, they are still detectable for nominal $x \geq 0.03$. Additionally, a systematic increase in La peak intensity is observed with x, peaking at x = 0.15. A similar trend is also observed in elemental mapping analyses, which further reveals a relatively homogeneous distribution of La in all doped crystals and a systematic increase in effective doping concentration with nominal x.

A representative SEM image, elemental maps, and the summed EDS spectrum for a doped crystal with nominal x = 0.05 are shown below (Figure 6), with corresponding data for

https://doi.org/10.1021/acs.inorgchem.5c04249
Inorg. Chem. 2026, 65, 291−302

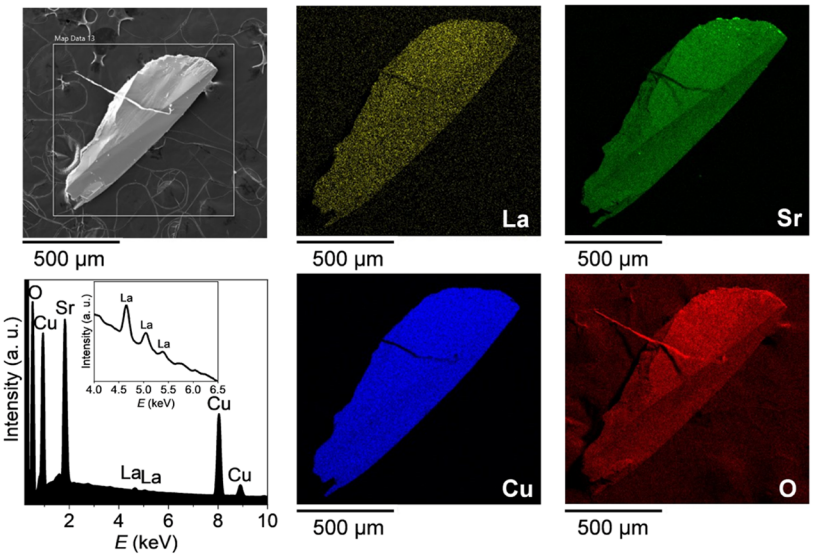


Figure 6. SEM image and EDS elemental mapping analysis of a $Sr_{1-x}La_xCu_2(BO_3)_2$ single crystal with nominal x = 0.05 reveal a relatively homogeneous distribution of La within the $SrCu_2(BO_3)_2$ matrix. The corresponding summed EDS spectrum clearly shows the presence of La emission lines. The inset shows a magnified region, where the La emission lines are clearly seen.

nominal x = 0.04 and 0.10 available in Supporting Information, Figure S3. Secondary phases detected in PXRD—$LaBO_3$ and CuO—are also observed on the surfaces of crystals starting from the nominal concentration of x = 0.04 for CuO (Supporting Information, Figure S3a) and x = 0.10 for $LaBO_3$. The $LaBO_3$ secondary phase becomes more visible for the highest nominal doping concentration of x = 0.15 (Supporting Information, Figure S4), in agreement with the PXRD results.

The average semiquantitative atomic percentages of Sr, Cu, O, and La in both undoped and La-doped $SrCu_2(BO_3)_2$ single crystals, obtained from SEM-EDS point analyses, are summarized in Supporting Information, Table S3. These values are compared with nominal values, i.e., the intended or theoretical amount of dopant defined by the chemical formulas. The table also includes additional ratios such as La/Cu, La/Sr, and Cu/Sr as well as semiquantitative estimates of effective La doping for each nominal concentration. The average La atomic percentage systematically increases with the nominal doping. The effective doping—i.e., the actual amount of dopant incorporated into the crystal structure—reaches approximately 50% of the nominal value for $x \leq 0.03$ (Supporting Information, Table S3). At higher doping levels (x = 0.05, 0.10, and 0.15), the effective doping continues to increase, albeit with smaller increments, reaching ~20% of the nominal values. Specifically, the effective doping was estimated to be 1.7(3) mol % for x = 0.05, 2.0(4) mol % for x = 0.10, and 2.7(3) mol % for x = 0.15 (Supporting Information, Table S3). While these EDS results confirm La incorporation into the $SrCu_2(BO_3)_2$ structure, they also indicate that doping is only partial, which emphasizes the challenges of chemical substitutions in this system. This finding aligns well with previous studies.[30,37,38]

3.3. Magnetic Susceptibility. Following the successful incorporation of La into the $SrCu_2(BO_3)_2$ structure, we next measured dc magnetic susceptibility in the 2–300 K temperature region, at a magnetic field of 1 kG. The behavior of the susceptibility curves (Figure 7) is consistent across all the nominal doping concentrations (measured up to x = 0.15)

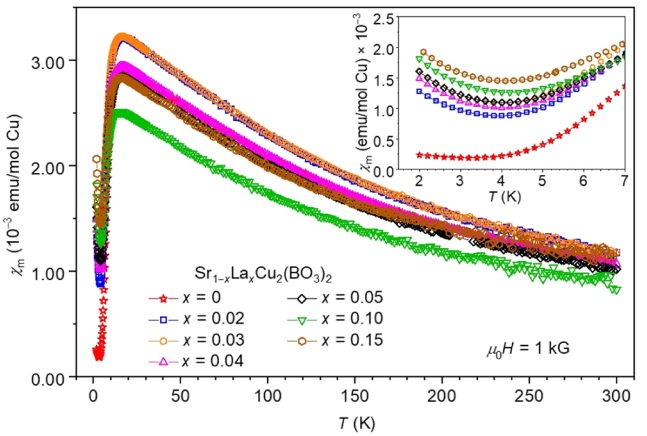


Figure 7. Temperature dependencies of magnetic susceptibility of $Sr_{1-x}La_xCu_2(BO_3)_2$ single crystals with nominal x = 0–0.15, measured at μ_0H = 1 kG. The inset magnifies the low-temperature region, which exhibits the Curie–Weiss upturn, and includes low-temperature fits based on eq 3, performed in the 2–6 K range with θ' fixed at −0.75 K.

and aligns well with previous reports in pristine and doped $SrCu_2(BO_3)_2$ samples.[35,37,38] Following the high-temperature Curie–Weiss region, a broad susceptibility maximum at temperature T_{max}, appears between 15.5 and 18.7 K. The values of T_{max} (Table 1) do not show significant changes with x, however, they exhibit a small decrease with the increasing nominal doping. At lower temperatures, the susceptibility exhibits a sharp suppression, indicative of the effective spin gap, followed by a low-temperature Curie–like upturn—a hallmark of unpaired Cu^{2+} S = 1/2 spins[35,37,38]—but which also includes a thermally activated contribution and a temperature-independent contribution from the ion cores (described by eq 3). The magnitude of this upturn systematically increases with the nominal La-doping concentration and is most pronounced at x = 0.15 (inset, Figure 7). The observed magnetic response is in good agreement with previous studies on La-doped single crystals.[37,38] The current study also shows that increasing nominal doping leads to a

https://doi.org/10.1021/acs.inorgchem.5c04249
Inorg. Chem. 2026, 65, 291–302

Table 1. Summary of Magnetic Parameters for $Sr_{1-x}La_xCu_2(BO_3)_2$ Single Crystals with Nominal x = 0–0.15[a]

$SrCu_2(BO_3)_2$ nominal doping	T_{max} (K)	Effective spin gap, Δ (K)	C' (emu K/mol Cu) low-T fit 2–3.4 K)	Estimated fraction of free Cu^{2+} spins (%)
x = 0	18.4(3)	28.2(3)	$1.05(7) \cdot 10^{-3}$	0.28(2)
x = 0.02	17.05(6)	24.7(2)	$4.3(2) \cdot 10^{-3}$	1.15(6)
x = 0.03	16.8(2)	23.0(2)	$5.4(2) \cdot 10^{-3}$	1.44(5)
x = 0.04	16.68(5)	23.1(3)	$5.1(2) \cdot 10^{-3}$	1.36(5)
x = 0.05	16.45(6)	22.1(2)	$5.6(2) \cdot 10^{-3}$	1.49(6)
x = 0.10	15.8(2)	20.8(1)	$6.9(2) \cdot 10^{-3}$	1.84(5)
x = 0.15	15.8(3)	20.3(4)	$9.2(4) \cdot 10^{-3}$	2.45(11)

[a]The characteristic temperature T_{max} is extracted from Lorentz fits to the magnetic susceptibility in the 15–21 K range. The effective spin gap is obtained from fits to the low temperature susceptibility data (2–6 K) using eq 3. The Curie constant C' is derived from Curie–Weiss fits to inverse susceptibility data at low temperature (2–3.4 K, Supplementary Information, Figure S5). The estimated fraction of free Cu^{2+} spins is derived from these fits.

higher concentration of free Cu^{2+} spins in the system, consistent with doping-induced Cu^{2+} spin-dimer breaking. A dimer breaking in Sr-site substituted samples was previously observed and directly probed by μSR in ref[38].

To estimate the evolution of the effective spin gap with La doping, low-temperature magnetic susceptibility data are fitted in the interval 2–6 K according to eq 3:[35]

$$\chi = \frac{C'}{T - \theta'} + ae^{-\Delta/T} + \chi_0 \quad (3)$$

The first term represents the spin-1/2 magnetic impurities, characterized by the Curie constant C' and their weak coupling captured by the Curie–Weiss temperature for the tail, θ'. The second term is the contribution from the antiferromagnetic dimer structure. The third term is a small diamagnetic contribution from the ion cores. The effective spin gap, Δ, is included in the thermally activated contribution. The results of the fits, the C', θ', and Δ parameters are presented in Supporting Information, Table S4. Due to a high correlation between the C' and θ' parameters, the fits are performed with θ' fixed at five different values from 0 to −1, with the fits results for θ' = −0.75 K being chosen as the most representative. The results reveal a gradual closing of the effective spin gap, Δ, from 28.2(3) to 20.3(4) K for nominal doping up to x = 0.15 (Table 1) relative to undoped $SrCu_2(BO_3)_2$. This finding is consistent with the results published in ref[35], where a similar

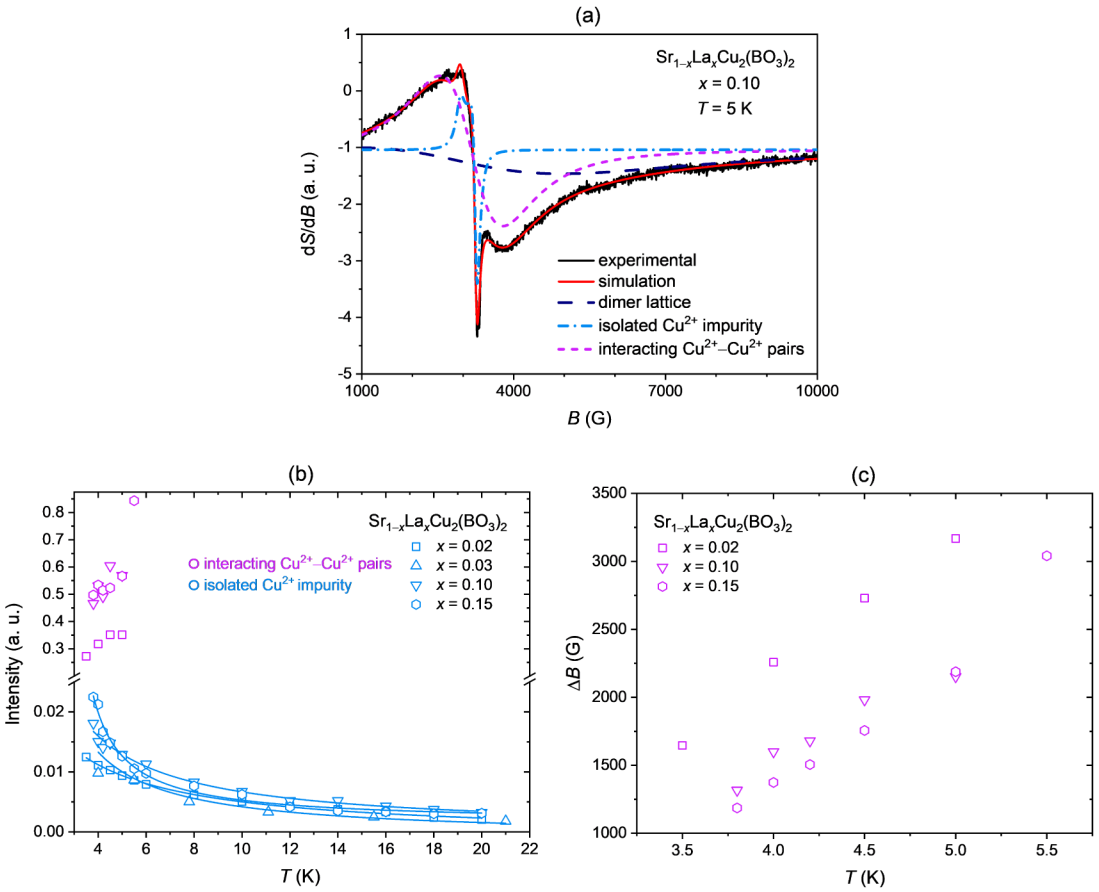


Figure 8. (**a**) X-band ESR spectrum of several $Sr_{1-x}La_xCu_2(BO_3)_2$ single crystals with x = 0.10 measured at 5 K. The corresponding simulation (red line) is composed of three Lorentzian components: (i) the broad dimer lattice signal (dashed dark blue lines), (ii) an anisotropic component attributed to the isolated Cu^{2+} impurity component (short dash-dot light-blue lines), and (iii) interacting Cu^{2+}–Cu^{2+} pairs that emerge between dimer-free Cu^{2+} spins (short dashed violet lines). (**b**) Temperature dependence of the signal intensities of the isolated Cu^{2+} impurity component and the interacting Cu^{2+}–Cu^{2+} pair component for selected nominal doping levels. (**c**) Temperature dependence of the line width ΔB of the interacting Cu^{2+}–Cu^{2+} pair component (iii) for x = 0.02, 0.10, and 0.15, showing a monotonic decrease with the decreasing temperature for all doping levels, consistent with the presence of antiferromagnetic exchange interactions between dimer-free Cu^{2+} spins.

https://doi.org/10.1021/acs.inorgchem.5c04249
Inorg. Chem. 2026, 65, 291–302

gap suppression for polycrystalline $Sr_{0.9}La_{0.1}Cu_2(BO_3)_2$ from 21.5 to 14.1 K was found. Specifically, the 7.4 K reduction in Δ observed in ref[35] equals the reduction observed in the current study for the nominal $x = 0.10$ sample.

The concentration of overall dimer-free Cu^{2+} spins in the La-doped samples is determined by fitting the linear 2−3.4 K temperature range of the inverse magnetic susceptibility data to a Curie−Weiss law (Supporting Information, Figure S5) similar to other reports.[41] The results of the fit (Table 1) show a general increase of the Curie constant C" with nominal doping. Specifically, a nominal doping of $x = 0.10$ approximately increases the concentration of dimer-free spins by a factor of ∼7 compared to the undoped crystal, rising from 0.28(2)% for the undoped system to 1.84(5)% for $x = 0.10$, and reaching 2.45(11)% for nominal $x = 0.15$. These values are in good agreement with the effective dopant concentrations obtained from EDS measurements (see Supporting Information, Table S3). Crystals with nominal $x = 0.04$ yield 1.36(5)%, which is about 2.5 times higher than the fraction of impurity spins in optical-floating-zone-grown crystals by Dabkowska et al.[37] (as reported in ref[38]). Note that the concentration of impurity spins observed in this study for La-doped samples is relatively small compared to that reported for Mg doping,[30] which suggests that La doping is more challenging.

3.4. X-Band Electron Spin Resonance Measurements (ESR). To gain deeper insights into the magnetism of La-doped $SrCu_2(BO_3)_2$, continuous wave X-band electron spin resonance (ESR) spectroscopy, a local probe technique well suited for detecting paramagnetic states in low-dimensional magnets,[49] is employed next. This study extends the use of ESR spectroscopy to La-doped $SrCu_2(BO_3)_2$—a system that has received little attention so far. Previous ESR studies have primarily focused on the undoped system,[48−52] with only one report on Mg-doped $SrCu_2(BO_3)_2$.[30]

In this study, temperature-dependent ESR spectra for La-doped single crystals with nominal $x = 0.02−0.15$ were measured down to approximately 4 K, and compared with the ESR data obtained on polycrystalline undoped $SrCu_2(BO_3)_2$ reported in the literature.[30] At high temperatures, the ESR spectra across all nominal doping concentrations closely follow the behavior observed in the undoped system (Supporting Information, Figure S6). The main signal, originating from the dimer lattice, broadens with a decrease in temperature, reflecting the development of spin correlations within the Shastry−Sutherland dimer lattice. At low temperatures, an additional component, only weakly observed in the undoped system at $T \leq 14$ K, emerges in the spectra of doped samples, at $T \leq 35$ K for nominal $x = 0.02$ and 0.03, and $T \leq 50$ K for higher nominal concentrations. As the nominal doping increases, this component becomes progressively more pronounced (Supporting Information, Figure S7). Its ESR signal intensity scaling with x aligns well with the increase of the Curie−Weiss upturn with nominal doping observed in low-temperature magnetic susceptibility, and further corroborates the presence of intrinsic Cu^{2+} impurities in the doped system as isolated, dimer-free Cu^{2+} spins emerging after the La doping. Furthermore, at the lowest investigated temperatures, $T \leq 5.5$ K, we observe the emergence of a third, broader component, which can be tentatively associated with the emerging correlations between dimer-free Cu^{2+} spins when their concentration increases.

For a quantitative analysis, the ESR spectra are fitted using up to three Lorentzian components depending on the temperature range (Figure 8a).

At high temperatures, only a broad line attributed to the Cu^{2+} dimer lattice is required. Below 50 K, an additional anisotropic component with axial g-factor anisotropy is included to account for the isolated Cu^{2+} intrinsic impurities. Here, $g_\parallel$ and $g_\perp$ represent the two g factor eigenvalues parallel and perpendicular to the crystallographic c axis, respectively. A corresponding uniaxial anisotropy is also applied to the line width, defined by $\Delta B_\parallel$ and $\Delta B_\perp$ for the field orientations along and perpendicular to the c axis, respectively. Below 5.5 K, a third broad isotropic Lorentzian line has to be introduced, which is tentatively assigned to the onset of emerging correlations between unpaired Cu^{2+} spins. The intensities of all three components, resulting from the fits, are normalized to the room temperature value for all samples.

At room temperature, the main dimer-lattice component is centered around $g \approx 2.1$. The line width, ΔB, remains similar across all nominal doping concentrations, ranging from 1350 to 1550 G (Supporting Information, Figure S8a). This matches the corresponding line width and g-factor values reported in the literature for undoped $SrCu_2(BO_3)_2$ powder.[49] Upon cooling, the line width of this component increases monotonically, saturating near 10 K at values between 4400 and 5100 G. This broadening reflects the gradual development of short-range antiferromagnetic correlations in the dimer lattice and becomes less dominant at low temperatures as the isolated Cu^{2+} impurity component begins to dominate the ESR response. The intensity of this component increases with decreasing temperature (Figure 8b), following a $1/T$ dependence across all nominal doping concentrations. The data are fitted using the Curie−Weiss law, yielding a Curie−Weiss temperature θ' between −2 and +2.5 K, effectively close to zero, confirming that the corresponding Cu^{2+} moments are only weakly interacting and supports their identification as isolated, dimer-free spins. Compared to the isolated Cu^{2+} impurity component, the intensities of the broader component assigned to liberated but interacting $Cu^{2+}−Cu^{2+}$ pairs, introduced in the low-temperature regime (3.5−5.5 K), are significantly higher across all doping concentrations (Figure 8b). Specifically, the interacting $Cu^{2+}−Cu^{2+}$ pair component intensity exceeds the isolated Cu^{2+} impurity component intensity by factors ranging from approximately 10 to 40, highlighting the emergence of magnetic correlations between dimer-free Cu^{2+} spins. These correlations become increasingly more prominent with a higher nominal doping. For instance, samples with $x = 0.10$ and 0.15 exhibit stronger intensities than $x = 0.02$, suggesting that higher nominal doping results in more pronounced $Cu^{2+}−Cu^{2+}$ interactions. Moreover, at higher nominal doping, these correlated states persist to higher temperatures, as evidenced by the interacting $Cu^{2+}−Cu^{2+}$ pair component up to 5.5 K for the $x = 0.15$ sample, compared to only up to 5 K for $x = 0.02$ and 0.10. This trend is further corroborated by the temperature dependence of the line width, ΔB, of the interacting $Cu^{2+}−Cu^{2+}$ pair component.

Overall, ΔB shows a systematic decrease with increasing doping concentration, as illustrated at 4 K (Figure 8c), where the line width reaches its highest value of 2260 G for $x = 0.02$, decreases to 1600 G for $x = 0.10$, and attains its lowest value of 1370 G for $x = 0.15$. Additionally, for each doping concentration individually, the line width exhibits a consistent monotonic decrease with decreasing temperature, indicative of

https://doi.org/10.1021/acs.inorgchem.5c04249
Inorg. Chem. 2026, 65, 291−302

the antiferromagnetic nature of the exchange interactions between dimer-free Cu^{2+} spins.[53,54] The *g*-factor of the interacting Cu^{2+}−Cu^{2+} pair component remains constant at approximately 2.12 for all doping levels across the whole temperature range (Supporting Information, Figure S8b).

Due to the large number of fitting parameters and their strong correlations, the line width and *g*-factor components of the isolated Cu^{2+} impurity component were partially constrained during analysis. Specifically, $\Delta B_{\parallel}$ was fixed across all data sets to ensure stable fitting. Throughout most of the temperature range, $\Delta B_{\perp}$ remained relatively constant, falling within the interval 150−200 G (Supporting Information, Figure S8c). However, below 5.5 K—coinciding with the emergence of component (iii)—a monotonic increase in $\Delta B_{\perp}$ was observed, providing an additional indication of developing correlations between dimer-free Cu^{2+} spin pairs. Similarly, $g_{\parallel}$ was fixed for all doping concentrations except for x = 0.02, where a gradual decrease was detected below 6 K. The perpendicular component, $g_{\perp}$, remained effectively constant around 2.065 across the full temperature range for all samples (Supporting Information, Figure S8d).

In contrast to the general trends observed across nominal x = 0.02−0.15, the spectra for nominal x = 0.05 deviate substantially for both the isolated Cu^{2+} impurity component and the interacting Cu^{2+}−Cu^{2+} pair component (Supporting Information, Figure S9a). Contrary to the rest of the samples, this sample exhibits a clear and distinct *g* factor anisotropy of the isolated Cu^{2+} impurity component, which allows a clear and unambiguous determination of both $\Delta B_{\parallel}$ and $\Delta B_{\perp}$. These line width components exhibit a substantial increase with decreasing temperature (Supporting Information, Figure S9b), exceeding the modest changes in the line width observed for the rest of the samples, which occur only below 5.5 K. The intensity of the isolated dimer-free Cu^{2+} component behaves similarly to the other samples (Supporting Information, Figure S9c), following a $1/T$ dependence and yielding a Curie−Weiss temperature, θ', close to 0. In contrast, the interacting Cu^{2+}−Cu^{2+} pair component for x = 0.05 shows further anomalies as its ΔB remains constant at a significantly lower value of approximately 750 G (Supporting Information, Figure S9d), deviating from the decreasing trend observed in the other samples.

In summary, X-band ESR measurements across all nominal La-doping concentrations reveal multiple components in the spectra: a broad signal from the spin dimer lattice, an anisotropic contribution, which denotes the presence of isolated Cu^{2+} impurities, and an additional low-temperature component arising from dimer-free Cu^{2+}−Cu^{2+} interactions. The evolution of the latter component below 5.5 K suggests antiferromagnetic correlations between interacting dimer-free Cu^{2+} spin pairs, which are enhanced with increasing doping.

3.5. High Magnetic Field Electron Spin Resonance Measurements. Magnetic susceptibility provides an indirect estimate of the spin gap or so-called "effective" spin gap through fitting low-temperature data. This effective gap represents an approximate or averaged measure of the gapped behavior of magnetic susceptibility and can be affected by the presence of in-gap states. As a result, even a modest density of localized spins or in-gap states can lower the effective gap as deduced from susceptibility fits while leaving the intrinsic singlet−triplet gap probed by the high-field ESR unchanged. The intrinsic or actual spin gap, defined as the excitation energy required for singlet−triplet excitation, can be directly determined using microscopic probes such as high-field ESR or inelastic neutron scattering. The first reported spin gap for $SrCu_2(BO_3)_2$ was Δ = 34 K in 1999.[20] In the present study, to obtain a more precise measurement of the spin gap for La-doped $SrCu_2(BO_3)_2$, a group of stacked single crystals with nominal x = 0.03 was analyzed using high-field ESR at multiple frequencies up to 500 GHz and magnetic fields up to 160 kG (Figure 9a).

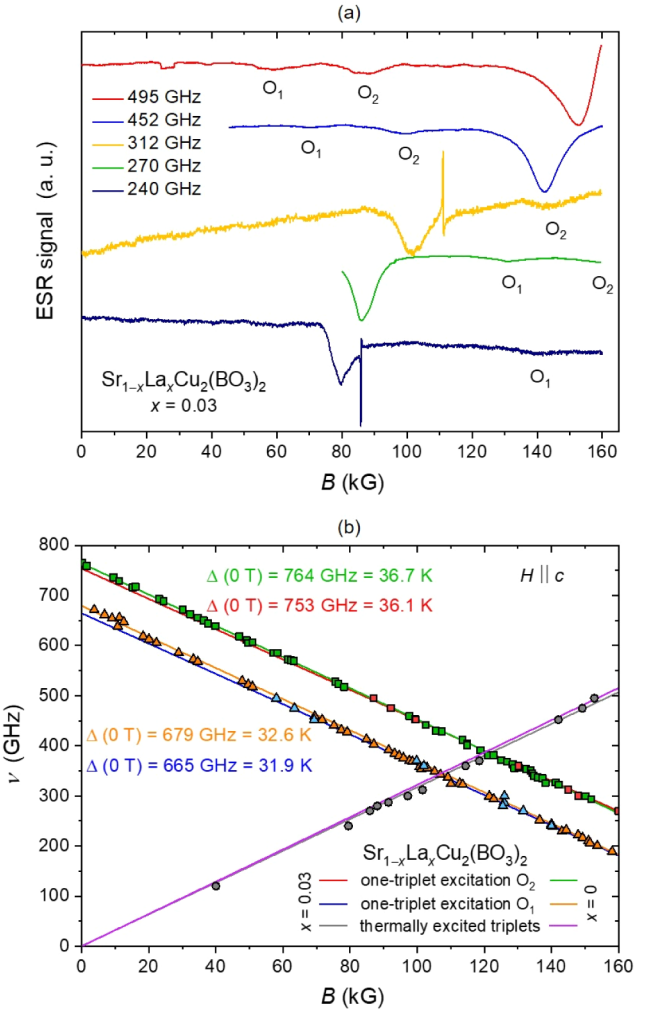


Figure 9. (**a**) Low-temperature high-field ESR spectra of stacked $Sr_{1-x}La_xCu_2(BO_3)_2$ single crystals with x = 0.03 at selected frequencies. (**b**) The corresponding frequency-field diagram (x = 0.03) at T = 1.7−2.9 K for H || c, comparing thermally excited triplets and two sets of one-triplet excitations, O_1 and O_2, with literature data for the undoped system (x = 0), showing a respective 0.6 and 0.7 K reduction of the spin gap induced by doping.

The main signals previously observed within this frequency-field range for the undoped system are two low-lying singlet−triplet excitations, O_1 and O_2, as well as paramagnetic signals attributed to thermally excited triplets.[55]

The frequency−field diagram of the undoped system in the orientation $H \parallel c$, reveals zero-field energy gaps of 764(2) GHz and 679(2) GHz for O_1 and O_2, respectively, corresponding to 36.7 and 32.6 K.[55] Comparing these values to those obtained experimentally from the frequency-field diagram of the x = 0.03 doped crystals (Figure 9b), the spin gaps are only found to be slightly reduced to 753 GHz (36.1 K) for O_1 and 665

https://doi.org/10.1021/acs.inorgchem.5c04249
Inorg. Chem. 2026, 65, 291−302

GHz (31.9 K) for O_2. These represent decreases of only 0.6 and 0.7 K compared to the undoped system, indicating that the effect of nominal $x = 0.03$ La doping has a minimal effect on the actual spin gap of $SrCu_2(BO_3)_2$. Since the O_1 and O_2 excitations reflect the intrinsic spin dynamics of the dimerized Cu^{2+} lattice and do not account for the presence of intrinsic dimer-free Cu^{2+} impurities or their local magnetic interactions, the observed minimal reduction in the spin gap indicates that the collective spin excitations within the main dimer lattice remain largely unaffected by nominal $x = 0.03$ doping. Consequently, the notable decrease in the effective spin gap of 4.7 K, determined from the magnetic susceptibility, is primarily influenced by localized magnetic moments associated with intrinsic impurity sites. Capturing additional excitations caused by intrinsic impurities and their interactions through high-field ESR will require measurements at higher frequencies and/or stronger magnetic fields as well as examination of the remaining samples covering the entire nominal doping range.

4. CONCLUSIONS

This study introduces a facile flux method to grow La-doped $SrCu_2(BO_3)_2$ single crystals with lateral sizes of up to 3 mm. A large range of La nominal doping concentrations, $x = 0.02$, 0.03, 0.04, 0.05, 0.10, and 0.15 in $Sr_{1-x}La_xCu_2(BO_3)_2$, is systematically explored. Doping-induced structural changes are subtle but systematic, causing a decrease in unit cell parameters with increasing La concentration. The successful incorporation of La into the parent $SrCu_2(BO_3)_2$ structure is corroborated by EDS-SEM analysis. The semiquantitative evaluation of effective doping concentrations reveals that La incorporation is <50% of the nominal values, reaching up to 2.7(3) mol % for nominal $x = 0.15$, highlighting the inherent difficulty of doping $SrCu_2(BO_3)_2$.

In addition to the structural modifications, La doping also induces systematic effects on the magnetism of $SrCu_2(BO_3)_2$. Compared to the undoped system, impurity-induced in-gap states introduced by La doping lead to a progressive reduction of the effective spin gap extracted from magnetic susceptibility measurements from 28.2 K for $x = 0$ to 20.3 K for nominal La doping of $x = 0.15$. Additionally, X-band ESR measurements reveal a systematic increase in the fraction of the dimer-free Cu^{2+} ($S = 1/2$) spins with nominal doping, along with the emergence of antiferromagnetic correlations between dimer-free Cu^{2+} spin pairs below 5.5 K. High-field ESR measurements further indicate that at low doping levels, the effective spin gap reduction observed in susceptibility primarily arises from these intrinsic impurity spins, while the collective spin dynamics of the Cu^{2+} dimer lattice remain largely intact. Despite these systematic changes in structure and magnetism, no superconductivity is observed across the entire range of La doping studied.

The present findings underscore the potential of flux growth for La doping in $SrCu_2(BO_3)_2$, providing a more efficient and accessible alternative to optical floating zone growth with the possibility of extending this method to other dopants.

■ ASSOCIATED CONTENT

Data Availability Statement

The data that support the findings of this study are openly available on Zenodo at: https://pubs.acs.org/doi.org/10.5281/zenodo.17952985.

Supporting Information

The Supporting Information is available free of charge at https://pubs.acs.org/doi/10.1021/acs.inorgchem.5c04249.

Rietveld refinement results, average semiquantitative atomic % values of constituent elements in $Sr_{1-x}La_xCu_2(BO_3)_2$ single crystals, determined by EDS-SEM, compared to nominal values, low-temperature fitting results of magnetic susceptibility, and low-temperature inverse susceptibility fits in the interval 2−3.4 K, high- and low-temperature X-band ESR spectra, and the development of multiple parameters for three components, derived from the simulations, for selected nominal doping concentrations (PDF)

■ AUTHOR INFORMATION

Corresponding Author

Mirela Dragomir − *Jožef Stefan Institute, Ljubljana 1000, Slovenia; Jožef Stefan International Postgraduate School, Ljubljana 1000, Slovenia;* orcid.org/0000-0002-4910-253X; Email: mirela.dragomir@ijs.si

Authors

Lia Šibav − *Jožef Stefan Institute, Ljubljana 1000, Slovenia; Jožef Stefan International Postgraduate School, Ljubljana 1000, Slovenia*

Tilen Knaflič − *Jožef Stefan Institute, Ljubljana 1000, Slovenia*

Graham King − *Canadian Light Source, Saskatoon, SK S7N 2 V3, Canada;* orcid.org/0000-0003-1886-7254

Zvonko Jagličić − *Institute of Mathematics, Physics and Mechanics, 1000 Ljubljana, Slovenia; Faculty of Civil and Geodetic Engineering, University of Ljubljana, Ljubljana 1000, Slovenia*

Maja Koblar − *Jožef Stefan Institute, Ljubljana 1000, Slovenia*

Kirill Povarov − *Dresden High Magnetic Field Laboratory (HLD-EMFL) and Würzburg-Dresden Cluster of Excellence ct.Qmat, Helmholtzzentrum Dresden-Rossendorf, Dresden 01328, Germany*

Sergei Zvyagin − *Dresden High Magnetic Field Laboratory (HLD-EMFL) and Würzburg-Dresden Cluster of Excellence ct.Qmat, Helmholtzzentrum Dresden-Rossendorf, Dresden 01328, Germany*

Denis Arčon − *Jožef Stefan Institute, Ljubljana 1000, Slovenia; Faculty of Mathematics and Physics, University of Ljubljana, Ljubljana 1000, Slovenia;* orcid.org/0000-0002-1207-8337

Complete contact information is available at: https://pubs.acs.org/10.1021/acs.inorgchem.5c04249

Notes

The authors declare no competing financial interest.

■ ACKNOWLEDGMENTS

The work was supported by Slovenian Research Agency (P2-0105, N1-0397, P1-0125), Young Researcher's Program, Marie Curie Individual Fellowship (Grant No. 101031415), and European Union's Horizon 2020 Research and Innovation Program. Part of the research described in this paper was performed at the Canadian Light Source, a national research facility of the University of Saskatchewan, which is supported by the Canada Foundation for Innovation (CFI), the Natural Sciences and Engineering Research Council (NSERC), the

Canadian Institutes of Health Research (CIHR), the Government of Saskatchewan, and the University of Saskatchewan. We also acknowledge support of the Deutsche Forschungsgemeinschaft through the Würzburg-Dresden Cluster of Excellence on Complexity and Topology in Quantum Matter—ct.qmat (EXC 2147, project No. 390858490) as well as the Dresden High Magnetic Field Laboratory (HLD) at Helmholtz-Zentrum Dresden-Rossendorf (HZDR), member of the European Magnetic Field Laboratory (EMFL).

REFERENCES

(1) Bednorz, J. G.; Müller, K. A. Possible high T_c superconductivity in the Ba-La-Cu-O system. *Z. Phys. B* **1986**, *64*, 189−193.
(2) *Introduction to Frustrated Magnetism*, Lacroix, C.; Mendels, P.; Mila, F., Eds.; Springer-Verlag: Berlin, Heidelberg, 2011.
(3) Anderson, P. W. Resonating valence bonds: A new kind of insulator? *Mater. Res. Bull.* **1973**, *8*, 153−160.
(4) Anderson, P. W. The resonating valence bond state in La_2CuO_4 and superconductivity. *Science* **1987**, *235*, 1196−1198.
(5) Hase, M.; Terasaki, I.; Uchinokura, K. Observation of the spin-Peierls transition in linear Cu^{2+} (spin1/2) chains in an inorganic compound $CuGeO_3$. *Phys. Rev. Lett.* **1993**, *70*, 3651−3654.
(6) Buyers, W. J. L.; Morra, R. M.; Armstrong, R. L.; Hogan, M. J.; Gerlach, P.; Hirakawa, K. Experimental evidence for the Haldane gap in a spin-1 nearly isotropic, antiferromagnetic chain. *Phys. Rev. Lett.* **1986**, *56*, 371−374.
(7) Azuma, M.; Hiroi, Z.; Takano, M.; Ishida, K.; Kitaoka, Y. Observation of a spin gap in $SrCu_2O_3$ comprising spin-1/2 quasi-one-dimensional two-leg ladders. *Phys. Rev. Lett.* **1994**, *73*, 3463−3466.
(8) Taniguchi, S.; Nishikawa, T.; Yasui, Y.; Kobayashi, Y.; Sato, M.; Nishioka, T.; Kontani, M.; Sano, K. Spin Gap Behavior of $S = 1/2$ Quasi-Two-Dimensional System CaV_4O_9. *J. Phys. Soc. Jpn.* **1995**, *64*, 2758−2761.
(9) Kageyama, H.; Kitano, T.; Oba, N.; Nishi, M.; Nagai, S.; Hirota, K.; Viciu, L.; Wiley, J. B.; Yasuda, J.; Baba, Y.; et al. Spin-Singlet Ground State in Two-Dimensional $S = 1/2$ Frustrated Square Lattice: $(CuCl)LaNb_2O_7$. *J. Phys. Soc. Jpn.* **2005**, *74* (6), 1702−1705.
(10) Calder, S.; Pajerowski, D. M.; Stone, M. B.; May, A. F. Spin-Gap and Two-Dimensional Magnetic Excitations in Sr_2IrO_4. *Phys. Rev. B* **2018**, *98*, 220402−220406.
(11) Smith, R. W.; Keszler, D. A. Synthesis, structure, and properties of the orthoborate $SrCu_2(BO_3)_2$. *J. Solid State Chem.* **1991**, *93*, 430−435.
(12) Kageyama, H.; Yoshimura, K.; Stern, R.; Mushnikov, N. V.; Onizuka, K.; Kato, M.; Kosuge, K.; Slichter, C. P.; Goto, T.; Ueda, Y. Exact Dimer Ground State and Quantized Magnetization Plateaus in the Two-Dimensional Spin System $SrCu_2(BO_3)_2$. *Phys. Rev. Lett.* **1999**, *82* (15), 3168−3171.
(13) Miyahara, S.; Ueda, K. Exact Dimer Ground State of the Two Dimensional Heisenberg Spin System $SrCu_2(BO_3)_2$. *Phys. Rev. Lett.* **1999**, *82*, 3701−3704.
(14) Sriram, S. B.; Sutherland, B. Exact ground state of a quantum mechanical antiferromagnet. *Phys. B+C* **1981**, *108*, 1069−1070.
(15) Knetter, C.; Bühler, A.; Müller-Hartmann, E.; Uhrig, G. S. Dispersion and Symmetry of Bound States in the Shastry−Sutherland Model. *Phys. Rev. Lett.* **2000**, *85*, 3958−3961.
(16) Dorier, J.; Schmidt, K. P.; Mila, F. Theory of Magnetization Plateaux in the Shastry−Sutherland Model. *Phys. Rev. Lett.* **2008**, *101*, 250402.
(17) Koga, A.; Kawakami, N. Quantum Phase Transitions in the Shastry-Sutherland Model for $SrCu_2(BO_3)_2$. *Phys. Rev. Lett.* **2000**, *84*, 4461−4464.
(18) Yang, J.; Sandvik, A. W.; Wang, L. Quantum criticality and spin liquid phase in the Shastry Sutherland model. *Phys. Rev. B* **2022**, *105*, L060409.
(19) Viteritti, L. L.; Rende, R.; Parola, A.; Goldt, S.; Becca, F. Transformer Wave Function for Two-Dimensional Frustrated Magnets: Emergence of a Spin-Liquid Phase in the Shastry−Sutherland Model. *Phys. Rev. B* **2025**, *111*, 134411.
(20) Nojiri, H.; Kageyama, H.; Onizuka, K.; Ueda, Y.; Motokawa, M. Direct Observation of the Multiple Spin Gap Excitations in Two-Dimensional Dimer System $SrCu_2(BO_3)_2$. *J. Phys. Soc. Jpn.* **1999**, *68*, 2906−2909.
(21) Kageyama, H.; Onizuka, K.; Yamauchi, T.; Ueda, Y.; Hane, S.; Mitamura, H.; Goto, T.; Yoshimura, K.; Kosuge, K. Anomalous Magnetizations in Single Crystalline $SrCu_2(BO_3)_2$. *J. Phys. Soc. Jpn.* **1999**, *68*, 1821−1823.
(22) Kageyama, H.; Nishi, M.; Aso, N.; Onizuka, K.; Yosihama, T.; Nukui, K.; Kodama, K.; Kakurai, K.; Ueda, Y. Direct evidence for the localized single-triplet excitations and the dispersive multitriplet excitations in $SrCu_2(BO_3)_2$. *Phys. Rev. Lett.* **2000**, *84*, 5876−5879.
(23) Onizuka, K.; Kageyama, H.; Narumi, Y.; Kindo, K.; Ueda, Y.; Goto, T. 1/3 Magnetization Plateau in $SrCu_2(BO_3)_2$ Stripe Order of Excited Triplets-. *J. Phys. Soc. Jpn.* **2000**, *69*, 1016−1018.
(24) Haravifard, S.; Graf, D.; Feiguin, A. E.; Batista, C. D.; Lang, J. C.; Silevitch, D. M.; Srajer, G.; Gaulin, B. D.; Dabkowska, H. A.; Rosenbaum, T. F. Crystallization of spin superlattices with pressure and field in the layered magnet $SrCu_2(BO_3)_2$. *Nat. Commun.* **2016**, *7*, 11956.
(25) Boos, C.; Crone, S. P. G.; Niesen, I. A.; Corboz, P.; Schmidt, K. P.; Mila, F. Competition Between Intermediate Plaquette Phases in $SrCu_2(BO_3)_2$ Under Pressure. *Phys. Rev. B* **2019**, *100*, 140413.
(26) Zayed, M. E.; Rüegg, C.; Larrea, J.; Läuchli, A. M.; Panagopoulos, C.; Saxena, S. S.; Ellerby, M.; McMorrow, D. F.; Klotz, T.; Klotz, S.; et al. 4-Spin Plaquette Singlet State in the Shastry−Sutherland Compound $SrCu_2(BO_3)_2$. *Nat. Phys.* **2017**, *13* (10), 962−966.
(27) Guo, J.; Sun, G.; Zhao, B.; Wang, L.; Hong, W.; Sidorov, V. A.; Ma, N.; Wu, Q.; Li, S.; et al. Quantum Phases of $SrCu_2(BO_3)_2$ from High-Pressure Thermodynamics. *Phys. Rev. Lett.* **2020**, *124*, 206602.
(28) Jiménez, J. L.; Crone, S. P. G.; Fogh, E.; Zayed, M. E.; Lortz, R.; Pomjakushina, E.; Conder, K.; Läuchli, A. M.; Weber, L.; Wessel, S.; et al. A Quantum Magnetic Analogue to the Critical Point of Water. *Nature* **2021**, *592*, 370−375.
(29) Cui, Y.; Liu, L.; Lin, H.; Wu, K.-H.; Hong, W.; Liu, X.; Li, C.; Hu, Z.; Xi, N.; Li, S.; et al. Proximate deconfined quantum critical point in $SrCu_2(BO_3)_2$. *Science* **2023**, *380* (6650), 1179−1184.
(30) Šibav, L.; Gosar, Ž.; Knaflič, T.; Jagličić, Z.; King, G.; Nojiri, H.; Arčon, D.; Dragomir, M. HigherMagnesiumDoping Effects on the Singlet Ground State of the Shastry-Sutherland $SrCu_2(BO_3)_2$. *Inorg. Chem.* **2024**, *63*, 20335−20346.
(31) Shastry, B. S.; Kumar, B. $SrCu_2(BO_3)_2$: A unique Mott Hubbard insulator. *Prog. Theor. Phys. Suppl.* **2002**, *145*, 1−16.
(32) Liu, J.; Trivedi, N.; Lee, Y.; Harmon, B. N.; Schmalian, J. Quantum Phases in a Doped Mott Insulator on the Shastry-Sutherland Lattice. *Phys. Rev. Lett.* **2007**, *99*, 227003−227007.
(33) Yang, B.; Kim, Y. B.; Yu, J.; Park, K. Doped valence-bond solid and superconductivity on the Shastry-Sutherland lattice. *Phys. Rev. B* **2008**, *77*, 104507−104517.
(34) Norrestam, R.; Carlson, S.; Kritikos, M.; Sjödin, A. Synthetic Structural, and Magnetic Studies of Strontium Copper(II) Borates with the Composition $Sr_{1-x}M_xCu_2(BO_3)_2$, M = Ba or Ca. *J. Solid State Chem.* **1994**, *113*, 74−77.
(35) Liu, G. T.; Luo, J. L.; Wang, N. L.; Jing, X. N.; Jin, D.; Xiang, T.; Wu, Z. H. Doping effects on the two-dimensional spin dimer compound $SrCu_2(BO_3)_2$. *Phys. Rev. B* **2005**, *71*, 014441.
(36) Choi, K.-Y.; Pashkevich, Y.; Lamonova, K.; Kageyama, H.; Ueda, Y.; Lemmens, P. Strong anharmonicity and spin-phonon coupling in the quasi-two-dimensional quantum spin system $Sr_{1-x}Ba_xCu_2(BO_3)_2$. *Phys. Rev. B* **2003**, *68*, 104418.
(37) Dabkowska, H. A.; Dabkowski, A. B.; Luke, G. M.; Dunsiger, S. R.; Haravifard, S.; Cecchinel, M.; Gaulin, B. D. Crystal growth and magnetic behaviour of pure and doped $SrCu_2(^{11}BO_3)_2$. *J. Cryst. Growth* **2007**, *306*, 123−128.
(38) Aczel, A. A.; MacDougall, G. J.; Rodriguez, J. A.; Luke, G. M.; Russo, P. L.; Savici, A. T.; Uemura, Y. J.; Dabkowska, H. A.; Wiebe, C.

https://doi.org/10.1021/acs.inorgchem.5c04249
Inorg. Chem. 2026, 65, 291−302

R.; Janik, J. A.; Kageyama, H. Impurity-induced singlet breaking in $SrCu_2(BO_3)_2$. *Phys. Rev. B* **2007**, *76*, 214427−214433.
(39) Liu, G. T.; Luo, J. L.; Guo, Y. Q.; Su, S. K.; Zheng, P.; Wang, N. L.; Jin, D.; Xiang, T. In-plane substitution effect on the magnetic properties of the two-dimensional spin-gap system $SrCu_2(BO_3)_2$. *Phys. Rev. B* **2006**, *73*, 014414.
(40) Haravifard, S.; Dunsinger, S. R.; El Shawish, S.; Gaulin, B. D.; Dabkowska, H. A.; Telling, M. T. F.; Perring, T. G.; Bonča, J. In-gap Spin Excitations and Finite Triplet Lifetimes in the Dilute Singlet Ground State System $SrCu_{2-x}Mg_x(BO_3)_2$. *Phys. Rev. Lett.* **2006**, *97*, 247206.
(41) Shi, Z.; Steinhardt, W.; Graf, D.; Corboz, P.; Weickert, F.; Harrison, N.; Jaime, M.; Marjerrison, C.; Dabkowska, H. A.; Mila, F.; Haravifard, S. Emergent bound states and impurity pairs in chemically doped Shastry-Sutherland system. *Nat. Commun.* **2019**, *10*, 1−9.
(42) Rahemtulla, A.; King, G.; Gomez, A.; Appathurai, N.; Leontowich, A. F. G.; Castle, R.; Burns, N.; Kim, C.-Y.; Moreno, B.; Kycia, S. The High Energy Diffraction Beamline at the Canadian Light Source. *J. Synchrotron Radiat* **2025**, *32*, 750−756.
(43) Toby, B. H.; Von Dreele, R. B. GSAS-II: the genesis of a modern open-source all purpose crystallography software package. *J. Appl. Crystallogr.* **2013**, *46*, 544−549.
(44) Zvyagin, S. A.; Krzystek, J.; van Loosdrecht, P. H. M.; Dhalenne, G.; Revcolevschi, A. Highfield ESR study of the dimerized-incommensurate phase transition in the spin-Peierls compound $CuGeO_3$. *Phys. B* **2004**, *346−347*, 1−5.
(45) Hill, J. M. *Doping experiments on low-dimensional oxides and a search for unusual magnetic properties of* $MgAlB_{14}$. Ph.D. dissertation; Iowa State University: Ames, Iowa, 2002.
(46) Maltsev, V.; Leonyuk, N.; Koporulina, E.; Dorokhova, G. Flux growth and morphology of $SrCu_2(BO_3)_2$ crystals. *J. Cryst. Growth* **2004**, *270*, 102−106.
(47) Maltsev, V.; Leonyuk, N.; Szymczak, R. A new advance in crystal growth of two-dimensional strontium cuprate−borate. *J. Cryst. Growth* **2005**, *277*, 541−545.
(48) Zorko, A. *Study of one- and two-dimensional magnetic systems with spin-singlet ground state*. Ph.D. dissertation; University of Ljubljana: Slovenia, 2004.
(49) Zorko, A.; Arčon, D.; Lappas, A.; Giapintzakis, J. Near critical behavior in the two-dimensional spin-gap system $SrCu_2(BO_3)_2$. *Phys. Rev. B* **2001**, *65*, 024417−024422.
(50) Zorko, A.; Arčon, D.; van Tol, H.; Brunel, L. C.; Kageyama, H. X-band ESR determination of Dzyaloshinsky-Moriya interaction in the two-dimensional $SrCu_2(BO_3)_2$ system. *J. Magn. Magn. Mater.* **2004**, *69*, 174420.
(51) Zorko, A.; Arčon, D.; Nuttall, C. J.; Lappas, A. X-band ESR study of the 2D spin-gap system $SrCu_2(BO_3)_2$. *J. Magn. Magn. Mater.* **2004**, *272*, 699−701.
(52) Zorko, A.; Arčon, D.; Kageyama, H.; Lappas, A. Magnetic anisotropy of the $SrCu_2(BO_3)_2$ system as revealed by X-band ESR. *Appl. Magn. Reson.* **2004**, *27*, 267−278.
(53) Kubo, R.; Tomita, K. A general theory of magnetic resonance absorption. *J. Phys. Soc. Jpn.* **1954**, *9*, 888−919.
(54) Bencini, A.; Gatteschi, D. *Electron Paramagnetic Resonance of Exchange Coupled Systems*; Springer-Verlag: Berlin, Heidelberg, NY, 1990.
(55) Nojiri, H.; Kageyama, H.; Ueda, Y.; Motokawa, M. ESR Study on the Excited State Energy Spectrum of $SrCu_2(BO_3)_2$—A Central Role of Multiple-Triplet Bound States. *J. Phys. Soc. Jpn.* **2003**, *72*, 3243−3253.

https://doi.org/10.1021/acs.inorgchem.5c04249
Inorg. Chem. 2026, 65, 291−302

SUPPLEMENTARY INFORMATION FILE

Influence of La-doping on the magnetic properties of the two-dimensional spin-gapped system $SrCu_2(BO_3)_2$

Lia Šibav[1,2], Tilen Knaflič[1], Graham King[3], Zvonko Jagličić[4,5], Maja Koblar[1], Kirill Povarov[6], Sergei Zvyagin[6], Denis Arčon[1,7], and Mirela Dragomir[1,2*]

[1] Jožef Stefan Institute, Jamova cesta 39, 1000 Ljubljana, Slovenia
[2] Jožef Stefan International Postgraduate School, Jamova cesta 39, 1000 Ljubljana, Slovenia
[3] Canadian Light Source, 44 Innovation Blvd, Saskatoon, SK S7N 2V3, Canada
[4] Institute of Mathematics, Physics and Mechanics, Jadranska ulica 19, 1000 Ljubljana, Slovenia
[5] Faculty of Civil and Geodetic Engineering, University of Ljubljana, Jamova cesta 2, 1000 Ljubljana, Slovenia
[6] Dresden High Magnetic Field Laboratory (HLD-EMFL) and Würzburg-Dresden Cluster of Excellence ct.qmat, Helmholtz-Zentrum Dresden-Rossendorf, 01328 Dresden, Germany
[7] Faculty of Mathematics and Physics, University of Ljubljana, Jadranska ulica 19, 1000 Ljubljana, Slovenia

*Corresponding author: mirela.dragomir@ijs.si

Table of Contents

Table S1 Room-temperature structural parameters extracted from Rietveld refinement analyses of synchrotron PXRD data collected on crushed $Sr_{1-x}La_xCu_2(BO_3)_2$ single crystals of all studied nominal doping concentrations, x = 0.02–0.15, compared with polycrystalline undoped $SrCu_2(BO_3)_2$. The refinements were performed in the $I\bar{4}2m$ space group.....S3

Figure S1 Photographs of the blue La-doped $SrCu_2(BO_3)_2$ (in mol%) single crystals grown in this study.....S3

Figure S2 Rietveld refinement profiles of synchrotron XRD data (λ = 0.3502 Å) collected on crushed $Sr_{1-x}La_xCu_2(BO_3)_2$ single crystals with selected nominal doping concentrations (**a**) x = 0.02, (**b**) 0.05, (**c**) 0.10, and (**d**) 0.15, collected at room temperature. The refinements were performed using the $I\bar{4}2m$ space group. S4

Table S2 Detailed results of Rietveld refinement analyses of synchrotron PXRD data collected on crushed $Sr_{1-x}La_xCu_2(BO_3)_2$ single crystals of selected nominal doping concentrations x = 0.02, 0.05, 0.10 and 0.15. The data were refined using the $I\bar{4}2m$ space group. S5

Table S3 The average semi-quantitative atomic % values of Sr, Cu, O and La in $Sr_{1-x}La_xCu_2(BO_3)_2$ single crystals with nominal x = 0–0.15, followed by La/Cu, La/Sr and Cu/Sr ratios, compared to the nominal values. The results were determined from SEM-EDS point analyses (20 points for each doping concentration) performed on the crystals. Due to the low relative atomic mass of boron, it could not be detected by EDS and was therefore omitted from the semi-quantitative analysis. S6

Figure S3 An SEM image and EDS elemental mapping analysis of a $Sr_{1-x}La_xCu_2(BO_3)_2$ single crystal with nominal x = 0.04 (**a**) and 0.10 (**b**) reveal a relatively homogeneous distribution of La within the $SrCu_2(BO_3)_2$ matrix. Few $LaBO_3$ impurity particles are observed on the surface. The corresponding EDS sum spectra clearly show the presence of La emission lines for both a) and b) samples.....S7

Figure S4 An SEM image (left) and EDS elemental mapping analysis (right) of a $Sr_{1-x}La_xCu_2(BO_3)_2$ single crystal with nominal x = 0.15, showing: (**a**) the presence of $LaBO_3$ impurity particles on the crystal surface and (**b**) the presence of both CuO and $LaBO_3$ impurity particles on the crystal surface. S8

Table S4 Results of the low-temperature magnetic susceptibility data fits (2–6 K range) for $Sr_{1-x}La_xCu_2(BO_3)_2$ single crystals with nominal x = 0–0.15 (Equation 3 in the main text). Five fixed θ' values were used due to its high correlation with C'. S9

Figure S5 Inverse magnetic susceptibility data for $Sr_{1-x}La_xCu_2(BO_3)_2$ single crystals with nominal x = 0–0.15, displaying low-temperature Curie–Weiss fits performed in the 2–3.4 K interval to estimate intrinsic Cu^{2+} (S = ½) impurities. S10

Figure S6 X-band ESR spectra of $Sr_{1-x}La_xCu_2(BO_3)_2$ single crystals with nominal (**a**) x = 0.02, (**b**) 0.03, (**c**) 0.04, (**d**) 0.05, (**e**) 0.10 and (**f**) 0.15, measured as quasi-polycrystalline samples at temperatures 40, 70, 110, 170 and 250 K, which show the dominant signal of the dimer lattice at high temperatures.. .....S11

Figure S7 Low-temperature X-band ESR spectra of $Sr_{1-x}La_xCu_2(BO_3)_2$ single crystals with nominal (**a**) x = 0.02, (**b**) 0.03, (**c**) 0.10, and (**d**) 0.15 at selected temperatures 5, 10 and 20 K, showing the development of the characteristic impurity signal correlated to intrinsic impurities–isolated dimer free Cu^{2+} spins. S12

Figure S8 (**a**) The logarithmic temperature behavior of the X-band ESR linewidth of the main dimer-lattice signal. (**b**) The temperature behavior of g-factor for the interacting Cu^{2+}–Cu^{2+} pair component for $Sr_{1-x}La_xCu_2(BO_3)_2$ single crystals with nominal x = 0.02, 0.10, and 0.15. (**c**) The temperature behavior of X-band ESR linewidth for the isolated Cu^{2+} impurity component, parallel ($\Delta B||$) and perpendicular ($\Delta B \perp$) to c crystallographic axis for $Sr_{1-x}La_xCu_2(BO_3)_2$ single crystals with nominal x = 0.02, 0.03, 0.10, and 0.15. (**d**) The temperature behavior of g-factor for the isolated Cu^{2+} impurity component, parallel ($g||$) and perpendicular ($g \perp$) to c crystallographic axis for $Sr_{1-x}La_xCu_2(BO_3)_2$ single crystals with nominal x = 0.02, 0.03, 0.10, and 0.15. .....S13

Figure S9 (**a**) X-band ESR spectrum of $Sr_{1-x}La_xCu_2(BO_3)_2$ single crystals with nominal x = 0.05 at 5 K. (**b**) The temperature behavior of X-band ESR linewidth for the isolated Cu^{2+} impurity component, parallel ($\Delta B||$) and perpendicular ($\Delta B \perp$) to c crystallographic axis for nominal x = 0.05. (**c**) Temperature dependence of the signal intensity of the isolated Cu^{2+} impurity component for nominal x = 0.05. (**d**) The temperature behavior of X-band ESR linewidth for the interacting Cu^{2+}–Cu^{2+} pair component for nominal x = 0.05.....S14

Table S1 Room-temperature structural parameters extracted from Rietveld refinement analyses of synchrotron PXRD data collected on crushed $Sr_{1-x}La_xCu_2(BO_3)_2$ single crystals of all studied nominal doping concentrations, $x = 0.02–0.15$, compared with polycrystalline undoped $SrCu_2(BO_3)_2$ according to ref. [1]. The refinements were performed in the $I\bar{4}2m$ space group.

Nominal x	a, b (Å)	c (Å)	V (Å^3)
0	8.9932(1)	6.6509(1)	537.91(2)
0.02	8.9932(1)	6.6498(9)	537.82(1)
0.03	8.9929(1)	6.6500(1)	537.81(2)
0.04	8.9928(5)	6.6500(4)	537.80(9)
0.05	8.9922(1)	6.6500(1)	537.72(2)
0.10	8.9878(1)	6.6458(1)	536.85(2)
0.15	8.9868(1)	6.6454(1)	536.70(1)

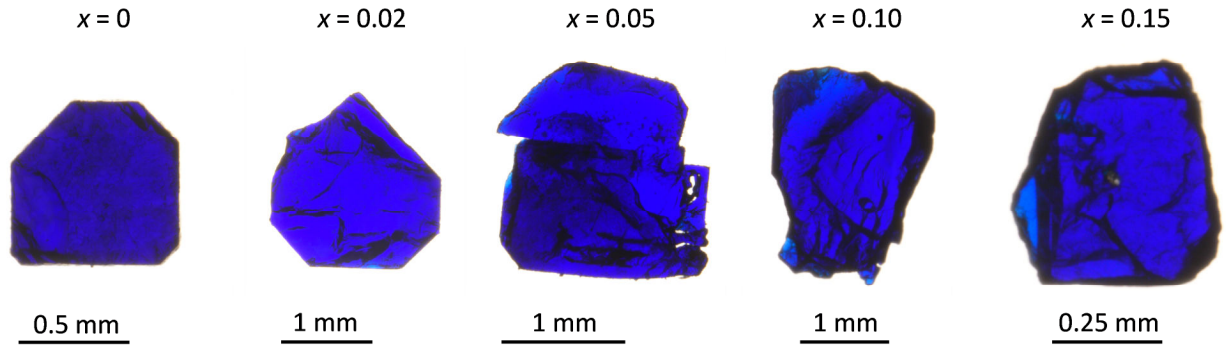


Figure S1 Photographs of the blue La-doped $SrCu_2(BO_3)_2$ (in mol%) single crystals grown in this study.

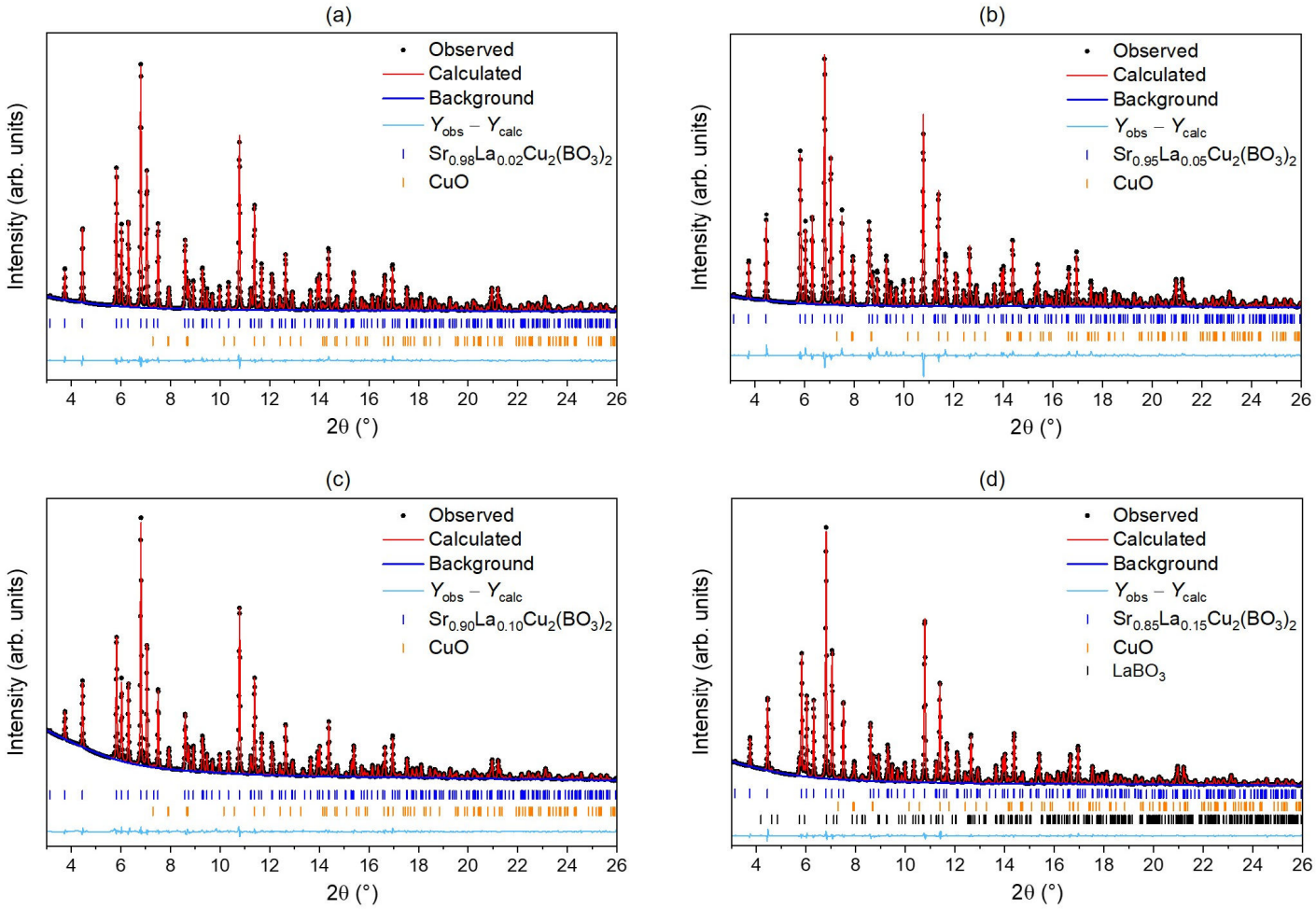


Figure S2 Rietveld refinement profiles of synchrotron XRD data (λ = 0.3502 Å) collected on crushed $Sr_{1-x}La_xCu_2(BO_3)_2$ single crystals with selected nominal doping concentrations (**a**) x = 0.02, (**b**) 0.05, (**c**) 0.10, and (**d**) 0.15, collected at room temperature. The refinements were performed using the $I\bar{4}2m$ space group.

Table S2 Detailed results of Rietveld refinement analyses of synchrotron PXRD data collected on crushed $Sr_{1-x}La_xCu_2(BO_3)_2$ single crystals of selected nominal doping concentrations x = 0.02, 0.05, 0.10 and 0.15. The data were refined using the $I\bar{4}2m$ space group.

	$Sr_{0.98}La_{0.02}Cu_2(BO_3)_2$	$Sr_{0.95}La_{0.05}Cu_2(BO_3)_2$	$Sr_{0.90}La_{0.10}Cu_2(BO_3)_2$	$Sr_{0.85}La_{0.15}Cu_2(BO_3)_2$
a, b (Å)	8.9932(1)	8.9922(1)	8.9878(1)	8.9868(1)
c (Å)	6.6498(1)	6.6500(1)	6.6458(1)	6.6454(1)
V (Å^3)	537.82(1)	537.72(2)	536.85(2)	536.70(1)
R_{wp} (%)	3.35	4.95	2.25	2.38
Atom	x/y/z Occ. $U_{11}/U_{22}/U_{33}$	x/y/z Occ. $U_{11}/U_{22}/U_{33}$	x/y/z Occ. $U_{11}/U_{22}/U_{33}$	x/y/z Occ. $U_{11}/U_{22}/U_{33}$
Sr	0/0.5/0 0.991* 0.0052(8)/0.0038(8)/0.0088(7)	0/0.5/0 0.983* 0.0045(10)/0.0021(10)/0.0081(8)	0/0.5/0 0.980* 0.0082(10)/0.0082(10)/0.0092(9)	0/0.5/0 0.973* 0.0080(8)/0.0062(8)/0.0120(7)
La	0/0.5/0 0.009* 0.0052(9)/0.0038(8)/0.0088(7)	0/0.5/0 0.017* 0.0045(10)/0.0021(10)/0.0081(8) 0/0/0	0/0.5/0 0.020* 0.0082(11)/0.0082(10)/0.0092(9)	0/0.5/0 0.027* 0.0085(8)/0.0062(8)/0.0120(7)
Cu	0.11439(7)/0.11439(7)/ 0.27991(19) 1.00 0.0039(3)/0.0039/0.0162(8)	0.11418(8)/0.11418/0.28199(20) 1.00 0.0008(4)/0.0008/0.0156(9)	0.11439(8)/0.11439(8)/0.27927(26) 1.00 0.0046(4)/0.0046(4)/0.0269(12)	0.11410(6)/0.11410(6)/0.27930(20) 1.00 0.0030(3)/0.0030(3)/0.0269(10)
B	0.2966(5)/0.2966(6)/0.2467(16) 1.00 0.0021(25)/0.0021(15)/0.007(5)	0.2928(6)/0.29278/0.2329(21) 1.00 0.0248(31)/0.0248/0.008(5)	0.2938(7)/0.2938(7)/0.2547(26) 1.00 0.0164/0.0164/0.0050	0.2934(5)/0.2934(5)/0.2485(19) 1.00 0.0148/0.0148/0.0050
O1	0.4010(4)/0.4010(4)/0.2073(10) 1.00 0.0085(19)/0.0085/0.061(6)	0.4029(4)/0.402913/0.2061(16) 1.00 0.0088(26)/0.0088/0.188(11)	0.4013(4)/0.4013(4)/0.2111(14) 1.00 0.0020(21)/0.0020(21)/0.054(7)	0.40166(29)/0.40166(29)/0.2136(11) 1.00 0.0032(15)/0.0032(15)/0.054(5)
O2	0.32722(27)/0.14648(30)/0.2588(10) 1.00 0.0070(17)/0.0022(18)/0.0129(22)	0.32785(4)/0.14367/0.26146 1.00 0.0058/0.0089/0.0169	0.32647(31)/0.1461(3)/0.2584(14) 1.00 0.0048(19)/0.0038(20)/0.0245(29)	0.32701(26)/0.14574(28)/0.2588(10) 1.00 0.0032(14)/0.0023(15)/0.0259(24)

*The fractional occupancies of Sr and La were fixed to the effective values, semi-quantitatively determined from SEM-EDS point analyses (Table S3).

Table S3 The average semi-quantitative atomic % values of Sr, Cu, O and La in $Sr_{1-x}La_xCu_2(BO_3)_2$ single crystals with nominal x = 0–0.15, as obtained from SEM-EDS point analyses, together with La/Cu, La/Sr and Cu/Sr ratios, versus the nominal values. The data was averaged from several crystals per concentration with approximatively 20 points collected on each crystal. Due to the low atomic number of boron, this element could not be detected by EDS and was therefore omitted from the semi-quantitative analysis.

Element	Concentration (at%)													
	x = 0		x = 0.02		x = 0.03		x = 0.04		x = 0.05		x = 0.10		x = 0.15	
	Effective	Nominal	Effective	Nominal	Effective	Nominal	Effective	Nominal	Effective	Nominal	Effective	Nominal	Effective	Nominal
Sr	13.9(4)	11.11	12.6(5)	10.89	13.1(7)	10.78	13.1(3)	10.67	12.4(5)	10.56	12.4(2)	10.00	12.4(2)	9.44
Cu	28(2)	22.22	27(1)	22.22	26(3)	22.22	25(1)	22.22	27(2)	22.22	26.0(9)	22.22	26(1)	22.22
O	59(2)	66.67	61(2)	66.67	61(3)	66.67	62(1)	66.67	60(2)	66.67	62(1)	66.67	62(1)	66.67
La	0	0	0.10(2)	0.22	0.16(5)	0.33	0.15(3)	0.44	0.18(6)	0.56	0.22(3)	1.11	0.30(6)	1.67
Sum, %	100.9	100	100.7	100	100.26	100	100.25	100	99.58	100	100.62	100	100.7	100
La/Cu	0	0	0.0036(8)	0.01	0.006(2)	0.015	0.006(1)	0.02	0.007(2)	0.025	0.009(1)	0.05	0.012(2)	0.075
La/Sr	0	0	0.008(2)	0.02	0.012(3)	0.03	0.011(2)	0.04	0.015(4)	0.05	0.018(2)	0.11	0.025(5)	0.18
Cu/Sr	1.99(9)	2	2.10(7)	2.04	2.0(1)	2.06	1.91(4)	2.08	2.2(1)	2.10	2.06(5)	2.22	2.08(6)	2.35
La mol%	0	0	0.9(2)	2	1.4(5)	3	1.3(2)	4	1.7(5)	5	2.0(3)	10	2.7(6)	15

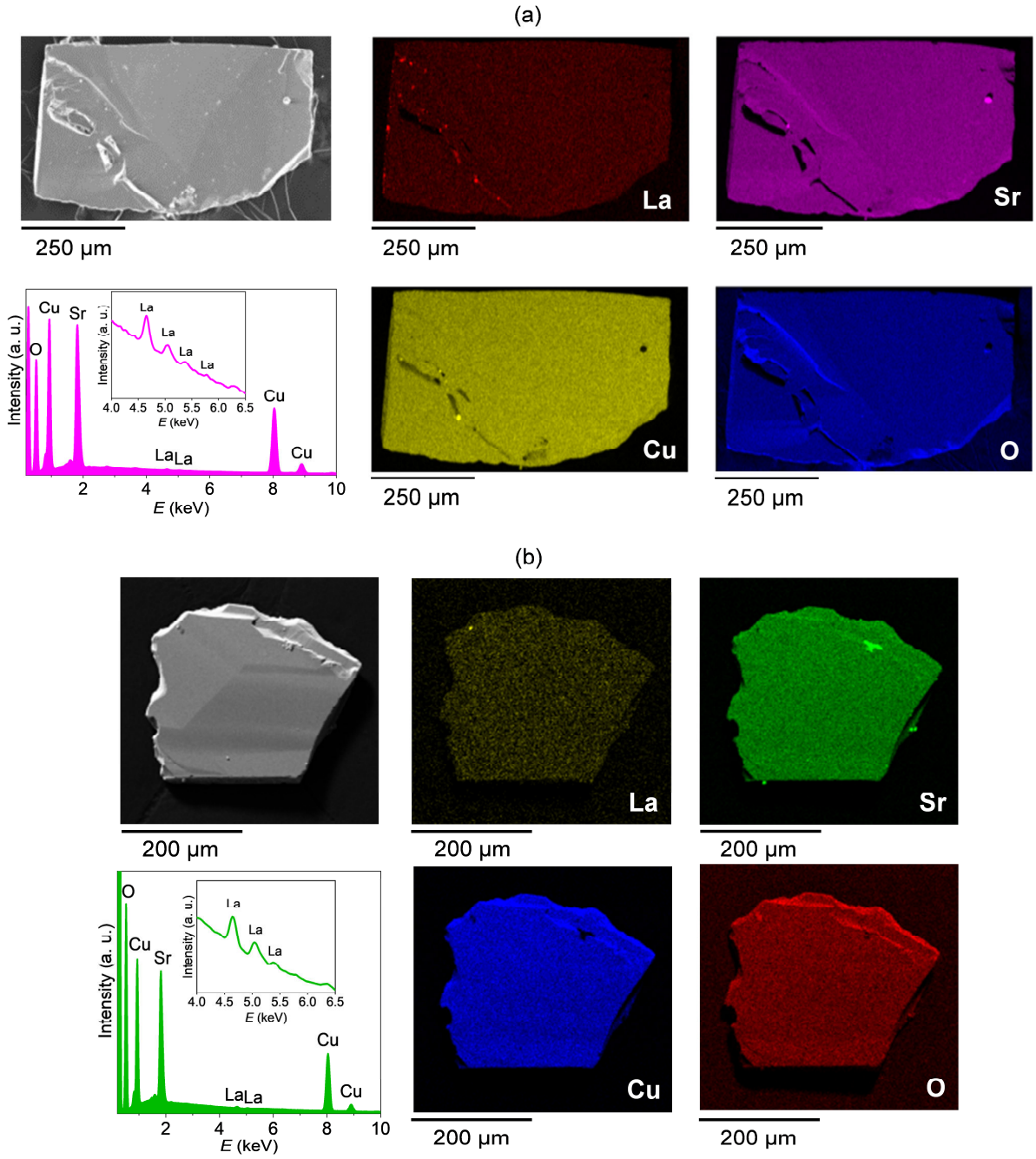


Figure S3 An SEM image and EDS elemental mapping analysis of a $Sr_{1-x}La_xCu_2(BO_3)_2$ single crystal with nominal $x = 0.04$ (**a**) and 0.10 (**b**) reveal a relatively homogeneous distribution of La within the $SrCu_2(BO_3)_2$ matrix. Few $LaBO_3$ impurity particles are observed on the surface. The corresponding EDS sum spectra clearly show the presence of La emission lines for both a) and b) samples. The insets show a magnified region where the La emission lines are distinctly visible. Few CuO impurity particles are additionally visible in a).

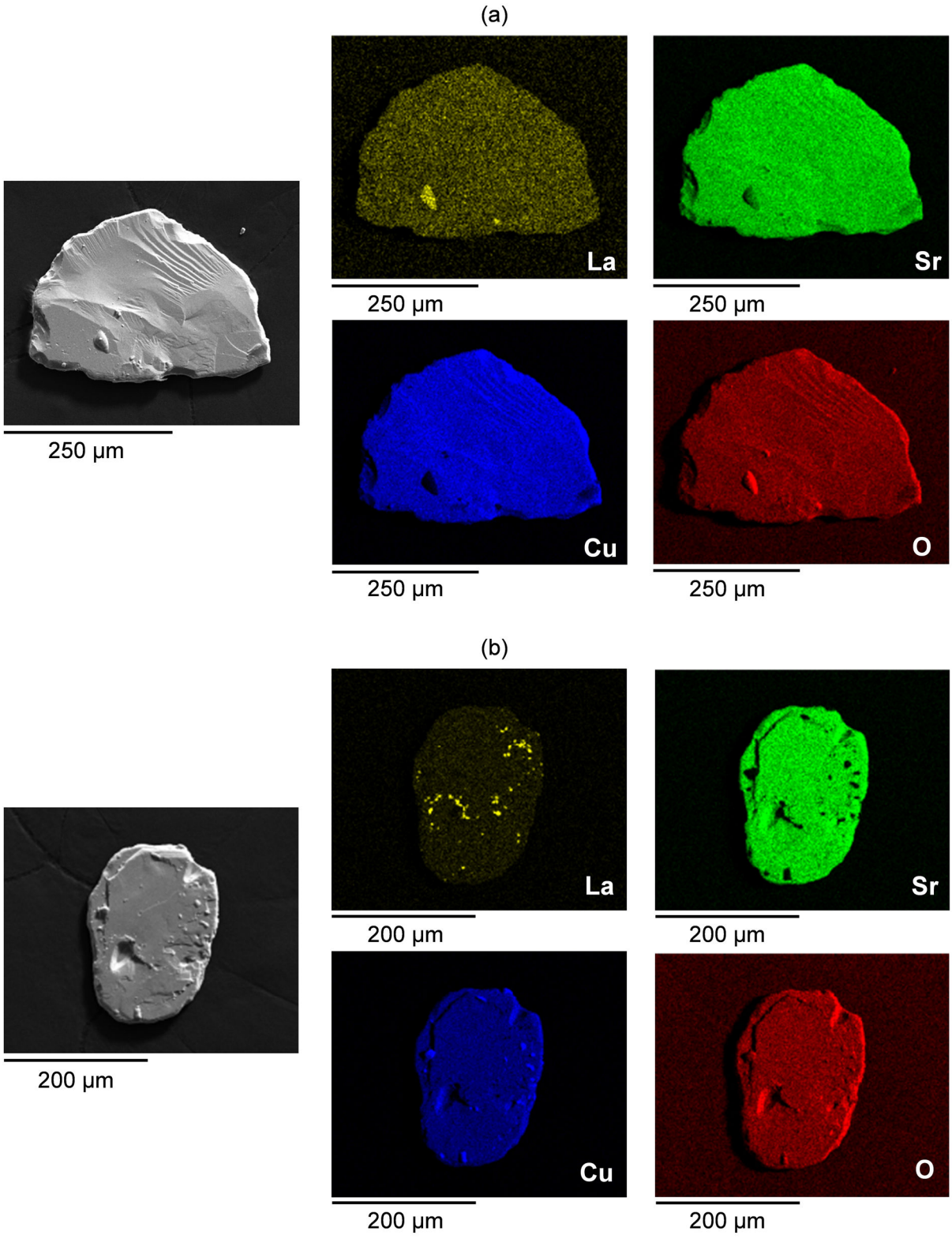


Figure S4 An SEM image (left) and EDS elemental mapping analysis (right) of a $Sr_{1-x}La_xCu_2(BO_3)_2$ single crystal with nominal x = 0.15, showing: (**a**) the presence of $LaBO_3$ impurity particles on the crystal surface and (**b**) the presence of both CuO and $LaBO_3$ impurity particles on the crystal surface.

Table S4 Results of the low-temperature magnetic susceptibility data fits (2–6 K range) for $Sr_{1-x}La_xCu_2(BO_3)_2$ single crystals with nominal x = 0–0.15 (Equation 3 in the main text). Five fixed θ' values were used due to a high correlation with C'.

Nominal x	C' (emu K/mol)	χ_0 (emu/mol)	θ'	Δ (K)	a (emu/mol)
x = 0	$3.4(1) \cdot 10^{-4}$	$7.1(6) \cdot 10^{-5}$	0	28.7(3)	$8.3(4) \cdot 10^{-2}$
	$4.1(2) \cdot 10^{-4}$	$5.7(6) \cdot 10^{-5}$	−0.25	28.5(3)	$8.1(4) \cdot 10^{-2}$
	$4.9(2) \cdot 10^{-4}$	$4.4(6) \cdot 10^{-5}$	−0.5	28.3(3)	$7.9(4) \cdot 10^{-2}$
	$5.7(2) \cdot 10^{-4}$	$3.1(7) \cdot 10^{-5}$	−0.75	28.2(3)	$7.8(3) \cdot 10^{-2}$
	$6.6(3) \cdot 10^{-4}$	$1.8(7) \cdot 10^{-5}$	−1	28.1(3)	$7.7(3) \cdot 10^{-2}$
x = 0.02	$1.95(1) \cdot 10^{-3}$	$3.09(6) \cdot 10^{-4}$	0	26.7(3)	$6.6(3) \cdot 10^{-2}$
	$2.37(1) \cdot 10^{-3}$	$2.31(5) \cdot 10^{-4}$	−0.25	25.9(2)	$5.9(2) \cdot 10^{-2}$
	$2.82(2) \cdot 10^{-3}$	$1.52(6) \cdot 10^{-4}$	−0.5	25.2(2)	$5.4(2) \cdot 10^{-2}$
	$3.32(2) \cdot 10^{-3}$	$7.2(7) \cdot 10^{-5}$	−0.75	24.7(2)	$5.1(2) \cdot 10^{-2}$
	$3.86(3) \cdot 10^{-3}$	$-9(9) \cdot 10^{-6}$	−1	24.2(2)	$4.8(2) \cdot 10^{-2}$
x = 0.03	$2.46(2) \cdot 10^{-3}$	$3.83(8) \cdot 10^{-4}$	0	25.3(3)	$5.4(2) \cdot 10^{-2}$
	$2.99(2) \cdot 10^{-3}$	$2.82(6) \cdot 10^{-4}$	−0.25	24.4(2)	$4.8(1) \cdot 10^{-2}$
	$3.58(2) \cdot 10^{-3}$	$1.79(6) \cdot 10^{-4}$	−0.5	23.6(2)	$4.4(1) \cdot 10^{-2}$
	$4.22(2) \cdot 10^{-3}$	$7.4(7) \cdot 10^{-5}$	−0.75	23.0(2)	$4.1(1) \cdot 10^{-2}$
	$4.91(3) \cdot 10^{-3}$	$-3.2(9) \cdot 10^{-5}$	−1	22.4(2)	$3.8(1) \cdot 10^{-2}$
x = 0.04	$2.25(2) \cdot 10^{-3}$	$3.65(9) \cdot 10^{-4}$	0	25.4(4)	$5.0(3) \cdot 10^{-2}$
	$2.74(3) \cdot 10^{-3}$	$2.73(9) \cdot 10^{-4}$	−0.25	24.5(3)	$4.5(2) \cdot 10^{-2}$
	$3.27(3) \cdot 10^{-3}$	$1.8(1) \cdot 10^{-4}$	−0.5	23.7(3)	$4.1(2) \cdot 10^{-2}$
	$3.86(4) \cdot 10^{-3}$	$8(1) \cdot 10^{-5}$	−0.75	23.1(3)	$3.8(2) \cdot 10^{-2}$
	$4.49(5) \cdot 10^{-3}$	$-1(1) \cdot 10^{-5}$	−1	22.5(3)	$3.6(2) \cdot 10^{-2}$
x = 0.05	$2.39(2) \cdot 10^{-3}$	$4.12(6) \cdot 10^{-4}$	0	24.8(3)	$4.4(2) \cdot 10^{-2}$
	$2.90(1) \cdot 10^{-3}$	$3.17(5) \cdot 10^{-4}$	−0.25	23.6(2)	$3.7(1) \cdot 10^{-2}$
	$3.46(2) \cdot 10^{-3}$	$2.16(5) \cdot 10^{-4}$	−0.5	22.8(2)	$3.37(8) \cdot 10^{-2}$
	$4.09(2) \cdot 10^{-3}$	$1.13(7) \cdot 10^{-4}$	−0.75	22.1(2)	$3.12(8) \cdot 10^{-2}$
	$4.68(3) \cdot 10^{-3}$	$3.4(8) \cdot 10^{-5}$	−1	22.0(2)	$3.15(9) \cdot 10^{-2}$
x = 0.10	$2.50(2) \cdot 10^{-3}$	$5.66(7) \cdot 10^{-4}$	0	23.8(3)	$3.0(1) \cdot 10^{-2}$
	$3.04(1) \cdot 10^{-3}$	$4.60(5) \cdot 10^{-4}$	−0.25	22.6(2)	$2.60(7) \cdot 10^{-2}$
	$3.64(1) \cdot 10^{-3}$	$3.51(4) \cdot 10^{-4}$	−0.5	21.6(1)	$2.33(4) \cdot 10^{-2}$
	$4.31(2) \cdot 10^{-3}$	$2.39(5) \cdot 10^{-4}$	−0.75	20.8(1)	$2.14(4) \cdot 10^{-2}$
	$5.04(2) \cdot 10^{-3}$	$1.26(7) \cdot 10^{-5}$	−1	20.1(2)	$2.00(5) \cdot 10^{-2}$
x = 0.15	$2.51(2) \cdot 10^{-3}$	$7.3(1) \cdot 10^{-4}$	0	22.8(4)	$2.8(2) \cdot 10^{-2}$
	$3.05(3) \cdot 10^{-3}$	$6.3(1) \cdot 10^{-4}$	−0.25	21.8(4)	$2.5(1) \cdot 10^{-2}$
	$3.64(4) \cdot 10^{-3}$	$5.2(1) \cdot 10^{-4}$	−0.5	21.0(4)	$2.3(1) \cdot 10^{-2}$
	$4.30(5) \cdot 10^{-3}$	$4.1(2) \cdot 10^{-4}$	−0.75	20.3(4)	$2.2(1) \cdot 10^{-2}$
	$5.02(6) \cdot 10^{-3}$	$3.0(2) \cdot 10^{-4}$	−1	19.7(4)	$2.0(1) \cdot 10^{-2}$

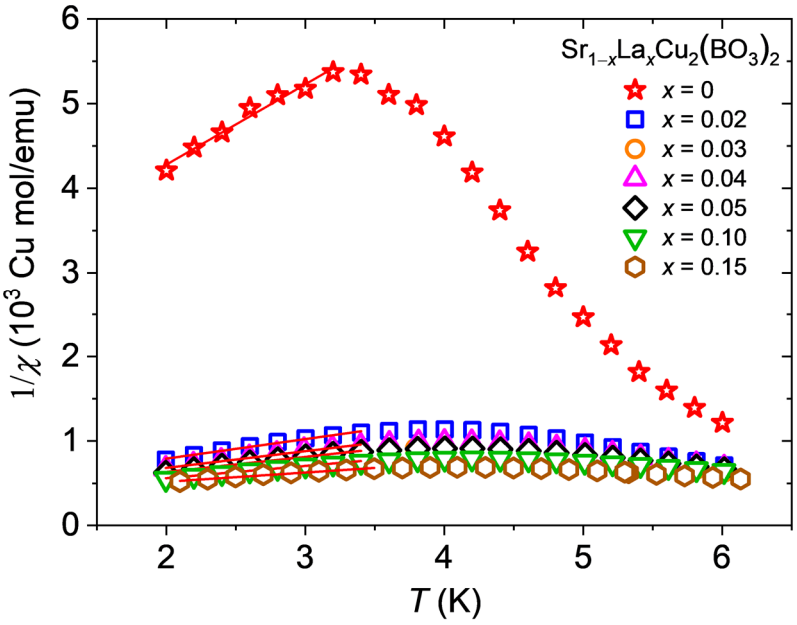


Figure S5 Inverse magnetic susceptibility data for $Sr_{1-x}La_xCu_2(BO_3)_2$ single crystals with nominal x = 0–0.15, displaying low-temperature Curie–Weiss fits performed in the 2–3.4 K interval to estimate intrinsic Cu^{2+} (S = ½) impurities.

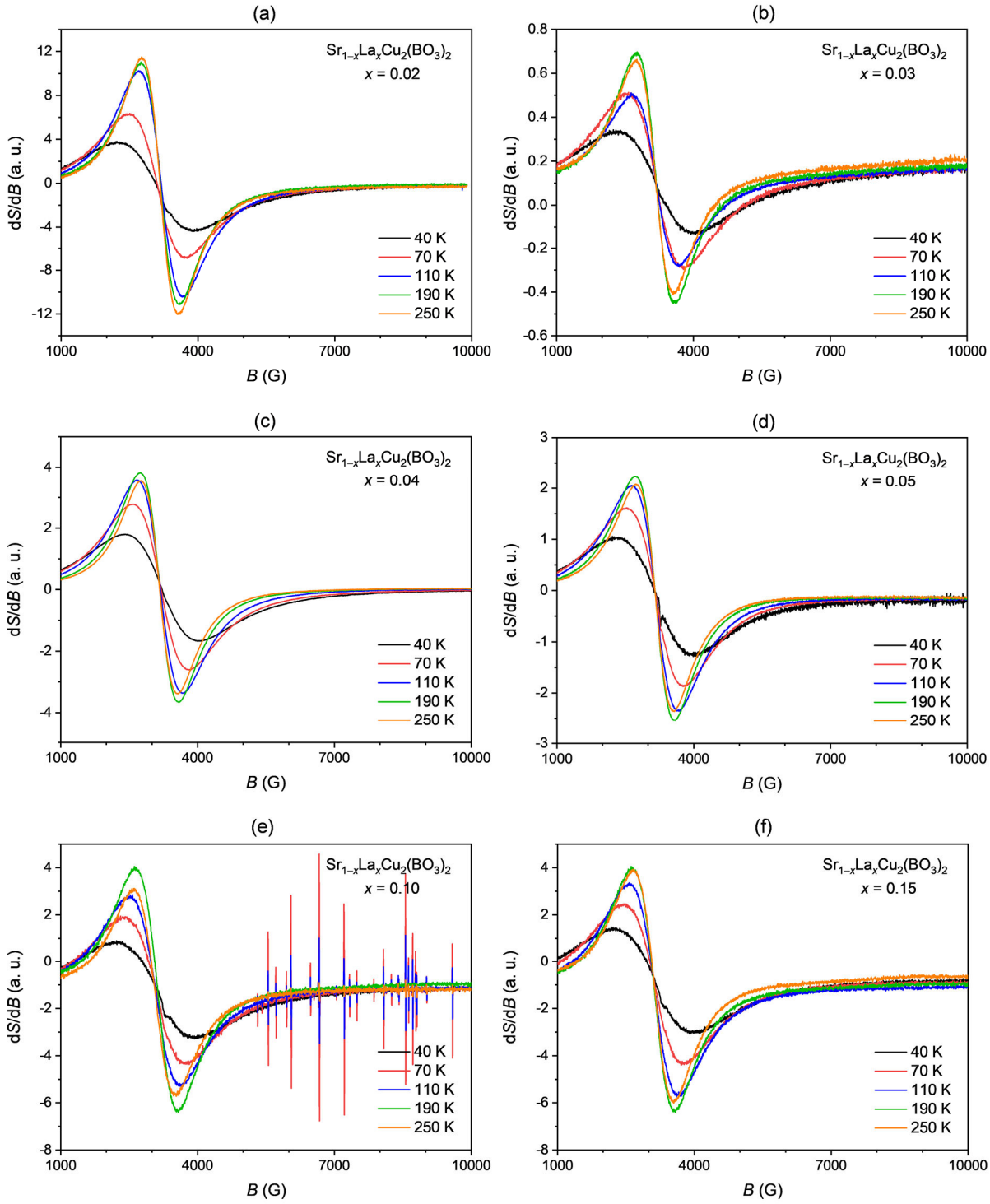


Figure S6 X-band ESR spectra of $Sr_{1-x}La_xCu_2(BO_3)_2$ single crystals with nominal (**a**) x = 0.02, (**b**) 0.03, (**c**) 0.04, (**d**) 0.05, (**e**) 0.10 and (**f**) 0.15, measured as quasi-polycrystalline samples at temperatures 40, 70, 110, 170 and 250 K, which show the dominant signal of the dimer lattice at high temperatures. Additional narrow absorption lines for x = 0.10 sample indicate the presence of an extrinsic paramagnetic impurity, not observed in PXRD or EDS-SEM.

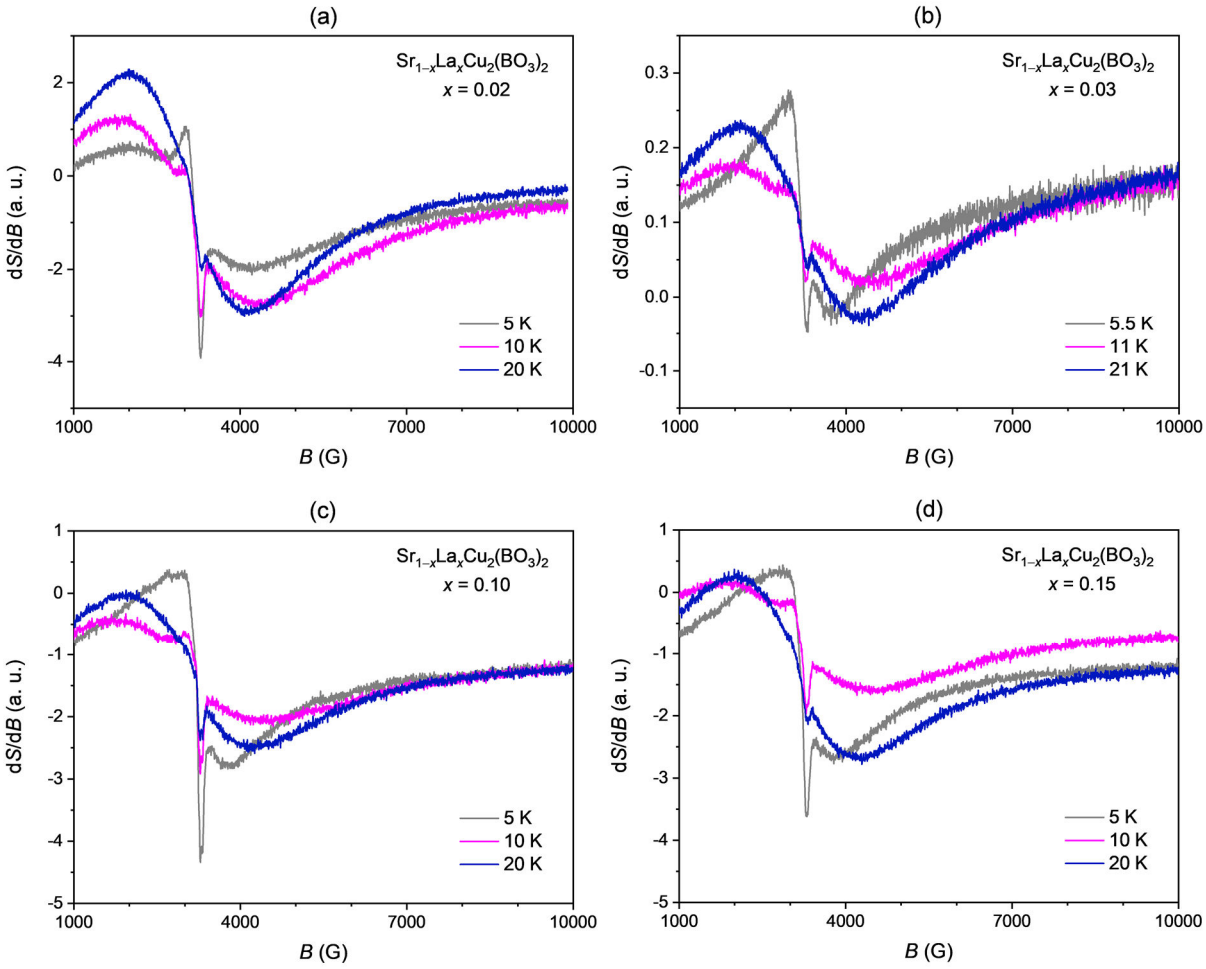


Figure S7 Low-temperature X-band ESR spectra of $Sr_{1-x}La_xCu_2(BO_3)_2$ single crystals with nominal (**a**) $x = 0.02$, (**b**) 0.03, (**c**) 0.10, and (**d**) 0.15 at selected temperatures 5, 10 and 20 K, showing the development of the characteristic impurity signal correlated to intrinsic impurities–isolated dimer free Cu^{2+} spins. Comparing the spectra at 5 and 10 K, an additional broadening is observed at 5 K, indicating the presence of an extra component associated with interactions between dimer-free Cu^{2+}–Cu^{2+} pairs.

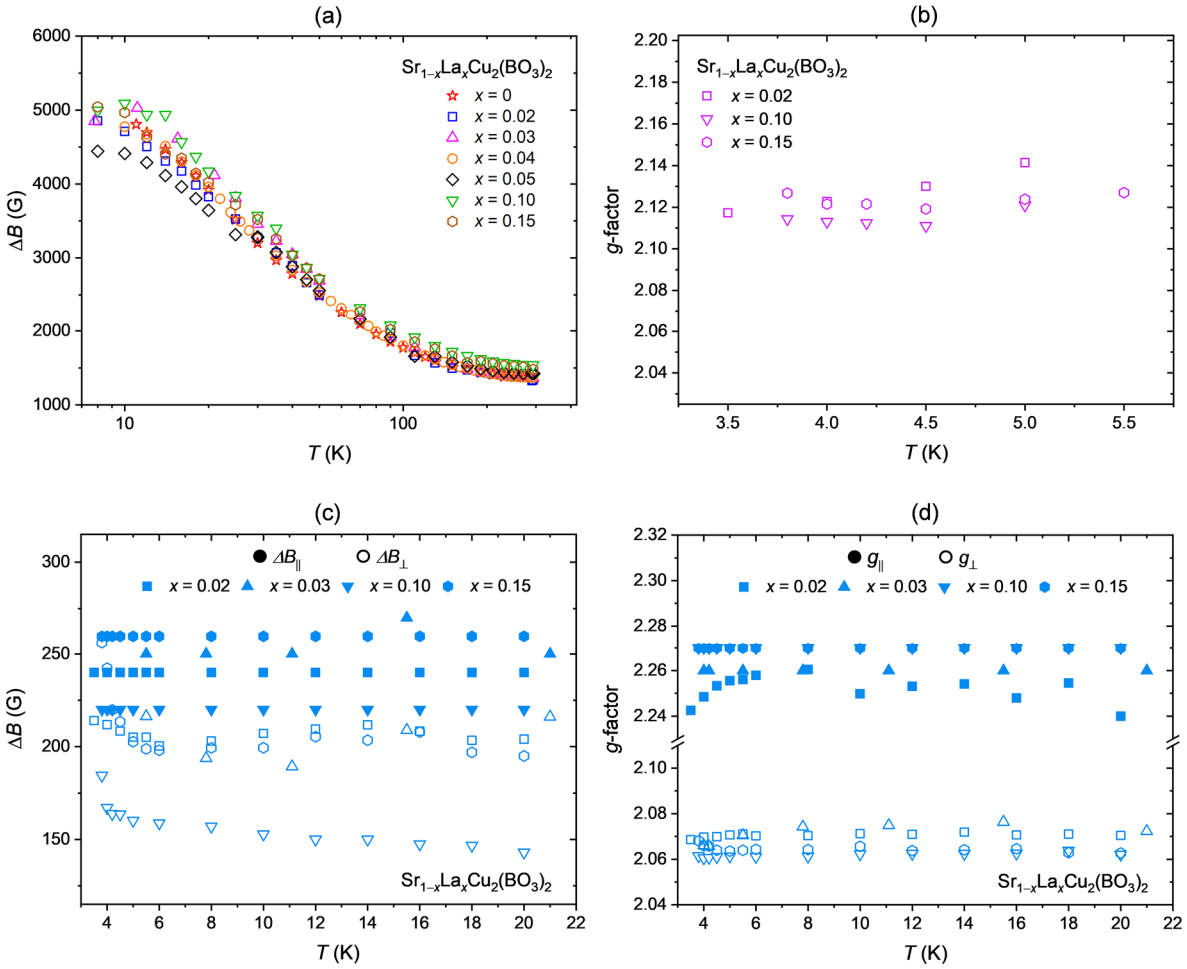


Figure S8 (**a**) The logarithmic temperature behavior of the X-band ESR linewidth of the main dimer-lattice signal. (**b**) The temperature behavior of *g*-factor for the interacting Cu^{2+}–Cu^{2+} pair component for $Sr_{1-x}La_xCu_2(BO_3)_2$ single crystals with nominal x = 0.02, 0.10, and 0.15. (**c**) The temperature behavior of X-band ESR linewidth for the isolated Cu^{2+} impurity component, parallel ($\Delta B_{||}$) and perpendicular ($\Delta B_{\perp}$) to *c* crystallographic axis for $Sr_{1-x}La_xCu_2(BO_3)_2$ single crystals with nominal x = 0.02, 0.03, 0.10, and 0.15. (**d**) The temperature behavior of *g*-factor for the isolated Cu^{2+} impurity component, parallel ($g_{||}$) and perpendicular ($g_{\perp}$) to *c* crystallographic axis for $Sr_{1-x}La_xCu_2(BO_3)_2$ single crystals with nominal x = 0.02, 0.03, 0.10, and 0.15.

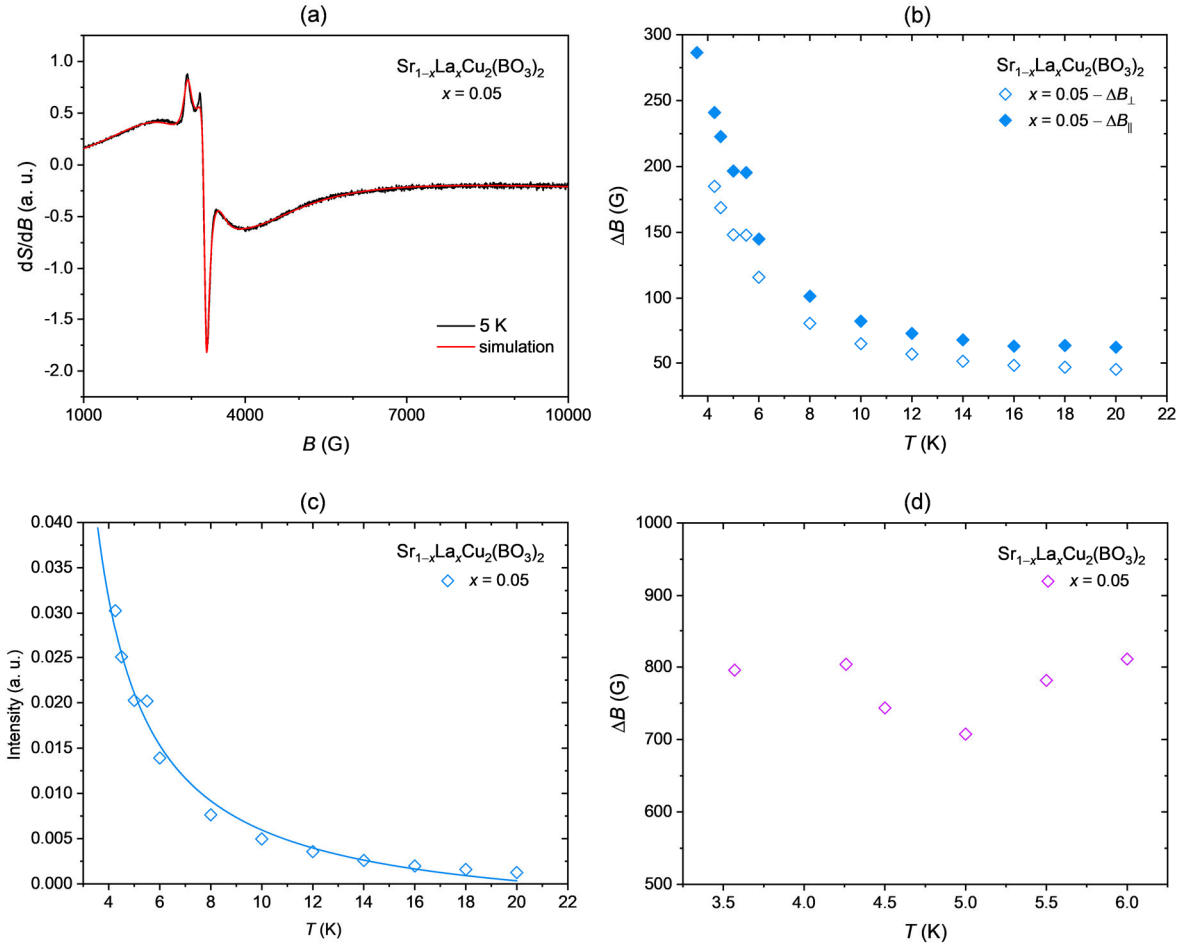


Figure S9 (**a**) X-band ESR spectrum of $Sr_{1-x}La_xCu_2(BO_3)_2$ single crystals with nominal $x = 0.05$ at 5 K, showing a clear uniaxial anisotropy opposed to samples with other nominal doping concentrations, and its simulation as a sum of three components. (**b**) The temperature behavior of X-band ESR linewidth for the isolated Cu^{2+} impurity component, parallel ($\Delta B_{||}$) and perpendicular ($\Delta B_{\perp}$) to *c* crystallographic axis for nominal $x = 0.05$, showing a significant increase in both crystallographic directions with the decreasing temperature, contrary to the rest of the samples. (**c**) Temperature dependence of the signal intensity of the isolated Cu^{2+} impurity component for nominal $x = 0.05$, which follows a Curie–Weiss law, giving a low Curie-Weiss temperature. This indicates minimal spin correlations, aligning with the rest of the samples. (**d**) The temperature behavior of X-band ESR linewidth for the interacting Cu^{2+}–Cu^{2+} pair component for nominal $x = 0.05$. Contrary to the rest of the samples, the linewidth remains constant and does not show a decrease with the decreasing temperature.

REFERENCES

[1] Šibav, L.; Gosar, Ž.; Knaflič, T.; Jagličić, Z.; King, G.; Nojiri, H.; Arčon, D.; Dragomir, M. Higher-Magnesium-Doping Effects on the Singlet Ground State of the Shastry-Sutherland $SrCu_2(BO_3)_2$. *Inorg. Chem.* **2024**, 63, 20335–20346. DOI: 10.1021/acs.inorgchem.4c02398

3.2.2 Effects of Na-doping on the Structure and Magnetism of $SrCu_2(BO_3)_2$

This Section covers a systematic investigation of hole-doping effects on the structure and magnetism of $SrCu_2(BO_3)_2$, experimentally assessing theoretical predictions of unconventional superconductivity potentially realized upon Sr substitutions with Na. The study was conducted on polycrystalline $Sr_{1-x}Na_xCu_2(BO_3)_2$ samples with nominal $x = 0.05$, 0.10 and 0.15, prepared by conventional solid-state method. The undoped reference sample was taken from the study in Section 3.3 [38].

Background

As highlighted in Section 3.1 and the Introduction of Section 3.2.1, theoretical predictions anticipated a potential unconventional superconductivity upon A-site electron- or hole-doping of $SrCu_2(BO_3)_2$ – specifically, by substituting the interlayer Sr^{2+} with an aliovalent cation, M^{3+} or M^{+}, respectively, resulting in $Sr_{1-x}M_xCu_2(BO_3)_2$ [31].

Similar to electron doping, discussed in Section 3.2.1, experimental investigations of hole doping of $SrCu_2(BO_3)_2$ have remained scarce and have highlighted challenges in achieving effective doping. To date, only three studies have explored A-site Na substitution in $SrCu_2(BO_3)_2$. The first study on polycrystalline $SrCu_2(BO_3)_2$ reported Na-doping at a single nominal concentration, $x = 0.1$, in $Sr_{1-x}Na_xCu_2(BO_3)_2$. The results indicated only a minimal doping influence on the magnetic properties, indicating a slight reduction in the unit cell parameters and a subtle closing of the spin gap from 21.5 to 19.8 K, while resistivity measurements confirming the retention of insulating behavior [40]. Subsequent efforts to grow $Sr_{1-x}Na_xCu_2(BO_3)_2$ single crystals with nominal $x = 0.05$ using the optical floating-zone method proved challenging. The growth process was reportedly highly sensitive to any minor variations in the growth conditions, yielding multiple grains rather than large single crystals [41]. The small crystals, isolated from these samples, showed limited effects of doping on the magnetic properties, consistent with the polycrystalline material in exhibiting a small reduction of the spin gap induced by doping and further detecting dimer-free Cu^{2+} spins by muon spin relaxation spectroscopy [42].

The identified experimental obstacles highlight the need for further investigations of the effects of Na-doping on the structure and magnetism of $SrCu_2(BO_3)_2$. With only a single nominal concentration assessed in both polycrystalline and single-crystalline samples, it remains unclear whether the observed effects are systematic across different doping levels. Additionally, the current studies do not provide any further structural analyses or local magnetic probes in polycrystalline samples, leaving both the extent of Na incorporation and its impact on the magnetic properties at the local scale uncertain.

Experimental

Synthesis

Polycrystalline $Sr_{1-x}Na_xCu_2(BO_3)_2$ samples with nominal concentrations $x = 0.05$, 0.10 and 0.15, were prepared by conventional solid-state method. The corresponding reactions are shown in Eq. (3.1):

$$1{-}x\,SrCO_3 + 2\,CuO + 2\,H_3BO_3 + x/2\,Na_2CO_3 \rightarrow Sr_{1-x}Na_xCu_2(BO_3)_2 + 1{-}x\,CO_2 + 3\,H_2O \quad (3.1)$$

High-purity $SrCO_3$ (Alfa Aesar, 99.994%), CuO (Aldrich, 99.99%), H_3BO_3 (Alfa Aesar, 99.9995%) and Na_2CO_3 (Chempur, 99.9%) were used as starting materials. The materials were weighed in stoichiometric proportions and hand-homogenized for one hour in an agate mortar. The resulting grey powder was pressed into pellets of 8 or 10 mm in diameter under a pressure of 5 tonnes. The syntheses were conducted in alumina crucibles through multiple heating cycles with intermediate grinding steps. The thermal treatment consisted of sequential heating steps at 170 °C and 450 °C (12 h each), followed by heating at 780 °C for 24 h and, finally, at 810 °C for an additional 24 h, all in air. Subsequently, two additional cycles of 6 days were performed an oxygen-rich atmosphere at 900 °C. The total synthesis time was around 20 days. In order to prevent the reaction of Na_2CO_3 with alumina, the pellets were placed on Pt foil in the alumina crucibles.

PXRD

The phase composition of the polycrystalline $Sr_{1-x}Na_xCu_2(BO_3)_2$ samples was investigated by powder X-ray diffraction (PXRD) using a Rigaku MiniFlex600-C Benchtop X-ray Diffractometer with Cu Kα radiation, in the 2θ range of 3–120° with a step size of 0.005° and a speed of 2.5°/min. A Rietveld least-square method was used for structural refinements, performed using the program GSAS-II [43] For the undoped sample, the PXRD was performed on a powder diffractometer Panalytical X'Pert Pro with Cu Kα1 radiation in 2θ range 20–120° with a step size of 0.016° and a counting time of 300 s.

EDS-SEM

The microstructural and compositional analyses of the powders were performed using Thermo Fisher Quanta 650 ESEM equipped with an energy-dispersive X-ray spectrometer (Oxford Instruments, AZtec Live, Ultim Max SDD 65 mm^2), using a 30 kV accelerating voltage. Prior to the analyses, polycrystalline $Sr_{1-x}Na_xCu_2(BO_3)_2$ with nominal $x = 0.05$, 0.10 and 0.15 were embedded in an epoxy resin matrix in the form of pellets, polished and carbon coated using sputter coater Balzers SCD 050 following the removal of the resin after polishing.

Magnetic susceptibility

Magnetic susceptibility measurements were performed on a Quantum Design MPMS3 SQUID magnetometer in a temperature interval 2−300 K in a static magnetic field of 1 kG. Prior to the measurements, polycrystalline $Sr_{1-x}Na_xCu_2(BO_3)_2$ samples with nominal $x = 0.05$, 0.10 and 0.15 were placed inside a plastic capsule, which was inserted into a standard straw sample holder and closed with a plastic stopper at one end. The temperatures at which susceptibility has a maximum, T_{max}, were determined from approximating the susceptibility around the maximum to a simple Lorentzian shape.

X-band ESR spectroscopy

Continuous wave (CW) electron spin resonance spectroscopy measurements were performed on a conventional Bruker E500 spectrometer, operating in the X-band at the resonant frequency 9.4 GHz, equipped with a Bruker 4122SHQE cylindrical resonator operating at 9.4 GHz, an Oxford Instruments ESR900 cryostat and an Oxford Instruments ITC503 temperature controller. The temperature dependency of the linewidth was measured from room temperature to 3.5 K with a typical modulation amplitude of 5 G, a modulation frequency of 100 kHz, and microwave power of 2 mW.

Results and Discussion

Solid-state synthesis of $Sr_{1-x}Na_xCu_2(BO_3)_2$ with $x = 0.05$, 0.10 and 0.15, mainly results in the targeted $SrCu_2(BO_3)_2$ phase, which adopts the $I\bar{4}2m$ space group, as identified from the laboratory PXRD data (Figure 3.3 a,b). A small amount of unreacted CuO is also detected, which is consistent with earlier findings on undoped as well as doped samples [36,41], and its quantity appears to increase with Na nominal Na-doping. An absence of any Na secondary phases could indicate a successful substitution of Sr by Na.

The unit cell parameters, extracted from Rietveld refinement analysis (details available in Table 3.1), show an increase in a parameter from 8.9932(1) Å to 8.99386(5) Å for $x = 0.15$. Meanwhile, the c parameter decreases monotonically from 6.6509(1) Å to 6.64862(5) Å for $x = 0.15$ (Figure 3.3 c). Overall, the unit cell volume shows a small (~0.03%), yet systematic decrease with nominal doping. Specifically, it decreases from 537.91(2) $Å^3$ for the undoped sample [38] to 537.738(5) $Å^3$ for nominal $x = 0.15$ (Figure 3.3 d). This decrease parallels the difference of ionic radii of the substituting ions, as the radius of the dopant, Na^+ (1.18 Å for coordination number CN = 8), is lower compared to Sr^{2+} (1.26 Å, CN = 8). A similar trend was also previously observed in the study of polycrystalline $SrCu_2(BO_3)_2$ samples doped with various A-site dopants, where a small decrease of both unit cell parameters, $a = 8.992$ Å and $c = 6.648$ Å, was observed for nominal $x = 0.10$ in $Sr_{1-x}Na_xCu_2(BO_3)_2$ with respect to the undoped system, which yielded $a = 8.995$ Å and $c = 6.649$ Å [40]. In the present study, the unit cell parameters extracted for the $x = 0.10$ sample give slightly higher values compared with those reported in the previous study, yielding $a = 8.99386(3)$ Å and $c = 6.64864(3)$ Å. Interestingly, single crystals of $Sr_{1-x}Na_xCu_2(BO_3)_2$ with $x = 0.05$, grown by optical floating zone in ref. [41], reportedly showed an increase in unit cell volume with respect to single crystals of the undoped system, increasing in c parameter from 6.654 to 6.657 Å, while the a parameter retained the same value of 8.998 Å.

A further inspection of structural details reveals that the intradimer Cu−Cu distance, which determines the nearest-neighbor antiferromagnetic exchange *J,* first increases from 2.9205(9) Å of the undoped system [38] to 2.9224(9) Å for $x = 0.05$ and further to 2.9509(10) Å for the $x = 0.10$ sample, before decreasing to 2.9375(11) Å for $x = 0.15$. The Cu−O−Cu angle shows a subtle decrease from 98.9(1)° for $x = 0$ [38] to 97.0(1)° for $x = 0.05$, then slightly increases to 97.4(1)° for $x = 0.10$ and, finally, decreases to 95.5(2)° for $x = 0.15$. As a higher angle allows a more effective overlap of the orbitals [3], this indicates a subtle softening antiferromagnetic exchange J with increasing nominal concentration. Moreover, the interdimer Cu−Cu distance, which determines next-nearest neighbor exchange *J'*, retains almost the same value of the undoped system, 5.1267(10) Å [38], for $x = 0.05$ sample, where it yields 5.1265(9) Å, then decreases to 5.1139(10) Å for $x = 0.10$, and finally subtly increases to 5.1156(11) Å for $x = 0.15$.

As qualitatively estimated from powder diffractograms, the Rietveld refinement analysis (Figure 3.4 and Table 3.1) also indicates an overall increase in CuO content with nominal doping. Starting at 0.4 wt% for the undoped system, the CuO content first increases to 2.6 and 2.1 wt% for the $x = 0.05$ and $x = 0.10$ samples, and finally increases to 6 wt% for the highest nominal concentration, $x = 0.15$. A comparable behavior was reported for polycrystalline samples upon A-site La doping, as discussed in Section 3.2.1.

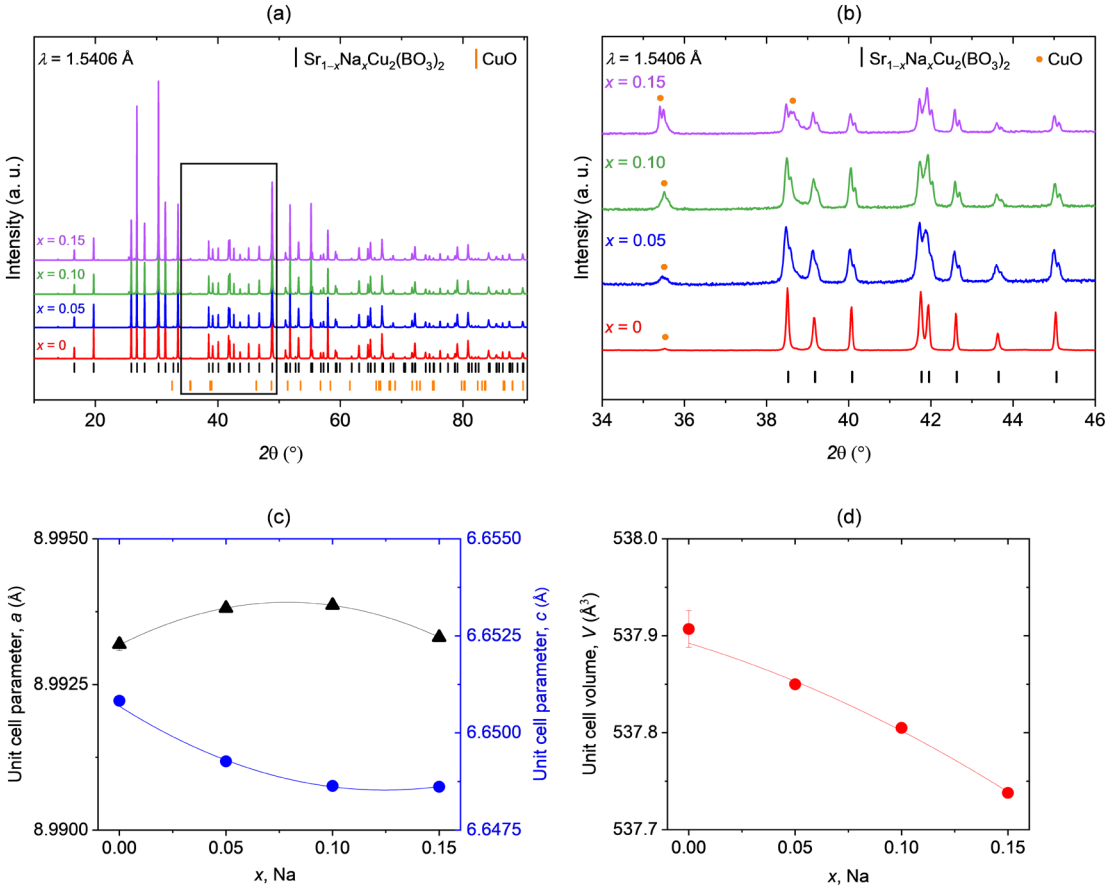


Figure 3.3: a) Laboratory PXRD patterns of polycrystalline $Sr_{1-x}Na_xCu_2(BO_3)_2$ with nominal $x = 0$, 0.05, 0.10, and 0.15 after solid-state reaction, which resulted in the main $SrCu_2(BO_3)_2$ phase, accompanied by minor amounts of unreacted CuO, compared to undoped $SrCu_2(BO_3)_2$ from ref. [38]. b) Enlarged view of the 34°—46° 2θ range marked with a black rectangle in a) for higher clarity. c) The evolution of the unit cell parameters a and c, extracted from Rietveld refinement analysis, as a function of nominal doping. d) The unit cell volume values, determined by Rietveld refinement analysis, as a function of nominal doping.

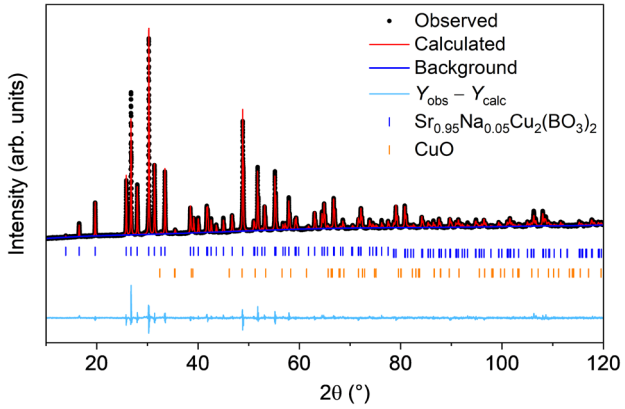


Figure 3.4: Profile fit of room-temperature laboratory PXRD (Cu Kα, λ = 1.5406 Å) of $Sr_{1-x}Na_xCu_2(BO_3)_2$ powders with the selected nominal concentration $x = 0.05$. The Rietveld refinement analysis was performed using the $I\bar{4}2m$ space group.

Table 3.1: Structural parameters derived from the Rietveld refinement analyses of polycrystalline $Sr_{1-x}Na_xCu_2(BO_3)_2$ with $x = 0$ [38], 0.05, 0.10, and 0.15, performed in $I\bar{4}2m$ space group. The data were collected at room temperature. Occupancies denoted by * were constrained to 1 during refinement.

	$SrCu_2(BO_3)_2$ ($x = 0$) [38]	$Sr_{0.95}Na_{0.05}Cu_2(BO_3)_2$ ($x = 0.05$)	$Sr_{0.9}Na_{0.1}Cu_2(BO_3)_2$ ($x = 0.10$)	$Sr_{0.85}Na_{0.15}Cu_2(BO_3)_2$ ($x = 0.15$)
a, b (Å)	8.9932(1)	8.9938(1)	8.9939(1)	8.9933(1)
c (Å)	6.6509(1)	6.6493(1)	6.6486(1)	6.6486(1)
V (Å^3)	537.91(2)	537.85(1)	537.81(1)	537.74(1)
R_{wp} (%)	5.29	3.79	4.48	4.70
Atom	x/y/z Occ. $U_{11}/U_{22}/U_{33}$ (Å^2) $U_{12}/U_{13}/U_{23}$ (Å^2)	x/y/z Occ. U_{iso} (Å^2)	x/y/z Occ. U_{iso} (Å^2)	x/y/z Occ. U_{iso} (Å^2)
Sr	0/0.5/0 0.996(3) 0.0085(1)/0.0051(1)/0.0099(8) 0/0/0	0/0.5/0 1.00* 0.0049(3)	0/0.5/0 1.00* 0.0049(3)	0/0.5/0 1.00* 0.0070(3)
Cu	0.1148(7)/0.1148(7)/0.2776(3) 1.00* 0.0043/0.0043/0.0278 0.0003/0.0027/0.0027	0.1149(1)/0.1149(1)/0.2793(1) 1.00* 0.0093(3)	0.1160(1)/0.1160(1)/0.2761(2) 1.00* 0.0175(4)	0.1155(1)/0.1155(1)/0.2732(1) 1.00* 0.0241(4)
B	0.2963(7)/0.2963(7)/0.2507(28) 1.012(15) 0.0080/0.0080/0.0120 0.0050/0.0050/0.0050	0.2902(4)/0.2902(4)/0.2376(13) 1.00* 0.0050	0.2934(6)/0.2934(6)/0.2511(18) 1.00* 0.0050	0.2868(6)/0.2868(6)/0.2266(13) 1.00* 0.0050
O1	0.4019(4)/0.4019(4)/0.2126(11) 1.00* 0.0095/0.0095/0.0304 0.050/0.0050/0.0050	0.3984(3)/0.3984(3)/0.2223(7) 1.00* 0.0240(12)	0.3985(3)/0.3985(3)/0.2085(6) 1.00* 0.0039(13)	0.3955(4)/0.3955(4)/0.2080(5) 1.00* 0.0050
O2	0.3274(3)/0.1440(3)/0.2523(13) 1.00* 0.0090/0.0080/0.0180 0.0010/0.0010/0.0020	0.3267(2)/0.1471(2)/0.2548(6) 1.00* 0.0050(6)	0.3343(3)/0.1468(3)/0.2457(10) 1.00* 0.0180(8)	0.3317(3)/0.1441(3)/0.2355(8) 1.00* 0.0106(9)

As the PXRD results suggest a possible successful substitution of Sr^{2+} with Na^+, a more detailed chemical analysis is required to confirm or dismiss this. Therefore, SEM/EDS analyses were employed on all three samples ($x = 0.05$, 0.10 and 0.15 in $Sr_{1-x}Na_xCu_2(BO_3)_2$). The SEM backscattered electron images (Figure 3.5 a–c) show the lamellar morphology of the grains in all samples, which reflects the layered $SrCu_2(BO_3)_2$ structure [38]. A few brighter-contrast grains are also observed on the surfaces of the matrix grains, which correspond to unreacted CuO, while no additional impurity phases are detected, both in agreement with the PXRD results (Figure 3.3 a,b).

However, the EDS point analyses on the $SrCu_2(BO_3)_2$ matrix (Figure 3.5 a–c) show no detectable Na, as neither the Na Kα emission line at 1.04 keV nor any other signals indicative of Na are present. The analysis detects only the constituent elements of the parent compound – Sr, Cu and O – with B not observed due to its low atomic mass. The obtained atomic % values are very similar for all three constituent elements regardless of the nominal doping (Table 3.2). The average values were determined from point analyses of 15 spots. This indicates that the incorporation of Na into the parent structure is either not realized during solid-state synthesis or it occurs at concentrations below the EDS detection limit.

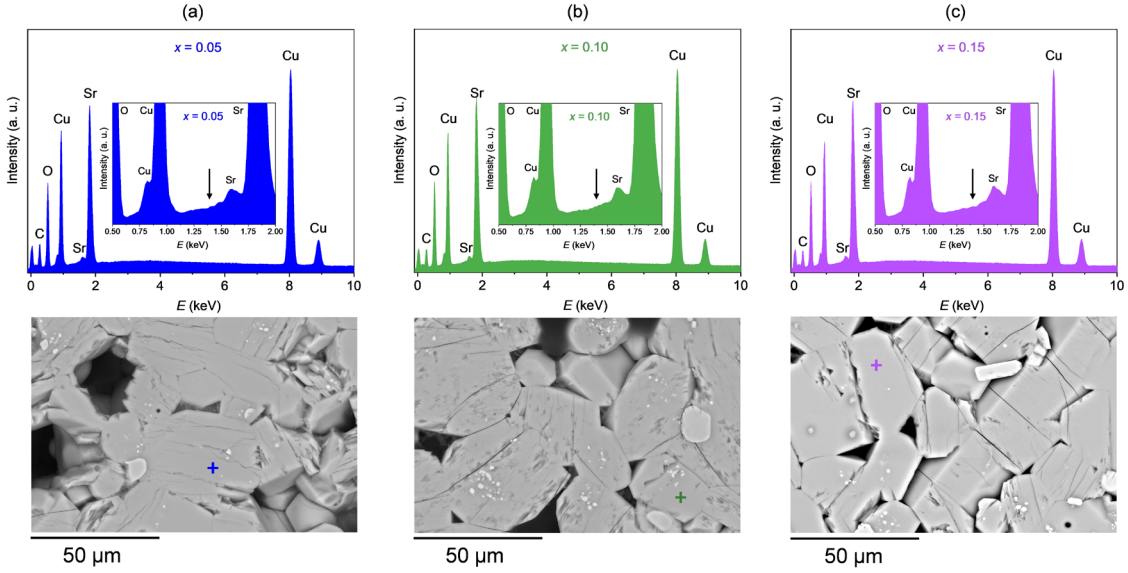


Figure 3.5: Representative normalized EDS point analysis spectra collected on the matrix of polycrystalline $Sr_{1-x}Na_xCu_2(BO_3)_2$ with nominal a) $x = 0.05$, b) 0.10 , and c) $x = 0.15$. The insets magnify the 0.50–2.00 keV region, where the expected position of Na Kα emission line is indicated by arrows, with arrows, indicating the absence of Na in the matrix. The corresponding SEM images for each nominal composition are displayed below the EDS spectra, with the analyzed area marked by a color-coded sign.

Table 3.2: The average semi-quantitative atomic percentage values of Sr, Cu, O and Na, obtained from point analyses collected on the matrix of $Sr_{1-x}Na_xCu_2(BO_3)_2$ samples with nominal $x = 0.05$, 0.10, and 0.15, together with Na/Cu, Na/Sr and Cu/Sr ratios. The values were determined from 15 different SEM-EDS point analyses on each sample matrix.

	Sample, $Sr_{1-x}Na_xCu_2(BO_3)_2$					
	***x* = 0.05**		***x* = 0.10**		***x* = 0.15**	
Element	**Actual**	**Nominal**	**Actual**	**Nominal**	**Actual**	**Nominal**
	Concentration (at%)					
Sr	12.7(3)	10.56	12.8(2)	10.00	12.7(1)	9.44
Cu	27.0(8)	22.22	26.7(6)	22.22	26.8(3)	22.22
O	60.4(8)	66.67	60.6(8)	66.67	60.5(4)	66.67
Na	0	0.56	0	1.11	0	1.67
Sum, %	100.1(19)	100	100.1(16)	100	100.0(8)	100
Na/Cu	0	0.025	0	0.05	0	0.075
Na/Sr	0	0.05	0	0.11	0	0.18
Cu/Sr	2.13(7)	2.10	2.09(2)	2.22	2.10(2)	2.35
	Concentration, mol%					
Na	0	5.0	0	10.0	0	15.0

EDS elemental mapping analysis reveals a segregation of Na in the intergranular regions of all the $Sr_{1-x}Na_xCu_2(BO_3)_2$ samples, which is most pronounced for the highest nominal doping, $x = 0.15$ (Figure 3.6).

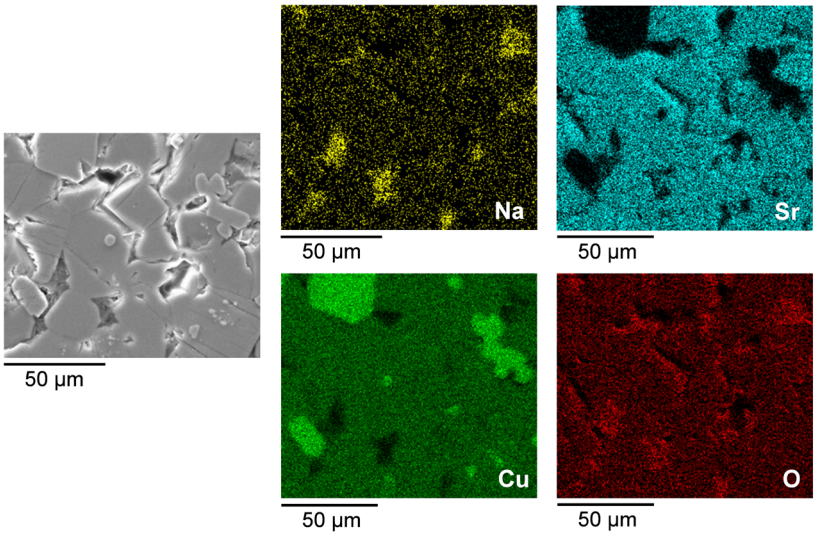


Figure 3.6: A representative SEM image and EDS elemental mapping analysis of polycrystalline $Sr_{1-x}Na_xCu_2(BO_3)_2$ with nominal $x = 0.15$ reveals a segregation of sodium in the intergranular regions. Unreacted CuO grains are also detected in this analysis.

To further investigate the presence of Na in these regions, point analysis spectra were collected in the vicinity of intergranular regions. These analyses show a clearly detectable Na Kα peak at 1.04 keV (Figure 3.7 a,b) for the sample with the lowest and highest nominal doping concentration, $x = 0.05$ and 0.15, respectively. This indicates that Na is present in these regions, thus agreeing with the elemental mapping results. These findings confirm that, rather than incorporating into the parent matrix, Na preferentially remains within the intergranular regions. As no Na secondary phases are detected in PXRD, it is likely that Na forms a glassy borate phase, consistent with literature reports that $Na_2O—B_2O_3$ systems can form both crystalline and glassy phases [44].

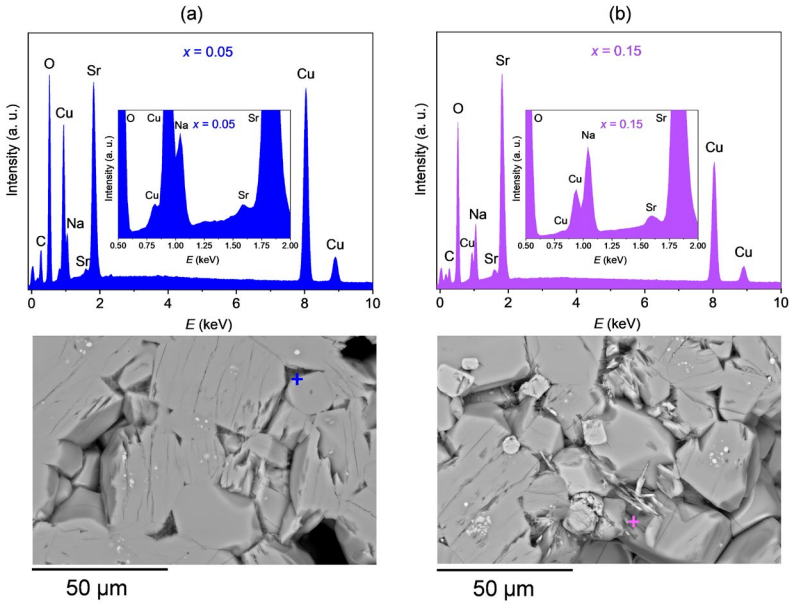


Figure 3.7: Normalized EDS point analysis spectra collected in the vicinity of intergranular areas of polycrystalline $Sr_{1-x}Na_xCu_2(BO_3)_2$ with a) nominal $x = 0.05$ and b) $x = 0.15$. The insets magnify the 0.50–2.00 keV region where the characteristic Na Kα emission line is clearly observed at 1.040 keV, confirming the segregation of Na within the intergranular areas. The corresponding SEM images for each nominal composition are displayed below the EDS spectra, with the analyzed area marked by a color-coded sign.

To investigate the possibility of Na being incorporated into the parent structure at concentrations below the EDS detection limit, magnetic susceptibility, χ, was employed to probe the effect of a possible Na-substitution on the magnetic properties of the parent compound. Qualitatively, all the doped samples with nominal $x = 0.05$, 0.10 and 0.15 show a similar behavior to the undoped system [38] as well as doped with different A- and B-site dopants according to the literature (Figure 3.8) [40,41]. High-temperature behavior follows a Curie-Weiss law, reaching a broad susceptibility maximum, T_{max}, around 15 K. Below T_{max}, a sharp decrease down to about 4 K is observed, indicative of the opening of the spin gap, ending in an upturn below 4 K, which is a hallmark of dimer-free Cu^{2+} $S = ½$ spins in the system. Qualitatively, the magnitude of the upturn increases for doped samples compared to the undoped parent compound, which indicates an increasing fraction of dimer-free Cu^{2+} ions in the doped system, thus implying that Na-doping of $SrCu_2(BO_3)_2$ induces spin-dimer breaking. This is consistent with a previous study on a $Sr_{1-x}Na_xCu_2(BO_3)_2$ single crystal with nominal $x = 0.05$, grown by optical-floating-zone [42] where a more pronounced low-temperature susceptibility upturn was observed compared to the undoped crystal. The influence of Na-doping on the antiferromagnetic interactions

in the system can be quantitatively estimated by fitting the high-temperature region to a Curie-Weiss law, Eq. (3.2), and determining the Weiss temperature, θ (Table 3.3) [38]:

$$\chi = \frac{C}{T - \theta} + \chi_0. \tag{3.2}$$

Here, C represents the Curie constant, T the temperature and χ_0 a temperature-independent term, which accounts for diamagnetic contribution of the ion cores and/or the signal of the sample holder.

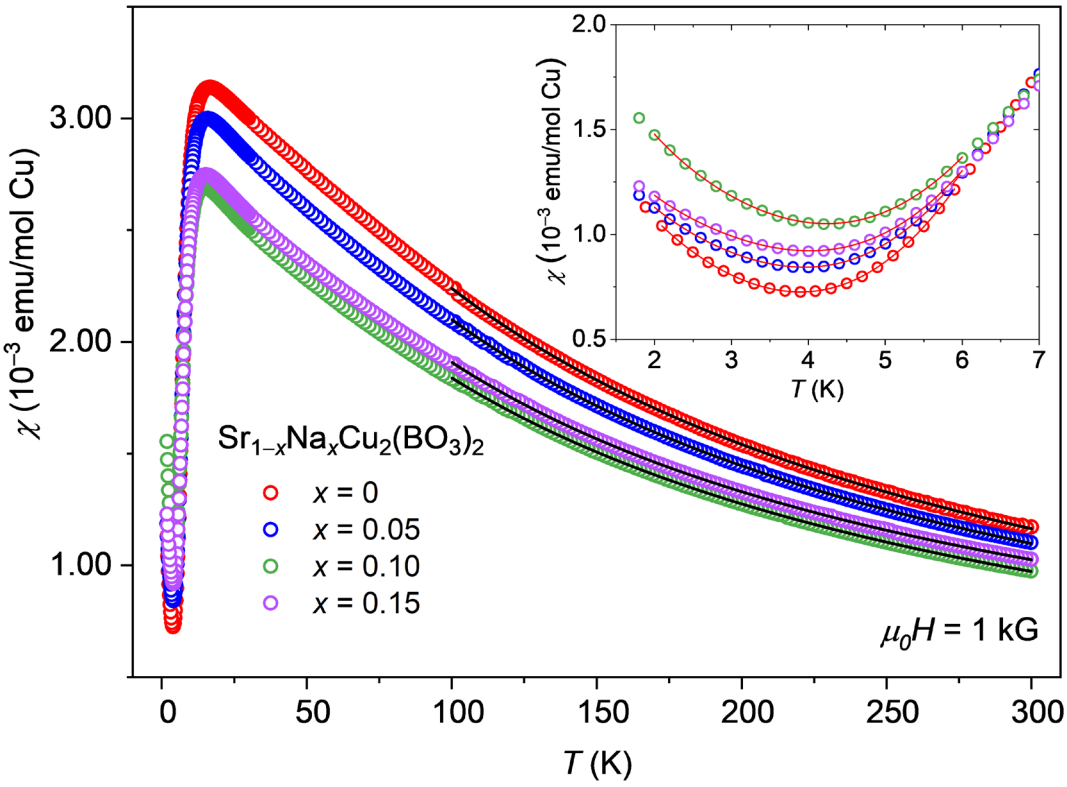


Figure 3.8: The magnetic susceptibility curves of undoped polycrystalline $SrCu_2(BO_3)_2$ [38] and $Sr_{1-x}Na_xCu_2(BO_3)_2$ with nominal $x = 0.05$, 0.10, and 0.15, measured at $\mu_0 H = 1$ kG. The low-temperature region, 2–10 K, is magnified in the inset, and includes low-temperature fits on the Curie-Weiss upturn based on Eq. (3.3), performed in the 2–6 K range with θ' fixed at −0.75 K.

Table 3.3: The complete results of high-temperature magnetic susceptibility data fits in the interval 100–300 K for $Sr_{1-x}Na_xCu_2(BO_3)_2$ powders ($x = 0$–0.15) using the Curie-Weiss law equation, Eq. (3.2).

	C (emu K/mol Cu)	θ (K)	χ_0 (emu/mol Cu)
$SrCu_2(BO_3)_2$ (ref. [38])	0.553(4)	−136(1)	$-9.2(6) \cdot 10^{-5}$
$Sr_{1.95}Na_{0.05}Cu_2(BO_3)_2$	0.486(3)	−127(1)	$-4.0(5) \cdot 10^{-5}$
$Sr_{1.9}Na_{0.1}Cu_2(BO_3)_2$	0.434(2)	−131.7(9)	$-3.1(4) \cdot 10^{-5}$
$Sr_{1.95}Na_{0.15}Cu_2(BO_3)_2$	0.414(3)	−122.0(9)	$4.5(4) \cdot 10^{-5}$

Compared to the undoped sample where takes the value of −136(1) K [38], the samples show a systematic decrease of the Curie-Weiss temperature to −122(1) K for the $x = 0.15$ sample (Table 3.3). This suggests a softening of the antiferromagnetic exchange interactions in the system with increasing doping levels. The temperature at which $\chi(T)$ reaches a maximum, T_{max}, shows only small changes, steadily but slightly decreasing from 16.63(2) K for the undoped system [38] to 15.29(1) K for nominal $x = 0.15$ (Table 3.4).

Table 3.4: Summary of magnetic parameters derived from various fits of susceptibility data for $Sr_{1-x}Na_xCu_2(BO_3)_2$ with $x = 0.05$, 0.10 and 0.15, compared to parameters of the undoped system, $x = 0$, from ref. [38]. The parameters were derived as described in the Journal Article in Section 3.2.1.

Sample/nominal x	**Δ [K]**	**T_{max} [K]**	**C' (low-T, 1.9–3.5 K) [emu K/ mol Cu]**	**Estimated fraction of impurities/ free Cu^{2+} spins [%]**	**High-T fit, θ [K]**
$SrCu_2(BO_3)_2$ (ref. [38]) $x = 0$	26.1(2)	16.63(2)	$3.5(1) \cdot 10^{-3}$	0.93(1)	−136(1)
$Sr_{1.95}Na_{0.05}Cu_2(BO_3)_2$ $x = 0.05$	28.2(3)	15.79(1)	$5.3(2) \cdot 10^{-3}$	1.41(6)	−127(1)
$Sr_{1.9}Na_{0.1}Cu_2(BO_3)_2$ $x = 0.10$	28.2(4)	15.49(1)	$6.3(1) \cdot 10^{-3}$	1.68(3)	−131.7(9)
$Sr_{1.85}Na_{0.15}Cu_2(BO_3)_2$ $x = 0.15$	29.4(5)	15.29(1)	$6.7(2) \cdot 10^{-3}$	1.80(6)	−122.0(9)

Below T_{max}, the susceptibility can be described as a sum of three terms as shown in Eq. (3.3) [40]:

$$\chi = \frac{C'}{T - \theta'} + a e^{\frac{-\Delta}{T}} + \chi_0. \tag{3.3}$$

The first term describes the Curie-Weiss behaviour of the upturn, with C' and θ' representing the Curie constant and the Curie-Weiss temperature, the second term represents a thermally activated contribution from the dimer lattice characterized by a spin gap, Δ, while the last term is added to account for intrinsic diamagnetism of the sample and/or the sample holder. In order to estimate the spin gap of doped samples, the data were fitted to Eq. (3.3) in the interval 2–6 K with θ' fixed at five different values from 0 to −1 (Table 3.5), due to a strong correlation of this parameter with the Curie constant, C'. Considering the results of the best fit with with θ' = –0.75 K, the spin gap exhibits a small increase from 26.1(2) [38] to 29.4(5) K for nominal doping up to $x = 0.15$ (Table 3.4). This behavior contrasts previous studies, which identified a suppression of the gap upon Na-substitution. In polycrystalline samples with nominal $x = 0.10$, the spin gap decreases from 21.5 to 19.8 K at 1 T [40], and a decrease from 27.8 to 24.4 K was also found for single crystals with nominal $x = 0.05$ [42].

Table 3.5: The complete results of magnetic susceptibility data fits in the temperature interval 2−6 K for different doping concentrations using Eq. (3.3). Due to a high correlation between fitted parameters C' and θ', the fitting was performed using multiple fixed θ' values between 0 to −1, assuming antiferromagnetic interactions between the intrinsic impurities − dimer-free Cu^{2+} ions.

	C' (emu K/mol Cu)	χ_0 (emu/mol Cu)	θ'	Δ (K)	a (emu/mol) Cu)
$SrCu_2(BO_3)_2$ $x = 0$ (ref. [38])	$1.72(2) \cdot 10^{-3}$	$2.25(6) \cdot 10^{-4}$	0	27.9(3)	$7.9(4) \cdot 10^{-2}$
	$2.07(1) \cdot 10^{-3}$	$1.59(5) \cdot 10^{-4}$	−0.25	27.2(2)	$7.2(2) \cdot 10^{-2}$
	$2.46(1) \cdot 10^{-3}$	$9.4(5) \cdot 10^{-5}$	−0.5	26.6(2)	$6.7(2) \cdot 10^{-2}$
	$2.88(2) \cdot 10^{-3}$	$2.8(4) \cdot 10^{-5}$	−0.75	26.1(1)	$6.3(1) \cdot 10^{-2}$
	$3.34(2) \cdot 10^{-3}$	$-3.9(5) \cdot 10^{-5}$	−1	25.6(2)	$5.9(1) \cdot 10^{-2}$
$Sr_{1.95}Na_{0.05}Cu_2(BO_3)_2$ $x = 0.05$	$1.35(2) \cdot 10^{-3}$	$4.59(8) \cdot 10^{-4}$	0	30.1(5)	$9.3(8) \cdot 10^{-2}$
	$1.63(2) \cdot 10^{-3}$	$4.07(7) \cdot 10^{-4}$	−0.25	29.4(4)	$8.4(6) \cdot 10^{-2}$
	$1.94(2) \cdot 10^{-2}$	$3.56(7) \cdot 10^{-4}$	−0.5	28.7(3)	$7.8(4) \cdot 10^{-2}$
	$2.27(2) \cdot 10^{-3}$	$3.04(6) \cdot 10^{-4}$	−0.75	28.2(3)	$7.2(3) \cdot 10^{-2}$
	$2.63(2) \cdot 10^{-3}$	$2.51(5) \cdot 10^{-4}$	−1	27.7(2)	$6.8(2) \cdot 10^{-2}$
$Sr_{1.9}Na_{0.1}Cu_2(BO_3)_2$ $x = 0.10$	$1.85(3) \cdot 10^{-3}$	$5.6(1) \cdot 10^{-4}$	0	31.4(9)	$9(1) \cdot 10^{-2}$
	$2.23(3) \cdot 10^{-3}$	$4.92(9) \cdot 10^{-4}$	−0.25	30.1(7)	$7.9(8) \cdot 10^{-2}$
	$2.64(2) \cdot 10^{-3}$	$4.23(8) \cdot 10^{-4}$	−0.5	29.1(5)	$6.9(5) \cdot 10^{-2}$
	$3.10(2) \cdot 10^{-3}$	$3.52(7) \cdot 10^{-4}$	−0.75	28.2(4)	$6.1(3) \cdot 10^{-2}$
	$3.59(2) \cdot 10^{-3}$	$2.81(6) \cdot 10^{-4}$	−1	27.5(3)	$5.6(2) \cdot 10^{-2}$
$Sr_{1.85}Na_{0.15}Cu_2(BO_3)_2$ $x = 0.15$	$1.22(3) \cdot 10^{-4}$	$5.8(1) \cdot 10^{-4}$	0	31.6(8)	$1.0(1) \cdot 10^{-1}$
	$1.47(3) \cdot 10^{-3}$	$5.37(9) \cdot 10^{-4}$	−0.25	30.7(7)	$9(1) \cdot 10^{-2}$
	$1.74(3) \cdot 10^{-3}$	$4.91(9) \cdot 10^{-4}$	−0.5	30.0(6)	$8.2(7) \cdot 10^{-2}$
	$2.04(3) \cdot 10^{-3}$	$4.45(8) \cdot 10^{-4}$	−0.75	29.4(5)	$7.5(6) \cdot 10^{-2}$
	$2.36(3) \cdot 10^{-2}$	$3.99(8) \cdot 10^{-4}$	−1	28.9(4)	$7.0(4) \cdot 10^{-2}$

To estimate the amount of dimer-free Cu^{2+} spins in the doped system, the low-temperature upturn in inverse susceptibility data is fitted to a Curie-Weiss law in the temperature range 2–3.4 K (Figure 3.9). The resulting Curie constant, C', increases with increasing nominal doping levels, from $3.5(1) \cdot 10^{-3}$ emu K/mol Cu for the undoped sample [38], to $5.3(2) \cdot 10^{-3}$ for $x = 0.05$, $6.3(1) \cdot 10^{-3}$ for $x = 0.10$, and, finally, to $6.7(2) \cdot 10^{-3}$ emu K/mol Cu for $x = 0.15$ (Table 3.4). This corresponds to an increase of estimated fraction of free Cu^{2+} spins from 0.93(1)% for $x = 0$ [38] to 1.41(6)% for $x = 0.05$, 1.68(3)% for $x = 0.10$ and, finally, 1.80(6)% for $x = 0.15$ (Table 3.4). Overall, at the highest nominal doping concentration, $x = 0.15$, the number of broken dimers is almost double compared to the undoped sample. The value obtained for the $x = 0.05$ sample is almost five times higher than the fraction of impurity spins in the Na-doped single crystal with nominal $x = 0.05$ grown by optical floating zone as reported in ref. [42] and comparable to 1.49(6)% achieved in La-doped single crystals with nominal $x = 0.05$ from ref. [42].

As noted earlier upon qualitative assessment of the upturn magnitude in doped samples, the increasing fractions of dimer-free Cu^{2+} spins as a function of nominal doping, estimated from the fits indicate that similarly to electron doping of $SrCu_2(BO_3)_2$ with La, hole doping with Na shows a detrimental effect on the spin-dimer lattice, which increases with nominal doping. The Cu^{2+} $S = 1/2$ spin-dimer breaking, induced by Na-doping, can be attributed to local perturbations in the magnetic $Cu_2(BO_3)_2^{2-}$ layers.

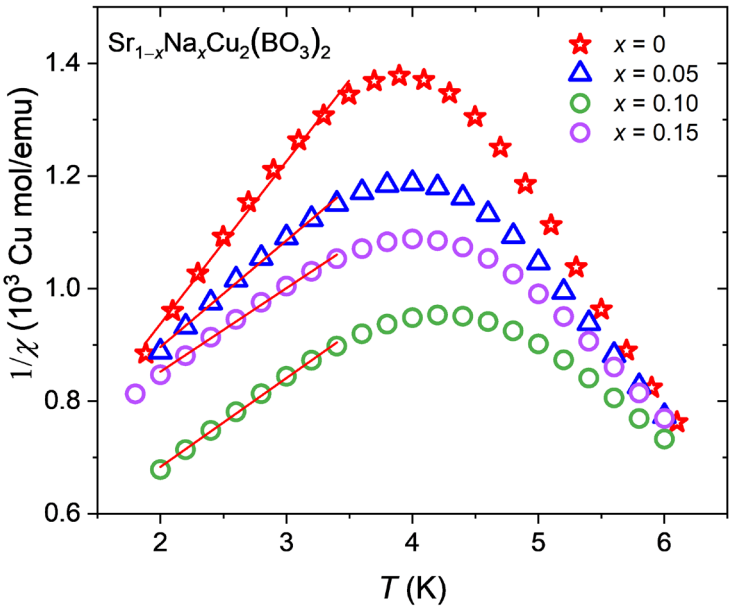


Figure 3.9: Low-temperature fits (T = 2–3.4 K) of the $1/\chi$ data to a Curie-Weiss lawfor polycrystalline $Sr_{1-x}Na_xCu_2(BO_3)_2$ with nominal x = 0.05, 0.10, and 0.15, compared to the undoped system from ref. [38]. The estimated fraction of dimer-free Cu^{2+} $S = 1/2$ spins in the system was derived from these fits for all samples.

Magnetic properties of Na-doped samples are further studied by a more sensitive and local magnetic probe, continuous wave X-band ESR spectroscopy. The temperature dependent behaviour of the samples is studied from room temperature down to 3.5 K and compared with the results for the undoped system from ref. [38]. At higher temperatures, the main dimer-lattice signal is observed for all samples. Upon decreasing the temperature, this signal gradually decreases in intensity while its linewidth broadens (Figure 3.10), reflecting the development of spin correlations within the spin-dimer lattice. This is consistent with previous studies on the undoped [45–48] and La-doped system. Concurrently, another signal appears around 3200 G, emerging at temperatures as high as 90 K for $x = 0.05$, 170 K for $x = 0.10$, and already at room temperature for $x = 0.15$ (Figure 3.10 b–d), thus persisting to progressively higher temperatures with increasing nominal doping.

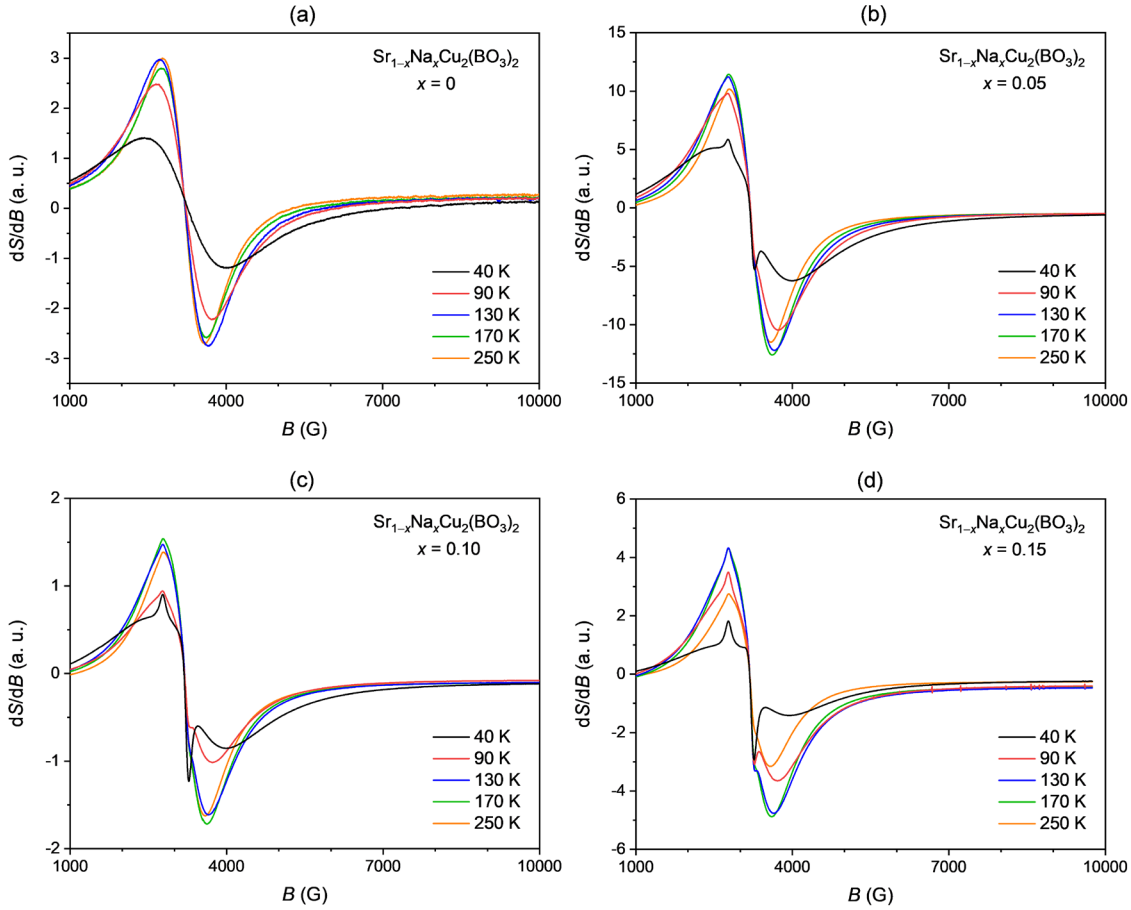


Figure 3.10: X-band ESR spectra of polycrystalline $Sr_{1-x}Na_xCu_2(BO_3)_2$ with nominal a) $x = 0.05$, b) 0.10 and c) 0.15, at selected temperatures 40, 90, 130, 170 and 250 K. The main dimer-lattice signal decreases with the decreasing temperature, while an additional signal emerges at 3200 G. As a function of nominal doping, this signal becomes gradually more pronounced at selected temperatures and also persists to higher temperatures.

The intensity of this signal, only weakly detected in the undoped system below 14 K (Figure 3.11 a, [38]), gradually increases upon cooling, becoming dominant below approximately 20 K, where it shows a clear axial g-factor anisotropy (Figure 3.11 b–d). Being a hallmark of Cu^{2+} ions, it unambiguously confirms the presence of dimer-free Cu^{2+} in the system and thus aligns with magnetic susceptibility results, confirming a Cu^{2+} spin-dimer breaking in the system induced by Na-doping. The observation of dimer breaking in the Na-doped system is consistent with previously reported muon spin relaxation spectroscopy results on a $Sr_{1-x}Na_xCu_2(BO_3)_2$ single crystal (nominal $x = 0.05$), grown by the optical floating zone method [42]. A fast Fourier transform of the transverse-field muon precession signal revealed three clearly distinguished frequency peaks for the doped crystal, whereas only two peaks were observed for the undoped sample. These two peaks resulted from two free Cu^{2+} spins, created by the muon perturbing the Cu–Cu spin dimer in the parent lattice. If the dimer had been broken as a result of doping, the muon would be in proximity only to one dimer-free Cu^{2+} spin, producing a smaller frequency shift and thereby explaining the emergence of the additional peak [42].

In the present study, the characteristic Cu^{2+} spin signal dominates the ESR spectrum, while the main dimer-lattice signal disappears at progressively higher temperatures with increasing nominal doping. This qualitatively indicates a growing fraction of dimer-free

Cu^{2+} spins, aligning with results obtained from low-temperature inverse susceptibility fits and confirming that some Na was incorporated, inducing spin-dimer breaking increases with increasing nominal doping.

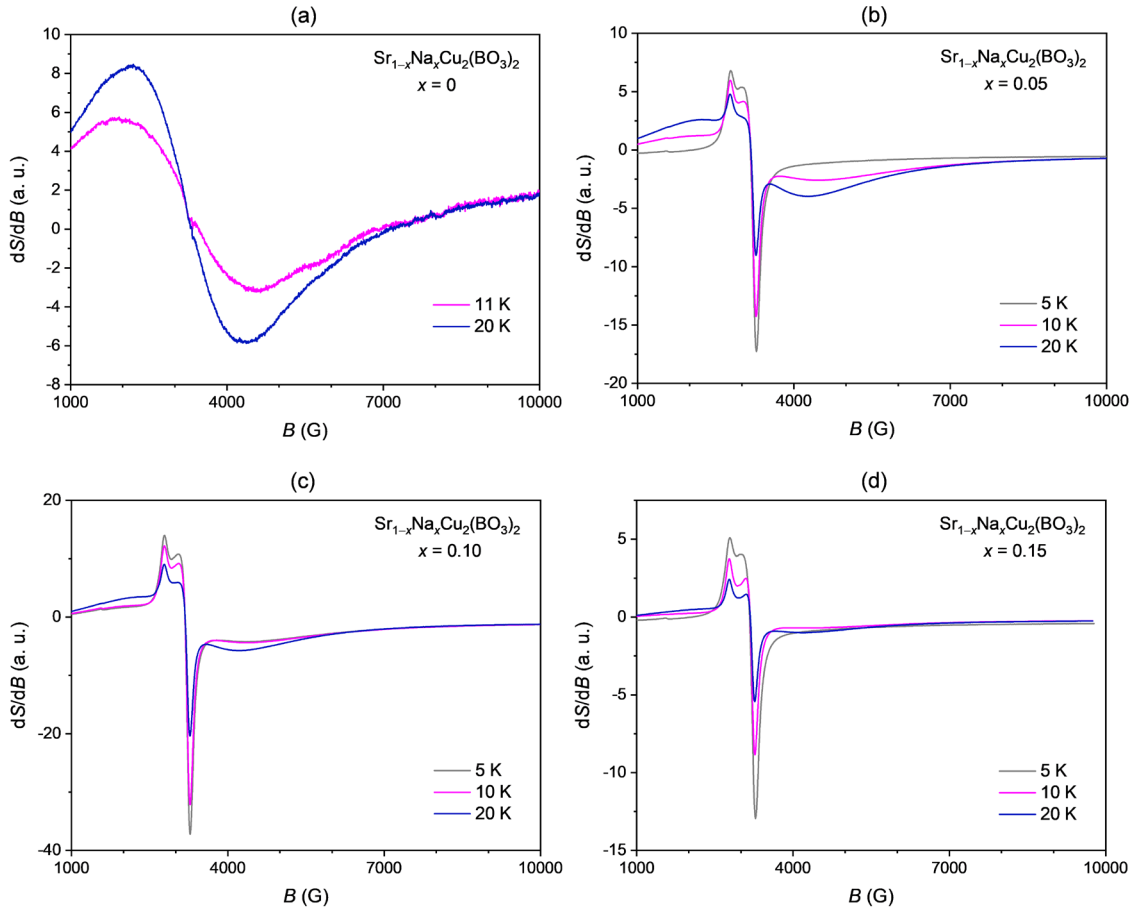


Figure 3.11: Low-temperature X-band ESR spectra of polycrystalline $Sr_{1-x}Na_xCu_2(BO_3)_2$ with nominal a) $x = 0$ at selected temperatures 11 and 20 K [38], b) 0.05, c) $x = 0.10$, and d) 0.15, at selected temperatures 5, 10 and 20 K. In all doped samples, the dimer-free Cu^{2+} impurity signal with axial g-factor anisotropy is dominant at low temperatures, while remaining barely detected for the undoped system. The main dimer-lattice disappears at progressively higher temperatures with nominal doping, indicating a higher fraction of Cu^{2+} $S = ½$ spins and thus a progressively more pronounced spin-dimer breaking as a function of nominal doping.

Overall, structural characterization of polycrystalline $Sr_{1-x}Na_xCu_2(BO_3)_2$ samples by PXRD reveals subtle structural changes, while EDS detects no Na incorporation in the parent matrix. The observed segregation of Na in the intergranular regions, together with the absence of Na secondary phases in PXRD, suggests that Na preferentially forms glassy borate phases. Although structural analyses do not confirm a Na incorporation, a significant effect on the magnetic properties is still detected.

Magnetization measurements and ESR spectroscopy, reveal the emergence of dimer-free Cu^{2+} spins, with their fraction rising with nominal doping. The prominent free Cu^{2+} signal with axial g-factor anisotropy observed in ESR experiments, which dominates the spectrum at low temperatures for all samples and persists up to room temperature at the highest nominal concentration ($x = 0.15$), clearly indicates a significant Na-doping-induced

spin-dimer breaking upon solid-state synthesis. These observations indicate that even minor Na-doping, undetectable by local structural or compositional analyses, exerts a significantly detrimental effect on the spin-dimer lattice and its magnetic properties.

Conclusions

This study experimentally investigates the effect of hole doping of the Shastry-Sutherland compound $SrCu_2(BO_3)_2$ with Na in polycrystalline samples with three nominal doping concentrations, $x = 0.05$, 0.10 and 0.15, in $Sr_{1-x}Na_xCu_2(BO_3)_2$. Powder X-ray diffraction shows only subtle structural changes and no Na-based secondary phases, suggesting a potential Na incorporation into the parent structure. However, SEM-EDS analysis detects no signs of Na within the $SrCu_2(BO_3)_2$ matrix, instead locating Na within the intergranular regions. The combined PXRD and SEM-EDS results indicate that Na is not effectively incorporated into the parent lattice, and is instead likely segregated into amorphous secondary phases, with any lattice incorporation remaining below the EDS detection limit. Despite this, magnetic susceptibility measurements, which indicate a subtle increase in the spin gap from 26.1 to 29.5 K, clearly reveal an emergence of dimer-free Cu^{2+} spins in the doped samples, with their fraction increasing systematically with nominal doping levels. These observations are corroborated by electron spin resonance spectroscopy, which unambiguously confirms both the presence and the progressive increase of dimer-free Cu^{2+} spins with nominal doping. Remarkably, at the highest nominal doping level, $x = 0.15$, the characteristic ESR signal of free Cu^{2+} spins with axial g-factor anisotropy persists up to room temperature, indicating a substantial dimer-spin breaking induced by Na-doping. Collectively, these results suggest that although Na incorporation remains below the detection limit of local structural analyses, it is nevertheless sufficient to induce Cu^{2+} $S = 1/2$ spin-dimer breaking upon solid-state synthesis, significantly affecting the spin-dimer lattice and its magnetic properties.

3.3 B-site Cu Nonmagnetic Substitutions in $SrCu_2(BO_3)_2$: Magnetic Dilution Effects

This Section covers a systematic study of magnetic dilution effects on the structure and magnetism of $SrCu_2(BO_3)_2$, which experimentally investigates theoretical predictions of a possible QSL state, which may be realized upon B-site isovalent doping, via Mg-doping. The study is conducted on four polycrystalline $SrCu_{2-x}Mg_x(BO_3)_2$ samples with nominal $x = 0$, 0.03, 0.05 and 0.10, prepared by a conventional solid-state method.

The samples show a subtle, yet systematic lattice expansion as a consequence of a partially successful substitution of Cu with Mg in the parent $SrCu_2(BO_3)_2$. The effective dopant incorporation is estimated at 7 mol%, demonstrating that the Mg-doping boundary can be pushed to higher values.

The effective Mg-doping achieved by this method leads to softening of antiferromagnetic exchange interactions in the system, resulting in a spin gap reduction from 26.1(2) to 15.9(4) K as well as a decrease of the Curie-Weiss temperature and the magnetic susceptibility maximum. The presence of dimer-free Cu^{2+} $S = 1/2$ spins, which increase in concentration with higher doping levels, points to a successful magnetic dilution, evidenced by Cu^{2+} dimer breaking.

Furthermore, the study of magnetization plateaus in Mg-doped system via high-field magnetic susceptibility up to 35 T reveals a suppression of the 1/8 pseudo-plateau at nominal $x = 0.10$, experimentally confirming a previously proposed expectation of suppression of this plateau at doping levels beyond $x = 0.05$ [49]. Additionally, an anomaly at an onset critical field $\mu_0 H'_{C0} \approx 9$ T, previously only weakly observed at nominal $x = 0.05$, is clearly detected at nominal $x = 0.10$, indicating the formation of impurity-driven spin configurations. This anomaly is indicative of impurity-driven spin configurations involving dimer-free Cu^{2+} $S = 1/2$ spins coupled coupled beyond Cu^{2+} intradimer distances, supporting the emergence of novel magnetic states stabilized at higher Mg-doping levels.

Although tuning of the $SrCu_2(BO_3)_2$ ground state by Mg-doping up to nominal $x = 0.10$ does not lead to a quantum spin liquid state, it shows a significant softening of antiferromagnetic interactions in the system, stabilizing novel impurity-driven magnetic states.

This Section addresses Aims 1 and 2 and evaluates Hypotheses 2–4.

Published in: L. Šibav, Ž. Gosar, T. Knaflič, Z. Jagličić, G. King, H. Nojiri, D. Arčon and M. Dragomir, "Higher-Magnesium-Doping Effects on the Singlet Ground State of the Shastry-Sutherland $SrCu_2(BO_3)_2$," *Inorg. Chem.*, vol. 63, no. 43, pp. 20335−20346, 2024, DOI: 10.1021/acs.inorgchem.4c02398. (IF = 4.7, 2025, Q1)

First author contribution: Conducted solid-state reactions and Rietveld refinement analysis of synchrotron PXRD data. Carried out scanning electron microscopy and energy-dispersive X-ray spectroscopy measurements. Performed magnetic susceptibility data fitting, electron paramagnetic resonance spectroscopy measurements and the corresponding data analysis. Co-prepared the original manuscript draft and participated in its review and editing together with co-authors.

Inorganic Chemistry

Open Access
This article is licensed under CC-BY 4.0

pubs.acs.org/IC Article

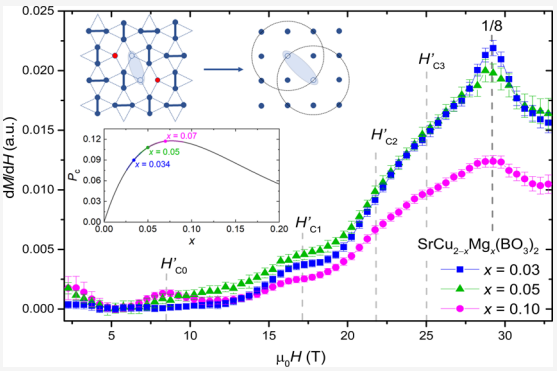
Higher-Magnesium-Doping Effects on the Singlet Ground State of the Shastry−Sutherland $SrCu_2(BO_3)_2$

Lia Šibav, Žiga Gosar, Tilen Knaflič, Zvonko Jagličić, Graham King, Hiroyuki Nojiri, Denis Arčon, and Mirela Dragomir*

Cite This: *Inorg. Chem.* 2024, 63, 20335−20346 Read Online

ACCESS | Metrics & More | Article Recommendations | Supporting Information

ABSTRACT: Doping of quantum antiferromagnets is an established approach to investigate the robustness of their ground state against the competing phases. Predictions of doping effects on the ground state of the Shastry−Sutherland dimer model are here verified experimentally on Mg-doped $SrCu_2(BO_3)_2$. A partial incorporation of Mg^{2+} on the Cu^{2+} site in the $SrCu_2(BO_3)_2$ structure leads to a subtle but systematic lattice expansion with the increasing Mg-doping concentration, which is accompanied by a slight decrease in the spin gap, the Curie−Weiss temperature, and the peak temperature of the susceptibility. These findings indicate a doping-induced breaking of Cu^{2+} spin-1/2 dimers that is also corroborated by X-band EPR spectroscopy that points to a systematic increase in the intensity of free Cu^{2+} sites with increasing Mg-doping concentration. Extending the Mg-doping up to nominal $x = 0.10$ yielding $SrCu_{1.9}Mg_{0.1}(BO_3)_2$, in the magnetization measurements taken up to 35 T, a suppression of the pseudo-1/8 plateau is found along with a clear presence of an anomaly at an onset critical field $\mu_0 H'_{C0} \approx 9$ T. The latter, absent in pure $SrCu_2(BO_3)_2$, emerges due to the pairwise coupling of liberated Cu^{2+} spin-1/2 entities in the vicinity of Mg-doping induced impurities.



1. INTRODUCTION

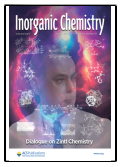
Quantum fluctuations, low dimensionality and geometric frustration are considered important ingredients for exotic states of matter such as quantum spin liquids[1,2] or high-T_C superconductivity.[3] In particular, low-dimensional materials with antiferromagnetic (AFM) interactions and coupled $S = 1/2$ moments are the most promising to experimentally explore the realization of such exotic states.[4−7] In the last decades, transition metal oxides exhibiting such physics have been actively studied. A particular interest is devoted to the family of high-T_C cuprate superconductors where the observation of two-dimensional (2D) antiferromagnetism in Mott-insulating parent compounds led to the suggestion of an intimate correlation of the gapped spin excitations with unconventional superconductivity in charge-doped compounds.[8] Following this discovery, numerous studies focused on other 2D spin systems with spin-gapped ground states.[9,10] While the spin-singlet ground state is commonly found in one-dimensional (1D) or quasi-1D materials,[11−15] there are only few examples of 2D spin-gapped systems[16−18] due to their tendency of long-range ordering guided by the interlayer exchange interactions.

One rare example of a spin-gapped 2D material is strontium copper orthoborate, $SrCu_2(BO_3)_2$.[18] As the first experimental realization of the theoretical Shastry-Sutherland model,[19] this frustrated 2D spin system contains spin dimers which are orthogonally coupled on a square lattice. In this model, the in-plane coupling of Cu^{2+} ($S = 1/2$) spins is described by the antiferromagnetic nearest neighbor (NN) coupling J and the next-nearest neighbor (NNN) coupling J':

$$\hat{H} = J \sum_{NN} S_i S_j + J' \sum_{NNN} S_i S_j + g\mu_B B \cdot \sum_i S_i \quad (1)$$

The last term in eq 1 is the Zeeman interaction with the external magnetic field, B. The model Hamiltonian has been successfully applied to $SrCu_2(BO_3)_2$ to interpret, e.g., the results of electron paramagnetic resonance (EPR)[20−25] and nuclear magnetic resonance (NMR) studies.[26−29] Importantly, the J'/J ratio in eq 1 dictates the magnetic ground state.[19,30] For $J'/J < 0.69$, the ground state is the exact dimer phase that is a product of singlets on Cu-dimers,[31] while a gapped plaquette singlet state or a plaquette valence bond solid phase is found for $0.69 < J'/J < 0.86$.[30,31] For $J'/J > 0.86$, the Néel phase or

Received: June 10, 2024
Revised: September 21, 2024
Accepted: September 26, 2024
Published: October 16, 2024



ACS Publications
© 2024 The Authors. Published by American Chemical Society

https://doi.org/10.1021/acs.inorgchem.4c02398
Inorg. Chem. 2024, 63, 20335−20346

the dimer valence bond solid phase is stabilized. Recently, a novel quantum spin liquid phase has been predicted to exist between the gapped plaquette-singlet phase and the antiferromagnetic phase.[32] Experimentally, the J'/J ratio in $SrCu_2(BO_3)_2$ was determined to be 0.68 (J = 100 K, J' = 68 K),[33] with more recent reports claiming a slightly smaller value of 0.63(1).[34,35] The value of J'/J positions $SrCu_2(BO_3)_2$ to the exact singlet-dimer state of the Shastry-Sutherland phase diagram. However, it is also very close to the quantum critical point that separates the singlet-dimer state to other competing phases.[28] This specific property of $SrCu_2(BO_3)_2$ opens up an intriguing possibility to investigate the stability and behavior of a frustrated quantum antiferromagnet close to a quantum critical point.

The exact dimer phase of $SrCu_2(BO_3)_2$ was first challenged in high-magnetic field experiments aiming to close the spin gap, Δ. The first estimate of a spin gap Δ of 19(1) K was from low-temperature magnetic susceptibility,[36] but more precise values of 34(1) K were obtained from other experiments such as high-field EPR.[37] Upon closing Δ with magnetic field, the presence of strong frustration is responsible for the Wigner-like crystallization of triplets at critical fields, giving rise to characteristic magnetization plateaus.[38] Namely, the magnetization plateaus at fractional values of the saturated magnetization of 1/8 and 1/4 were initially observed.[18,36] Later, other intermediate fractional plateaus were also reported such as 1/3[39] and 1/9, 1/7, 1/6, 1/5, 2/9,[40] adding to the extreme richness of the $SrCu_2(BO_3)_2$ phase diagram. A very recent study showed evidence of a spin nematic phase or bound-state condensate in $SrCu_2(BO_3)_2$ before the 1/8 plateau and beyond 21 T, which is understood as a condensate of bosonic Cooper pairs.[41] Alternatively, the ground state of $SrCu_2(BO_3)_2$ may be altered by means of physical pressure or chemical pressure through substitutions. Applying hydrostatic pressure on $SrCu_2(BO_3)_2$[27,42,43] was shown to induce two quantum phase transitions: (i) around 1.7 GPa, where the dimer singlet phase transitions to a plaquette singlet phase below 2 K, (ii) at 3−4 GPa, where another antiferromagnetic phase is realized below 4 K.[44]

On the other hand, the effects of chemical pressure or chemical-doping-induced impurities on the ground state of $SrCu_2(BO_3)_2$ are less understood due to difficulties in chemical modifications of this compound. However, theoretical studies have predicted that altering the ground state of $SrCu_2(BO_3)_2$ by chemical doping could result in exotic magnetic states such as quantum spin liquids or superconductors.[45,46] In spite of these promising theoretical predictions, the literature on the experimental doping of $SrCu_2(BO_3)_2$ is scarce[47−52] as introducing dopants into the crystal structure of $SrCu_2(BO_3)_2$ has been proven to be a very challenging process even for low doping concentrations.

The chemical substitutions on the Sr site, located between the Cu−O−B layers in the $SrCu_2(BO_3)_2$ structure, could exert both chemical pressure on the Cu−Cu exchange pathways and charge imbalance through a different valence state of the dopant, affecting the Cu magnetic moment. Doping on the Sr site with Y, Na, La, Zn or Al led to a suppression of the spin gap in polycrystalline samples,[49] but the gap was not fully closed and no superconductivity was observed. Single crystals of Na- and La-doped $SrCu_2(BO_3)_2$ have also been grown by the optical floating zone method.[50] Although the X-ray diffraction (XRD) measurements showed that these compounds are single-phase and their in-plane lattice parameter depends systematically on the dopant content x, a detailed structural and local-probe investigation such as EPR or NMR of these dopants is still missing. Moreover, a quantum spin liquid is anticipated to be realized by magnetic dilution—partially substituting the magnetic Cu^{2+} ions with nonmagnetic isovalent cations, which could break the spin dimers and establish a long-range quantum entanglement at the lowest temperatures.[47] Magnetic dilution, i.e., Mg^{2+} substitutions on the Cu^{2+} site, has been proven to be chemically even more challenging and only a few reports exist on Mg-doped $SrCu_2(BO_3)_2$. Previous studies focused on $SrCu_{2-x}Mg_x(BO_3)_2$ with nominal $x \leq 0.05$ including measurements such as muon spin relaxation studies (μSR)[47] magnetometry at high magnetic fields,[49] and neutron scattering.[51] Subtle changes in magnetism with Mg doping have been suggested. The μSR studies on single crystals of nominal x = 0.05[47] revealed that Mg doping disrupts the formation of local singlets, as evidenced by the emergence of a third frequency shift branch attributable to the dopant effect. This third branch represents the case when the muon resides at a site in the superexchange path where a local singlet cannot form due to doping, leading to the conclusion that Mg-doping prevents the formation of some singlets both in and out of the Cu−B−O planes.

High-field magnetometry studies showed that impurities disrupt the formation of superstructures of bound triplet states, breaking them into smaller patches. This significant softening of the superstructures causes the smearing of the pseudo-1/n plateaus in the doped sample, with the expectation that these plateaus would be totally suppressed with increased doping. Further studies are desired to better understand the impurity-induced emergent states, to search for other possible novel phases at high fields, in particular on samples with higher Mg concentrations.

Neutron-scattering experiments have shown the appearance of new magnetic excitations into the singlet−triplet gap.[51] High resolution time-of-flight neutron scattering measurements on single crystals of $SrCu_{2-x}Mg_x(BO_3)_2$ with nominal x = 0.05 Mg have shown that doping of the magnetic Cu^{2+} site with nonmagnetic, isoelectronic Mg^{2+} introduces new magnetic excitations into the singlet energy gap, and gives a finite lifetime to all three single-triplet excitations, while also substantially broadening the two-triplet bound state. However, there are no studies on samples with Mg concentrations $x > 0.05$. Moreover, there are no studies on the local structure around the dopants using local-probe magnetic resonance techniques such as EPR or NMR.

As the ionic radii of Cu^{2+} and Mg^{2+} are almost identical (∼0.57 Å) for a square planar coordination,[53] the observed subtle and nonsystematic structural changes are not surprising. This renders also the determination of the true range of doping difficult. However, while Cu^{2+} can adopt both an octahedral and a square planar coordination, as in $SrCu_2(BO_3)_2$, Mg^{2+} chemically prefers an octahedral coordination. Therefore, achieving a substantial concentration of Mg incorporated into the $SrCu_2(BO_3)_2$ structure still remains a challenge. With the aim of pushing the doping level to higher values and addressing the robustness of the exact dimer phase, this paper reports a comprehensive study of Mg-doping of polycrystalline $SrCu_2(BO_3)_2$, targeting the 10 mol % nominal doping concentration or x = 0.10 in $SrCu_{2-x}Mg_x(BO_3)_2$. To achieve such high doping levels, a different source of magnesium was used, namely $Mg_2CO_3(OH)_2 \cdot 3.75\ H_2O$, which is expected to increase the reactivity and help with Mg-incorporation. A

https://doi.org/10.1021/acs.inorgchem.4c02398
Inorg. Chem. 2024, 63, 20335−20346

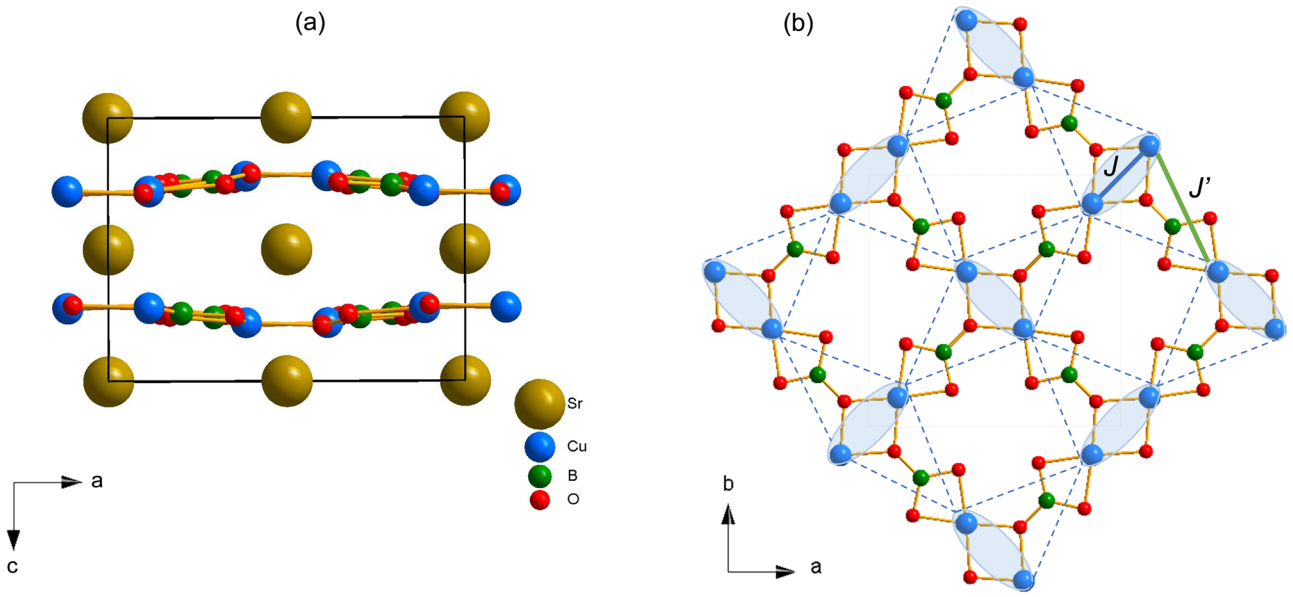


Figure 1. (a) The $SrCu_2(BO_3)_2$ structure viewed along the *b*-axis. The Cu−B−O layers can be seen separated by Sr^{2+} ions. (b) View perpendicular to the Cu−B−O layer which shows the orthogonal Cu^{2+} spins coupled across the dimer bonds with the *NN* coupling *J*, represented by the blue solid line, and across the next-neighbor bonds with the *NNN* coupling *J'*, represented by the green solid line.

successful substitution of Cu with Mg in the parent $SrCu_2(BO_3)_2$ structure is proven by powder XRD and energy-dispersive X-ray spectroscopy. It is then shown that Mg-doping leads to a softening of the magnetism in $SrCu_2(BO_3)_2$ as suggested by a systematic decrease in the spin gap, Δ, the Curie−Weiss temperature, θ, and the maximum of the magnetic susceptibility, T_{max}. The effects of Mg-doping on the Cu^{2+} dimers are further evaluated with EPR spectroscopy. These measurements show that the EPR spectra broaden with Mg-doping due to the increase in the concentration of intrinsic paramagnetic dimer-free Cu^{2+} sites that are coupled to the spin dimers. Finally, the weak anomaly at an onset critical field of $H'_{C0} \approx 9$ T, previously first observed by Shi et al.[48] for their $x = 0.05$ Mg-doped $SrCu_{2-x}Mg_x(BO_3)_2$, is here investigated using high-field magnetization measurements up to 35 T. We find that this anomaly is more pronounced for $x = 0.10$ and its intensity systematically increases with Mg concentration. This work thus constitutes a systematic study of the effect of magnetic dilution on the magnetic properties of $SrCu_2(BO_3)_2$ and opens alternative pathways toward higher substitutional doping of $SrCu_2(BO_3)_2$.

2. EXPERIMENTAL SECTION

2.1. Materials and Methods. Pristine and Mg-doped $SrCu_2(BO_3)_2$ polycrystalline samples $SrCu_{2-x}Mg_x(BO_3)_2$ with x being 0.03, 0.05, and 0.1, respectively, were synthesized by the traditional solid-state method and using boric acid as the boron source. The overall reactions are summarized in eqs 2 and 3:

$$SrCO_3 + 2CuO + 2H_3BO_3 \rightarrow SrCu_2(BO_3)_2 + CO_2 + 3H_2O \quad (2)$$

$$SrCO_3 + (2-x)CuO + 2H_3BO_3 + \left(x/2\right)Mg_2CO_3(OH)\cdot yH_2O \rightarrow SrCu_{2-x}Mg_x(BO_3)_2 + \left(x/2\right)CO_2 + \left[(x\cdot y)/2\right]H_2O \quad (3)$$

The starting materials were high-purity $SrCO_3$ (Alfa Aesar, 99.994%), CuO (Aldrich, 99.99%) and H_3BO_3 (Alfa Aesar, 99.9995%). The starting material used as Mg-source was $Mg_2CO_3(OH)_2 \cdot yH_2O$ ($y \approx 3$) (Alfa Aesar, 99.996%). The coefficient y in $Mg_2CO_3(OH)_2 \cdot yH_2O$ ($y \approx 3$) was determined to be 3.75 by thermal gravimetric analysis. This precursor was stored and weighed in a MBraun glovebox under an argon atmosphere of <0.1 ppm of O_2 and <0.1 ppm of H_2O.

The starting materials were weighed in stoichiometric ratios and hand-homogenized in an agate mortar for an hour. The homogenized gray powder was then pressed into pellets with an 8 or 10 mm diameter with a force of 5 tonnes. The pellets were fired for multiple cycles with several intermediate grindings, following the thermal profile: 780 °C for 24 h and 810 °C for 24 h in air plus multiple 3- or 6-day cycles at 900 °C in O_2 atmosphere, until no changes were noticed in the PXRD pattern. More details about this synthesis procedure can be found in reference.[54]

2.2. Characterization. *2.2.1. X-ray Powder Diffraction (PXRD).* The phase composition of the obtained samples was investigated by powder X-ray diffraction (PXRD) using a PANalytical X'Pert Pro powder diffractometer with Cu$K\alpha_1$ radiation in 2θ range 10−120° with a step size of 0.016° and a counting time of 300 s per step.

Synchrotron powder X-ray diffraction data were also collected at the Brockhouse high energy wiggler beamline at the Canadian Light Source (CLS) using an area detector of a 200 × 200 μm pixel size, and a $\lambda = 0.3502$ Å radiation with Ni as calibrant. The powders were packed into Kapton capillaries and measured in 2θ range 1−26°. The structural refinements were performed with the Rietveld method using the program GSAS-II.[55]

2.2.2. Scanning Electron Microscopy (SEM) and Energy-Dispersive X-ray Spectroscopy (EDS). For the microstructural investigations, Mg-doped $SrCu_2(BO_3)_2$ powders were embedded in an epoxy resin matrix polished and carbon coated using a sputter coater model Balzers SCD 050. The imaging and compositional analyses were performed using Thermo Fisher Quanta 650 ESEM equipped with an energy-dispersive X-ray spectrometer (Oxford Instruments, AZtec Live, Ultim Max SDD 65 mm^2) and a field-emission-gun scanning electron microscope (FE-SEM; JEOL JSM-7600) further equipped with an energy-dispersive X-ray spectrometer (EDS; INCA Oxford 350 EDS SDD), electron backscatter diffraction (EBSD) and a wavelength-dispersive X-ray spectrometer (WDXS; INCAWave 500). The accelerating voltage was 20 kV.

2.2.3. Magnetic Susceptibility. The magnetic susceptibility measurements were performed on an MPMS-XL-5 SQUID magnetometer from Quantum Design within the 1.9−300 K temperature range and an applied magnetic field of 1 kG. Powder samples were

https://doi.org/10.1021/acs.inorgchem.4c02398
Inorg. Chem. 2024, 63, 20335−20346

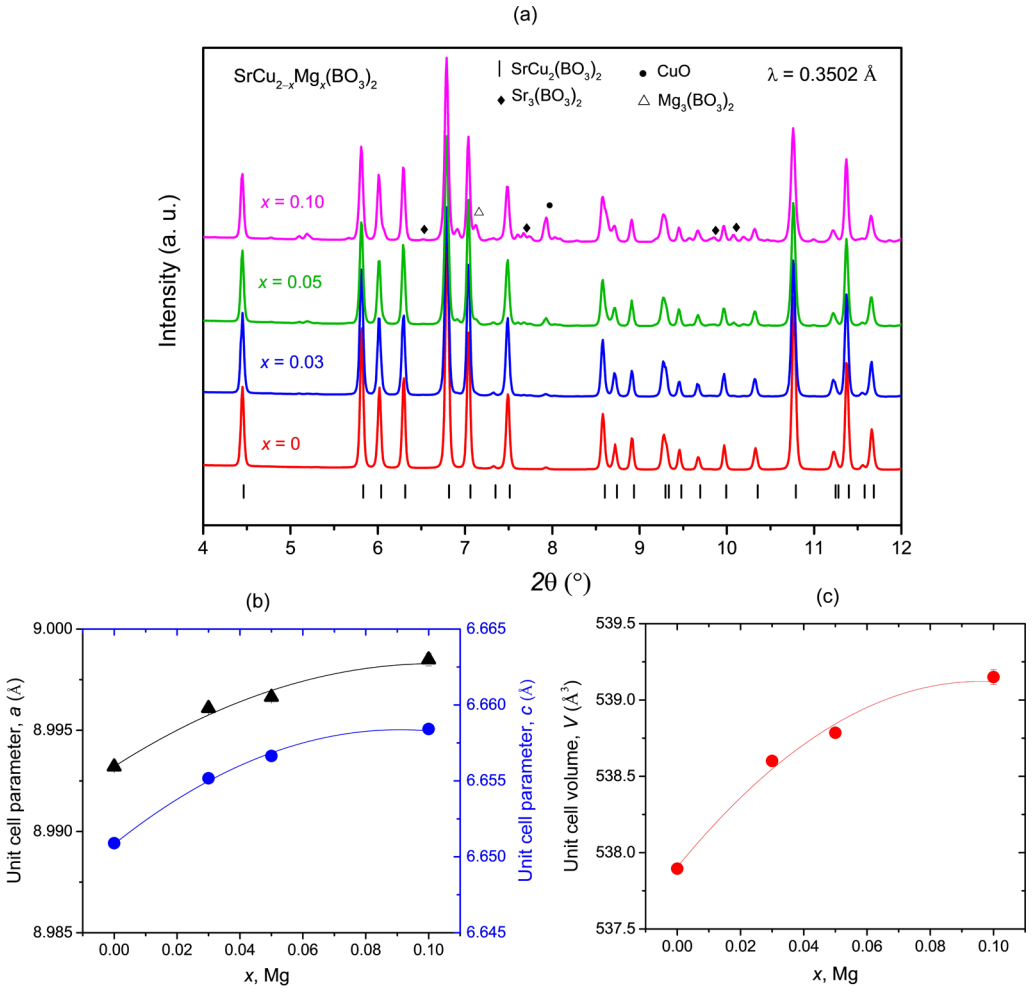


Figure 2. (a) A selected region of the room-temperature synchrotron PXRD patterns of $SrCu_{2-x}Mg_x(BO_3)_2$ with x = 0.03, 0.05 and 0.10, respectively. The formation of the dominant tetragonal $SrCu_2(BO_3)_2$ phase can be seen in all patterns. Some CuO impurity (marked with solid circles), Mg-based secondary phases (open triangles) and $Sr_3(BO_3)_2$ (solid diamonds) were also detected in the doped samples. A systematic increase in the unit cell parameters (b) and the unit cell volume (c) with Mg-doping is observed.

placed inside a plastic capsule, which was inserted into a standard straw sample-holder and closed with a plastic stopper at one end.

2.2.4. High-Field Magnetic Susceptibility. High-field magnetization measurements were performed at 0.4 K in pulsed magnetic fields up to 35 T at Institute for Materials Research, Tohoku University. About 50 mg of polycrystalline Mg-doped $SrCu_2(BO_3)_2$ was inserted into Kapton tubes, which were closed with stoppers from both sides. Measurements for each sample composition were performed multiple times. The reported results were binned in 0.5 T wide intervals and averaged between the data acquisition runs. The individual measurements are presented in the Supporting Information.

2.2.5. Electron Paramagnetic Resonance Spectroscopy (EPR). The continuous wave (CW) X-band electron paramagnetic resonance spectroscopy experiments were performed on a Bruker E500 spectrometer operating at 9.37 GHz, equipped with a Varian TEM104 dual cavity resonator, an Oxford Instruments ESR900 cryostat and an Oxford Instruments ITC503 temperature controller. Samples were measured at temperatures ranging from room temperature down to 4 K, typically applying 2 mW of microwave power and a 5 G modulation amplitude with the modulation frequency of 50 kHz. In a typical experiment, approximately 30 mg of powder sample, sealed in a standard 4 mm EPR quartz tubes under dynamic vacuum, were used for each measurement.

3. RESULTS AND DISCUSSION

3.1. Powder X-ray Diffraction (PXRD). At room temperature, $SrCu_2(BO_3)_2$ crystallizes in the $I\bar{4}2m$ space group—first reported in 1991 by Smith and Keszler,[56] where distorted planar CuO_4 units and rigid BO_3 triangular groups form two-dimensional puckered layers of $[Cu(BO_3)_2]^{2-}$ units at $z \approx 1/4$ stacked along the [001] direction. These layers are separated by nonmagnetic Sr^{2+} ions located at z = 0, 1/2 – Figure 1a. The distortion from planar CuO_4 rectangles is a consequence of sharing an O–O edge with a B atom while the other O–O edge is shared with a Cu atom. As a result of this distortion, the $[Cu(BO_3)_2]^{2-}$ layers are corrugated. The Cu–O distances measured along the c-axis are larger than 3.25 Å. All the in-plane Cu^{2+} sites (S = 1/2) are crystallographically equivalent and a two-dimensional network of copper dimers is formed with the neighboring pairs oriented orthogonal to each other – Figure 1b. The first nearest neighbor (*NN*) Cu^{2+} pairs are distanced by 2.903 Å while the next-nearest neighbor (*NNN*) distance is at 5.133 Å.

High-resolution X-ray powder diffractogram of the pristine $SrCu_2(BO_3)_2$ shows the presence of the main $SrCu_2(BO_3)_2$ phase, with traces of CuO – Figure 2a. We note that the minute presence of the persistent CuO impurity could not be avoided in powder samples, which is in agreement with

https://doi.org/10.1021/acs.inorgchem.4c02398
Inorg. Chem. 2024, 63, 20335–20346

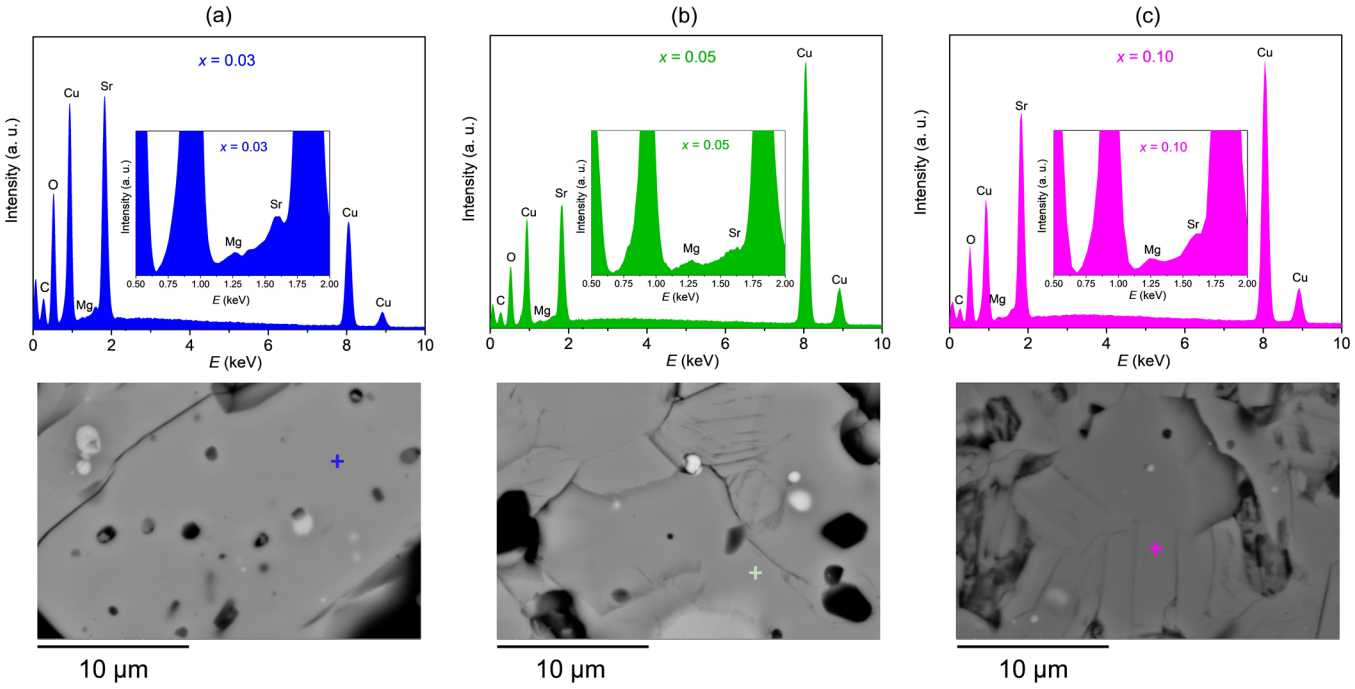


Figure 3. Representative EDS point analysis spectra collected on the matrix for $SrCu_{2-x}Mg_x(BO_3)_2$ with nominal $x = 0.03$ (a), $x = 0.05$ (**b**), and $x = 0.1$ (c). The corresponding SEM images can be seen below the EDS spectra. Colored squares mark the regions which EDS spectra were collected from.

previous reports.[50,56] The Rietveld refinement analysis of the powder diffraction data yields $a = 8.9932(1)$ Å and $c = 6.6509(1)$ Å. These parameters are in very good agreement with the values reported in the literature, e.g., $a = 8.998(1)$ Å and $c = 6.654(1)$ Å from reference[50] versus $a = 8.991(1)$ Å and $c = 6.660(3)$ Å in reference[56] or $a = 8.995(1)$ Å and $c = 6.649(1)$ Å reported in references.[49,52]

Upon Mg-doping, the same two phases are consistently observed: the majority of the $SrCu_2(BO_3)_2$ phase accompanied by the minor CuO impurity. However, the presence of CuO impurity grows with the nominal Mg concentration. Magnesium-based secondary phases are also present in the samples, as detected later with EDS analysis, with amounts increasing with the Mg concentration — Figure 2a.

The presence of these impurities underlines difficulties to incorporate Mg into the square planar coordination of Cu in the parent $SrCu_2(BO_3)_2$ structure and suggests that the actual Mg-doping values are lower than the nominal values. Nevertheless, the current synthesis approach leads to Mg incorporation judging from a monotonic shift of the diffraction peaks toward lower 2θ values and a systematic increase of the unit cell parameters and volume with the increasing Mg-doping concentration — Figure 2b,c. The Rietveld refinement profiles are available in the Supporting Information, Figure S1. The unit cell parameters and unit cell volumes for $SrCu_{2-x}Mg_x(BO_3)_2$ with different x as obtained from Rietveld refinement analysis are directly compared in the Supporting Information, Table S1. Up to nominal $x = 0.05$, both a and c lattice parameters show a steady increase with Mg concentration, but then tend to saturate toward nominal $x = 0.10$. Specifically, the refined room temperature unit cell parameters increase to $a = 8.9961(1)$ Å and $c = 6.6552(1)$ Å for nominal $x = 0.03$, to $a = 8.9966(2)$ Å and $c = 6.6566(2)$ Å for nominal $x = 0.05$ and up to $a = 8.9985(3)$ and $c = 6.6584(3)$ Å for nominal $x = 0.10$, respectively — Figure 2b. Comparing these unit cell parameters with the available literature data for nominal $x = 0.05$, showing $a = 8.994(1)$ Å, and $c = 6.648(1)$ Å ,[50] this study shows a slightly larger Mg-doping induced lattice expansion for this doping concentration. However, the difference is still within the 3% tolerance of the unit cell volume regularly reported for undoped $SrCu_2(BO_3)_2$.[49,52,56] Compared to the parent pristine sample, the largest unit cell volume expansion of 0.23% is for the nominal $x = 0.10$. This increase is small and reflects the similarity in the ionic radius of Cu^{2+} and Mg^{2+} ions as well as the limited amount of the incorporated Mg^{2+}. When comparing $x = 0.05$ and $x = 0.10$ samples, the relative change in both lattice parameters is extremely small and it amounts only about 0.002 Å. This suggests that the synthesis approach used in this study may have an upper limit for the effective Mg-doping into the $SrCu_2(BO_3)_2$ structure up to these values.

A closer look at the structural details further reveals a systematic decrease in the Cu−Cu distance between Cu^{2+} pairs from 2.9205(9) Å for pristine $SrCu_2(BO_3)_2$ ($x = 0$) to 2.9085(13) Å for $SrCu_{1.95}Mg_{0.05}(BO_3)_2$ ($x = 0.05$) and 2.9025(24) Å for $SrCu_{1.9}Mg_{0.1}(BO_3)_2$ ($x = 0.10$). A shorter Cu−Cu bond length (blue line labeled ***J*** in Figure 1b) should also reduce the Cu−O−Cu bond angle. The Cu−O−Cu bond angle indeed slightly decreases with Mg doping, from 98.9(1)° for the undoped sample ($x = 0$) to 98.5(2)° for $x = 0.05$, and 98.3(3)° for $x = 0.10$. As the Cu−O−Cu bond angle plays a substantial role in defining the effective superexchange interaction in strongly correlated transition metal oxides,[57] this decrease in the bond angle tuned by the chemical pressure in the Mg-doped samples may lead to a small decrease in the strength of the intradimer antiferromagnetic exchange J. Meanwhile, a systematic increase in the interdimer distance Cu−Cu between the orthogonal dimers (green line labeled J' in Figure 1b) from 5.1267(10) Å for $SrCu_2(BO_3)_2$ ($x = 0$) to 5.1326(13) Å for $SrCu_{1.95}Mg_{0.05}(BO_3)_2$ ($x = 0.05$) and

https://doi.org/10.1021/acs.inorgchem.4c02398
Inorg. Chem. 2024, 63, 20335−20346

Inorganic Chemistry pubs.acs.org/IC Article

Table 1. Average Semiquantitative Atomic % Values of O, Mg, Cu and Sr together with the Mg/Cu, Mg/Sr and Cu/Sr Ratios[a]

	Sample, $SrCu_{2-x}Mg_x(BO_3)_2$					
	x = 0.03		x = 0.05		x = 0.10	
Element	Actual	Nominal	Actual	Nominal	Actual	Nominal
			Concentration, at %			
O	63(2)	66.67	57(7)	66.67	57(7)	66.67
Mg	0.4(1)	0.33	0.6(1)	0.54	0.8(3)	1.11
Cu	24(2)	21.89	27(4)	21.67	28(4)	21.11
Sr	12.6(4)	11.11	15(3)	11.11	14(3)	11.11
Sum, %	100.0(2)	100.0	99.6(4)	100.0	99.8(3)	100.0
Mg/Cu	0.016	0.015	0.02	0.025	0.03	0.053
Mg/Sr	0.030	0.03	0.04	0.05	0.06	0.1
Cu/Sr	1.94	1.97	1.8	1.95	2.0	1.9
			Concentration, mol %			
Mg	3.4(8)	3.0	5(1)	5.0	7(2)	10.0

[a]These results were obtained from ∼35 different SEM-EDS point analyses on $SrCu_{2-x}Mg_x(BO_3)_2$ samples with x = 0.03, 0.05, and 0.10. The semiquantifications were performed excluding boron as it was not possible to detect such a light element.

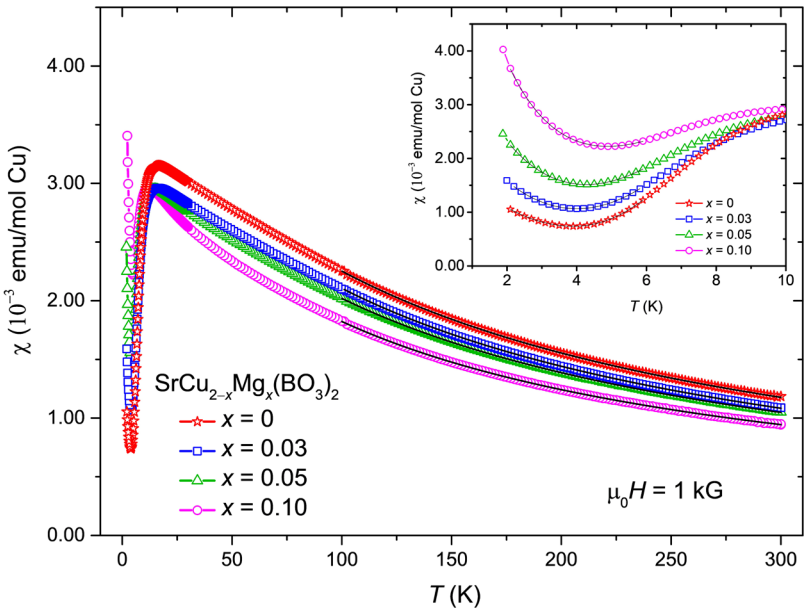


Figure 4. Magnetic susceptibility curves measured at μ_0H = 1 kG for $SrCu_{2-x}Mg_x(BO_3)_2$ powders with x = 0, 0.03, 0.05, and 0.10 nominal doping concentration. The inset shows the expanded low-temperature 1.9−10 K region where the upturn in the magnetic susceptibility can be clearly seen to increase with Mg concentration. Black lines represent the fitted data with eq 4 for the high-T regime, 100−300 K, and using eq 5 for the low-T region, 2−6 K − here θ' was fixed at −0.75 K.

5.1369(25) Å for $SrCu_{1.9}Mg_{0.1}(BO_3)_2$ (x = 0.10) is observed. This is consistent with the overall lattice expansion − Figure 2c.

3.2. Scanning Electron Microscopy (SEM) and Energy-Dispersive X-ray Spectroscopy (EDS). The PXRD data clearly shows that the substitution of Cu^{2+} with Mg^{2+} in $SrCu_2(BO_3)_2$ is possible, although not fully up to the nominal Mg concentrations. However, a detailed chemical analysis is mandatory to unambiguously confirm the incorporation of Mg and to obtain more quantitative information on the actual dopant concentration and distribution within the matrix as well as the morphology of the samples. For this reason, SEM and EDS analyses were carried out next. From the backscattered electron images, the lamellar $SrCu_2(BO_3)_2$ matrix can be observed along with the presence of darker and lighter zones, which suggest the presence of impurities containing lighter and heavier elements, respectively. The lighter zone corresponds to the CuO impurity thus corroborating the PXRD results in Figure 2. The darker zones are attributed to the Mg-rich regions in the sample−more details on this can be found in the Supporting Information, Figure S2.

Representative EDS point analysis spectra collected on ∼35 spots on $SrCu_{2-x}Mg_x(BO_3)_2$ samples with nominal x = 0.03, 0.05, and 0.10 and the corresponding SEM images are summarized in Figures 3a−c. The line at 1.25 eV in the EDS spectrum is the hallmark of the Mg emission and should thus be taken as a semiquantitative measure for the presence of Mg in the sample − Table 1. From the EDS point analysis, a clearly distinguished Mg emission peak is visible in all cases and thus unambiguously confirms the presence of Mg in the matrix for

https://doi.org/10.1021/acs.inorgchem.4c02398
Inorg. Chem. 2024, 63, 20335−20346

Table 2. Variation of Spin Gap, Δ, Extracted from Low-Temperature Susceptibility Fits in the Range 1.9−6 K, the T_{max}, Which Is the χ Maximum Temperature, the Curie Constant C' for the Low-Temperature Upturn in χ (for the Optimal Fit, a θ' = −0.5 K Was Used) and the Estimated Concentrations of Unpaired Cu^{2+} Moments, and the Curie−Weiss Temperature, θ, Extracted from Curie−Weiss Fits of the Susceptibility Data in the Temperature Interval 100−300 K, for Different Mg-Doping Concentrations

Sample/Nominal x	Δ [K]	T_{max} [K]	C' (low-T, 1.9−3.5 K) in emu K/mol Cu	Estimated fraction of impurities / free Cu spins in %	Estimated Mg, in mol % / actual x	High-T fit, θ [K]
$SrCu_2(BO_3)_2$ $x = 0$	26.1(2)	16.6(2)	$3.6(1) \cdot 10^{-3}$	0.95(1)		−135(1)
$SrCu_{1.97}Mg_{0.03}(BO_3)_2$ $x = 0.03$	22.0(2)	16.2(3)	$5.2(2) \cdot 10^{-3}$	1.37(4)	2.7(1)	−136(1)
$SrCu_{1.95}Mg_{0.05}(BO_3)_2$ $x = 0.05$	19.6(2)	14.8(2)	$7.2(2) \cdot 10^{-3}$	1.9(1)	3.9(1)	−129(1)
$SrCu_{1.9}Mg_{0.1}(BO_3)_2$ $x = 0.10$	15.9(4)	12.2(1)	$10.7(2) \cdot 10^{-3}$	2.85(5)	5.7(1)	−110(1)

all three doping concentrations. Although the average semiquantitative values yield an approximate $x = 0.07$ for the nominal $x = 0.10$ sample, a clear trend showing an increase in x with the nominal doping concentrations is observed—see Table 1. The EDS point analysis also reveals a saturation of the Mg concentration that is successfully incorporated into the parent $SrCu_2(BO_3)_2$ structure, which is in qualitative agreement with the conclusions drawn from PXRD in Figure 2b,c.

The presence of CuO and Mg-based secondary phase impurities observed in PXRD as well as in SEM stem from the partial incorporation of Mg into the parent $SrCu_2(BO_3)_2$ structure.

The actual relative percentages of these impurities were difficult to calculate since a structural information file for the $Mg_2(BO_3)_2$ phase is missing. However, we roughly estimated that the amount of impurities is below 1 wt % for $Sr_3(BO_3)_2$ and below 2 wt % for CuO. The difficulty in reaching higher Mg concentrations in the $SrCu_2(BO_3)_2$ lattice could be linked to the low mobility of the Mg^{2+} ions, which can be rationalized based on the fundamental diffusion mechanism and theory.[58] The atomic diffusivity depends on the composition, temperature and pressure. In our case, the low $SrCu_2(BO_3)_2$ decomposition temperature of ∼950 °C limits the maximum annealing temperatures to 900 °C. At this temperature, Mg^{2+} diffusion processes are slow, with diffusion constant values between 10^{-14}−10^{-11} m^2 s^{-1} which severely limits the possibility for successful Mg-doping.

3.3. Magnetic Susceptibility. Next, an investigation of the Mg-doping effects on the magnetic properties is presented. The magnetic susceptibilities, $\chi = M/H$, measured for undoped and Mg-doped $SrCu_2(BO_3)_2$ powders in the 1.9−300 K temperature range are compared in Figure 4. All samples generally show a qualitatively similar behavior: at high temperatures, χ follows the Curie−Weiss law, reaching a maximum at around ∼15 K, followed by a rapid suppression upon further cooling before it starts to increase again at the lowest temperatures. In order to quantitatively compare all samples, a fit of χ to a Curie−Weiss law in the high-temperature range of the data, between 100−300 K, is performed − eq 4:

$$\chi = \frac{C}{T - \theta} + \chi_0 \tag{4}$$

Here C denotes the Curie constant, θ is the Curie−Weiss temperature, while χ_0 represents a small temperature-independent diamagnetic contribution of the ion cores and/or the remnant signal of the sample holder. For the parent $SrCu_2(BO_3)_2$ sample, the fit to eq 4 yields a $\theta = -135(1)$ K, which is in excellent agreement with the literature data and can be described with the Shastry-Sutherland model given in eq 1. For Mg-doped samples, a systematic and quite pronounced reduction in θ is observed — Table 2: θ decreases to −129(1) K and then to −110(1) K for nominal $x = 0.05$ and 0.10, respectively. Although one has to take these values with a grain of salt, the systematic reduction in θ with Mg-content implies a softening of the antiferromagnetic exchange interactions driven by the small structural changes observed in PXRD in Figure 2.

It can be further noticed that the temperature at which $\chi(T)$ has a maximum, T_{max}, also decreases from 16.6(2) K for the undoped sample to 12.2(1) K for the nominal $x = 0.10$ sample. This parallels the reduction in θ discussed above and is also consistent with the softening of antiferromagnetic exchange interactions.

Similarly, the introduction of nonmagnetic Mg^{2+} ions into the lattice affects also the low-temperature magnetic susceptibility.

Magnetic susceptibility data, as shown in the inset of Figure 4, show a characteristic Curie upturn at low temperatures, which is a hallmark of unpaired Cu^{2+} ions. In an attempt to quantitatively analyze $\chi(T)$ at low temperatures, we assume that it has three contributions[49] − a dominant thermally activated contribution from the spin-dimer lattice characterized by the spin-gap Δ, a Curie−Weiss contribution from the unpaired Cu^{2+} moments in the lattice introduced by Mg-doping and quantified by their Curie constant C', and the same temperature-independent contribution χ_0 that was considered also in the high-temperature analysis:

$$\chi = \frac{C'}{T - \theta'} + ae^{-\Delta/T} + \chi_0 \tag{5}$$

In these fits, a very small Curie−Weiss temperature $\theta' = -0.5$ K was fixed for optimal fitting. This minute θ' probably accounts for weak residual interactions between orphan Cu^{2+} moments. Remarkably, just like θ and T_{max}, the effective spin gap also decreases with Mg-content from 26.1(2) K for $x = 0$ to just 15.9(4) K for the nominal $x = 0.10$ sample, respectively. It should be stressed that the extracted Δ for the undoped sample matches the value from the literature where the same modeling was applied.[49] Moreover, for nominal $x = 0.05$, a spin gap of 19.6(1) K is obtained which is in good agreement with the value reported in reference[47] for the same nominal doping concentration.

https://doi.org/10.1021/acs.inorgchem.4c02398
Inorg. Chem. 2024, 63, 20335−20346

Inorganic Chemistry pubs.acs.org/IC Article

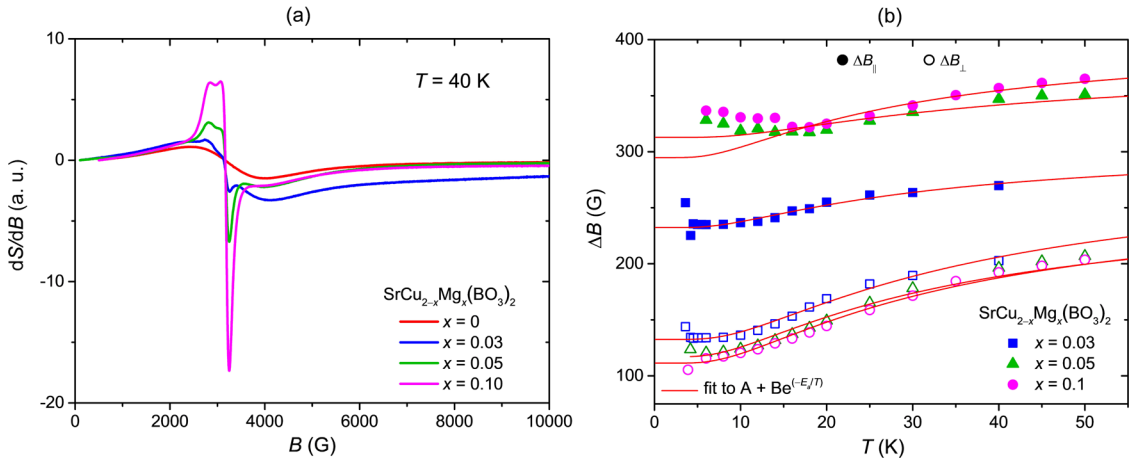


Figure 5. (a) The comparison of X-band EPR spectra of undoped $SrCu_2(BO_3)_2$ and Mg-doped $SrCu_2(BO_3)_2$ measured at 40 K. The EPR spectra of Mg-doped $SrCu_2(BO_3)_2$ powders clearly show the presence of intrinsic Cu moments from broken Cu^{2+} dimers, represented by the sharp component with an axial g-factor anisotropy. (b) The temperature behavior of X-band EPR line width data for low-temperature impurity peaks in the *ab*-plane, ($\Delta B_\perp$) and along the *c*-axis-plane ($\Delta B_\parallel$) for $SrCu_{2-x}Mg_x(BO_3)_2$ with nominal x = 0, 0.03, 0.05, and 0.10. Solid lines are fits to the empirical A + B exp($-E_a/T$) expression yielding a thermally activated energy $E_a \approx 30$ K for all sample compositions.

Although the presented analysis of χ for the spin-dimer phase may not yield exact values for the different magnetic parameters, the systematic decrease in θ, T_{max} as well as in Δ – Table 2 – clearly points to a detrimental effect that Mg-doping has on the quantum magnetism of $SrCu_2(BO_3)_2$. The minute structural changes of the Cu^{2+} dimer lattice in the Mg-doped samples – Figure 2 – are probably not sufficient to adequately change the J'/J ratio and trigger the transition to a plaquette-singlet, quantum spin liquid or Néel states as the spin gap remains open for all Mg concentrations. Yet, these structural changes are sufficient to fine-tune the intradimer and/or interdimer exchange interactions and thus to affect the extracted susceptibility parameters.

It is very intriguing that these changes occur concomitantly with the enhanced low-temperature Curie upturn in χ (for the full analysis see the Supporting Information, Tables S2 and S3). This upturn cannot be attributed to any of the CuO and Mg-based secondary impurity phases detected in PXRD, as none of them is expected to show a similar paramagnetic contribution. We therefore conclude that the low-temperature upturn in χ is in fact intrinsic to Mg-doped $SrCu_2(BO_3)_2$ and is associated with the intrinsic lattice defects emerging when the nonmagnetic substitutional Mg^{2+} ions break the Cu-spin dimers. This conclusion is further supported by low temperature X-band EPR data (*vide infra*).

In order to quantify the paramagnetic defects in the lattice introduced by Mg-doping, the low-temperature Curie constant C' is calculated from Curie–Weiss fits in the temperature interval 1.9 K – 3.5 K and listed in Table 2. The individual fits are presented in the Supporting Information, Figure S3. A systematic increase in the C' constant with Mg concentration is observed and thus the estimated fraction of impurities also increases with Mg concentration. Note that a similar Curie upturn is found already in the undoped powder sample for which the calculated Cu^{2+}-impurity concentration corresponds to ~0.95%. Such concentration is comparable to the literature data for powder samples.[36] Moreover, for the nominal x = 0.03, the low-temperature upturn in doped samples is comparable with the literature.[48] However, for the highest nominal x = 0.05 and 0.10, C' significantly exceeds literature values thus implying that our approach to Mg doping allows for higher Mg-concentrations in the $SrCu_2(BO_3)_2$ lattice.

3.4. X-Band Electron Paramagnetic Resonance Measurements (EPR). In the next step, a local probe technique, X-band EPR is employed to investigate the intrinsic Cu^{2+} defects that are created in the lattice upon Mg-doping. While EPR studies have been previously reported for undoped $SrCu_2(BO_3)_2$ in the form of single crystals or powders,[20−25] there are, however, no reports on EPR spectroscopy studies on doped $SrCu_2(BO_3)_2$ yet. For Mg-doped samples, high temperature EPR spectra are still dominated by the well-known signal of the dimer lattice – Supporting Information, Figure S4. This signal broadens upon cooling due to the development of spin correlations and its intensity approximately mimics the temperature dependence of χ. The main broad signal almost completely disappears below 10 K, i.e., when $T < \Delta$. At low temperatures, another signal with an axial *g*-factor anisotropy becomes visible – Supporting Information, Figure S4. While it is barely detectable for undoped $SrCu_2(BO_3)_2$, it becomes significantly more pronounced in Mg-doped samples. Its presence is especially evident in the nominal x = 0.10 sample, where it dominates the spectrum already at 40 K as shown in Figure 5a, and can still be traced up to room temperature – Supporting Information, Figure S4(d). The intensity of this EPR component increases with the decrease in temperature and with increasing Mg-doping concentration, as it is shown in Supporting Information, Figure S5(d). This parallels the low-temperature dependence of the magnetic susceptibility and it is thus concluded that both contributions have the same origin—the intrinsic Cu moments from broken Cu^{2+} dimers.

The EPR spectra are thus simulated to a sum of two components: a broad Lorentzian line with a large line width $\Delta B_{1/2}$ that considers the main signal of the dimer lattice and the low-temperature component with an axial *g*-factor anisotropy characterized by $g_\parallel$ and $g_\perp$ as the two *g*-factor eigen-values along the *c*-axis and in the *ab*-plane crystallographic directions. In the latter case, a similar uniaxial anisotropy in the line width with two values for the line width $\Delta B_\parallel$ and $\Delta B_\perp$, respectively, is also assumed. For the main component at g = 2.095, $\Delta B_{1/2} \approx 1400$ G at room

https://doi.org/10.1021/acs.inorgchem.4c02398
Inorg. Chem. 2024, 63, 20335−20346

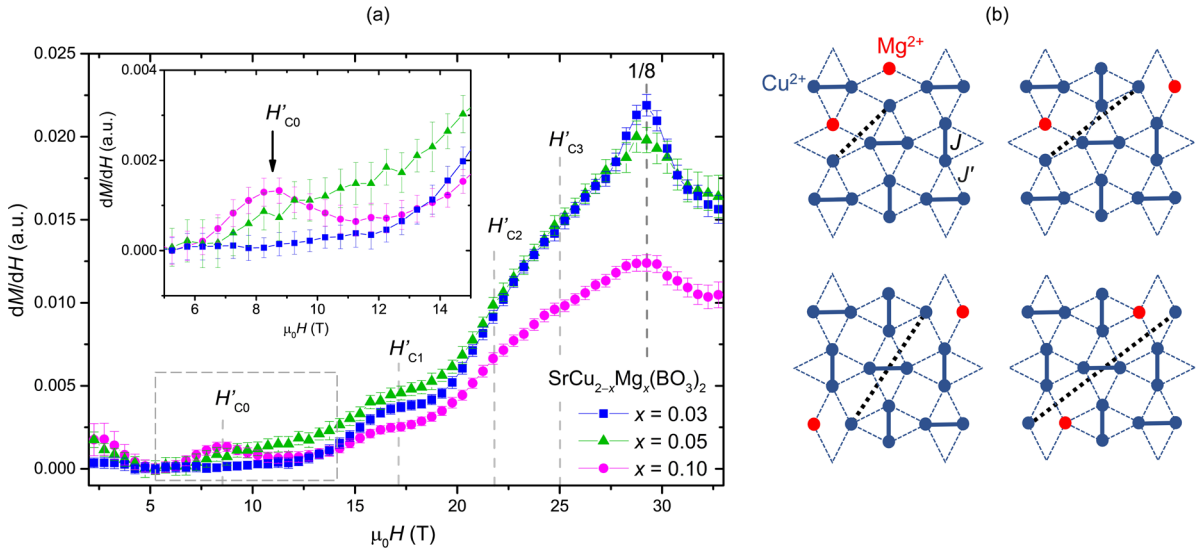


Figure 6. (a) High-field magnetic susceptibility measurements for $SrCu_{2-x}Mg_x(BO_3)_2$ with nominal x = 0.03, 0.05, and 0.10 powders in the region up to the pseudo-1/8 plateau. The critical field notations are termed after reference.[48] The presented measurements are a result of an average of multiple pulsed experiments. The data shown here is the binned average of the individual measurements with a bin interval of 0.5 T - see Supporting Information, Figure S7 for individual results. (b) Special 2-impurity configurations of dimer-free Cu^{2+} S = 1/2 spins remaining from Mg-magnetic dilution and coupled at distances beyond intradimer Cu^{2+} bonds. The anomaly at $\mu_0 H'_{C0} \approx 9$ T highlighted in the inset of (a) is due to such next-nearest Cu^{2+} impurity pairs.

temperature is nearly identical for undoped as well as Mg-doped samples − Supporting Information, Figure S5a, and is consistent with the values determined for undoped $SrCu_2(BO_3)_2$ powders from the literature.[20]

On cooling, $\Delta B_{1/2}$ initially monotonically increases in all samples, showing a similar temperature dependence that has also been previously reported for undoped $SrCu_2(BO_3)_2$. However, below 40 K, we find a more significant increase in $\Delta B_{1/2}$ for nominal x = 0.05 and 0.10 samples when compared to x = 0 or undoped $SrCu_2(BO_3)_2$ − Supporting Information, Figure S5a. This indicates the emergence of internal fields in doped samples that provide additional broadening mechanism associated with the presence of intrinsic impurities. The low-temperature "impurity" EPR component can be described in all samples with similar EPR parameters: $g_{\parallel}$= 2.38, $g_{\perp}$ = 2.008 − Supporting Information, Figure S5c, and a similarly pronounced line width anisotropy $\Delta B_{\parallel} \approx 320$ G and $\Delta B_{\perp} \approx 120$ G − Figure 5b.

Below 50 K, $\Delta B_{\parallel}$ and $\Delta B_{\perp}$ start to decrease with the decreasing temperature. This temperature dependence can be empirically described by a thermally activated mechanism, $\Delta B \propto \exp(-E_a/T)$ − Figure 5b, with the activation energy $E_a \approx 30$ K for all cases. The extracted value for E_a is very similar to the spin-gap values from spin susceptibility measurements, which suggests that these "impurity" spins are directly detecting the spin dynamics of the nearby unbroken Cu spin dimers.

The spins contributing to this low-temperature signal are thus indeed intrinsic Cu^{2+} defects from Mg-broken spin dimers sitting in the $[Cu(BO_3)]^-$ layers. Mg-doping is thus indeed successful and creates intrinsic Cu^{2+} defects that couple to the parent dimer lattice and effectively probe its spin dynamics.

3.5. High Magnetic Field Measurements. Variations in the parameters extracted from χ and X-band EPR with the increasing concentration of intrinsic defects may influence the magnetization plateaus and stabilize some novel states. Therefore, next, the magnetization curves, $M(H)$, to fields up to 35 T for $SrCu_{2-x}Mg_x(BO_3)_2$ with nominal x = 0.03, 0.05, and 0.10 samples at T = 0.4 K are reported. The onset of different phases that are stabilized as a function of magnetic field are best observed in dM/dH plots − Figure 6a. In dM/dH, a plateau and a step appear as a dip and a peak, respectively. The dip can be seen as a kink when there is another increasing dM/dH component. In Figure 6a, it can be seen that dM/dH displays a peak at $\mu_0 H_{C4}$ = 29 T that corresponds to the onset of pseudo-1/8 plateau, analogous to the 1/8 plateau found in undoped $SrCu_2(BO_3)_2$.[36] We also found a reduction of dM/dH related to the 1/8 plateau phase in higher field site. With increasing Mg-doping, the peak slightly shifts toward lower fields and, most importantly, it is severely suppressed. This is consistent with expectations presented in reference 48 that the pseudo-1/n plateaus would be suppressed with increasing doping. The anomalies in dM/dH at $\mu_0 H'_{C3} \approx 25.0$ T and $\mu_0 H'_{C2} \approx 21.7$ T are less prominent in the present measurements, presumably because of the powder nature of the studied samples. According to reference,[48] H'_{C2} corresponds to localized bound states of triplets, whereas H'_{C3} is the anomaly of the localized bound states with extra localized triplets in the vicinity. The bump in dM/dH at $\mu_0 H'_{C1} \approx 17.1$ T is observed for all the Mg-doping concentrations. Following iPEPS calculations from reference 48, this anomaly appears upon doping when two magnesium impurities break nearest-neighboring dimers. The two liberated Cu^{2+} S = 1/2 spins couple to a singlet that converts to a triplet at H'_{C1}. Strong coupling of these pairs of Cu^{2+} liberated spins renders them unobservable in X-band EPR spectra. Interestingly, for nominal x = 0.10, this anomaly appears the least pronounced. The most important result of these measurements is the observance of a clear maximum in dM/dH at $\mu_0 H \approx 9$ T. The scaling of the dM/dH maximum at H'_{C0} with the intrinsic defect concentration determined from magnetic susceptibility and "impurity-peak" X-band EPR intensity suggests that liberated Cu^{2+} moments must contribute to the stabilization of novel impurity-driven spin configurations. Previously, hints

https://doi.org/10.1021/acs.inorgchem.4c02398
Inorg. Chem. 2024, 63, 20335−20346

of an extra magnetic structure stabilized at this field were deduced from tunnel diode oscillator magnetic susceptibility measurements and were attributed to the stabilization of the coupled Cu^{2+} moments liberated by Mg-doping on the next-nearest (or even more distant) dimers.[48] Four examples of possible arrangements of pairs of liberated Cu^{2+} $S = 1/2$ spins are represented in Figure 6b. Due to the longer exchange pathways, the coupling of liberated Cu^{2+} spins is weaker for these configurations and thus the gap to the excited triplet state closes at lower fields than in case of nearest-neighboring liberated spins.

We thus next calculate the probability for the occurrence of next-nearest liberated Cu^{2+} moments. For this purpose, we make an approximation where we substitute the spin dimer lattice with a square lattice, where each lattice site represents the center of a nonmagnetic spin dimer − Supporting Information, Figure S6(a) and (b). When two Mg impurities locate on two next-nearest dimers, this translates to two Cu^{2+} moments on next-nearest sites of the square lattice − Supporting Information, Figure S6(c) and (d). Following reference 59, we calculate the probability doping dependence $P_c(x)$ for such configurations, shown in Supporting Information, Figure S6(e). These results show, that with increasing doping values, the probability for the next-nearest configuration of liberated Cu^{2+} moments initially increases and reaches a maximum at nominal $x \approx 0.07$. This analysis is thus in agreement with the observed increase of the dM/dH maximum at H'_{C0} and provides an additional support for the origin of H'_{C0}.

The X-band EPR data discussed above may provide an extra insight into such next-nearest neighboring configurations of coupled Cu^{2+} spins. At elevated temperatures, liberated Cu^{2+} spins relax mainly via nearby triplet excitations thermally activated across the spin gap $\Delta = 30$ K − as a result, ΔB follows the thermally activated temperature dependence as shown in Figure 5b. However, at temperatures well below Δ, this broadening mechanism becomes less efficient and thus spin correlations between Cu^{2+} moments on next-nearest broken dimers provide an additional broadening mechanism. This is especially pronounced in the samples with nominal $x = 0.05$ and 0.10, where $\Delta B_{\|}$ starts to increase again below ∼15 K, which roughly corresponds to a critical field H'_{C0}. A combined high-field magnetization study together with X-band EPR data therefore supports the picture of coupled Cu^{2+} moments on nearest and next-nearest broken dimers as derived from iPEPS computations in reference 48.

4. CONCLUSIONS

This work shows that it is possible to push the Mg-doping boundary to higher values and thus tackle the phase diagram of $SrCu_2(BO_3)_2$ over broader parameter space. It is demonstrated that by changing the source of Mg during the synthesis, the doping is pushed to an upper nominal limit of nominal $x = 0.10$ in $SrCu_{2-x}Mg_x(BO_3)_2$. This large concentration of Mg as dopant has not been reported before, as it is notoriously difficult to introduce Mg impurities into $SrCu_2(BO_3)_2$ due to low Mg^{2+} diffusion constants at applied reaction temperatures. At these higher Mg-doping levels more pronounced structural changes in Mg-doped samples are observed: the unit cell parameters and volume show a systematic increase with the increasing doping concentration. However, the incorporation of Mg in the $SrCu_2(BO_3)_2$ structure does not equal the nominal Mg concentration and even tends to saturate at lower values according to PXRD and SEM-EDS analyses. Nevertheless, the achieved Mg doping concentrations are already sufficient to affect the magnetic properties as expressed by a significant and systematic reduction of the spin gap, the Curie−Weiss temperature and the magnetic susceptibility maximum temperature with the increasing dopant concentration. These measurements are thus consistent with the breaking of Cu^{2+} dimers by magnetic dilution and are further corroborated by X-band EPR spectroscopy. Finally, reaching higher Mg^{2+} doping levels allows the detection of the $\mu_0 H'_{C0} \approx 9$ T anomaly more clearly. This anomaly is indicative of special configurations of dimer-free Cu^{2+} $S = 1/2$ spins remaining from magnetic dilution and coupled at distances beyond the intradimer Cu^{2+} bonds.[48] While the presented data on powder samples shows the potential of this synthesis approach, it also opens the next challenge of growing single crystals with incorporated nominal $x = 0.10$ or higher concentration of Mg to perform a more in-debt study of the 9 T anomaly.

■ ASSOCIATED CONTENT

Supporting Information

The Supporting Information is available free of charge at https://pubs.acs.org/doi/10.1021/acs.inorgchem.4c02398.

Rietveld refinement results, additional EDS data, low-temperature fits of the magnetic susceptibility, the EPR spectra of undoped and Mg-doped $SrCu_{2-x}Mg_x(BO_3)_2$ (with nominal $x = 0.03$, 0.05, and 0.10), schematics of a Cu^{2+} spin dimer lattice with two dimer-breaking impurity Mg^{2+} ions, and the calculated probability of doping dependence $P_c(x)$ for two Mg impurities located on two next-nearest dimers (PDF)

■ AUTHOR INFORMATION

Corresponding Author

Mirela Dragomir − *Jožef Stefan Institute, Ljubljana 1000, Slovenia; Jožef Stefan International Postgraduate School, Ljubljana 1000, Slovenia;* orcid.org/0000-0002-4910-253X; Email: mirela.dragomir@ijs.si

Authors

Lia Šibav − *Jožef Stefan Institute, Ljubljana 1000, Slovenia; Jožef Stefan International Postgraduate School, Ljubljana 1000, Slovenia*

Žiga Gosar − *Jožef Stefan Institute, Ljubljana 1000, Slovenia; Faculty of Mathematics and Physics, University of Ljubljana, Ljubljana 1000, Slovenia*

Tilen Knaflič − *Jožef Stefan Institute, Ljubljana 1000, Slovenia; Research Institute, Institute for the Protection of Cultural Heritage of Slovenia, Ljubljana 1000, Slovenia*

Zvonko Jagličić − *Physics and Mechanics, Institute of Mathematics, Ljubljana 1000, Slovenia; Faculty of Civil and Geodetic Engineering, University of Ljubljana, Ljubljana 1000, Slovenia*

Graham King − *Canadian Light Source, Saskatoon, SK S7N 2V3, Canada;* orcid.org/0000-0003-1886-7254

Hiroyuki Nojiri − *Institute for Materials Research, Tohoku University, Sendai 980-8577, Japan*

Denis Arčon − *Jožef Stefan Institute, Ljubljana 1000, Slovenia; Faculty of Mathematics and Physics, University of Ljubljana, Ljubljana 1000, Slovenia;* orcid.org/0000-0002-1207-8337

Complete contact information is available at:
https://pubs.acs.org/10.1021/acs.inorgchem.4c02398

Notes

The authors declare no competing financial interest.

■ ACKNOWLEDGMENTS

This project has received funding from the European Union's Horizon 2020 Research and Innovation Programme under the Marie Skłodowska-Curie grant agreement no. 101031415. Support from the Slovenian Research and Innovation Agency (J2-2496, P2-0105, P2-0348, P1-0125) and the Jožef Stefan Institute Director's Fund is gratefully acknowledged. Part of the research described in this paper was performed at the Canadian Light Source, a national research facility of the University of Saskatchewan, which is supported by the Canada Foundation for Innovation (CFI), the Natural Sciences and Engineering Research Council (NSERC), the National Research Council (NRC), the Canadian Institutes of Health Research (CIHR), the Government of Saskatchewan, and the University of Saskatchewan. A part of this work was supported by GIMRT program of the Institute for Materials Research, Tohoku University. Maja Koblar is acknowledged for help with sample preparation for the SEM-EDS analyses. Assoc. Prof. Andrej Zorko, Asst. Prof. Matej Pregelj, and Damjan Vengust are acknowledged for assistance with the setup for the EPR measurements.

■ REFERENCES

(1) Balents, L. Spin liquids in frustrated magnets. *Nature* **2010**, *464*, 199−208.
(2) Broholm, C.; Cava, R. J.; Kivelson, S. A.; Nocera, D. G.; Norman, M. R.; Senthil, T. Quantum spin liquids. *Science* **2020**, *367*, 263.
(3) Anderson, P. W. The resonating valence bond state in La_2CuO_4 and superconductivity. *Science* **1987**, *235*, 1196−1198.
(4) Vasiliev, A.; Volkova, O.; Zvereva, E.; Markina, M. Milestones of low-D quantum magnetism. *npj Quant. Mater.* **2018**, *3*, 18.
(5) Anderson, P. W. Resonating valence bonds: A new kind of insulator. *Mater. Res. Bull.* **1973**, *8*, 153−160.
(6) Mezzacapo, F. Ground-state phase diagram of the quantum $J_1 - J_2$ model on the square lattice. *Phys. Rev. B* **2012**, *86*, No. 045115.
(7) Basov, D.; Averitt, R.; Hsieh, D. Towards properties on demand in quantum materials. *Nat. Mater.* **2017**, *16*, 1077−1088.
(8) Anderson, P. W. Sources of Quantum Protection in high-T_C superconductivity. *Science* **2000**, *288*, 480−482.
(9) Taillefer, L. Superconductivity and quantum criticality. *Phys. Canada* **2011**, *67* (2), 109−112.
(10) Lee, P. A.; Nagaosa, N.; Wen, X.-G. Doping a Mott insulator: Physics of high-temperature superconductivity. *Rev. Mod. Phys.* **2006**, *78*, 17.
(11) Azuma, M.; Hiroi, Z.; Takano, M.; Ishida, K.; Kitaoka, Y. Observation of a Spin Gap in $SrCu_2O_3$ Comprising Spin-$^1/_2$; Quasi-1D Two-Leg Ladders. *Phys. Rev. Lett.* **1994**, *73*, No. 3463.
(12) Barnes, T.; Riera, J. Susceptibility and excitation spectrum of $(VO)_2P_2O_7$ in ladder and dimer-chain models. *Phys. Rev. B* **1994**, *50*, 6817−6822.
(13) Tsirlin, A. A.; Shpanchenko, R. V.; Antipov, E. V.; Bougerol, C.; Hadermann, J.; Van Tendeloo, G.; Schnelle, W.; Rosner, H. Spin ladder compound $Pb_{0.55}Cd_{0.45}V_2O_5$: Synthesis and investigation. *Phys. Rev. B* **2007**, *76*, No. 104429.
(14) Kodama, K.; Fukamachi, T.; Harashina, H.; Kanada, M.; Kobayashi, Y.; Kasai, M.; Sasaki, H.; Sato, M.; Kakurai, K. Spin-Gap Behavior of $CuNb_2O_6$. *J. Phys. Soc. Jpn.* **1998**, *67*, 57−60.
(15) Dagotto, E.; Rice, T. M. Surprises on the Way from One-to Two-Dimensional Quantum Magnets: The Ladder Materials. *Science* **1996**, *271*, 618−623.
(16) Taniguchi, S.; Nishikawa, T.; Yasui, Y.; Kobayashi, Y.; Sato, M.; Nishioka, T.; Kontani, M.; Sano, K. Spin gap behavior of $S = 1/2$ quasi-two-dimensional system CaV_4O_9. *J. Phys. Soc. Jpn.* **1995**, *64*, 2758−2761.
(17) Kodama, K.; Harashina, H.; Shamoto, S. I.; Taniguchi, S.; Sato, M.; Kakurai, K.; Nishi, M. Evolution of Spin Gap in the Excitation Spectra of Quasi-Two-Dimensional $S = 1/2$ System CaV_4O_9. *J. Phys. Soc. Jpn.* **1996**, *65*, 1941−1944.
(18) Kageyama, H. New Two-Dimensional Spin Gap Material $SrCu_2(BO_3)_2$. *J. Phys. Soc. Jpn.* **2000**, *69*, 65−71.
(19) Shastry, B. S.; Sutherland, B. Exact ground state of a quantum mechanical antiferromagnet. *Physica B+C* **1981**, *108*, 1069−1070.
(20) Zorko, A.; Arčon, D.; Lappas, A.; Giapintzakis, J. Near critical behavior in the two-dimensional spin-gap system $SrCu_2(BO_3)_2$. *Phys. Rev. B* **2001**, *65*, 024417−024422.
(21) Nojiri, H.; Kageyama, H.; Ueda, Y.; Motokawa, M. ESR Study on the Excited State Energy Spectrum of $SrCu_2(BO_3)_2$—A Central Role of Multiple-Triplet Bound States. *J. Phys. Soc. Jpn.* **2003**, *72*, 3243−3253.
(22) Zorko, A. Study of one- and two-dimensional magnetic systems with spin-singlet ground state. Ph.D. dissertation; University of Ljubljana: Slovenia, 2004. Accessed on 18th September 2023.
(23) Zorko, A.; Arčon, D.; Nuttall, C. J.; Lappas, A. X-band ESR study of the 2D spin-gap system $SrCu_2(BO_3)_2$. *J. Magn. Magn. Mater.* **2004**, *272*, E699−E701.
(24) Cépas, O.; Kakurai, K.; Regnault, L. P.; Ziman, T.; Boucher, J. P.; Aso, N.; Nishi, M.; Kageyama, H.; Ueda, Y. Dzyaloshinski-Moriya Interaction in the 2D Spin Gap System $SrCu_2(BO_3)_2$. *Phys. Rev. Lett.* **2001**, *87*, No. 167205.
(25) Zorko, A.; Arčon, D.; Kageyama, H.; Lappas, A. Magnetic anisotropy of the $SrCu_2(BO_3)_2$ system as revealed by X-band ESR. *Appl. Magn. Reson.* **2004**, *27*, 267−278.
(26) Takigawa, M.; Matsubara, S.; Horvatić, M.; Berthier, C.; Kageyama, H.; Ueda, Y. NMR Evidence for the Persistence of a Spin Superlattice Beyond the 1/8 Magnetization Plateau in $SrCu_2(BO_3)_2$. *Phys. Rev. Lett.* **2008**, *101*, No. 037202.
(27) Waki, T.; Arai, K.; Takigawa, M.; Saiga, Y.; Uwatoko, Y.; Kageyama, H.; Ueda, Y. A Novel Ordered Phase in $SrCu_2(BO_3)_2$ under High Pressure. *J. Phys. Soc. Jpn.* **2007**, *76*, 073710−073714.
(28) Cui, Y.; Liu, L.; Lin, H.; Wu, K.-H.; Hong, W.; Liu, X.; Li, C.; Hu, Z.; Xi, N.; Li, S.; Yu, R.; Sandvik, A. W.; Yu, W. Proximate deconfined quantum, critical point in $SrCu_2(BO_3)_2$. *Science* **2023**, *380*, 1179−1184.
(29) Kohlrautz, J.; Haase, J.; Green, E. L.; Zhang, Z. T.; Wosnitza, J.; Herrmannsdörfer, T.; Dabkowska, H. A.; Gaulin, B. D.; Stern, R.; Kühne, H. Field-stepped broadband NMR in pulsed magnets and application to $SrCu_2(BO_3)_2$ at 54 T. *J. Magn. Reson.* **2016**, *271*, 52−59.
(30) Koga, A.; Kawakami, N. Quantum Phase Transitions in the Shastry-Sutherland Model for $SrCu_2(BO_3)_2$. *Phys. Rev. Lett.* **2000**, *84*, 4461−4461.
(31) Kodama, K.; Yamazaki, J.; Takigawa, M.; Kageyama, H.; Onizuka, K.; Ueda, Y. Cu nuclear spin-spin coupling in the dimer singler state in $SrCu_2(BO_3)_2$. *J. Phys.: Condens. Matter* **2002**, *14*, L319.
(32) Yang, J.; Sandvik, A. W.; Wang, L. Quantum criticality and spin liquid phase in the Shastry Sutherland model. *Phys. Rev. B* **2022**, *105*, L060409.
(33) Miyahara, S.; Ueda, K. Exact Dimer Ground State of the Two Dimensional Heisenberg Spin System $SrCu_2(BO_3)_2$. *Phys. Rev. Lett.* **1999**, *82*, 3701−3704.
(34) Jaime, M.; Daou, R.; Crooker, S. A.; Weickert, F.; Uchida, A.; Feiguin, A. E.; Batista, C. D.; Dabkowska, H. A.; Gaulin, B. D. Magnetostriction and magnetic texture to 100.75 T in frustrated $SrCu_2(BO_3)_2$. *Proc. Natl. Acad. Sci. U. S. A.* **2012**, *109*, 12404−12407.
(35) Matsuda, Y. H.; Abe, N.; Takeyama, S.; Kageyama, H.; Corboz, P.; Honecker, A.; Manmana, S. R.; Foltin, G. R.; Schmidt, K. P.; Mila,

F. Magnetization of $SrCu_2(BO_3)_2$ in ultrahigh magnetic fields up to 118 T. *Phys. Rev. Lett.* **2013**, *111*, No. 137204.
(36) Kageyama, H.; Yoshimura, K.; Stern, R.; Mushnikov, N. V.; Onizuka, K.; Kato, M.; Kosuge, K.; Slichter, C. P.; Goto, T.; Ueda, Y. Exact Dimer Ground State and Quantized Magnetization Plateaus in the Two-Dimensional Spin System $SrCu_2(BO_3)_2$. *Phys. Rev. Lett.* **1999**, *82*, 3168−3171.
(37) Nojiri, H.; Kageyama, H.; Onizuka, K.; Ueda, Y.; Motokawa, M. Direct Observation of the Multiple Spin Gap Excitations in Two-Dimensional Dimer System $SrCu_2(BO_3)_2$. *J. Phys. Soc. Jpn.* **1999**, *68*, 2906−2909.
(38) Kodama, K.; Takigawa, M.; Horvatic, M.; Berthier, C.; Kageyama, H.; Ueda, Y.; Miyahara, S.; Becca, F.; Mila, F. Magnetic Superstructure in the Two-dimensional Quantum Antiferromagnet $SrCu_2(BO_3)_2$. *Science* **2002**, *298*, 395−398.
(39) Onizuka, K.; Kageyama, H.; Narumi, Y.; Kindo, K.; Ueda, Y.; Goto, T. 1/3 Magnetization Plateau in $SrCu_2(BO_3)_2$ - Stripe Order of Excited Triplets -. *J. Phys. Soc. Jpn.* **2000**, *69*, 1016.
(40) Sebastian, S.; Harrison, N.; Sengupta, P.; Batista, C. D.; Francoual, S.; Palm, E.; Murphy, T.; Marcano, N.; Dabkowska, H. A.; Gaulin, B. D. Fractalization drives crystalline states in a frustrated spin system. *Proc. Natl. Acad. Sci. U. S. A.* **2008**, *105*, 20157−20160.
(41) Fogh, E.; Nayak, M.; Prokhnenko, O.; Bartkowiak, M.; Munakata, K.; Soh, J.-R.; Turrini, A. A.; Zayed, M. E.; Pomjakushina, E.; Kageyama, H.; Nojiri, H.; Kakurai, K.; Normand, B.; Mila, F.; Rønnow, H. M. Field-induced bound-state condensation and spin-nematic phase in $SrCu_2(BO_3)_2$ revealed by neutron scattering up to 25.9 T. *Nat. Commun.* **2024**, *15*, 442.
(42) Haravifard, S.; Graf, D.; Feiguin, A. E.; Batista, C. D.; Lang, J. C.; Silevitch, D. M.; Srajer, G.; Gaulin, B. D.; Dabkowska, H. A.; Rosenbaum, T. F. Crystallization of spin superlattices with pressure and field in the layered magnet $SrCu_2(BO_3)_2$. *Nat. Commun.* **2016**, *7*, 11956−11961.
(43) Sakurai, T.; Hirao, Y.; Hijii, K.; Okubo, S.; Ohta, H.; Uwatoko, Y.; Kudo, K.; Koike, Y. Direct Observation of the Quantum Phase Transition of $SrCu_2(BO_3)_2$ by High-Pressure and Terahertz Electron Spin Resonance. *J. Phys. Soc. Jpn.* **2008**, *87*, 033701−033705.
(44) Guo, J.; Sun, G.; Zhao, B.; Wang, L.; Hong, W.; Sidorov, V. A.; Ma, N.; Wu, Q.; Li, S.; Meng, Z. Y.; Sandvik, A. W.; Sun, L. Quantum phases of $SrCu_2(BO_3)_2$ from high-pressure thermodynamics. *Phys. Rev. Lett.* **2020**, *124*, 206602−206608.
(45) Shastry, B. S.; Kumar, B. $SrCu_2(BO_3)_2$: A unique Mott Hubbard insulator. *Prog. Theor. Phys. Suppl.* **2002**, *145*, 1−16.
(46) Yang, B.-J.; Kim, Y. B.; Yu, J.; Park, K. Doped valence-bond solid and superconductivity on the Shastry-Sutherland lattice. *Phys. Rev. B* **2008**, *77*, No. 104507.
(47) Aczel, A. A.; MacDougall, G. J.; Rodriguez, J. A.; Luke, G. M.; Russo, P. L.; Savici, A. T.; Uemura, Y. J.; Dabkowska, H. A.; Wiebe, C. R.; Janik, J. A.; Kageyama, H. Impurity-induced singlet breaking in $SrCu_2(BO_3)_2$. *Phys. Rev. B* **2007**, *76*, 214427−214433.
(48) Shi, Z.; Steinhardt, W.; Graf, D.; Corboz, P.; Weickert, F.; Harrison, N.; Jaime, M.; Marjerrison, C.; Dabkowska, H. A.; Mila, F.; Haravifard, S. Emergent bound states and impurity pairs in chemically doped Shastry-Sutherland system. *Nat. Commun.* **2019**, *10*, 1−9.
(49) Liu, G. T.; Luo, J. L.; Wang, N. L.; Jing, X. N.; Jin, D.; Xiang, T.; Wu, Z. H. Doping effects on the two-dimensional spin dimer compound $SrCu_2(BO_3)_2$. *Phys. Rev. B* **2005**, *71*, No. 014441.
(50) Dabkowska, H. A.; Dabkowski, A. B.; Luke, G. M.; Dunsiger, S. R.; Haravifard, S.; Cecchinel, M.; Gaulin, B. D. Crystal growth and magnetic behaviour of pure and doped $SrCu_2(^{11}BO_3)_2$. *J. Cryst. Growth* **2007**, *306*, 123−128.
(51) Haravifard, S.; Dunsinger, S. R.; El Shawish, S.; Gaulin, B. D.; Dabkowska, H. A.; Telling, M. T. F.; Perring, T. G.; Bonča, J. In-gap Spin Excitations and Finite Triplet Lifetimes in the Dilute Singlet Ground State System $SrCu_{2-x}Mg_x(BO_3)_2$. *Phys. Rev. Lett.* **2006**, *97*, No. 247206.
(52) Liu, G. T.; Luo, J. L.; Guo, Y. Q.; Su, S. K.; Zheng, P.; Wang, N. L.; Jin, D.; Xiang, T. In-plane substitution effect on the magnetic properties of the two-dimensional spin-gap system $SrCu_2(BO_3)_2$. *Phys. Rev. B* **2006**, *73*, No. 014414.
(53) Shannon, R. D. Revised Effective Ionic Radii and Systematic Studies of Interatomic Distances in Halides and Chalcogenides. *Acta Crystallogr.* **1976**, *A32*, 751−767.
(54) Dragomir, M.; Šibav, L. Synthesis peculiarities of $SrCu_2(BO_3)_2$. Manuscript in preparation **2024**.
(55) Toby, B. H.; Von Dreele, R. B. GSAS-II: the genesis of a modern open-source all purpose crystallography software package. *J. Appl. Crystallogr.* **2013**, *46*, 544−549.
(56) Smith, R. W.; Keszler, D. A. Synthesis, structure, and properties of the orthoborate $SrCu_2(BO_3)_2$. *J. Solid State Chem.* **1991**, *93*, 430−435.
(57) Goodenough, J. B. *Magnetism and the Chemical Bond*; Interscience Publisher: New York, 1963.
(58) Van Orman, J. A.; Crispin, K. L. Diffusion in Oxides. *Rev. Mineral. Geochem.* **2010**, *72*, 757−825.
(59) Pohl, U. W.; Busse, W. Probability tables for small clusters of impurity atoms in sc, bcc, and fcc lattices assuming long-range interaction. *J. Chem. Phys.* **1989**, *90*, 6877−6880.

https://doi.org/10.1021/acs.inorgchem.4c02398
Inorg. Chem. 2024, 63, 20335−20346

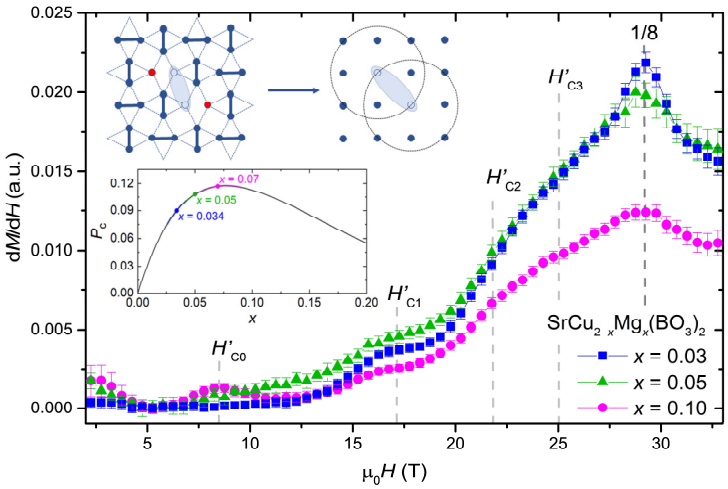
Supplementary Information File

Higher-Magnesium-Doping Effects on the Singlet Ground State of the Shastry-Sutherland $SrCu_2(BO_3)_2$

Lia Šibav[1,2], Žiga Gosar[1,3], Tilen Knaflič[1,4], Zvonko Jagličić[5,6], Graham King[7], Hiroyuki Nojiri[8], Denis Arčon[1,3], and Mirela Dragomir[1,2*]

[1]Jožef Stefan Institute, Jamova cesta 39, 1000 Ljubljana, Slovenia
[2]Jožef Stefan International Postgraduate School, Jamova cesta 39, 1000 Ljubljana, Slovenia
[3]Faculty of Mathematics and Physics, University of Ljubljana, Jadranska ulica 19, 1000 Ljubljana, Slovenia
[4]Institute for the Protection of Cultural Heritage of Slovenia, Research Institute, Poljanska cesta 40, 1000 Ljubljana, Slovenia
[5]Institute of Mathematics, Physics and Mechanics, Jadranska ulica 19, 1000 Ljubljana, Slovenia
[6]Faculty of Civil and Geodetic Engineering, University of Ljubljana, Jamova cesta 2, 1000 Ljubljana, Slovenia
[7]Canadian Light Source, 44 Innovation Blvd, Saskatoon, SK S7N 2V3, Canada
[8] Institute for Materials Research, Tohoku University, Katahira 2-1-1, Sendai, 980-8577 Japan

*Corresponding author: mirela.dragomir@ijs.si



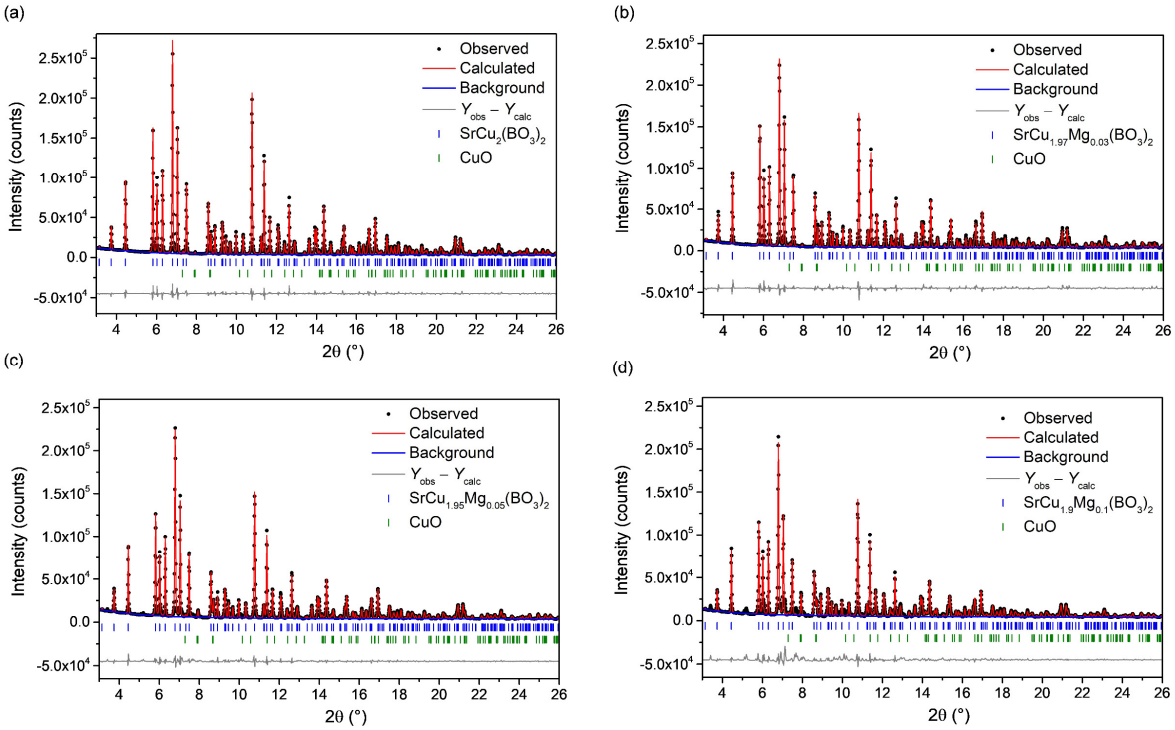


Figure S1. Profile fits of $SrCu_{2-x}Mg_x(BO_3)_2$ with $x = 0$ **(a)**, 0.03 **(b)**, 0.05 **(c)**, and 0.10 **(d)** using the $I\bar{4}2m$ space group. The synchrotron PXRD data (λ = 0.3502 Å) was collected at room-temperature.

Table S1. Structural parameters derived from the Rietveld refinements of $SrCu_{2-x}Mg_x(BO_3)_2$ with x = 0, 0.03, 0.05, and 0.10, at room temperature with $I\bar{4}2m$ space group. A systematic increase in the unit cell parameters a, b and c and the unit cell volume is observed with increasing Mg-doping concentration.

	$SrCu_2(BO_3)_2$ (x = 0)	$SrCu_{1.97}Mg_{0.03}(BO_3)_2$ (x = 0.03)	$SrCu_{1.95}Mg_{0.05}(BO_3)_2$ (x = 0.05)	$SrCu_{1.9}Mg_{0.1}(BO_3)_2$ (x = 0.1)
a, b (Å)	8.9932(1)	8.9961(1)	8.9966(2)	8.9985(3)
c (Å)	6.6509(1)	6.6552(1)	6.6566(2)	6.6584(3)
V (Å^3)	537.91(2)	538.60(2)	538.79(3)	539.15(5)
R_{wp} (%) R_{exp} (%)	5.29 2.26	6.02 2.39	5.45 2.27	10.49 3.16
$S = R_{wp}/R_{exp}$	2.34	2.52	2.94	3.32
Atom	x/y/z Occ. $U_{11}/U_{22}/U_{33}$ $U_{12}/U_{13}/U_{23}$	x/y/z Occ. $U_{11}/U_{22}/U_{33}$ $U_{12}/U_{13}/U_{23}$	x/y/z Occ. $U_{11}/U_{22}/U_{33}$ $U_{12}/U_{13}/U_{23}$	x/y/z Occ. $U_{11}/U_{22}/U_{33}$ $U_{12}/U_{13}/U_{23}$
Sr	0/0.5/0 0.996(3) 0.0085(1)/0.0051(1)/0.0099(8) 0/0/0	0/0.5/0 1.015(3) 0.0120/0.0050/0.0105 0/0/0	0/0.5/0 1.017(5) 0.0086(14)/0.0099(15)/0.0115(10) 0/0/0	0/0.5/0 0.985(9) 0.0073(27)/0.0082(29)/0.0131(21) 0/0/0
Cu	0.1148(7)/0.1148(7)/0.2776(3) 1.00* 0.0043/0.0043/0.0278 0.0003/0.0027/0.0027	0.1149(9)/0.1149(9)/0.2799(2) 0.985* 0.0055/0.0055/0.0201 0.0050/0.0076/0.0076	0.1143(1)/0.1143(1)/0.2788(3) 0.975* 0.0023(6)/0.0023(6)/0.0315(16) 0.0006(12)/0.0014(16)/0.0014(16)	0.1140(2)/0.1140(2)/0.2798(6) 0.950* 0.0024/0.0024/0.0344 0.0008/0.0012/0.0012
Mg	- - - -	0.1149(9)/0.1149(9)/0.2799(2) 0.015* 0.0055/0.0055/0.0201 0.0050/0.0076/0.0076	0.1143(1)/0.1143(1)/0.2788(3) 0.025* 0.0294/0.0294/0.0281 0.0050/0.0050/0.0050	0.1140(2)/0.1140(2)/0.2798(6) 0.050* 0.0050/0.0050/0.0072 0.0050/0.0050/0.0050*
B	0.2963(7)/0.2963(7)/0.2507(28) 1.012(15) 0.0080/0.0080/0.0120 0.0050/0.0050/0.0050	0.2944(8)/0.2944(8)/0.2329(27) 1.058(19) 0.0080/0.0080/0.0120 0.0050/0.0050/0.0050	0.2950(9)/0.2950(9)/0.254(4) 1.006(20) 0.0080/0.0080/0.0120 0.0050/0.0050/0.0050	0.2923(19)/0.2923(19)/0.257(7) 1.010(4) 0.0122/0.0122/0.0080 0.0106/0.0050/0.0050
O1	0.4019(4)/0.4019(4)/0.2126(11) 1.00* 0.0095/0.0095/0.0304 0.050/0.0050/0.0050	0.4010(5)/0.4010(5)/0.2079(13) 0.967(11) 0.0090/0.0090/0.0399 0.0021/0.0050/0.0050	0.4016(5)/0.4016(5)/0.2096(15) 1.015(14) 0.0136/0.0136/0.0192 0.0050/0.0039/0.0039	0.4015(11)/0.4015(11)/0.2086(26) 0.992(27) 0.0142/0.0142/0.0146 0.0120/0.0050/0.0050
O2	0.3274(3)/0.1440(3)/0.2523(13) 1.00* 0.0090/0.0080/0.0180 0.0010/0.0010/0.0020	0.3261(4)/0.1446(4)/0.2594(13) 1.072(7) 0.0121/0.0197/0.0097 0.0033/0.0050/0.0050	0.3263(4)/0.1446(4)/0.2515(18) 1.048(8) 0.0140/0.0143/0.0146 0.0032/0.0021/0.0050	0.3270(8)/0.1435(8)/0.256(3) 1.001(16) 0.0086/0.0050/0.0050 0.0010/0.0050/0.0017

* These parameters were fixed to the nominal values during the refinement.

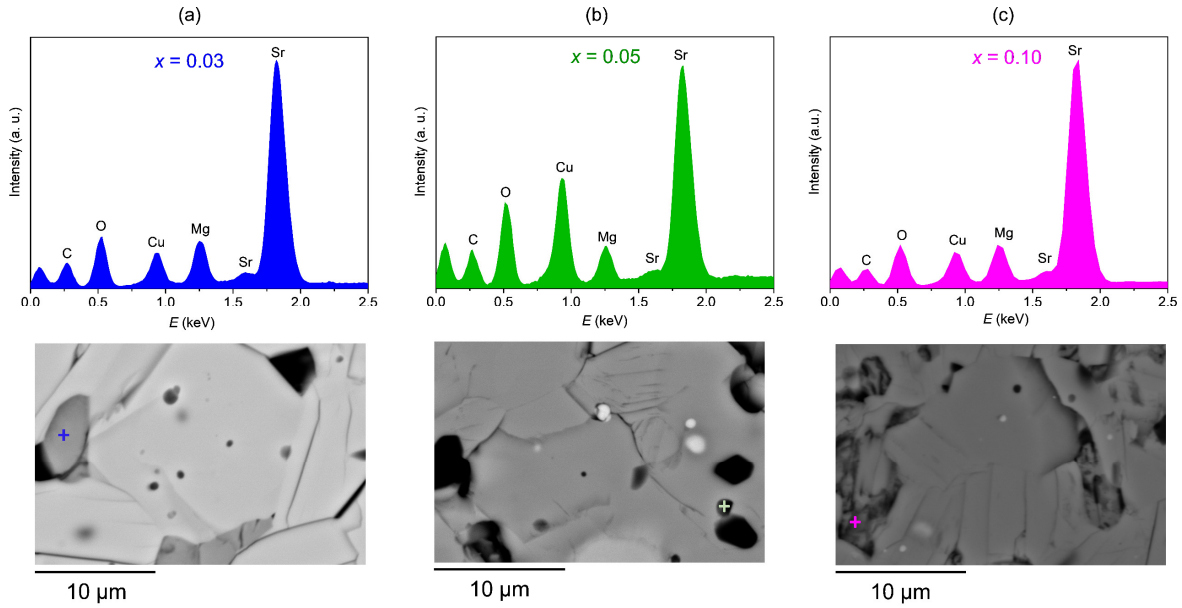


Figure S2. Normalised EDS point analysis spectra collected on the impurity sites for $SrCu_{2-x}Mg_x(BO_3)_2$, with $x = 0.03$, **(a)**, $x = 0.05$ **(b)** and $x = 0.10$ **(c)**. A higher concentration of Mg is suggested from the impurity sites compared to the doped $SrCu_2(BO_3)_2$ matrix. The corresponding SEM images can be seen below the EDS spectra.

Table S2. The complete results of magnetic susceptibility data fits in the temperature interval 2–6 K for different doping concentrations using the equation for total susceptibility at low temperatures (**Equation 5** in the main text). Due to a high correlation between the fitted parameters C' and θ', the fitting was performed using multiple fixed θ' values between 0 to −1, assuming antiferromagnetic interactions between the intrinsic impurities – dimer-free Cu^{2+} ions.

	C' (emu K/mol Cu)	χ_0 (emu/mol Cu)	θ'	Δ (K)	α (emu/mol Cu)
$SrCu_2(BO_3)_2$ $x = 0$	$1.72(2) \cdot 10^{-3}$	$2.37(6) \cdot 10^{-4}$	0	27.9(3)	$7.9(4) \cdot 10^{-2}$
	$2.07(1) \cdot 10^{-3}$	$1.72(5) \cdot 10^{-4}$	−0.25	27.2(2)	$7.2(2) \cdot 10^{-2}$
	$2.46(1) \cdot 10^{-3}$	$1.06(5) \cdot 10^{-4}$	−0.5	26.6(2)	$6.7(2) \cdot 10^{-2}$
	$2.88(2) \cdot 10^{-3}$	$4.0(5) \cdot 10^{-5}$	−0.75	26.1(1)	$6.3(1) \cdot 10^{-2}$
	$3.34(2) \cdot 10^{-3}$	$-2.7(5) \cdot 10^{-5}$	−1	25.6(2)	$5.9(1) \cdot 10^{-2}$
$SrCu_{1.97}Mg_{0.03}(BO_3)_2$ $x = 0.03$	$2.51(2) \cdot 10^{-3}$	$3.37(6) \cdot 10^{-4}$	0	24.1(2)	$4.2(1) \cdot 10^{-2}$
	$3.03(2) \cdot 10^{-3}$	$2.39(6) \cdot 10^{-4}$	−0.25	23.3(2)	$3.8(1) \cdot 10^{-2}$
	$3.61(2) \cdot 10^{-3}$	$1.40(6) \cdot 10^{-4}$	−0.5	22.6(2)	$3.55(9) \cdot 10^{-2}$
	$4.24(3) \cdot 10^{-3}$	$3.8(8) \cdot 10^{-5}$	−0.75	22.0(2)	$3.33(9) \cdot 10^{-2}$
	$4.92(4) \cdot 10^{-3}$	$-6(1) \cdot 10^{-5}$	−1	21.5(2)	$3.2(1) \cdot 10^{-2}$
$SrCu_{1.95}Mg_{0.05}(BO_3)_2$ $x = 0.05$	$3.69(2) \cdot 10^{-3}$	$4.95(9) \cdot 10^{-4}$	0	22.8(3)	$3.3(1) \cdot 10^{-2}$
	$4.48(2) \cdot 10^{-3}$	$3.41(7) \cdot 10^{-4}$	−0.25	21.5(2)	$2.81(8) \cdot 10^{-2}$
	$5.37(2) \cdot 10^{-3}$	$1.81(6) \cdot 10^{-4}$	−0.5	20.5(1)	$2.52(5) \cdot 10^{-2}$
	$6.35(3) \cdot 10^{-3}$	$1.7(8) \cdot 10^{-5}$	−0.75	19.6(2)	$2.32(5) \cdot 10^{-2}$
	$7.42(4) \cdot 10^{-3}$	$-1.5(1) \cdot 10^{-4}$	−1	18.9(2)	$2.18(4) \cdot 10^{-2}$
$SrCu_{1.9}Mg_{0.1}(BO_3)_2$ $x = 0.10$	$6.43(1) \cdot 10^{-3}$	$6.04(6) \cdot 10^{-4}$	0	21.0(2)	$2.20(6) \cdot 10^{-2}$
	$7.86(3) \cdot 10^{-3}$	$3.2(1) \cdot 10^{-4}$	−0.25	18.8(2)	$1.75(6) \cdot 10^{-2}$
	$9.48(6) \cdot 10^{-3}$	$1(2) \cdot 10^{-5}$	−0.5	17.1(3)	$1.51(7) \cdot 10^{-2}$
	$1.13(1) \cdot 10^{-2}$	$-3.1(3) \cdot 10^{-5}$	−0.75	15.9(4)	$1.38(6) \cdot 10^{-2}$
	$1.33(1) \cdot 10^{-2}$	$-6.5(5) \cdot 10^{-4}$	−1	14.9(4)	$1.31(6) \cdot 10^{-2}$

Table S3. The complete results of high-temperature magnetic susceptibility data fits in the interval 100–300 K for different doping concentrations using the Curie-Weiss law equation (**Equation 4** in the main text).

	C (emu K/mol Cu)	θ (K)	χ_0 (emu/mol Cu)
$SrCu_2(BO_3)_2$	0.553(4)	−136(1)	$-9.2(6) \cdot 10^{-5}$
$SrCu_{1.97}Mg_{0.03}(BO_3)_2$	0.517(2)	−133.3(7)	$-1.09(4) \cdot 10^{-4}$
$SrCu_{1.95}Mg_{0.05}(BO_3)_2$	0.480(2)	−129.9(6)	$-6.9(3) \cdot 10^{-5}$
$SrCu_{1.9}Mg_{0.1}(BO_3)_2$	0.379(2)	−110.1(9)	$2.1(4) \cdot 10^{-5}$

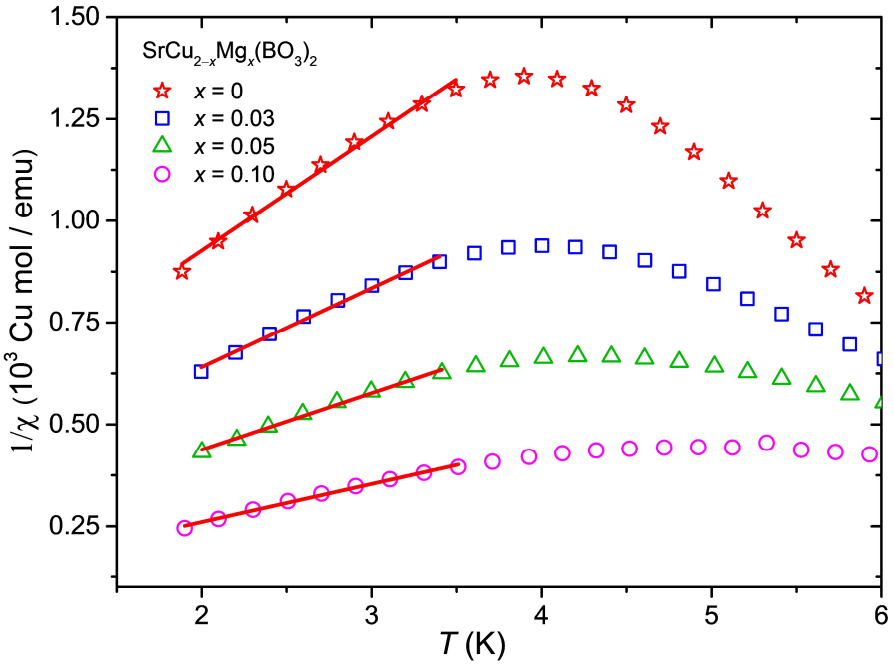


Figure S3. The low-temperature fits of the 1/χ data to **Equation 4** (main text) at T = 1.8–3.5 K for undoped and doped $SrCu_{2-x}Mg_x(BO_3)_2$ samples with x = 0, 0.03, 0.05, and 0.10. The concentration of Cu^{2+} S = 1/2 impurities was extracted from these fits for all doping concentrations.

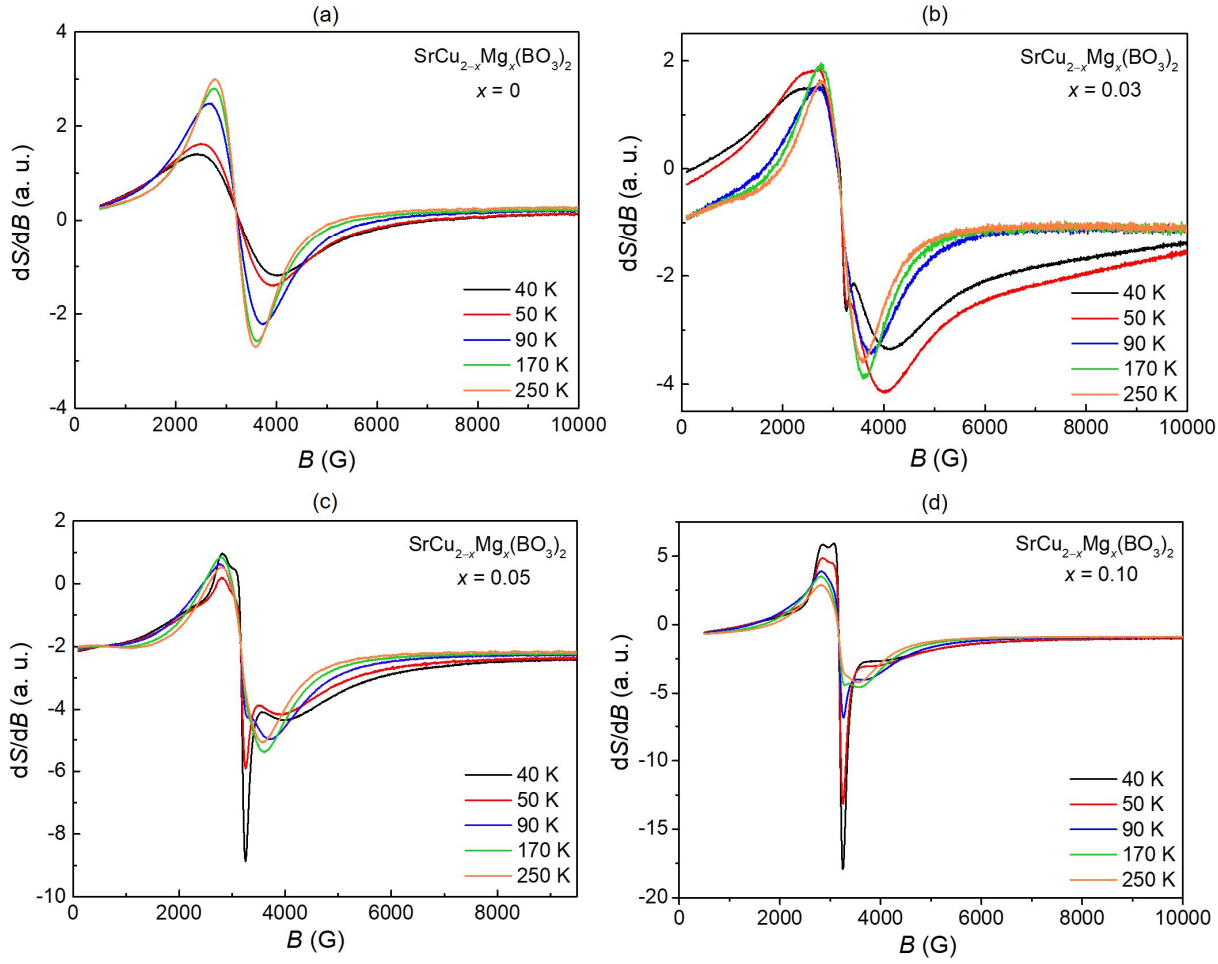


Figure S4. The EPR spectra of undoped $SrCu_2(BO_3)_2$ or $x = 0$ **(a)** and $SrCu_{2-x}Mg_x(BO_3)_2$ with $x = 0.03$ **(b)**, $x = 0.05$ **(c)**, and $x = 0.10$ **(d)** measured at temperatures of 40, 50, 90, 170, and 250 K, respectively, which show the development of low-temperature impurity peak that increases in intensity with increasing Mg-doping concentration.

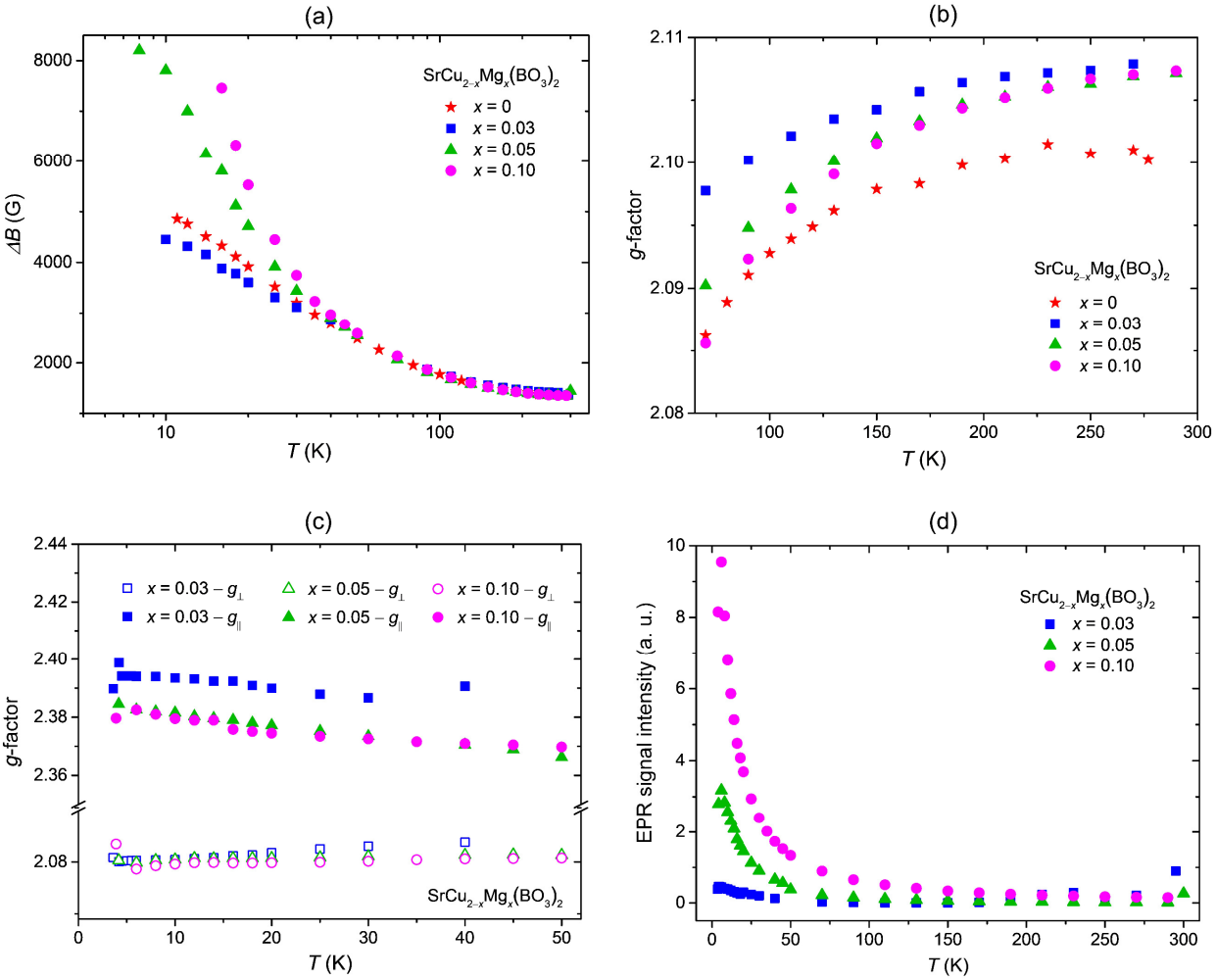


Figure S5. (a) The logarithmic temperature behaviour of the X-band EPR linewidth of the main dimer-lattice signal. **(b)** The temperature behaviour of the *g*-factor of the main dimer-lattice signal in $SrCu_{2-x}Mg_x(BO_3)_2$ with x = 0, 0.03, 0.05, and 0.10. **(c)** The temperature behaviour of the X-band EPR *g*-factors $g_{||}$ and $g_{\perp}$ as the two *g*- factor values along the *c* and *ab*-plane crystallographic directions for low-temperature "impurity" peaks for $SrCu_{2-x}Mg_x(BO_3)_2$ with x = 0.03, 0.05 and 0.10. **(d)** The temperature dependence of the X-band EPR signal intensity for low-temperature "impurity" peaks for x = 0.03, 0.05 and 0.10 samples.

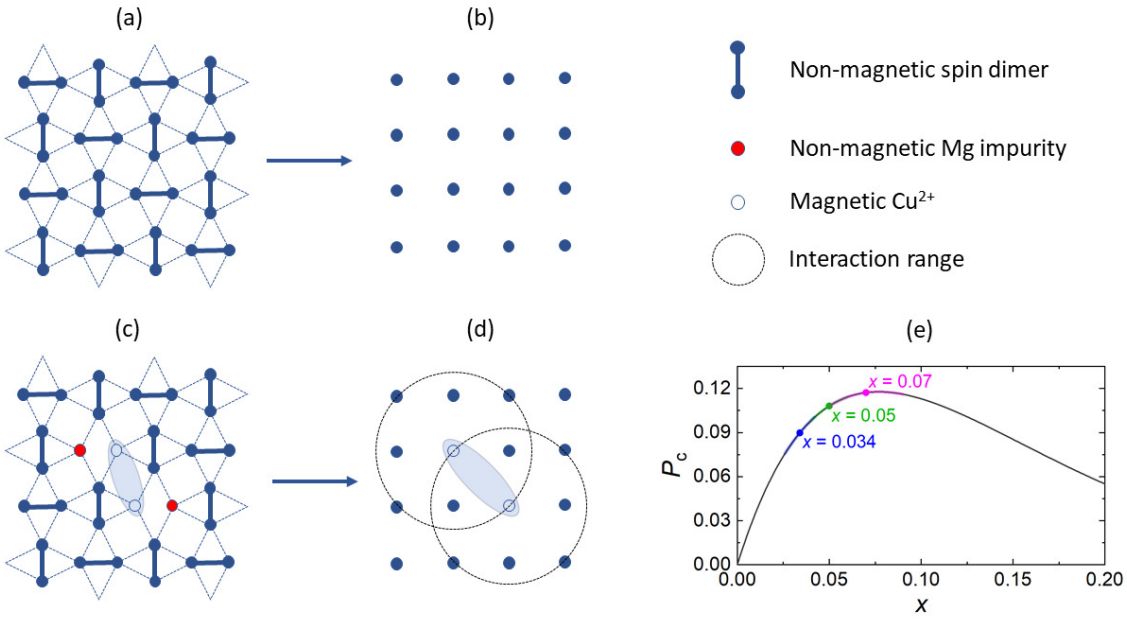


Figure S6. (a) Schematic image of Cu^{2+} spin dimer lattice, shown as two solid blue circles joined by a solid blue line. **(b)** Square lattice of Cu^{2+} spin dimers, where every lattice site marks the position of a centre of a dimer. Each dimer is represented by a solid blue circle. **(c)** Schematic image of a Cu^{2+} spin dimer lattice with two dimer-breaking impurity Mg^{2+} ions (solid red circles). Open blue circles show liberated magnetic Cu^{2+} spins. The shaded ellipse shows coupling of the two next-nearest-neighbouring magnetic Cu^{2+} spins. **(d)** Transformation of the spin dimer lattice with two impurities to the square lattice, similar as in (b). Solid blue circles show non-magnetic spin dimers and open blue circles magnetic Cu^{2+}. The shaded ellipse shows the case of coupling of two next-nearest-neighbouring Cu^{2+} and the dashed circles mark the interaction range for this case. **(e)** Calculated doping dependence of probability $P_c(x)$ for the formation of two next-nearest-neighbouring liberated magnetic Cu^{2+} spins as shown in (d). Blue, green and magenta points on the curve show the probability values for the experimentally determined doping x = 0.034, 0.05 and 0.07. Respective colour-shaded parts of the curve show the range of the uncertainty in x.

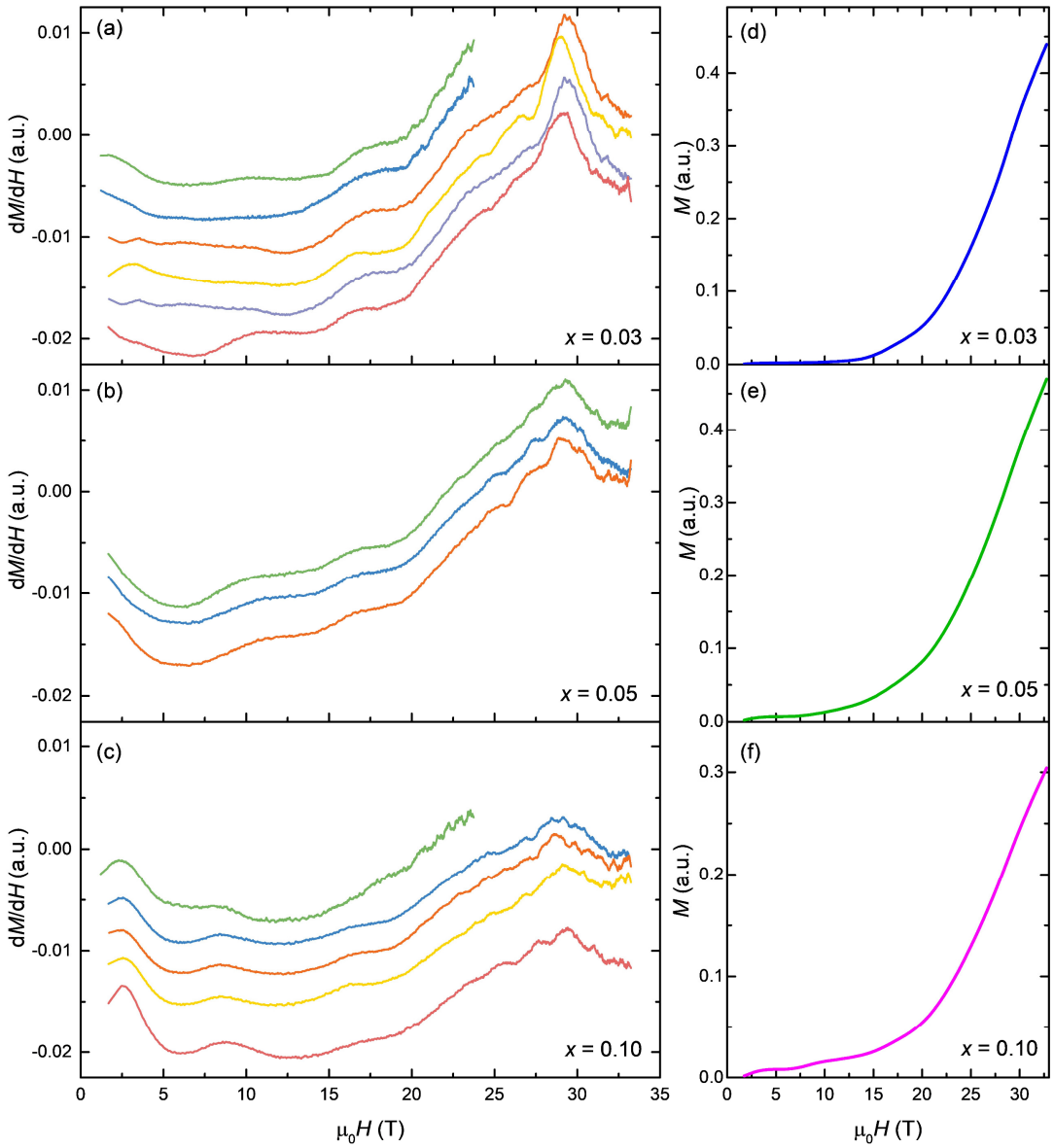


Figure S7. High magnetic field measurements performed in a pulsed magnetic field on $SrCu_{2-x}Mg_x(BO_3)_2$ powders. On the left the derivative dM/dH ($\mu_0 H$) is shown for x = 0.03 (**a**), 0.05 (**b**), and 0.10 (**c**). The derivative was numerically calculated from the time series of the raw magnetisation data and the magnetic field. A Savitzky-Golay filter with window length of 21 and a polynomial order of 1 (linear approximation) was applied for smoothing. The plots were vertically offset for clarity. The data for the lowest and highest 5% of magnetic fields reached during the pulse were omitted because the magnetic field changes slowly at these fields, resulting in higher errors. On the right side, the corresponding averaged magnetisation curves are shown for x = 0.03 (**d**), 0.05 (**e**), and 0.10 (**f**).

3.4 Conclusions

The first part of the dissertation presents a systematic study of chemical doping of $SrCu_2(BO_3)_2$, with particular emphasis on the effects of doping on the structure and magnetism of the parent compound. The investigation examines A-site electron doping with La and hole doping with Na as well as B-site substitutions with Mg.

Firstly, within the scope of electron doping with La, the flux method is introduced as a simple and widely accessible technique to grow La-doped $SrCu_2(BO_3)_2$ single crystals. Crystal growth was performed using polycrystalline $Sr_{1-x}La_xCu_2(BO_3)_2$ samples as starting materials, since the polycrystalline samples did not indicate any successful incorporation of La. Plate-like $Sr_{1-x}La_xCu_2(BO_3)_2$ single crystals of excellent crystallinity were successfully grown across a broad selection of nominal doping concentrations, $x = 0.02$, 0.03, 0.04, 0.05, 0.10, and 0.15, measuring up to 3 mm in lateral directions. Synchrotron PXRD on crushed crystals reveals an absence of La secondary phases up to $x = 0.05$ along with an overall unit cell volume decrease (from 537.91(2) Å^3 for the undoped system to 536.68(1) Å^3 for nominal $x = 0.15$), indicating a successful incorporation of La in the parent structure upon doping. The incorporation is unambiguously confirmed by EDS-SEM, which provides a semi-quantitative estimate of effective La-doping at <50% of the nominal values.

Besides the structural modifications, systematic effects on the magnetism of $SrCu_2(BO_3)_2$ are induced by La-doping. Magnetic susceptibility reveals a progressive reduction of the effective spin gap, from 28.2 K to 20.3 K for nominal $x = 0.15$. Moreover, the low-temperature susceptibility upturn indicates the presence of dimer-free Cu^{2+} ($S = 1/2$) spins and a systematic increase in their proportion as a function of nominal doping. This is corroborated by ESR, which further identifies antiferromagnetic correlations emerging between dimer-free Cu^{2+} spin pairs below ~5.5 K, which become more pronounced with increasing nominal doping. Overall, the magnetic studies show that La-doping of $SrCu_2(BO_3)_2$ results in progressive spin-dimer breaking with nominal doping. It is further demonstrated that at low doping levels, the gradual reduction of the spin-gap primarily emanates from spin-dimer breaking, whereas the collective spin dynamics of the Cu^{2+} dimer lattice remain largely preserved.

The results thus establish the feasibility of the flux method to incorporate La into the parent $SrCu_2(BO_3)_2$ structure as a practical alternative to optical floating zone growth, with the potential to extend this approach to other dopants.

Secondly, hole doping of $SrCu_2(BO_3)_2$ with Na was investigated in polycrystalline samples at three nominal doping concentrations, $x = 0.05$, 0.10 and 0.15, in $Sr_{1-x}Na_xCu_2(BO_3)_2$. The absence of Na secondary phases in powder X-ray diffraction, along with subtle changes in the unit cell parameters (a volume decrease from 537.91(2) Å^3 to 537.738(5) Å^3 to for nominal $x = 0.15$), initially suggest a potentially successful incorporation of Na into the parent structure. However, no signs of Na incorporation within the $SrCu_2(BO_3)_2$ matrix are detected by SEM-EDS analysis, which identifies Na within the intergranular regions instead. The combination of PXRD and SEM-EDS results indicates that instead of incorporating into the parent structure upon solid-state synthesis, Na likely segregates into glassy secondary phases, while any lattice incorporation might remain below the EDS detection limit. A possible incorporation of Na below the EDS detection limit was examined by two magnetic probes of higher sensitivity.

Magnetic susceptibility indicates a subtle increase in the spin gap from 26.1 to 29.5 K, yet also clearly reveals a presence of dimer-free Cu^{2+} spins in the doped samples, which exhibit a systematic increase in fraction with nominal doping. Electron spin resonance spectroscopy corroborates these findings, unambiguously confirming both the presence of

dimer-free Cu^{2+} spins as well as the progressive increase in their concentration with nominal doping. The detection of a clear free Cu^{2+} spin signal with axial g-factor anisotropy, persisting up to room temperature for the highest nominal doping, $x = 0.15$, demonstrates that Na-doping induces significant spin-dimer breaking upon solid-state synthesis and thereby substantially affects the spin-dimer lattice and its magnetic properties.

A-site electron doping with La and hole doping with Na show different levels of incorporation into the parent lattice. Although the dopant incorporation remains below the nominal concentration in both cases, the effective incorporation of La in single crystals is higher than that of Na in polycrystalline samples. Both dopants induce a subtle decrease in the unit cell volume, which is more pronounced for La. The latter also exhibits a more pronounced influence on the spin gap – a decrease from 28.2 to 20.3 K, while for Na-doping, the gap increases only from 26.6 to 29.4 K. The introduction of both dopants in the structure disrupts the dimer lattice by inducing spin-dimer breaking. This is more pronounced for La-doping, where dimer-free Cu^{2+} $S = 1/2$ spins additionally develop correlations below 5.5 K, which are not detected for Na-doping. No superconductivity is observed for either dopant.

Thirdly, B-site magnetic dilution with Mg was studied in polycrystalline $SrCu_{2-x}Mg_x(BO_3)_2$ samples with nominal $x = 0.03$, 0.05 and 0.10. The study reveals that the effective Mg-doping can be realized at higher values than previously reported for single-crystalline samples. Despite the presence of secondary Mg phases in PXRD, a systematic increase in the unit cell parameters and volume is observed with increasing nominal doping concentration (from 537.91(2) $Å^3$ to 539.15(5) $Å^3$ for nominal $x = 0.10$). A partially effective incorporation of Mg in the parent structure is unambiguously confirmed by EDS-SEM, giving a semi-quantitative estimate of the highest effective Mg-doping at approximately $x = 0.07$ for nominal $x = 0.10$.

Magnetic studies reveal a systematic softening of antiferromagnetic interactions within the dimer lattice upon Mg-doping, manifested in a significant closing of the spin gap from 26.6 to 12.1 K, and a systematic decrease of the Curie-Weiss temperature and the magnetic susceptibility maximum temperature with increasing nominal doping. These results, corroborated by X-band ESR spectroscopy, are consistent with Cu^{2+} spin-dimer breaking due to magnetic dilution. Investigating the effect of Mg-doping on the magnetization plateaus up to 35 T shows a clear observation of the $\mu_0 H'_{C0} \approx 9$ T anomaly at the highest nominal doping, $x = 0.10$. This anomaly reflects special configurations of dimer-free Cu^{2+} $S = 1/2$ spins resulting from magnetic dilution, which interact at distances exceeding the intra-dimer Cu^{2+} bonds. Furthermore, the pseudo-1/8 plateau exhibits a slight shift towards lower fields with increasing doping and is significantly suppressed at nominal $x = 0.10$. This is consistent with expectations from a previous study on single crystals with nominal doping up to $x = 0.05$ which predicted a suppression of pseudo-$1/n$ plateaus at higher doping levels. The study thus demonstrates a pronounced detrimental effect of Mg-doping on the spin-dimer lattice.

Similarly to previous reports, both B-site magnetic dilution and A-site charge doping indicate that achieving effective doping in this system remains challenging, as the incorporation is only partial in both cases, leading to subtle yet systematic changes in the $SrCu_2(BO_3)_2$ unit cell parameters. However, at high nominal doping levels, the achieved effective doping is nevertheless sufficient to induce spin-dimer breaking, which increases with nominal doping. The dimer-breaking is more pronounced for magnetic dilution, which also results in a more pronounced spin-gap reduction, almost twice as large for Mg-doping (12.1 K) compared to La-doping (20.1 K) at $x = 0.10$.

Chapter 4

Single-Crystal Growth of Rare-Earth Heptatantalates $RETa_7O_{19}$ with a Perfect Triangular Lattice

4.1 Motivation

The search for new quantum spin liquid candidates continues to drive extensive research into low-dimensional and geometrically frustrated magnetic systems. Originally, the first systems in which magnetic frustration was recognized were triangular-lattice antiferromagnets [50]. These were later regarded as prototypical two-dimensional systems anticipated to host a QSL state upon the introduction of this concept by Anderson in 1973 [16]. This seminal work in QSL research considered isotropic Heisenberg exchange interactions between spin-1/2 moments. In contrast, it was subsequently theoretically proposed [51] and experimentally demonstrated that such interactions stabilize long-range magnetic order [52–54]. More recently, theoretical studies have proposed that a quantum spin liquid phase may instead emerge in triangular two-dimensional systems with anisotropic interactions arising from spin-orbit coupling [55–57]. This occurs in ions with unquenched orbital angular momentum, such as low-coordinate transition metals and *f*-block elements [58].

A particularly promising case of such a system are rare-earth heptatantalates, $RETa_7O_{19}$, which have been investigated since the mid-20th century for their potential in laser devices and nonlinear optical applications [59–62]. Crystallizing in the noncentrosymmetric $P\bar{6}c2$ space group (structure displayed in Results and Discussion, Section 4.2), these compounds are free of chemical disorder or intersite ion mixing, an important structural characteristic that, alongside a perfect triangular lattice and weak interlayer magnetic interactions, represents key structural factors associated with the emergence of QSL behavior [32,63].

Recently, a representative of this family, $NdTa_7O_{19}$, was identified as the first triangular-lattice quantum spin-liquid candidate with dominant Ising-like spin correlations [32]. Multiple magnetic measurements performed on a high-quality polycrystalline sample revealed no signs of magnetic order in this compound down to 40 mK and indicated the presence of a large magnetic anisotropy [32]. However, the understanding of such states crucially relies on studies performed on high-quality single crystals, which allow a precise determination of anisotropy and momentum-resolved investigations of spin correlations. To enable such studies, an optimized flux-growth method was developed, yielding high-quality $NdTa_7O_{19}$ single crystals suitable for advanced magnetic characterization.

This Chapter presents the optimization process and key parameters for successful single-crystal growth, along with evidence for enhanced magnetic anisotropy compared to polycrystalline samples.

As noted in [32], an alternative experimental approach to examine the effects of anisotropy in triangular-lattice antiferromagnets is studying additional members of the $RETa_7O_{19}$ family. In 2023, this was pursued in [63], which reported on the synthesis, structure and magnetism of polycrystalline candidates with RE = Pr, Sm, Eu, Gd, Dy and Ho. Magnetic measurements revealed an absence of long-range magnetic order or field-induced magnetic transitions down to 2 K in all cases. In agreement with [32], these findings highlight the potential of the heptatantalate family to realize further exotic states and quantum phenomena.

Furthermore, a very recent report presented solid-state synthesis of $CeTa_7O_{19}$ and single-crystal growth of $YbTa_7O_{19}$ by flux method, employing polycrystalline YbOCl as Yb source and a mixture of Ta_2O_5 and Ta as a flux. The results suggest that a quantum spin-liquid state may also be realized in these candidates [64].

The optimized method for $NdTa_7O_{19}$ growth, presented in Section 4.2, was successfully extended to other members of the $RETa_7O_{19}$ family (RE = Er, Gd, Dy) to examine the influence of different rare-earth ions on the magnetic behavior and explore the possibility of additional QSL candidates within the heptatantalate series. However, for $YbTa_7O_{19}$, difficulties in obtaining single crystals by this method were encountered. Further information and background of the study are provided in the Introduction in Section 4.2.

4.2 Optimized Flux Single-Crystal Growth of the Quantum Spin Liquid Candidate $NdTa_7O_{19}$ and Other Rare-Earth Heptatantalates, $ErTa_7O_{19}$ and $GdTa_7O_{19}$

This Section introduces a flux growth protocol for obtaining high quality single crystals of $NdTa_7O_{19}$, the first Ising-type quantum spin liquid candidate on a perfect triangular lattice. The resulting crystals exhibit predominantly plate-like and hexagonal morphologies, with lateral dimensions up to 3.5 mm and thicknesses up to 2 mm, the largest reported to date.

Additionally, the established growth conditions for $NdTa_7O_{19}$ were further applied to two other rare-earth heptatantalate candidates, $ErTa_7O_{19}$ and $GdTa_7O_{19}$. The $ErTa_7O_{19}$ crystals exhibit lateral sizes up to 2.5 mm and thicknesses up to 0.5 mm, while $GdTa_7O_{19}$ attain lateral sizes up to 4 mm and thicknesses up to 0.5 mm.

The resulting crystals of all three heptatantalate representatives are suitable for multiple magnetic measurements, allowing a more precise and detailed characterization of the ground state compared to previously available polycrystalline materials. The magnetic characterization included in this dissertation comprises magnetic susceptibility, presented below, and ESR spectroscopy results for $NdTa_7O_{19}$, given in Appendix A. The susceptibility shows no signs of magnetic ordering for $NdTa_7O_{19}$ and $ErTa_7O_{19}$, while revealing a paramagnetic behavior for $GdTa_7O_{19}$. The established flux method offers a promising route towards successful growth of additional rare-earth heptatantalates in the series.

This Section addresses Aims 4–7 and evaluates Hypotheses 7–10.

Published in: L. Šibav, Ž. Gosar, T. Knaflič, Z. Jagličić, G. King, H. Nojiri, D. Arčon and M. Dragomir, "Optimized Flux Single-Crystal Growth of the Quantum Spin Liquid Candidate $NdTa_7O_{19}$ and Other Rare-Earth Heptatantalates, $ErTa_7O_{19}$ and $GdTa_7O_{19}$," *Cryst. Growth Des.*, vol. 25, no. 12, pp. 4646–4654, 2025, DOI: 10.1021/acs.cgd.5c00624. (IF = 3.4, 2025, Q1 Crystallography, Q2 Materials Science and Chemistry)

First author contribution: Conducted solid-state synthesis of $NdTa_7O_{19}$, as well as $ErTa_7O_{19}$, $GdTa_7O_{19}$ and the main flux component, $K_2Mo_3O_{10}$. Performed laboratory PXRD of the samples and Rietveld refinement analysis of the data. Carried out crystal growth experiments and optimized growth conditions for all three rare-earth heptatantalates. Characterized the crystal composition by scanning electron microscopy and energy-dispersive X-ray spectroscopy measurements. Co-prepared the first draft of the manuscript and participated in its review and editing together with co-authors.

CRYSTAL GROWTH & DESIGN

Open Access

This article is licensed under CC-BY 4.0

pubs.acs.org/crystal

Article

Optimized Flux Single-Crystal Growth of the Quantum Spin Liquid Candidate $NdTa_7O_{19}$ and Other Rare-Earth Heptatantalates, $ErTa_7O_{19}$ and $GdTa_7O_{19}$

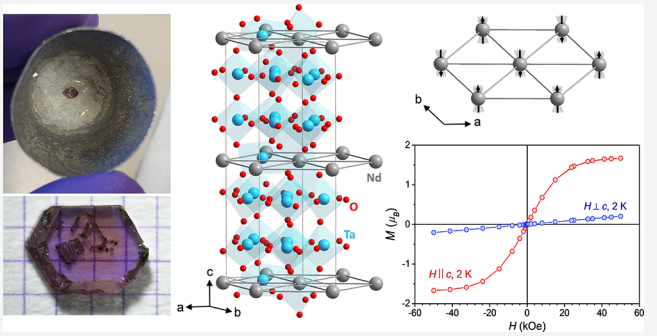
Lia Šibav, Matic Lozinšek, Zvonko Jagličić, Tina Arh, Panchanana Khuntia, Andrej Zorko, and Mirela Dragomir*

Cite This: *Cryst. Growth Des.* 2025, 25, 4646−4654

Read Online

ACCESS | Metrics & More | Article Recommendations | Supporting Information

ABSTRACT: Single crystals are essential for characterizing a wide range of magnetic states, including exotic ones such as quantum spin liquids. This study reports a flux method for growing single crystals of $NdTa_7O_{19}$, the first quantum spin liquid candidate on a triangular spin-lattice with dominant Ising-like spin correlations. Purple $NdTa_7O_{19}$ single crystals with hexagonal morphology were successfully grown by using a $K_2Mo_3O_{10}$−B_2O_3 flux. With lateral sizes up to 3.5 mm and a thickness up to 2 mm, these are the largest dimensions reported to date. The chemical composition was confirmed by powder and single-crystal X-ray diffraction along with scanning electron microscopy with energy dispersive X-ray spectroscopy. Aiming for an accurate determination of the magnetic anisotropy and its effect on the magnetic properties, $NdTa_7O_{19}$ crystals were additionally analyzed by magnetic susceptibility, revealing a substantial anisotropy without long-range magnetic ordering down to 2 K. Single crystals of two novel rare-earth heptatantalates, $ErTa_7O_{19}$ and $GdTa_7O_{19}$, were also grown, and their magnetic properties investigated. The magnetic anisotropy of $ErTa_7O_{19}$ closely resembles that of isostructural $NdTa_7O_{19}$, indicating the possibility of a similar exotic magnetic ground state. In contrast, $GdTa_7O_{19}$ shows paramagnetic behavior, consistent with previous results obtained for polycrystalline samples.

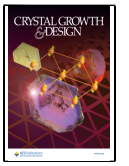


1. INTRODUCTION

Rare-earth heptatantalates, abbreviated as $RETa_7O_{19}$, with RE representing a trivalent rare-earth element, are promising materials for nonlinear optics and laser technology due to their noncentrosymmetric structure as well as high chemical and thermal stability, high concentration of optically active ions, high mechanical strength, and high thermal conductivity.[1−4] Among this series, $NdTa_7O_{19}$ is regarded as the most auspicious candidate for such applications.[2,4]

Recently, $NdTa_7O_{19}$ has also been identified as a very intriguing magnetic material, more specifically, a potential triangular antiferromagnet with an Ising quantum spin liquid ground state.[5] Low-dimensional antiferromagnets realized on a perfect triangular lattice, such as $NdTa_7O_{19}$, are highly desired as a large magnetic anisotropy could explain a possible quantum spin liquid ground state.[6,7] Indication of a spin liquid ground state in $NdTa_7O_{19}$ was found via absence of magnetic Bragg peaks in neutron powder diffraction at temperatures down to 40 mK,[5] the presence of magnetic diffuse scattering, and persistent, low-temperature spin dynamics detected via muon spectroscopy, thus combining most suitable experimental techniques that can be used to detect such elusive states.[8] The splitting of crystal-electric field levels and bulk magnetic measurements on this material further suggested the presence of large magnetic anisotropy.[5] However, since these measurements were conducted on polycrystalline $NdTa_7O_{19}$, a more precise determination of magnetic anisotropy is dependent on the availability of single crystals.[9−11] Single crystals would also allow for more refined magnetic measurements, e.g., enabling wave-vector-resolved insight into spin correlations or the detection of the anticipated fractionalized excitations. Furthermore, given that materials with frustrated lattices and enhanced quantum properties tend to be particularly sensitive to defects (e.g., chemical disorder, undesirable impurities, etc.),[8,11] there is a clear preference for high-quality single crystals of $NdTa_7O_{19}$ over polycrystalline samples, where such defects are minimized.

Received: April 30, 2025
Revised: May 17, 2025
Accepted: May 19, 2025
Published: June 2, 2025



© 2025 The Authors. Published by American Chemical Society

https://doi.org/10.1021/acs.cgd.5c00624
Cryst. Growth Des. 2025, 25, 4646−4654

Single crystals of $NdTa_7O_{19}$ have been previously grown for optical applications by a flux method using two different fluxes, $Li_2B_4O_7$[1,3] and $K_2Mo_3O_{10}$—with a small addition of B_2O_3.[3,4] The literature reports showed a preference for starting from the constituent oxides Nd_2O_3 and Ta_2O_5[1−4] instead of polycrystalline $NdTa_7O_{19}$, which could be due to the fact that solid-state synthesis resulted in nonstoichiometric powders.[4] The largest crystals grown from the oxides were limited to 1.5 mm in lateral size.[12] Starting with constituent oxides is, however, less advantageous than starting from a polycrystalline powder of the correct composition. Different dissolution rates of the constituent oxides affect concentrations of reagents in the melts and drive the melt into a different supersaturated regime, from which nucleation of undesired phases takes place.[13] Indeed, the phase diagrams showed a narrow primary crystallization region of the $NdTa_7O_{19}$ phase as well as multiple regions of formation of secondary phases, which included $Nd_{0.33}TaO_3$ and $NdTaO_4$.[1,3,4] This could also be the reason why these reports[1−4] only provide rough guidelines rather than exact protocols required for the growth of high-quality, millimeter-sized single crystals.

With the aim of growing $NdTa_7O_{19}$ crystals of suitable size for magnetic measurements and other techniques that require larger crystals, such as neutron scattering or muon spectroscopy, and of establishing a more precise protocol that could be extended to other rare-earth members of the $RETa_7O_{19}$ family, in this study, we chose in this study to explore a flux growth method using $K_2Mo_3O_{10}$−B_2O_3 as the flux.[14] This flux has a high dissolution ability due to the high chemical activity of alkali polymolybdates, as well as a relatively low melting temperature.[4] The presence of small amounts of B_2O_3 increases the solubility, decreases the saturation temperature, and reduces the flux volatility without significantly altering the flux viscosity.[15] These benefits have previously been successfully exploited for single-crystal growth of other systems such as rare-earth borates $REAl_3(BO_3)_4$[16−22] or rare-earth phosphates.[23]

In this study, nearly single-phase polycrystalline $NdTa_7O_{19}$ was successfully prepared. A previously reported solid-state method[24] was optimized, resulting in a 98(1) wt % of the main phase, which was used as a starting material for flux growth of $NdTa_7O_{19}$ single crystals of predominantly hexagonal, plate-like morphologies with lateral sizes up to 3.5 mm and thicknesses up to 2 mm—the largest $NdTa_7O_{19}$ single crystals reported to date. The flux method presented here was further employed to grow single crystals of two other novel rare-earth heptatantalates, $ErTa_7O_{19}$ and $GdTa_7O_{19}$. The composition and morphology of all newly grown crystals were characterized by powder X-ray diffraction (PXRD) and single-crystal X-ray diffraction (SCXRD) as well as scanning electron microscopy (SEM) coupled with energy dispersive X-ray spectroscopy (EDS). Furthermore, magnetic susceptibility measurements were employed to investigate the magnetic anisotropy.

2. EXPERIMENTAL SECTION

2.1. Solid-State Synthesis. Three polycrystalline $RETa_7O_{19}$ members, $NdTa_7O_{19}$, $ErTa_7O_{19}$, and $GdTa_7O_{19}$, were synthesized by a solid-state reaction similar to a previously reported procedure.[24] Stoichiometric amounts of Nd_2O_3 (Thermo Scientific, 99.99%), Er_2O_3 (Thermo Scientific, 99.99%), and Gd_2O_3 (Thermo Scientific, 99.99%), together with Ta_2O_5 (Alpha Aesar, 99.85 or 99.99%), were weighed, hand-homogenized in an agate mortar, and pressed into pellets with a 10 mm diameter using a force of 50 kN. Prior to the synthesis, all three rare-earth oxides were preannealed at 1000 °C for 24 h. Multiple synthesis cycles (5−9) were performed at temperatures T = 900−1200 °C with intermediate regrinding, resulting in about 8.5 g (5 mmol) of the polycrystalline product. As the main flux component, potassium molybdate ($K_2Mo_3O_{10}$, about 30 mmol), is not commercially available, it was synthesized using K_2CO_3 (Chempur, 99.9%) and MoO_3 (Merck, 99.9%) by a solid-state reaction at 500 °C, for two cycles of 72 h each, with intermediate grinding (eq 1)

$$K_2CO_3 + 3MoO_3 \rightarrow K_2Mo_3O_{10} + CO_2\uparrow \quad (1)$$

2.2. Single-Crystal Growth. Polycrystalline $RETa_7O_{19}$ samples, obtained by solid-state reactions, were used as starting materials for flux-growth experiments, employing a $K_2Mo_3O_{10}$−B_2O_3 flux. In each growth experiment, polycrystalline $RETa_7O_{19}$, $K_2Mo_3O_{10}$, and B_2O_3 were weighed in the predetermined mass ratio, hand-homogenized in an agate mortar, and placed into platinum (Pt) crucibles, which were placed into alumina crucibles covered by alumina caps (Figure 1). For the $NdTa_7O_{19}$ single-crystal growth experiments, Pt crucibles with a volume of 5 mL were used, while $ErTa_7O_{19}$ and $GdTa_7O_{19}$ growths were performed in 10 mL Pt crucibles.

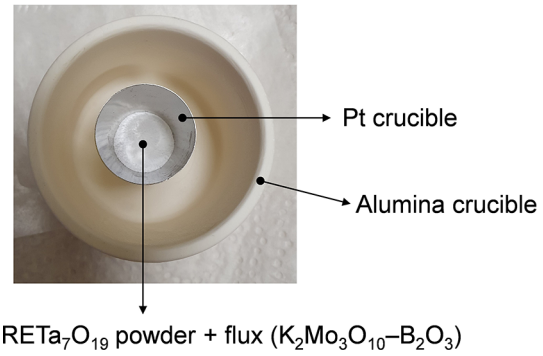


Figure 1. Experimental setup for single-crystal growth, showing a platinum crucible containing the reaction mixture of $NdTa_7O_{19}$ and the $K_2Mo_3O_{10}$−B_2O_3 flux, placed inside an alumina crucible, which was covered with an alumina cap.

In $NdTa_7O_{19}$ single-crystal growth, cooling was done in two steps; first, a slower cooling step of 0.5, 1, or 2 °C/h was employed, followed by a rapid cooling step of 10 or 50 °C/h (Table 1) with a minimal dwell time at the transition temperature in between the steps. At the end of rapid cooling, the reaction mixture was allowed to cool naturally. The crystals were separated from the crucible by using deionized water in an ultrasonic bath.

Table 1. Summary of Tested Parameters for $NdTa_7O_{19}$ Flux Growth

parameter	tested conditions
batch size (g)	0.6, 0.7, 0.9, 1, 1.1, 1.2, 1.6, 2.2, 3, 4.4
flux-to-material mass ratio	5:1, 8:1, 9:1, 10:1, 15:1
flux composition ($K_2Mo_3O_{10}$−B_2O_3 mass ratio)	2.3:1, 4:1, 8:1, 9:1, 99:1
dwell temperature (°C)	700, 1100, 1150, 1200
dwell time (h)	2, 24, 48
slower cooling rate (°C/h)	0.5, 1, 2
transition temperature (°C)	500, 950
rapid cooling rate (°C/h)	10, 50

The following growth parameters were optimized for $NdTa_7O_{19}$: (i) batch size, (ii) flux-to-material mass ratio, (iii) flux composition ($K_2Mo_3O_{10}$−B_2O_3 mass ratio), (iv) dwell temperature, (v) dwell time, and (vi) cooling rate. These parameters were varied and optimized in order to grow the largest number of $NdTa_7O_{19}$ single crystals (Table

https://doi.org/10.1021/acs.cgd.5c00624
Cryst. Growth Des. 2025, 25, 4646−4654

1). The optimal conditions were slightly modified for subsequent growth experiments of $ErTa_7O_{19}$ (Table 2). The dwell time, dwell temperature, transition temperature, and rapid cooling rate were kept constant at 24 h, 1100 °C, 950 and 10 °C/h.

Table 2. Summary of Tested Parameters for $ErTa_7O_{19}$ Flux Growth

parameter	tested conditions
batch size (g)	0.8, 0.9, 1.1, 1.22, 1.35, 2.2
flux-to-material mass ratio	6:1, 7:1, 8:1, 9:1, 10:1
flux composition ($K_2Mo_3O_{10}$–B_2O_3 mass ratio)	3:1, 4:1, 5:1, 9:1
slow cooling rate (°C/h)	0.3, 0.5, 0.7, 0.8. 1, 2, 5

Flux growth of $GdTa_7O_{19}$ was performed using a 4:1 $K_2Mo_3O_{10}$–B_2O_3 mass ratio, an 8:1 flux-to-material mass ratio, and a batch size of 0.90 g. Two slow cooling rates were tested, 0.8 and 0.5 °C/h. The remaining parameters of the temperature profile were identical to those employed for $ErTa_7O_{19}$ growth.

2.3. Powder X-ray Diffraction. Polycrystalline $RETa_7O_{19}$ samples obtained by solid-state synthesis were first examined by PXRD using a Rigaku MiniFlex600-C Benchtop XRD with Cu Kα radiation in the 2θ range 3–120° with a step size of 0.010° and a speed of 2.5°/min. The primary flux component, $K_2Mo_3O_{10}$, was also examined using the same conditions, albeit with a smaller 2θ range of 3–90°. Phase identification was performed using SmartLab Studio II software. The Rietveld refinements were performed using the least-squares method in GSAS-II.[25]

2.4. Single-Crystal X-ray Diffraction. The grown crystals were first examined under a polarizing microscope. Selected crystals of appropriate sizes were mounted on MiTeGen Dual Thickness MicroLoops with Baysilone-Paste (Bayer-Silicone, Mittelviskos) and measured on a Rigaku OD XtaLAB Synergy-S Dualflex diffractometer equipped with a PhotonJet-S microfocus Ag Kα X-ray source and an Eiger2 R CdTe 1M hybrid-photon-counting detector. *CrysAlisPro* software[26] was employed for data collection and reduction. Crystal structures were solved by *olex2.solve* and refined by *SHELXL*[27] within *OLEX2* program.[28]

2.5. Laue Diffraction. White beam X-ray backscatter diffraction was used to assess the surface quality and the crystallographic orientation of the single crystals. A real-time Laue system (Laue-Camera GmbH) was used with an X-ray Seifert ID3003 generator equipped with an MWL 120 detector.

2.6. SEM and EDS. For the SEM analyses, a few small $NdTa_7O_{19}$ single crystals were placed on carbon tape and carbon coated using a Balzers SCD 050 sputter coater. The imaging and compositional analyses were performed on a Thermo Fisher Quanta 650 ESEM instrument equipped with an energy-dispersive X-ray spectrometer–EDS (Oxford Instruments, AZtec Live, Ultim Max SDD 65 mm^2). The accelerating voltage used was 20 kV in all cases.

2.7. Magnetic Susceptibility. The magnetic susceptibility measurements were carried out using an MPMS-XL-5 SQUID magnetometer from Quantum Design in the 2–300 K temperature range in an applied magnetic field of 1 kOe. A single crystal of $NdTa_7O_{19}$ (16 mg), $ErTa_7O_{19}$ (4 mg), and $GdTa_7O_{19}$ (2 mg) was glued to a straw with diamagnetic Apiezon N grease in different orientations to the external magnetic field. The field dependence of the isothermal magnetization was measured between −50 and 50 kOe at 2 K.

3. RESULTS AND DISCUSSION

3.1. Solid-State Synthesis. The primary flux component, $K_2Mo_3O_{10}$, was synthesized using a solid-state thermal method

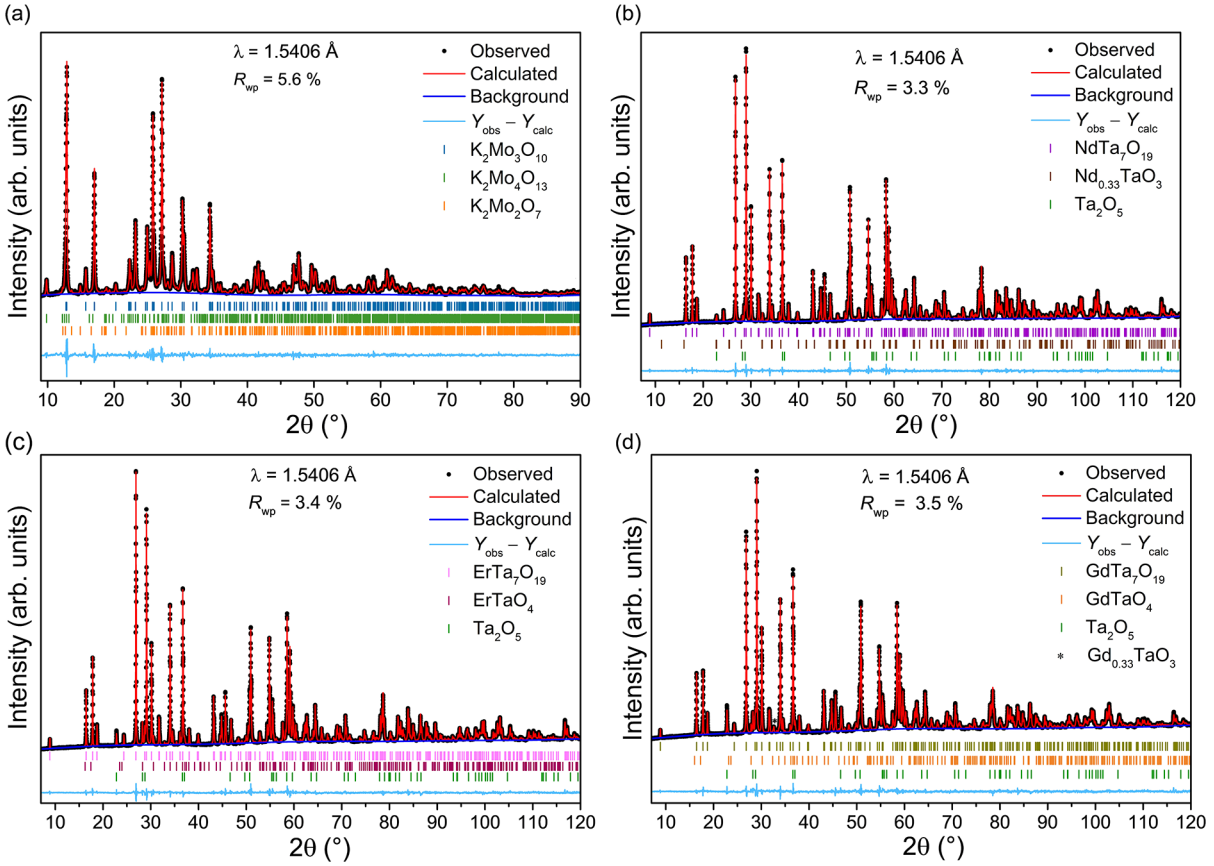


Figure 2. Rietveld refinement profiles of laboratory PXRD data (Cu Kα, T = 293 K) of (a) the primary flux component, $K_2Mo_3O_{10}$, (b) $NdTa_7O_{19}$, (c) $ErTa_7O_{19}$, and (d) $GdTa_7O_{19}$. The Bragg 2θ positions are marked as bars below each diffractogram.

https://doi.org/10.1021/acs.cgd.5c00624
Cryst. Growth Des. 2025, 25, 4646–4654

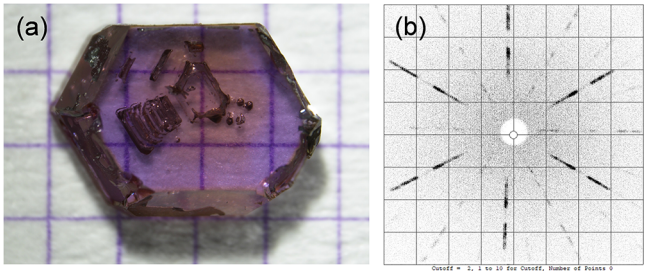


Figure 3. (a) Hexagonal $NdTa_7O_{19}$ crystal grown in this study on a millimeter grid and (b) corresponding X-ray Laue back-reflection pattern observed along the *c* crystallographic direction, displaying the 6-fold symmetry.

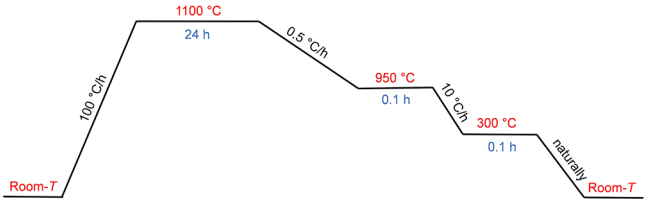


Figure 4. Optimal temperature profile for flux growth of $NdTa_7O_{19}$ using the $K_2Mo_3O_{10}$–B_2O_3 flux. The dwell temperature, 1100 °C, and the cooling rate of the first step, 0.5 °C/h, were identified as critical crystal-growth parameters.

Table 3. Optimal Growth Parameters for $NdTa_7O_{19}$

parameter	optimal conditions
batch size (g)	0.9–1.1
flux-to-material mass ratio	8:1–10:1
flux composition ($K_2Mo_3O_{10}$–B_2O_3 mass ratio)	4:1
dwell temperature (°C)	1100
slow cooling rate (°C/h)	0.5

Table 4. Optimal Growth Parameters for $ErTa_7O_{19}$

parameter	optimal conditions
batch size (g)	0.8–0.9
flux-to-material mass ratio	7:1–8:1
flux composition ($K_2Mo_3O_{10}$–B_2O_3 mass ratio)	3:1–5:1
dwell temperature (°C)	1100
slow cooling rate (°C/h)	0.8

according to eq 1, as it is not commercially available. Rietveld refinement analysis on the resulting polycrystalline $K_2Mo_3O_{10}$ showed 82.0(4) wt % of the main phase (*C*2/*c* space group), 9.2(2) wt % of $K_2Mo_4O_{13}$, and 8.8(3) wt % of $K_2Mo_2O_7$ (Figure 2a). The additional molybdates were likely formed by the loss of potassium. This was subsequently optimized to an almost pure phase, 98(1) wt %, $K_2Mo_3O_{10}$. However, the crystal growths were performed using the batch presented in Figure 2a.

As mentioned in the previous section, this study aimed to perform single-crystal growth experiments starting from polycrystalline $RETa_7O_{19}$ to avoid the secondary phases previously reported in the literature.[1−4] Thus, the three phases $NdTa_7O_{19}$, $ErTa_7O_{19}$, and $GdTa_7O_{19}$ were first prepared by solid-state synthesis. The phase identifications and Rietveld refinement analyses of the powder data indicated that the three members of the series are isostructural and adopt the $P\bar{6}c2$ space group, in good agreement with the literature (Figure 2b–d).[29,30] Detailed results of the Rietveld refinement analysis are available in the Supporting Information, Table S1. A 0.6% decrease in the unit cell volume is observed from Nd (V = 668.536(4) Å^3) to Gd (V = 664.780(7) Å^3) and a 1% reduction to the Er member (V = 661.418(5) Å^3), as expected following the decreasing radii of the rare-earth ions due to the lanthanoid contraction.[31] A parallel trend is observed with the magnetic intralayer RE–RE distance, which decreases from 6.2228(1) Å for Nd to 6.2119(1) Å for Gd and 6.2018(1) Å for the Er member, while the magnetic interlayer distances decrease from 9.9678(1) Å for Nd to 9.9465(1) Å for Gd and 9.9285(1) Å for the Er member.

A small fraction of secondary phases was observed in the powder X-ray diffractograms of each heptatantalate (Figure 2b–d), identified as unreacted Ta_2O_5 and two additional rare-earth tantalates. The Rietveld refinement analysis revealed 1.2(2) wt % of Ta_2O_5 and 1.2(1) wt % of $Nd_{0.33}TaO_3$ for the $NdTa_7O_{19}$ sample, while the $ErTa_7O_{19}$ sample contained 5.1(1) wt % of Ta_2O_5 and 2.2(1) wt % of $ErTaO_4$, with the $GdTa_7O_{19}$ sample containing a slighter larger content of impurities, namely, 7.9(1) wt % Ta_2O_5, 1.6(1) wt % $GdTaO_4$, and 1.0(1) wt % $Gd_{0.33}TaO_3$. One way to minimize the amount of these phases is to increase the annealing temperature in the solid-state reactions and the dwell time. Despite the small amount of impurities, the powders were used for single-crystal growth, as the process can also serve as a

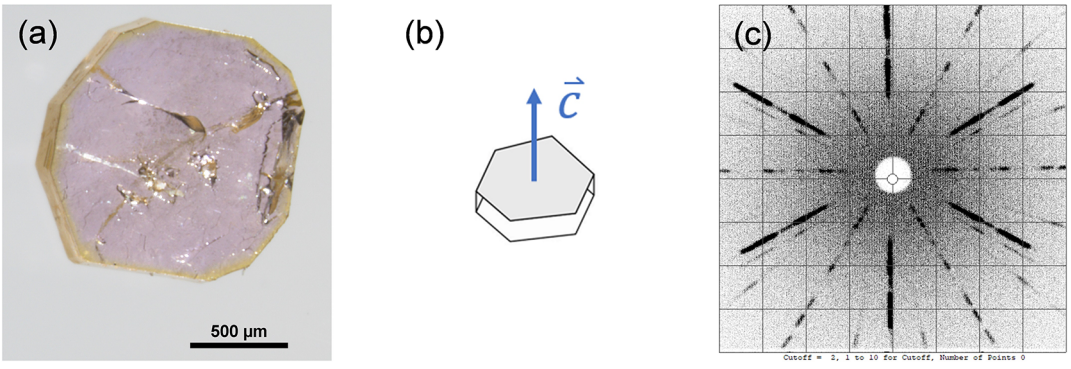


Figure 5. (a) $ErTa_7O_{19}$ single crystal grown by the flux method. (b) Expected orientation of the crystallographic *c*-axis of an $ErTa_7O_{19}$ crystal. (c) Corresponding X-ray Laue back-reflection pattern collected on an $ErTa_7O_{19}$ single crystal showing the 6-fold axis along the *c*-crystallographic direction.

https://doi.org/10.1021/acs.cgd.5c00624
Cryst. Growth Des. 2025, 25, 4646−4654

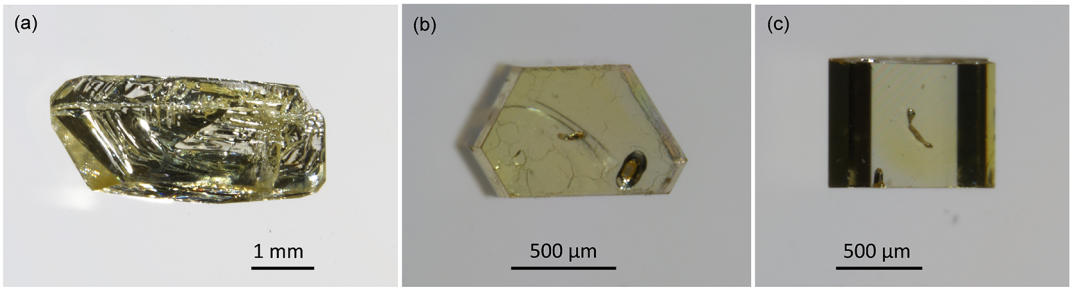


Figure 6. (a) Largest as-grown pseudohexagonal $GdTa_7O_{19}$ crystal. (b) Frontal view and (c) side view of another, smaller, hexagonal $GdTa_7O_{19}$ single crystal grown in this study.

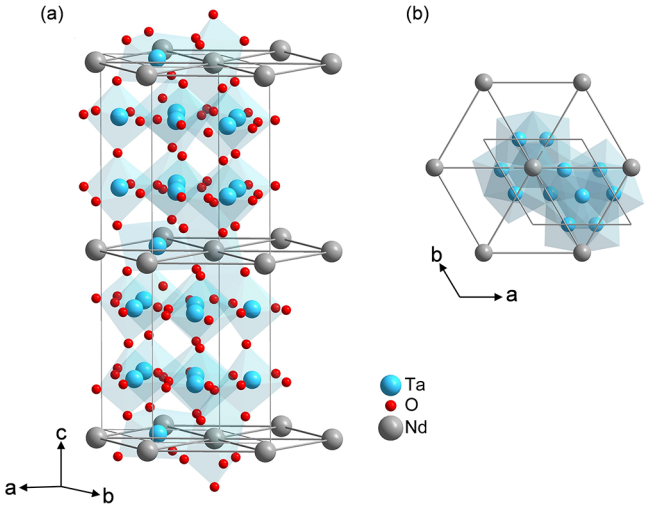


Figure 7. (a) Crystal structure of $RETa_7O_{19}$ (here RE = Nd). (b) View from the *c*-axis as projected onto the *ab*-plane, showing the perfect triangular lattice within the magnetic layers, separated by two nonmagnetic layers of TaO_7 polyhedra. The oxygen atoms in (b) are omitted for clarity.

purification method, ensuring no significant impact on the study.

3.2. Single-Crystal Growth. The optimized single-crystal growth procedure employed in this study resulted in purple transparent $NdTa_7O_{19}$ crystals of predominantly hexagonal morphologies (Figure 3a), which measured up to 3.5 mm in lateral size and up to 2 mm in thickness.

The orientation of the crystals[1−4,12]—with hexagonal planes being parallel to the *ab* plane and perpendicular to the *c*-crystallographic direction (Figure 3a)—was confirmed by Laue X-ray diffraction (Figure 3b).

The optimization of the temperature profile for $NdTa_7O_{19}$ flux growth identified the dwell temperature and the slow cooling rate as pivotal parameters (Figure 4). The optimal dwell temperature was determined to be 1100 °C. While previous studies[2,4] reported higher dwell temperatures of 1150 and 1200 °C, in the present study, these elevated temperatures resulted in increased flux volatility, which led to the formation of numerous nucleation sites and, consequently, smaller single crystals (see Supporting Information, Figure S2 for pictures of the resulting crystals). The optimized cooling rate of the first step, which yielded the largest crystal sizes, was 0.5 °C/h. Higher cooling rates of 1 or 2 °C/h resulted in multiple smaller crystals. The dwell time was found to be a less significant parameter; observations indicated that a 48 h dwell time did not result in substantially different crystal sizes compared to a shorter 24 h dwell time.

Other parameters tested during the growth process (displayed in Table 1) included the following: (i) the batch size, (ii) the flux-to-material mass ratio, and (iii) the flux composition.

(i) The optimal batch size was determined to be approximately 1 g. Attempts to increase crystal sizes by doubling or further increasing the mass proved ineffective, resulting only in the formation of multiple smaller crystals.

(ii) The optimal range of flux-to-material mass ratios was found to be between 8:1 and 10:1. Other ratios, including 5:1 and 15:1, were also investigated; however, they did not yield any large single crystals.

(iii) The flux composition also turned out to be a crucial parameter, being the primary factor affecting the crystal morphology, while additionally influencing the crystal size. Experiments with a $K_2Mo_3O_{10}$−B_2O_3 mass ratio of 9:1 resulted in plate-like crystals. An increase of the B_2O_3 content in the $K_2Mo_3O_{10}$−B_2O_3 mass ratio led to increased thicknesses of the crystals, transitioning from plate-like toward isometric morphologies (Supporting Information, Figure S1), which was also observed in previous literature reports.[2−4]

The optimal $K_2Mo_3O_{10}$−B_2O_3 mass ratio of 4:1 yielded predominantly hexagonal crystals of approximately 1 mm thickness. Elongated morphologies, as previously reported in the literature,[2−4] were not observed. Further experiments with higher or lower ratios (Table 1) failed to produce large single crystals (Figure S2). The optimal parameters for $NdTa_7O_{19}$ growth are summarized in Table 3.

Seeding, which plays a crucial role in crystal growth, was also investigated in this study. A small crystal ('seed') obtained from a previous experiment was placed at the bottom of the crucible to hinder multiple nucleation.[32] This method promotes controlled nucleation and facilitates the growth of high-quality single crystals with fewer defects. However, in our case, seeding had minimal impact on crystal size, indicating that it is not a critical factor in these growth processes.

The optimal $NdTa_7O_{19}$ crystal growth conditions were also employed for the growth of $ErTa_7O_{19}$ single crystals, with some optimization of the cooling rates (Table 2). The largest crystals were grown using a cooling rate of 0.8 °C/h, while lower rates of 0.5 and 0.3 °C/h resulted in increased flux volatility, as deduced from the mass loss.

The flux-to-material mass ratios that yielded the largest crystal sizes were 7:1 and 8:1, while the optimal batch size was found to be 0.8−0.9 g. Higher masses resulted in the formation

https://doi.org/10.1021/acs.cgd.5c00624
Cryst. Growth Des. 2025, 25, 4646−4654

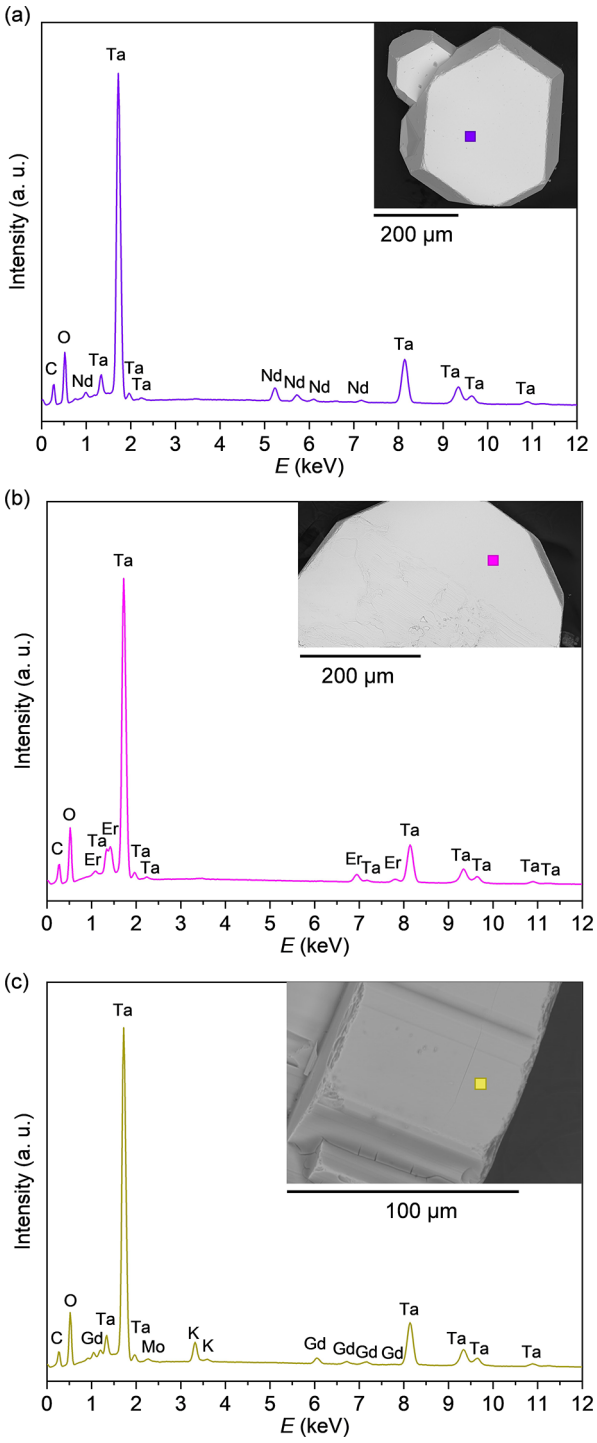


Figure 8. (a) SEM−EDS spectrum of a hexagonal $NdTa_7O_{19}$ crystal, with the analysis area marked by a violet square, confirming stoichiometric Nd, Ta, and O ratios. (b) SEM−EDS spectrum of an $ErTa_7O_{19}$ crystal, with the analysis area indicated by a pink square, confirming Er, Ta, and O. (c) SEM−EDS spectrum of a $GdTa_7O_{19}$ crystal, with the analysis area marked by a yellow square (inset), detecting Gd, Ta, O, and traces of K and Mo (from the residual flux on the surface).

of multiple smaller crystals. The optimal $K_2Mo_3O_{10}$−B_2O_3 mass ratios ranged from 3:1 to 5:1. Similarly as in the $NdTa_7O_{19}$ growth, the crystal morphology was influenced by the flux composition. Specifically, a higher content of B_2O_3 in the $K_2Mo_3O_{10}$−B_2O_3 flux resulted in decreased lateral sizes of the crystals and increased thicknesses. The optimal growth parameters are summarized in Table 4.

Pink $ErTa_7O_{19}$ crystals exhibited predominantly hexagonal morphologies (Figure 5a) with lateral sizes of up to 2.5 mm and thicknesses of up to 0.5 mm. The orientation of $ErTa_7O_{19}$ crystals (Figure 5b) was confirmed by X-ray Laue diffraction (Figure 5c).

For $GdTa_7O_{19}$ single-crystal growth, the optimal $NdTa_7O_{19}$ growth conditions were employed, as listed in Table 3. Similar to the other two representatives of the series, yellow $GdTa_7O_{19}$ single crystals exhibited pseudohexagonal morphologies with lateral sizes up to 4 mm and thicknesses up to 0.5 mm (Figure 6a−c).

3.3. Chemical Analysis. The grown single crystals of $NdTa_7O_{19}$, $ErTa_7O_{19}$, and $GdTa_7O_{19}$ were analyzed by PXRD and SCXRD. All structural information can be found in the Supporting Information, Tables S1−S6. All the structures were solved and refined in the $P\bar{6}c2$ space group.[29] Initially, the $P6_3/mcm$ space group was identified for $CeTa_7O_{19}$ and the $RETa_7O_{19}$ series.[33] However, a year later, the same author reported a preference for the $P\bar{6}c2$ space group.[34]

The RE ions form a perfect triangular lattice (side view: Figure 7a, top view: Figure 7b), where each RE ion is coordinated by eight oxygen ions, forming distorted REO_8 polyhedra that share edges with neighboring TaO_6 octahedra. The magnetic layers are separated by two nonmagnetic Ta layers composed of TaO_7 polyhedra.

A systematic decrease in the unit cell volume (Supporting Information, Table S2), the magnetic interlayer distances, and the RE−RE distances is observed from RE = Nd to Er, following the decrease in the ionic radii (Supporting Information, Tables S4−S6).[31] These findings are consistent with the observations on the polycrystalline heptatantalates (see Section 3.1 and Table S1).

The SEM−EDS point analysis was employed for elemental analysis and to identify possible flux inclusions. A representative SEM−EDS point analysis spectrum of a $NdTa_7O_{19}$ crystal, along with the corresponding SEM image of the crystal (Figure 8a), shows peaks of all the constituent elements without any flux components or other impurities. The average atomic percent values obtained from 11 point analyses are 3.7(1) atom% Nd, 26.0(1) atom% Ta, and 70.4(1) atom% O, perfectly corresponding to the theoretical ratio 1:7:19 and thereby confirming the stoichiometry of the sample. A few dark spots observed on the surface correspond to particles of the main flux component, $K_2Mo_3O_{10}$.

The EDS point analyses of $ErTa_7O_{19}$ (Figure 8b) and $GdTa_7O_{19}$ single crystals (Figure 8c) confirm the presence of Er, Gd, Ta, and O. For $ErTa_7O_{19}$, the average elemental composition from 10 point analyses is 3.5(2) atom % Er, 25.8(1) atom % Ta, and 70.4 atom % of O with trace amounts of K, 0.1(1) atom %, and Mo, 0.2(1) atom %, likely from the flux on the surface. The $GdTa_7O_{19}$ crystal shows slightly higher flux residues (Figure 8c) with 7-point analyses yielding 3.5(3) atom % Gd, 21.6(7) atom % Ta, 67.1(3) atom % O, 6.3(4) atom % K, and 1.5(6) atom % Mo.

3.4. Magnetic Properties. The magnetic susceptibility of $NdTa_7O_{19}$ (Figure 9a) shows no signs of magnetic ordering down to 2 K, which suggests a possible dynamical magnetic ground state and is consistent with previous results obtained on polycrystalline $NdTa_7O_{19}$.[5]

When the magnetic field H of 1 kOe is applied parallel ($H \parallel c$) and perpendicular ($H \perp c$) to the c-axis (Figure 9b), a very

https://doi.org/10.1021/acs.cgd.5c00624
Cryst. Growth Des. 2025, 25, 4646−4654

Crystal Growth & Design pubs.acs.org/crystal Article

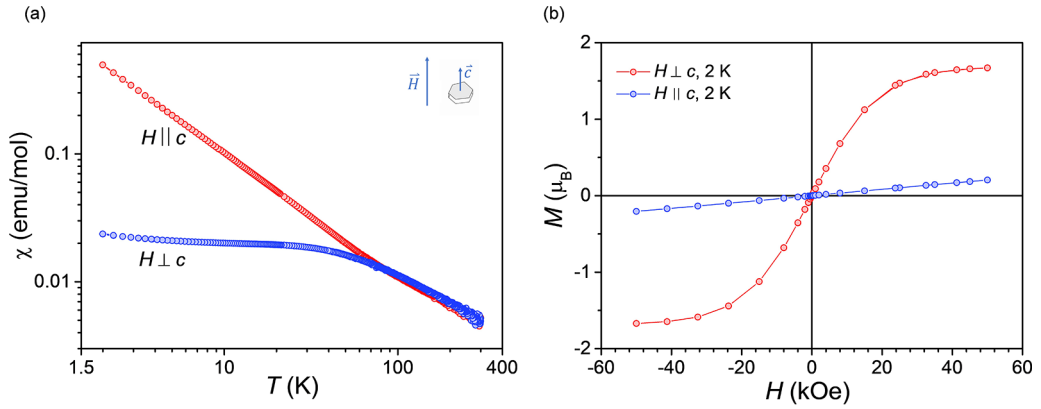


Figure 9. Magnetic susceptibility of a $NdTa_7O_{19}$ single crystal (a) and $M(H)$ curves (b), showing a pronounced difference in the magnetic response in both principal crystallographic directions, $H \parallel c$ and $H \perp c$, which represents direct evidence of the easy-axis magnetic anisotropy.

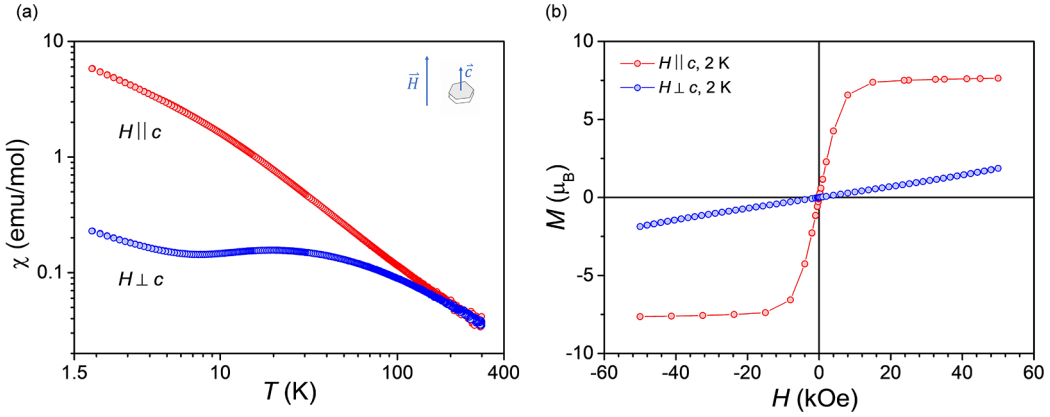


Figure 10. (a) Magnetic susceptibility of a $ErTa_7O_{19}$ single crystal showing a significant difference in the magnetic response in the crystallographic directions $H \parallel c$ and $H \perp c$ as a consequence of large magnetic anisotropy. (b) $M(H)$ curves for $H \perp c$ and $H \parallel c$ at 2 K. A significant magnetic anisotropy is also observed, similar to (a).

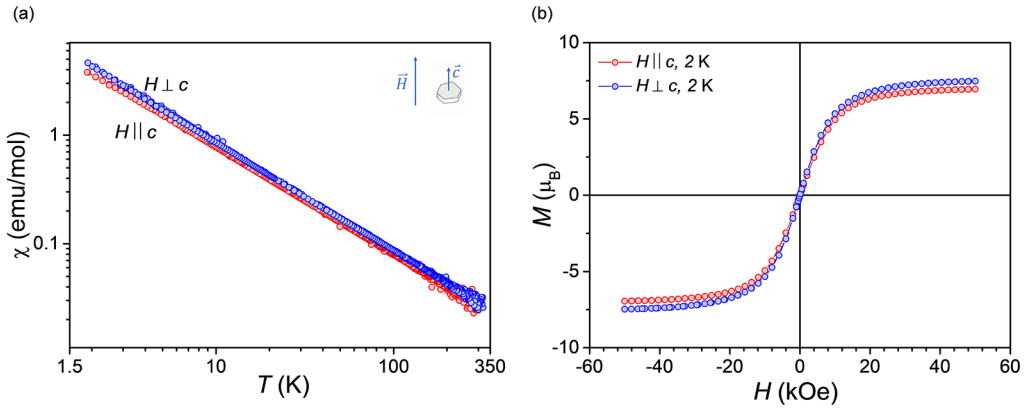


Figure 11. (a) Magnetic susceptibility of a $GdTa_7O_{19}$ single crystal showing the absence of anisotropy, i.e., a nearly identical paramagnetic response for both $H \parallel c$, and $H \perp c$, typical of a paramagnet. (b) $M(H)$ curves for $H \parallel c$ and $H \perp c$ at 2 K, showing a similar magnetic response in both directions, in line with observations in (a).

similar paramagnetic response is observed for both crystallographic directions as the temperature decreases. However, below 90 K, the magnetic responses of the two orientations become increasingly different in size and behavior. This divergence is evident in both the magnetic susceptibility (Figure 9a) and field-dependent magnetization at 2 K, $M(H)$ (Figure 9b), providing clear evidence of easy-axis single-ion magnetic anisotropy, as previously suggested by crystal-electric-field modeling of polycrystalline samples.[5]

A similar magnetic response to $NdTa_7O_{19}$ is also observed in the magnetic susceptibility and field-dependent magnetization of $ErTa_7O_{19}$ (Figure 10a,b). In the external field of 1 kOe, a paramagnetic behavior is observed in both crystallographic directions at high temperatures to about 150 K. However, as the temperature decreases to 2 K, a significant divergence in the magnetic response for both crystallographic directions is observed, $H \parallel c$ and $H \perp c$, again providing evidence of easy-axis-type magnetic anisotropy. The absence of magnetic

https://doi.org/10.1021/acs.cgd.5c00624
Cryst. Growth Des. 2025, 25, 4646−4654

ordering down to 2 K suggests a similar dynamic magnetic ground state as previously observed for $NdTa_7O_{19}$.[5]

The magnetic response of $GdTa_7O_{19}$ to a field of 1 kOe (Figure 11a) is substantially different from those of the previous two representatives of the $RETa_7O_{19}$ series and corresponds to that of an isotropic paramagnet. The results of susceptibility and field-dependent magnetization (Figure 11b) are very similar for both crystallographic directions, showing the absence of anisotropy in the magnetism of this compound. This isotropic magnetic behavior is consistent with findings from a recent study,[35] which reported rare-earth dependent magnetic properties for six polycrystalline $RETa_7O_{19}$ compounds RE = Pr, Sm, Eu, Gd, Dy, and Ho.

4. CONCLUSIONS

High-quality single crystals of $NdTa_7O_{19}$, the first Ising quantum spin liquid candidate on a triangular lattice, were successfully grown using the $K_2Mo_3O_{10}$–B_2O_3 flux. With lateral sizes up to 3.5 mm, thicknesses up to 2 mm, and hexagonal, plate-like morphologies, these crystals are the largest reported to date.

To maximize the yield and reduce the formation of secondary neodymium phases, the crystals were grown from polycrystalline $NdTa_7O_{19}$, obtained by optimizing a previously reported solid-state method.[24] This optimized flux method was extended to grow large, high-quality single crystals of two additional compounds in the series, $ErTa_7O_{19}$ and $GdTa_7O_{19}$.

A substantial easy-axis magnetic anisotropy in $NdTa_7O_{19}$ was observed in its magnetic susceptibility at low temperatures down to 2 K, providing clear proof of the anisotropy indicated by earlier modeling of the crystal electric field in the polycrystalline sample.[5] Similarly, $ErTa_7O_{19}$ also exhibited a pronounced magnetic anisotropy of the same type. No evidence of magnetic ordering is found down to 2 K, suggesting a possible exotic magnetic ground state for this representative. In contrast, $GdTa_7O_{19}$ showed a paramagnetic behavior, in agreement with findings from polycrystalline samples.[35]

The obtained high-quality single crystals will allow new insight into the exciting magnetism of these frustrated magnets. More detailed and *q*-resolved investigations of the magnetic ground state, magnetic correlations, and excitations are now possible. Furthermore, the flux method holds the potential for successful growth of additional rare-earth heptatantalates in the series.

■ ASSOCIATED CONTENT

Supporting Information

The Supporting Information is available free of charge at https://pubs.acs.org/doi/10.1021/acs.cgd.5c00624.

> Summary of SCXRD data, data collection and structure refinement details; structural parameters derived from Rietveld refinement fits of polycrystalline $NdTa_7O_{19}$, $ErTa_7O_{19}$ and $GdTa_7O_{19}$ laboratory PXRD data; and additional images of $NdTa_7O_{19}$ single crystals (PDF)

Accession Codes

Deposition Numbers 2407250–2407252 contain the supplementary crystallographic data for this paper. These data can be obtained free of charge via the joint Cambridge Crystallographic Data Centre (CCDC) and Fachinformationszentrum Karlsruhe Access Structures service.

■ AUTHOR INFORMATION

Corresponding Author

Mirela Dragomir − *Jožef Stefan Institute, 1000 Ljubljana, Slovenia; Jožef Stefan International Postgraduate School, 1000 Ljubljana, Slovenia;* orcid.org/0000-0002-4910-253X; Email: mirela.dragomir@ijs.si

Authors

Lia Šibav − *Jožef Stefan Institute, 1000 Ljubljana, Slovenia; Jožef Stefan International Postgraduate School, 1000 Ljubljana, Slovenia*

Matic Lozinšek − *Jožef Stefan Institute, 1000 Ljubljana, Slovenia; Jožef Stefan International Postgraduate School, 1000 Ljubljana, Slovenia;* orcid.org/0000-0002-1864-4248

Zvonko Jagličić − *Faculty of Civil and Geodetic Engineering, University of Ljubljana, 1000 Ljubljana, Slovenia; Institute of Mathematics, Physics and Mechanics, 1000 Ljubljana, Slovenia*

Tina Arh − *Jožef Stefan Institute, 1000 Ljubljana, Slovenia; Faculty of Mathematics and Physics, University of Ljubljana, 1000 Ljubljana, Slovenia;* orcid.org/0000-0003-4468-1832

Panchanana Khuntia − *Department of Physics and Quantum Centre of Excellence for Diamond and Emergent Materials, Indian Institute of Technology Madras, 600036 Chennai, India*

Andrej Zorko − *Jožef Stefan Institute, 1000 Ljubljana, Slovenia; Faculty of Mathematics and Physics, University of Ljubljana, 1000 Ljubljana, Slovenia*

Complete contact information is available at: https://pubs.acs.org/10.1021/acs.cgd.5c00624

Funding

This work was supported by the Slovenian Research and Innovation Agency (Young Researcher's program, Program P2−0105, P2−0348, P1-0125, and Project No. J1−50008), the Marie Skłodowska-Curie Individual Fellowship (Grant No. 101031415), and the European Research Council Starting Grant (Grant No. 950625) under the European Union's Horizon 2020 Research and Innovation Program.

Notes

The authors declare no competing financial interest.

■ ACKNOWLEDGMENTS

Assoc. Prof. Mario Novak and Dr. Mirta Herak from University of Zagreb are acknowledged for Laue diffraction measurements and valuable discussions.

■ REFERENCES

(1) Cavalli, E.; Leonyuk, L. I.; Leonyuk, N. I. Flux growth and optical spectra of $NdTa_7O_{19}$ crystals. *J. Cryst. Growth* **2001**, *224*, 67−73.

(2) Leonyuk, N. I.; Cavalli, E.; Calestani, G.; Kuleshov, N. V.; Dawes, J. M.; Maltsev, V. V.; Koporulina, E. V.; Volkova, E. A.; Pilipenko, O. V. A new generation of nonlinear optical and laser crystals of rare earth borate and tantalate families. *J. Optoelectron. Adv. Mater.* **2007**, *9*, 1206−1214.

(3) Volkova, E. A.; Maltsev, V. V.; Leonyuk, N. I. Phase formation in neodymium tantalate based flux systems. *J. Optoelectron. Adv. Mater.* **2003**, *5*, 881−885.

(4) Volkova, E. A.; Alekseev, A. V.; Leonyuk, N. I. Crystallization of neodymium heptatantalate from molybdate based flux systems. *J. Cryst. Growth* **2004**, *270*, 145−149.
(5) Arh, T.; Sana, B.; Pregelj, M.; Khuntia, P.; Jagličić, Z.; Le, M. D.; Biswas, P. K.; Manuel, P.; Mangin-Thro, L.; Ozarowski, A.; Zorko, A. The Ising triangular-lattice antiferromagnet neodymium heptatantalate as a quantum spin liquid candidate. *Nat. Mater.* **2022**, *21*, 416−422.
(6) Anderson, P. W. Resonating valence bonds: A new kind of insulator. *Mater. Res. Bull.* **1973**, *8*, 153−160.
(7) Wannier, G. H. Antiferromagnetism. The Triangular Ising Net. *Phys. Rev.* **1950**, *79*, 357−364.
(8) Khatua, J.; Sana, B.; Zorko, A.; Gomilšek, M.; Sethupathi, K.; Rao, M. S. R.; Baenitz, M.; Schmidt, B.; Khuntia, P. Experimental signatures of quantum and topological states in frustrated magnetism. *Phys. Rep.* **2023**, *1041*, 1−60.
(9) Shekhar, C.; Borrmann, H.; Felser, C.; Kreiner, G.; Manna, K.; Schmidt, M.; Sü*β*, V. Single crystal growth for topology and beyond. *Max Planck Institute for Chemical Physics of Solids*, 2018, Retrieved from https://www.cpfs.mpg.de/ssc/crystal-growth.pdf.
(10) Berry, T.; Ng, N.; McQueen, T. M. Tools and Tricks for Single Crystal Growth. *Chem. Mater.* **2024**, *36*, 4929−4944.
(11) Sales, B. Introduction to the Synthesis of Quantum Materials: Some General Guidelines and A Few Tricks. In *Fundamentals of Quantum Materials, A Practical Guide to Synthesis and Exploration*; Paglione, J. P., Butch, N. P., Rodriguez, E. E., Eds.; World Scientific Publishing Co. Pte. Ltd.: Singapore, 2021; pp 1−7.
(12) Cavalli, E.; Volkova, E.; Calestani, G.; Leonyuk, N. I. Structural and morphological characterization of flux grown YTa_7O_{19}, Nd:YTa_7O_{19}, Nd:$LaTa_7O_{19}$ and $NdTa_7O_{19}$ crystals. *Mater. Res. Bull.* **2009**, *44*, 1127−1131.
(13) Bugaris, D. E.; zur Loye, H.-C. Materials Discovery by Flux Crystal Growth: Quaternary and Higher Order Oxides. *Angew. Chem., Int. Ed.* **2012**, *51*, 3780−3811.
(14) Leonyuk, N. I.; Leonyuk, L. I. Growth and characterization of $RM_3(BO_3)_4$ crystals. *Prog. Cryst. Growth Charact.* **1995**, *31*, 179−278.
(15) Leonyuk, N. I. Recent developments in the growth and characterization of $RM_3(BO_3)_4$ crystals for science and modern applications. *Prog. Cryst. Growth Charact.* **1995**, *31*, 279−312.
(16) Nekrasova, L. V.; Leonyuk, N. I. $YbAl_3(BO_3)_4$ and $YAl_3(BO_3)_4$ crystallization from $K_2Mo_3O_{10}$-based high-temperature solutions: Phase relationships and solubility diagrams. *J. Cryst. Growth* **2008**, *311*, 67.
(17) Wang, G.; Gallagher, H. G.; Han, T. P. J.; Henderson, B. Crystal growth and optical characterisation of Cr^{3+}-doped $YAl_3(BO_3)_4$. *J. Cryst. Growth* **1995**, *153*, 169−174.
(18) Tu, C.; Huang, Y.; Qiu, M.; Luo, Z. The growth of Nd^{3+}: $Gd_xY_{1-x}Al_3(BO_3)_4$ crystals. *J. Cryst. Growth* **1999**, *206*, 249−251.
(19) Zhu, Z. -J.; Li, J.; Wu, B.; You, Z. Study of Pure and Yb^{3+}-doped $GdAl_3(BO_3)_4$ Crystal. *J. Synth. Cryst.* **2008**, *37*, 507−513.
(20) Zhu, Z.; Li, J.; Alain, B.; Jia, G.; You, Z.; Lu, X.; Wu, B.; Tu, C. Growth, spectroscopic and laser properties of Yb^{3+}-doped $GdAl_3(BO_3)_4$ crystal: a candidate for infrared laser crystal. *Appl. Phys. B Laser Opt.* **2006**, *86*, 71−75.
(21) Tu, C.; Qiu, M.; Huang, Y.; Chen, X.; Jiang, A.; Luo, Z. The study of a self-frequency-doubling laser crystal Nd^{3+}: $GdAl_3(BO_3)_4$. *J. Cryst. Growth* **2000**, *208*, 487−492.
(22) Jia, G.; Tu, C.; Li, J.; Zhu, Z.; You, Z.; Wang, Y.; Wu, B. Spectroscopic Growth and Thermal and Spectral Properties of a New Nonlinear Optical Crystal $TmAl_3(BO_3)_4$. *Cryst. Growth Des.* **2005**, *5*, 949−952.
(23) Novikov, M. P.; Nerkasov, A. N.; Gorbachev, P. N. About zonality of kularite. *Exp. Geosci.* **2021**, *27*, 92−94.
(24) Chrétien, M. M.; Bodiot, D. Étude sur les oxydes doubles de niobium, ou de tantale, et d'un lanthanide; différenciations respectives de ces éléments. *Compt. Rend* **1966**, *C263/2*, 882−884.
(25) Toby, B. H.; Von Dreele, R. B. GSAS-II: the genesis of a modern open-source all purpose crystallography software package. *J. Appl. Crystallogr.* **2013**, *46*, 544−549.
(26) Rigaku, O. D. *CrysAlisPro*; Rigaku Corporation: Wrocław: Poland, 2024.
(27) Sheldrick, G. M. Crystal Structure Refinement with SHELXL. *Acta Crystallogr., Sect. C: Cryst. Struct. Commun.* **2015**, *71*, 3−8.
(28) Dolomanov, O. V.; Bourhis, L. J.; Gildea, R. J.; Howard, J. A. K.; Puschmann, H. OLEX2: A Complete Structure Solution, Refinement and Analysis Program. *J. Appl. Crystallogr.* **2009**, *42*, 339−341.
(29) Schaffrath, U.; Gruehn, R. Zum chemischen Transport von Verbindungen des Typs $LnTa_7O_{19}$(Ln = La-Nd) mit einer Bemerkung zur Strukturverfeinerung von NdTa7O19. *Z. Anorg. Allg. Chem.* **1990**, *588*, 43−54.
(30) Zuev, M. G.; Politova, E. D.; Stefanovich, S. Y. X-ray-diffraction characteristics, nonlinear-optical and electrophysical properties of RTa_7O_{19} tantalates where (R = La-Tm, Y). *Zh. Neorg. Khim.* **1991**, *36*, 1540−1543.
(31) Shannon, R. D. Revised Effective Ionic Radii and Systematic Studies of Interatomic Distances in Halides and Chalcogenides. *Acta Crystallogr.* **1976**, *A32*, 751−767.
(32) Tachibana, M. *Beginner's Guide to Flux Crystal Growth*; Springer Japan KK: Tokyo, 2017.
(33) Gatehouse, B. M. Crystal structures of some niobium and tantalum oxides. Part V. $CeTa_7O_{19}$. *J. Solid State Chem.* **1979**, *27*, 209−213.
(34) Johnson, A. W. S.; Gatehouse, B. M. Convergent-Beam Electron Diffraction Symmetry from a Disordered Structure (Ce, Ta)Ta_6O_{19}. *Acta Crystallogr.* **1980**, *B36*, 523−526.
(35) Wang, L.; Ouyang, Z.; Xiao, T.; Li, Z.; Tian, Z. Synthesis, structure and magnetism of RTa_7O_{19} (R = Pr, Sm, Eu, Gd, Dy, Ho) with perfect triangular lattice. *J. Alloys Compd.* **2023**, *937*, 168390−168397.

https://doi.org/10.1021/acs.cgd.5c00624
Cryst. Growth Des. 2025, 25, 4646−4654

Supporting Information

Optimized flux single-crystal growth of the quantum spin liquid candidate $NdTa_7O_{19}$ and other rare-earth heptatantalates, $ErTa_7O_{19}$ and $GdTa_7O_{19}$

Lia Šibav[1,2], Matic Lozinšek[1,2], Zvonko Jagličić[3,4], Tina Arh[1,5], Panchanana Khuntia[6,7], Andrej Zorko[1,5] and Mirela Dragomir[1,2*]

[1]*Jožef Stefan Institute, Jamova cesta 39, 1000 Ljubljana, Slovenia*

[2]*Jožef Stefan International Postgraduate School, Jamova cesta 39, 1000 Ljubljana, Slovenia*

[3]*Faculty of Civil and Geodetic Engineering, University of Ljubljana, Jamova cesta 2, 1000 Ljubljana, Slovenia*

[4]*Institute of Mathematics, Physics and Mechanics, Jadranska cesta 19, 1000 Ljubljana, Slovenia*

[5]*Faculty of Mathematics and Physics, University of Ljubljana, 1000 Ljubljana, Slovenia*

[6]*Department of Physics, Indian Institute of Technology Madras, 600036 Chennai, India*

[7]*Quantum Centre of Excellence for Diamond and Emergent Materials, Indian Institute of Technology Madras, 600036 Chennai, India*

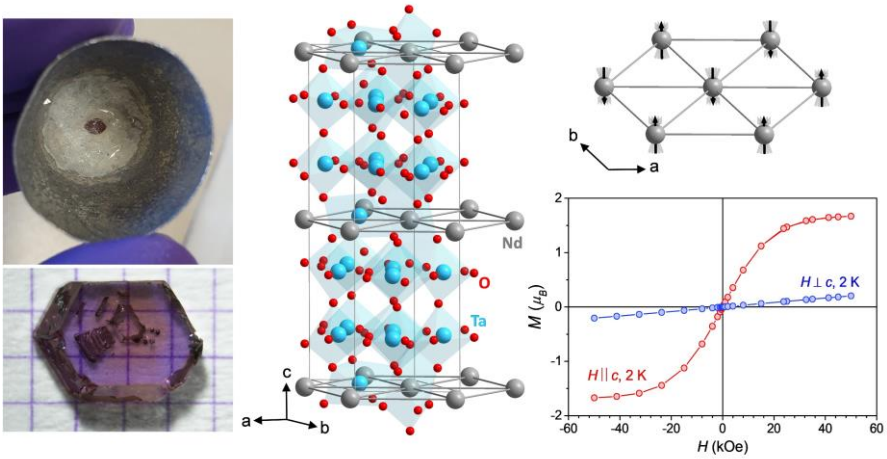


Table S1. A summary of Rietveld refinement analysis results on the polycrystalline $NdTa_7O_{19}$, $ErTa_7O_{19}$ and $GdTa_7O_{19}$. The data was collected at room-temperature using Cu Kα radiation (λ = 1.5406 Å).

	$NdTa_7O_{19}$	**$GdTa_7O_{19}$**	**$ErTa_7O_{19}$**
Space group	$P\bar{6}c2$	$P\bar{6}c2$	$P\bar{6}c2$
***a*, *b* (Å)**	6.22277(3)	6.21188(4)	6.20178(3)
***c* (Å)**	19.93551(5)	19.89306(8)	19.85693(5)
***V* (Å^3)**	668.536(4)	664.780(6)	661.418(5)
***R_{wp}* (%)**	3.30	3.45	3.43
***R_{exp}* (%)**	2.32	2.35	2.30
***S* (R_{wp}/R_{exp})**	1.42	1.47	1.49
Atom	*x*/*y*/*z* *U*iso	*x*/*y*/*z* *U*iso	*x*/*y*/*z* *U*iso
R	0.66667/0.33333/0 0.0036(6)	0.66667/0.33333/0 0.0188(16)	0.66667/0.33333/0 0.0057(7)
Ta1	0.33333/0.66667/0 0.0050	0.33333/0.66667/0 0.0023(8)	0.33333/0.66667/0 0.0050
Ta2	0.63963(25)/0.63957(30)/0.15589(1) 0.00318(19)	0.64033(26)/0.63831(29)/0.15576(2) 0.00666(26)	0.64019(28)/0.63793(31)/0.15550(1) 0.00353(22)
O1	0.7391(28)/0.977(5)/0.15315(19) 0.0133(15)	0.7372(27)/0.973(5)/0.15324(26) 0.0171(21)	0.7305(28)/0.958(5)/0.15198(20) 0.0190(18)
O2	0.5688(8)/0.6210(10)/0.05810(18) 0.0050	0.5690(14)/0.6051(15)/0.05869(23) 0.0127(23)	0.5747(12)/0.6121(14)/0.05700(19) 0.0104(18)
O3	0.6216(14)/0.5838(14)/0.2500 0.0050	0.6240(23)/0.5889(25)/0.2500 0.015(4)	0.6187(16)/0.5803(15)/0.2500 0.0050
O4	0.33333/0.66667/0.1639(5) 0.0050	0.33333/0.66667/0.1658(5) 0.0050	0.33333/0.66667/0.1639(5) 0.0050
O5	0.66667/0.33333/0.1301(6) 0.0068(31)	0.66667/0.33333/0.1263(8) 0.022(5)	0.66667/0.33333/0.1271(6) 0.006(3)

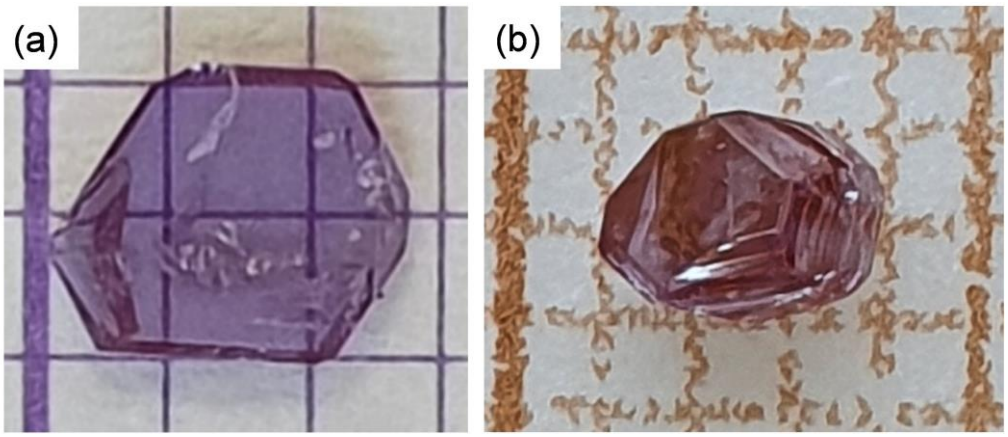


Figure S1. Single crystals of $NdTa_7O_{19}$. (**a**) A plate-like crystal grown with a 9:1 $K_2Mo_3O_{10}/B_2O_3$ flux mass ratio. (**b**) A crystal with larger thickness, grown with a 4:1 $K_2Mo_3O_{10}/B_2O_3$ mass ratio.

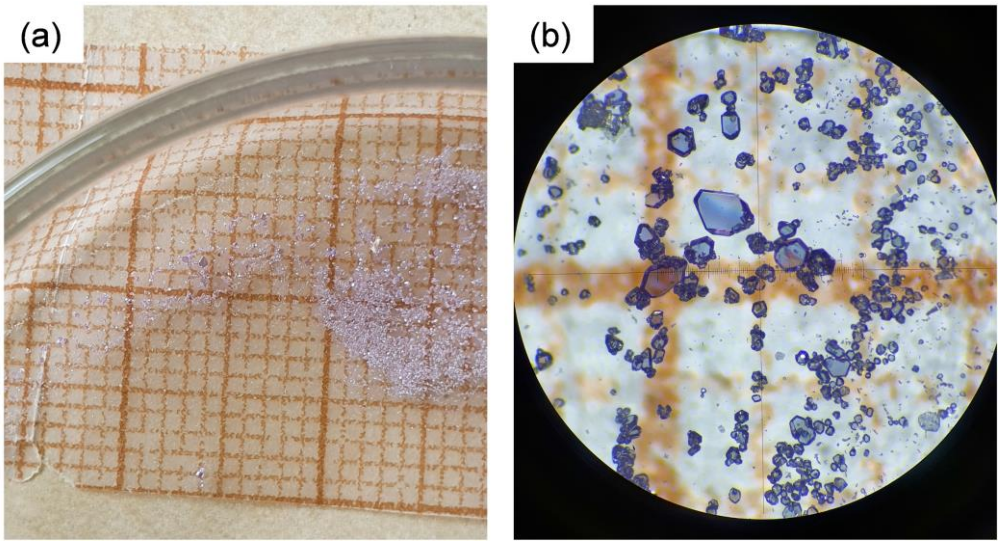


Figure S2. Representative images of small $NdTa_7O_{19}$ single crystals, grown in the process of optimization that did not yield crystals of significant size: (**a**) displayed on a millimeter grid for size reference and (**b**) magnified optical microscope image on a millimeter grid, emphasizing the crystal morphology.

Table S2. Summary of single-crystal X-ray diffraction crystal data, data collection and structure refinement details for the crystal structures of $NdTa_7O_{19}$, $GdTa_7O_{19}$, and $ErTa_7O_{19}$.

Compound	**$NdTa_7O_{19}$**	**$GdTa_7O_{19}$**	**$ErTa_7O_{19}$**
M_r	1714.89	1727.90	1737.91
Crystal system	hexagonal	hexagonal	hexagonal
Space group	$P\bar{6}c2$	$P\bar{6}c2$	$P\bar{6}c2$
a [Å]	6.21494(10)	6.20871(10)	6.19718(6)
b [Å]	6.21494(10)	6.20871(10)	6.19718(6)
c [Å]	19.9382(4)	19.9087(4)	19.8613(2)
α [°]	90	90	90
β [°]	90	90	90
γ [°]	120	120	120
V [Å^3]	666.94(3)	664.62(3)	660.581(16)
Z	2	2	2
ρ_{calc} [g/cm^3]	8.539	8.634	8.737
Crystal size [mm^3]	0.090 × 0.077 × 0.050	0.208 × 0.135 × 0.029	0.160 × 0.139 × 0.077
Radiation type	Ag Kα	Ag Kα	Ag Kα
λ [Å]	0.56087	0.56087	0.56087
T [K]	100	100	100
μ [mm^{-1}]	32.772	33.482	34.408
$F(000)$	1446	1454	1462
θ_{max} [°]	32.324	32.245	30.653
Index ranges	$-11 \le h \le 11$ $-9 \le k \le 11$ $-36 \le l \le 35$	$-11 \le h \le 10$ $-11 \le k \le 9$ $-35 \le l \le 37$	$-11 \le h \le 10$ $-11 \le k \le 11$ $-36 \le l \le 35$
Reflections collected	13542	16495	40463
Independent reflections	1471	1525	1431
Reflections with [$I > 2\sigma(I)$]	1432	1462	1374
R_{int}	0.0473	0.0573	0.1374
R_{sigma}	0.0231	0.0249	0.0335
Data/restraints/parameters	1471/0/45	1525/6/45	1431/6/46
S	1.174	1.158	1.201
R_1, wR_2 [$I > 2\sigma(I)$]	0.0198, 0.0447	0.0196, 0.0408	0.0237, 0.0524
R_1, wR_2 [all data]	0.0208, 0.0450	0.0213, 0.0415	0.0254, 0.0545
$\Delta\rho_{min}$, $\Delta\rho_{max}$ [eÅ^{-3}]	−1.528, 2.546	−2.330, 2.121	−3.816, 3.301
Flack x	−0.010(15)	0.007(14)	BASF = 0.63(4) [a]

[a] refined as an inversion twin

CSD Deposition Numbers 2407250 (for $NaTa_7O_{19}$), 2407251 (for $GdTa_7O_{19}$), and 2407252 (for $ErTa_7O_{19}$) contain the supplementary crystallographic data for this paper. These data can be obtained free of charge from FIZ Karlsruhe via www.ccdc.cam.ac.uk/structures.

The anisotropic thermal ellipsoid of atom O1 in crystal structures of $GdTa_7O_{19}$, and $ErTa_7O_{19}$ was restrained with ISOR 0.001 to prevent it from becoming non-positive definite.

Note: the checkCIF reports show two alerts level A for the $NaTa_7O_{19}$ and four for $ErTa_7O_{19}$. These are caused by large residual electron density minima and maxima. Full single-crystal datasets have been measured on several different crystals of each compound. The aforementioned issues were observed consistently in all analyzed single crystals. Typically, the problems were exacerbated in larger crystals, which indicates possible absorption effects.

Table S3. Fractional atomic coordinates and equivalent isotropic displacement parameters ($Å^2$) for the crystal structures of $NdTa_7O_{19}$, $GdTa_7O_{19}$, and $ErTa_7O_{19}$.

	Atom	*x*	*y*	*z*	U_{eq}
$NdTa_7O_{19}$	Ta1	0.3333	0.6667	0	0.00588(14)
	Ta2	0.63907(7)	0.63951(6)	0.15602(2)	0.00639(6)
	Nd1	0.6667	0.3333	0	0.0069(2)
	O1	0.7512(10)	1.0016(18)	0.15375(15)	0.0086(5)
	O2	0.5709(8)	0.6222(7)	0.0568(2)	0.0072(6)
	O3	0.6246(10)	0.5791(11)	0.25	0.0068(9)
	O4	0.3333	0.6667	0.1681(4)	0.0064(9)
	O5	0.6667	0.3333	0.1314(4)	0.0072(11)
$GdTa_7O_{19}$	Ta1	0.3333	0.6667	0	0.00573(14)
	Ta2	0.63905(7)	0.63898(6)	0.15581(2)	0.00605(5)
	Gd1	0.6667	0.3333	0	0.0069(2)
	O1	0.7529(10)	1.0037(18)	0.15345(15)	0.0080(5)
	O2	0.5718(7)	0.6194(6)	0.05606(19)	0.0064(6)
	O3	0.6243(9)	0.5791(10)	0.25	0.0081(9)
	O4	0.3333	0.6667	0.1677(4)	0.0073(9)
	O5	0.6667	0.3333	0.1310(4)	0.0091(11)
$ErTa_7O_{19}$	Ta1	0.3333	0.6667	0	0.0091(2)
	Ta2	0.63927(9)	0.63829(8)	0.15558(2)	0.00901(8)
	Er1	0.6667	0.3333	0	0.0097(2)
	O1	0.7524(14)	1.002(3)	0.15316(19)	0.0113(6)
	O2	0.5723(9)	0.6156(8)	0.0553(3)	0.0103(9)
	O3	0.6226(11)	0.5786(13)	0.25	0.0100(12)
	O4	0.3333	0.6667	0.1663(5)	0.0088(12)
	O5	0.6667	0.3333	0.1311(5)	0.0106(14)

Table S4. Selected bond distances (Å) and angles (°) for the crystal structure of $NdTa_7O_{19}$.

Bond distance (Å)			
Nd–O2	2.435(4)	Ta2–O1	1.996(10)
Nd–O5	2.620(8)	Ta2–O2	2.014(4)
Ta1–O2	1.987(4)	Ta2–O3	1.9043(10)
Ta2–O1^{vi}	1.982(10)	Ta2–O4	2.0044(11)
Ta2–O1^{iv}	2.422(4)	Ta2–O5	2.054(2)
Angle (°)			
O2^{v}–Ta1–O2	166.2(2)	O3–Ta2–O5	94.0(3)
O2^{ii}–Ta1–O2	99.9(2)	O4–Ta2–O1^{iv}	64.8(2)
O2^{iii}–Ta1–O2	90.72(17)	O4–Ta2–O2	86.5(2)
O2^{i}–Ta1–O2	80.4(2)	O4–Ta–O5	128.94(5)
O1–Ta2–O1^{iv}	137.8(3)	O5–Ta2–O1^{iv}	64.5(2)
O1^{vi}–Ta2–O1	85.0(2)	O2^{i}–Nd1–O2	63.53(19)
O1^{vi}–Ta2–O1^{iv}	137.1(3)	O2^{ix}–Nd1–O2	100.62(19)
O1–Ta2–O2	89.05(14)	O2^{viii}–Nd1–O2	155.57(19)
O1^{vi}–Ta2–O2	99.58(15)	O2^{vii}–Nd1–O2	100.11(11)
O1–Ta2–O4	73.68(12)	O2–Nd1–O5^{i}	117.72(9)
O1^{vi}–Ta2–O4	157.75(14)	O2–Nd1–O5	62.28(9)
O1^{vi}–Ta2–O5	73.30(13)	Ta2^{x}–O1–Ta2^{iii}	102.8(3)
O1–Ta2–O5	153.57(16)	Ta2–O1–Ta2iii	102.1(3)
O2–Ta2–O1^{iv}	81.41(14)	Ta2^{x}–O1–Ta2	154.9(2)
O2–Ta2–O5	80.1(2)	Ta2^{xi}–O3–Ta2	159.5(3)
O3–Ta2–O1	101.53(19)	Ta2^{iv}–O4–Ta2	118.58(9)
O3–Ta2–O1^{iv}	84.01(18)	Ta2^{vii}–O5–Ta2	114.49(16)
O3–Ta2–O1^{vi}	91.41(18)	Ta2–O2–Nd1	111.94(16)
O3–Ta2–O2	165.4(2)	Ta2–O5–Nd1	103.8(2)
O3–Ta2–O4	86.9(3)	Ta1–O2–Nd1	108.06(17)

Symmetry codes: (i) $-y+1, -x+1, -z$; (ii) $x, x-y+1, -z$; (iii) $-y+1, x-y+1, z$; (iv) $-x+y, -x+1, z$; (v) $-x+y, y, -z$; (vi) $-y+2, x-y+1, z$; (vii) $-y+1, x-y, z$; (viii) $x, x-y, -z$; (ix) $-x+y+1, y, -z$; (x) $-x+y+1, -x+2, z$; (xi) $x, y, -z+1/2$.

Table S5. Selected bond distances (Å) and angles (°) for the crystal structure of $GdTa_7O_{19}$.

Bond distance (Å)			
Gd1–O2	2.407(3)	Ta2–O1	2.007(9)
Gd1–O5	2.607(8)	Ta2–O2	2.020(4)
Ta1–O2	1.990(3)	Ta2–O3	1.9049(10)
Ta2–O1^{viii}	1.968(9)	Ta2–O4	2.0036(11)
Ta2–O1^{vi}	2.422(3)	Ta2–O5	2.050(2)
Angle (°)			
O2^{iii}–Ta1–O2	99.7(2)	O3–Ta2–O5	94.3(3)
O2^{i}–Ta1–O2	91.60(15)	O4–Ta2–O1^{iv}	65.1(2)
O2^{v}–Ta1–O2	165.3(2)	O4–Ta2–O2	86.8(2)
O2–Ta1–O2^{ii}	78.9(2)	O4–Ta2–O5	129.00(5)
O1^{vi}–Ta2–O1^{iv}	137.0(3)	O5–Ta2–O1^{iv}	64.4(2)
O1^{vi}–Ta2–O1	84.67(18)	O2^{ix}–Gd1–O2	100.22(11)
O1–Ta2–O1^{iv}	138.2(3)	O2^{ii}–Gd1–O2	63.36(17)
O1^{vi}–Ta2–O2	99.24(14)	O2^{viii}–Gd1–O2	155.53(18)
O1–Ta2–O2	89.45(13)	O2^{vii}–Gd1–O2	100.56(18)
O1^{vi}–Ta2–O4	157.58(12)	O2–Gd1–O5^{ii}	117.63(9)
O4–Ta2–O1	73.76(11)	O2–Gd1–O5	62.37(8)
O1^{vi}–Ta2–O5	73.42(11)	Ta2^{xi}–O1–Ta2^{i}	102.9(3)
O1–Ta2–O5	153.33(16)	Ta2^{xi}–O1–Ta2	155.15(17)
O2–Ta2–O1^{iv}	81.29(13)	Ta2–O1–Ta2^{i}	101.7(3)
O2–Ta2–O5	79.5(2)	Ta2–O3–Ta2^{xi}	159.7(3)
O3–Ta2–O1	101.46(18)	Ta2^{i}–O4–Ta2	118.63(9)
O3–Ta2–O1^{iv}	84.05(18)	Ta2^{x}–O5–Ta2	114.37(17)
O3–Ta2–O1^{vi}	91.57(17)	Ta2–O5–Gd1	104.0(2)
O3–Ta2–O2	165.3(2)	Ta2–O2–Gd1	112.37(14)
O3–Ta2–O4	86.9(3)	Ta1–O2–Gd1	108.87(16)

Symmetry codes: (i) $-y+1, x-y+1, z$; (ii) $-y+1, -x+1, -z$; (iii) $x, x-y+1, -z$; (iv) $-x+y, -x+1, z$; (v) $-x+y, y, -z$; (vi) $-y+2, x-y+1, z$; (vii) $-x+y+1, y, -z$; (viii) $x, x-y, -z$; (ix) $-x+y+1, -x+1, z$; (x) $-y+1, x-y, z$; (x) $-x+y+1, -x+2, z$; (xi) $x, y, -z+1/2$.

Table S6. Selected bond distances (Å) and angles (°) for the crystal structure of $ErTa_7O_{19}$.

Bond distance (Å)			
Er1–O2	2.373(4)	Ta2–O1	1.997(13)
Er1–O5	2.603(10)	Ta2–O2	2.024(5)
Ta1–O2	1.993(5)	Ta2–O3	1.9042(12)
Ta2–O1^{viii}	1.972(13)	Ta2–O4	2.0011(13)
Ta2–O1^{iv}	2.419(4)	Ta2–O5	2.039(3)
Angle (°)			
O2–Ta1–O2^{ii}	92.5(2)	O3–Ta2–O5	94.4(3)
O2–Ta1–O2^{i}	99.9(3)	O4–Ta2–O1^{ii}	64.8(3)
O2–Ta1–O2^{iii}	77.3(3)	O4–Ta2–O2	86.6(3)
O2–Ta1–O2^{v}	164.2(3)	O4–Ta2–O5	128.94(7)
O1–Ta2–O1^{ii}	137.7(4)	O5–Ta2–O1^{ii}	64.7(3)
O1^{vi}–Ta2–O1	84.4(2)	O2^{viii}–Er1–O2	100.7(2)
O1^{vi}–Ta2–O1^{ii}	137.7(4)	O2^{vii}–Er1–O2	155.4(2)
O1^{vi}–Ta2–O2	99.00(18)	O2–Er1–O2^{iii}	63.2(2)
O1–Ta2–O2	89.93(16)	O2^{ix}–Er1–O2	100.27(15)
O1^{vi}–Ta2–O4	157.35(16)	O2^{iii}–Er1–O5	117.59(12)
O1–Ta2–O4	73.58(15)	O2–Er1–O5	62.41(12)
O1–Ta2–O5	153.5(2)	Ta2^{x}–O1–Ta2	155.4(2)
O1^{vi}–Ta2–O5	73.71(15)	Ta2^{x}–O1–Ta2^{iv}	102.2(4)
O2–Ta2–O1^{ii}	81.00(17)	Ta2–O1–Ta2^{iv}	102.2(4)
O2–Ta2–O5	79.1(3)	Ta2–O3–Ta2^{xi}	160.0(4)
O3–Ta2–O1^{ii}	84.0(2)	Ta2^{ii}–O4–Ta2	118.88(10)
O3–Ta2–O1	101.4(2)	Ta2^{ix}–O5–Ta2	114.5(2)
O3–Ta2–O1^{vi}	92.0(2)	Ta2–O2–Er1	112.90(19)
O3–Ta2–O2	165.0(3)	Ta2–O5–Er1	103.8(3)
O3–Ta2–O4	87.2(3)	Ta1–O2–Er1	109.8(2)

Symmetry codes: (i) $x, x-y+1, -z$; (ii) $-x+y, -x+1, z$; (iii) $-y+1, -x+1, -z$; (iv) $-y+1, x-y+1, z$; (v) $-x+y, y, -z$; (vi) $-y+2, x-y+1, z$; (vii) $x, x-y, -z$; (viii) $-x+y+1, y, -z$; (ix) $-y+1, x-y, z$; (x) $-x+y+1, -x+2, z$; (xi) $x, y, -z+1/2$.

4.3 Synthesis and Crystal Growth of Other $RETa_7O_{19}$ Candidates, $DyTa_7O_{19}$ and $YbTa_7O_{19}$

The $RETa_7O_{19}$ single-crystal growth studies included two additional candidates, $DyTa_7O_{19}$ and $YbTa_7O_{19}$, aiming to obtain crystals and investigating their magnetic behavior.

Experimental

Solid-state synthesis and single-crystal growth of $DyTa_7O_{19}$ and $YbTa_7O_{19}$, as well as their characterization by PXRD, single-crystal XRD and magnetic susceptibility were performed following the procedures described in Chapter 4.2 for the first three rare-earth heptatantalates studied (RE = Nd, Gd, Er), with a sole difference of 0.005° 2θ step in PXRD for the $YbTa_7O_{19}$ sample. In solid-state synthesis, Dy_2O_3 (Thermo Scientific, 99.9%), and Yb_2O_3 (Thermo Scientific, 99.9%) were used as precursors of the rare-earth elements, and both oxides were pre-annealed at 1000 °C for 24 hours prior to synthesis. Single-crystal growth of $DyTa_7O_{19}$ and $YbTa_7O_{19}$ was performed using the same conditions as for $GdTa_7O_{19}$, with a single slow cooling rate of 0.8 °C/h applied for $DyTa_7O_{19}$.

Results and discussion

Two additional representatives of the rare-earth heptatantalate series, $DyTa_7O_{19}$ and $YbTa_7O_{19}$, were successfully prepared via conventional solid-state synthesis. Rietveld refinement analysis of the powder X-ray diffraction data (Figure 4.1, Table 4.1) confirms that both compounds adopt the same crystal structure and space group ($P\bar{6}c2$) as the previously discussed members of the series (Section 4.1), indicating structural robustness of the framework across the rare-earth substitution.

A clear systematic decrease of the unit cell parameters is observed with decreasing rare-earth ionic radius (Figure 4.2). The unit cell volume decreases from 668.536(4) $Å^3$ for $NdTa_7O_{19}$ to 662.870(7) $Å^3$ for $DyTa_7O_{19}$ and 660.146(15) $Å^3$ for $YbTa_7O_{19}$, corresponding to volume reductions of 0.9% and 1.3%, respectively. This behavior is consistent with the lanthanoid contraction and confirms that the structural framework responds predictably to chemical pressure introduced by smaller R^{3+} ions.

Importantly, this lattice contraction directly affects the magnetic sublattice. Both intralayer and interlayer RE–RE distances decrease progressively from Nd to Dy and Yb (from 6.2228(1) Å/9.9678(1) Å to 6.1979(1) Å/9.9218(1) Å), which is expected to modify magnetic exchange pathways and interaction strengths. Thus, rare-earth substitution provides an effective route to tune the magnetic lattice geometry without altering the overall structural topology.

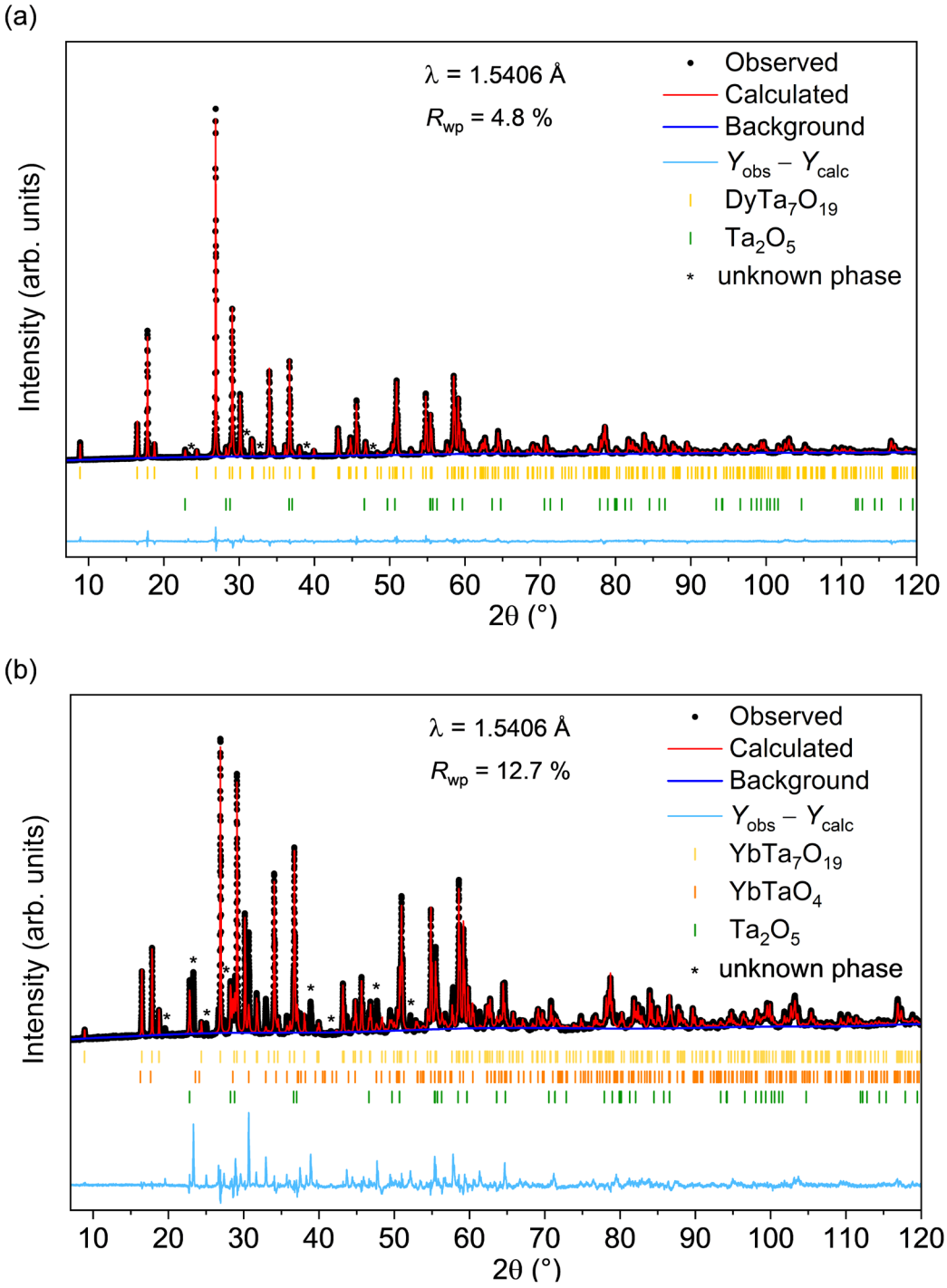


Figure 4.1: Rietveld refinement profiles of laboratory PXRD data (Cu Kα, $T = 293$ K) of a) $DyTa_7O_{19}$ and b) $YbTa_7O_{19}$. The Bragg 2θ positions are marked as bars below each diffractogram.

Table 4.1: Results of Rietveld refinement analysis on polycrystalline $DyTa_7O_{19}$ and $YbTa_7O_{19}$, performed on room-temperature data collected using Cu Kα radiation (λ = 1.5406 Å).

	$DyTa_7O_{19}$	**$YbTa_7O_{19}$**
Space group	$P\bar{6}c2$	$P\bar{6}c2$
***a*, *b* (Å)**	6.2061(1)	6.1979(1)
***c* (Å)**	19.8728(1)	19.8436(27)
***V* (Å^3)**	662.870(7)	660.146(15)
R_{wp} (%)	4.58	12.69
R_{exp} (%)	3.07	4.57
S (R_{wp}/R_{exp})	1.49	2.78
Atom	$x/y/z$ U_{iso} (Å^2)	$x/y/z$ U_{iso} (Å^2)
R	0.66667/0.33333/0 0.0050	0.66667/0.33333/0 0.0188(16)
Ta1	0.33330/0.66670/0.00000 0.0075(8)	0.33330/0.66670/0.00000 0.0080(16)
Ta2	0.6401(4)/0.6398(5)/0.155539(22) 0.0053(3)	0.6354(5)/0.6429(6)/0.15556(5) 0.0050
O1	0.7549(27)/0.995(5)/0.15286(24) 0.0050	0.726(5)/0.941(8)/0.1558(7) 0.006(7)
O2	0.6092(29)/0.5882(26)/0.05724(24) 0.0143(26)	0.592(4)/0.549(4)/0.0600(7) 0.0050
O3	0.622(6)/0.587(6)/0.25000 0.026(5)	0.637(6)/0.531(5)/0.25000 0.0050
O4	0.33330/0.66670/0.1636(6) 0.0050	0.33330/0.66670/0.1652(15) 0.0050
O5	0.66670/0.33330/0.1264(8) 0.019(6)	0.66670/0.33330/0.1003(19) 0.005

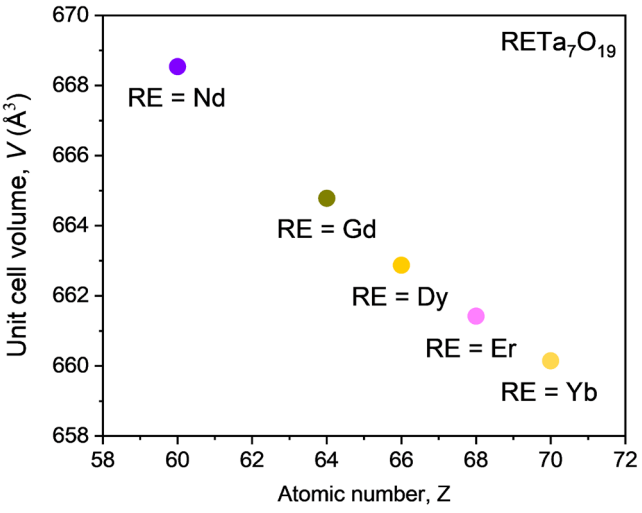


Figure 4.2: The comparison of unit cell volume of five polycrystalline $RETa_7O_{19}$ samples from Chapter 4, as determined by Rietveld refinement analysis.

In PXRD patterns of $DyTa_7O_{19}$ and $YbTa_7O_{19}$ samples, additional phases were observed in addition to the main phase. In case of $DyTa_7O_{19}$, the main phase was at 96.2(1) wt%, while the unreacted Ta_2O_5 constituted 3.8(1) wt% of the sample. A few low-intensity peaks remained unidentified. Consequently, at least one additional phase was excluded from the Rietveld refinement analysis. The amount of this phase, or of multiple unidentified phases, is estimated to approximately 1–2 wt%.

In case of $YbTa_7O_{19}$, a considerable presence of secondary phases is detected in PXRD, in agreement with ref. [64]. Rietveld refinement analysis revealed a significantly smaller amount of the main phase compared to the other series candidates, yielding only 74.0(2) wt% of $YbTa_7O_{19}$. The two additional identified phases comprised 11.2(2) wt% of $YbTaO_4$ and 14.8(2) wt% of unreacted Ta_2O_5, while additional unidentified phases were excluded from the refinement. Performing additional solid-state synthesis cycles at higher temperatures to facilitate the formation of the main phase led to $YbTa_7O_{19}$ decomposition. The significantly lower phase purity observed for this series representative after solid-state synthesis suggests that this compound is more difficult to stabilize under the employed synthesis conditions compared to the other rare-earth heptatantalates. This may be related to the small ionic radius of Yb^{3+}—the smallest within the rare-earth series studied—which can influence the relative stability of competing Yb–Ta–O phases, thereby shifting the phase formation equilibrium.

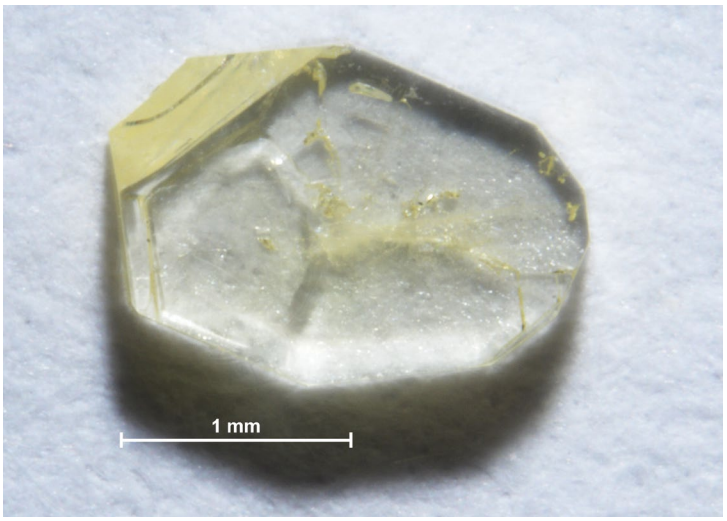


Figure 4.3: A $DyTa_7O_{19}$ single crystal, obtained in this work.

Performing single-crystal growth of $DyTa_7O_{19}$ using the optimal growth conditions for $GdTa_7O_{19}$ as listed in Section 4.2 at a cooling rate of 0.8 °C/h successfully yielded yellow $DyTa_7O_{19}$ single crystals, which exhibited hexagonal morphologies and lateral sizes up to 1.5 mm, with heights reaching up to 1 mm (Figure 4.3). The main, $DyTa_7O_{19}$, phase, was confirmed by both powder and single-crystal XRD.

In contrast, the $YbTa_7O_{19}$ growth experiments did not result in the formation of the targeted phase. Instead, multiple small single crystals formed, which were identified as secondary phases, such as $Yb_3Ta_{17}O_{47}$ and $YbTaO_4$, using single-crystal XRD. Additional crystalline phases were also present but could not be identified. This outcome is consistent with the reduced phase stability of $YbTa_7O_{19}$ already indicated by the results of solid-state synthesis.

The magnetic behavior of $DyTa_7O_{19}$ (Figure 4.4 a,b) resembles that of $NdTa_7O_{19}$ and $ErTa_7O_{19}$, described in Section 4.2. Under an applied field of 1 kOe, magnetic

susceptibility shows a paramagnetic behavior from high temperatures down to about 200 K in both principal crystallographic directions, $H \parallel c$ and $H \perp c$. With further temperature decrease, the magnetic response starts to differ, exhibiting a pronounced divergence in both crystallographic directions at low temperatures. This suggests a significant magnetic anisotropy of easy-axis type also for this candidate. The absence of any signs magnetic ordering down to 2 K indicates a possible dynamical magnetic ground state similar to that observed for $NdTa_7O_{19}$.

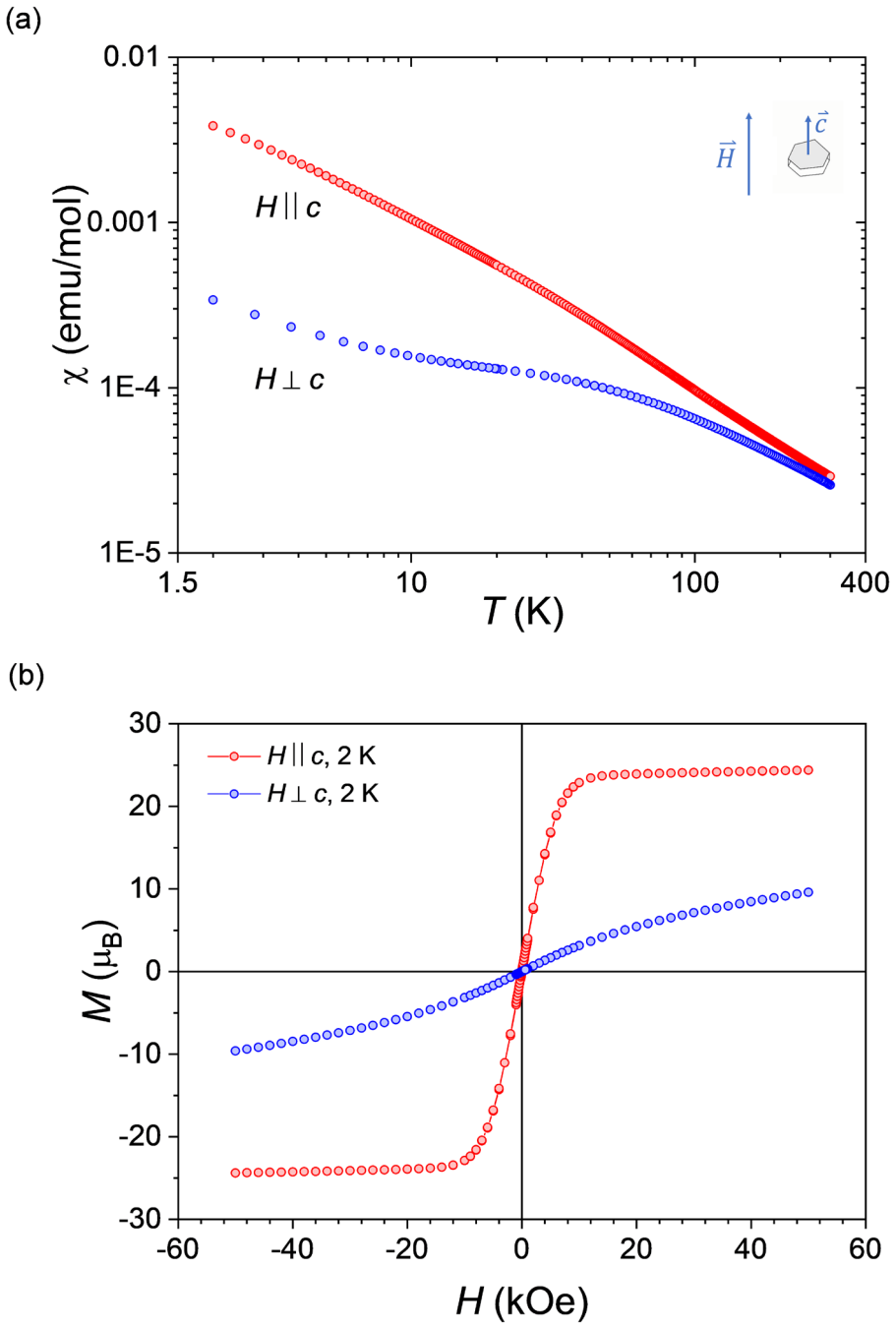


Figure 4.4: a) Magnetic susceptibility of a $DyTa_7O_{19}$ single crystal, exhibiting a significant difference in the magnetic response in both principal crystallographic directions, $H \parallel c$ and $H \perp c$, resulting from large magnetic anisotropy. b) $M(H)$ curves for $H \perp c$ and $H \parallel c$ at 2 K, showing a pronounced magnetic anisotropy, similar to (a).

4.4 Conclusions

Motivated by the recent identification of $NdTa_7O_{19}$ as the first perfect triangular-lattice quantum spin liquid candidate with dominant Ising-like correlations, the second part of this dissertation highlights the importance of access to single crystals in QSL research for a precise determination of the ground state. This Chapter presents a procedure to grow single crystals of four rare-earth heptatantalates, $RETa_7O_{19}$ (RE = Nd, Er, Gd and Dy), which represent a family of perfect triangular lattice antiferromagnets. This study establishes a robust protocol to obtain high-quality single crystals of $NdTa_7O_{19}$, employing $K_2Mo_3O_{10}$–B_2O_3 as the main flux. The resulting purple $NdTa_7O_{19}$ crystals exhibit hexagonal, plate-like morphologies. Reaching lateral sizes up to 3.5 mm and thicknesses up to 2 mm, the crystals are the largest reported to date. The morphologies are primarily governed by the $K_2Mo_3O_{10}$–B_2O_3 mass ratio, with higher B_2O_3 content promoting increased thicknesses of the crystals, transitioning from plate-like towards isometric morphologies. The chemical composition was confirmed by powder and single-crystal X-ray diffraction, complemented by scanning electron microscopy equipped with energy-dispersive X-ray spectroscopy. Low-temperature magnetic susceptibility and ESR spectroscopy confirm a pronounced easy-axis magnetic anisotropy, supporting earlier crystal electric field modelling in the polycrystalline sample [32], yet identifying a considerably more pronounced anisotropy for single crystals. The crystals are suitable for further measurements, allowing a precise magnetic characterization of a disordered magnetic ground state for this compound.

The crystal growth protocol for $NdTa_7O_{19}$ was adapted to three other rare-earth heptatantalate representatives – $ErTa_7O_{19}$, $GdTa_7O_{19}$ and $DyTa_7O_{19}$. Similar magnetic anisotropy to that of $NdTa_7O_{19}$ is observed in $ErTa_7O_{19}$ and $DyTa_7O_{19}$, suggesting a potentially similar exotic magnetic ground state. Conversely, $GdTa_7O_{19}$ exhibits paramagnetism, corroborating earlier studies on polycrystalline samples [63]. The availability of high-quality single crystals of these additional heptatantalates enables comprehensive, momentum-resolved investigations of the magnetic ground state, correlations, and excitations, and demonstrate that the flux method could be extended to the growth of further rare-earth heptatantalates within the series.

Chapter 5

Conclusions and Outlook

This dissertation investigated the synthesis, crystal growth and magnetic properties of two-dimensional magnets, focusing on chemical doping of the first experimental realization of the Shastry-Sutherland model, $SrCu_2(BO_3)_2$, and flux single-crystal growth of four rare-earth heptatantalates, $RETa_7O_{19}$, which include the quantum spin liquid candidate $NdTa_7O_{19}$.

To date, efforts to tune the magnetic exchange couplings in $SrCu_2(BO_3)_2$, aimed at realizing exotic quantum states, have focused predominantly on applying pressure, while the alternative strategy of chemical doping has received only limited attention. The first part of the present work advances this direction by providing a comprehensive and systematic investigation of chemical doping of $SrCu_2(BO_3)_2$, examining the effects of both A- and B-site substitutions on the structure and magnetism of this system. A-site charge doping is explored through electron doping with La and hole doping with Na, while B-site magnetic dilution is examined via Mg-doping. By extending the range of nominal concentrations to higher values than previously studied, this work provides additional analyses of the doped system, including a detailed structural analysis through Rietveld refinement and SEM-EDS, as well as ESR spectroscopy as a local magnetic probe, supporting Hypothesis 3. Furthermore, the flux method is identified as a viable alternative to the optical floating-zone technique for the growth of La-doped $SrCu_2(BO_3)_2$, supporting Hypotheses 5 and 6.

The overall findings indicate that Aims 1–3 were achieved and demonstrate the following:

1. All the studied dopants induce small yet systematic changes in the unit cell parameters as a function of nominal doping, supporting Hypothesis 4. However, the effective doping levels are lower than the nominal values. The highest effective doping is achieved with Mg, while the incorporation of Na into the parent structure appears to occur only in trace amounts. This corroborates previous observations that achieving effective doping in $SrCu_2(BO_3)_2$ is inherently challenging. Within the scope of the present synthesis approaches, the system is thus found to accommodate only limited substitutions.
2. Although the effective doping remains below the nominal levels, it is sufficient to induce pronounced changes in the magnetic properties, which increase systematically with nominal doping. Firstly, both La- and Mg-doping induce a pronounced reduction of the effective spin gap, with Mg achieving nearly twice the gap reduction compared to La. Secondly, both charge doping and magnetic dilution give rise to spin-dimer breaking, which is most pronounced in the case of Mg. Considering both the spin gap decrease and dimer breaking, it can be concluded

that both A- and B-site doping locally disrupt the dimer lattice, with direct substitution of Cu ions being more effective than charge doping. Finally, for La- and Mg-doping, correlations between dimer-free Cu^{2+} ions, resulting from dimer breaking, develop at low temperatures. For La-doping, these correlations showcase antiferromagnetic nature, whereas for Mg-doping, they are reflected by the emergence of the $\mu_0 H'_{C0} \approx 9$ T anomaly and the suppression of the pseudo-1/8 plateau for Mg-doping. These findings support Hypothesis 2.

3. Experimental verification of theoretical predictions, anticipating a potential superconductivity for A-site charge doping and quantum spin liquid state for magnetic dilution of $SrCu_2(BO_3)_2$, demonstrates that, within the employed methods and nominal concentrations, these states are not realized, rejecting Hypothesis 1. This could be attributed to the small amount of dopant incorporated in the parent structure.

In conclusion, to enhance effective dopant incorporation, systematic optimization of optical floating-zone growth is proposed, followed by in-depth structural and compositional analyses to determine effective dopant incorporation. The nominal doping levels would range from lower values (up to $x = 0.05$) to higher concentrations than previously reported (e.g., $x = 0.10$ and 0.15).

In addition, to extend the doping studies employing methods discussed in the dissertation, the following investigations could be pursued:

- Investigating the local atomic environment and oxidation state of Cu^{2+} using X-ray absorption spectroscopy (XAS).
- Examining the effect of A-site charge doping on the magnetization plateaus of $SrCu_2(BO_3)_2$ at high magnetic fields.

The second part of the dissertation focuses on single-crystal growth of four rare-earth heptatantalates, $RETa_7O_{19}$ (RE = Nd, Er, Gd, and Dy). This work enabled the growth of high-quality single crystals of $NdTa_7O_{19}$, the first Ising-spin QSL candidate realized on a perfect triangular lattice, with the largest crystal dimensions reported to date. This supports Hypotheses 7 and 8. The crystals now allow a precise magnetic characterization of this distinct type of QSL candidate, which was previously limited to polycrystalline samples. This provides new insights into the exotic magnetism of triangular antiferromagnet QSL candidates.

The optimized growth protocol allowed obtaining crystals of three additional representatives of the heptatantalate family, with $ErTa_7O_{19}$ and $GdTa_7O_{19}$ reported for the first time. This partially supports Hypothesis 9 with the exception of the Yb member. An advantage of the approach lies in its simplicity, as it does not require complex or specialized equipment. Both $ErTa_7O_{19}$ and $DyTa_7O_{19}$ exhibit magnetic anisotropies similar to that of $NdTa_7O_{19}$, suggesting a potentially similar exotic ground state for these compounds. Further investigations on the Er candidate revealed a distinct magnetic phenomenon, highlighting the importance of these materials to extend the field of two-dimensional magnets, and supporting Hypothesis 10.

These results indicate that Aims 4–7 were achieved to different extents, with Aim 4 fully achieved and Aims 5–7 largely achieved. With respect to Aim 5, the $ErTa_7O_{19}$, $GdTa_7O_{19}$ and $DyTa_7O_{19}$ single crystals were successfully grown, whereas $YbTa_7O_{19}$ could not be obtained. The magnetic ground state of the $RETa_7O_{19}$ candidates, addressed in Aim 6, was determined only for $GdTa_7O_{19}$, which remains paramagnetic down to 2K. For the remaining compounds, the present work established a pronounced magnetic anisotropy. A full determination of the ground state was completed for $ErTa_7O_{19}$ in subsequent collaborative studies, which also advanced its investigation for $NdTa_7O_{19}$. The phase

relationships in the RE_2O_3—Ta_2O_5 systems, addressed in Aim 7, were explored through solid-state synthesis of the $RETa_7O_{19}$ precursors, revealing the formation of competing secondary phases such as $RETaO_4$. The obtained results provide relevant insight into phase relations under the employed synthesis conditions; however, the aim itself is inherently broad and extends beyond the scope of the present study.

The use of more advanced growth techniques, such as the optical floating-zone method or chemical vapor transport, is proposed as a future approach to obtain high-quality crystals of potentially larger dimensions.

In summary, the work presented in this dissertation advances the field of two-dimensional magnetism along two independent directions. The systematic doping study of the Shastry–Sutherland compound $SrCu_2(BO_3)_2$ clarifies the intrinsic limitations and effects of chemical substitution on the parent lattice at both the local and bulk scales, while the growth and characterization of rare-earth heptatantalates establish a new platform for exploring perfect triangular lattice physics and exotic low-temperature magnetic behavior, including potential quantum-spin-liquid states. The successful substitution of La for Sr in $SrCu_2(BO_3)_2$ demonstrates that flux growth can enable dopant incorporation where standard solid-state synthesis fails.

While it has long been predicted that perturbations of spin-dimer lattices could induce novel magnetic states, experimental demonstrations are scarce. The present study bridges this gap by showing that spin-dimer breaking, achieved in this case by chemical doping in $SrCu_2(BO_3)_2$, leads to the emergence of new correlations and in-gap states, demonstrating these effects in a real material. The optimized flux method to grow $NdTa_7O_{19}$ enables detailed studies of properties and spin dynamics of this novel type of quantum spin liquids. Application of this protocol to Er, Gd, and Dy heptatantalate members demonstrates its potential to grow additional representatives of the series, opening the door to systematic investigation of potentially novel and exotic magnetic states as well as the study of the influence of different cations on spin dynamics. Furthermore, the initial studies of $ErTa_7O_{19}$ ground state have already revealed a novel magnetic phenomenon in the field of low-dimensional magnets.

Appendix A

$NdTa_7O_{19}$ Single Crystal Anisotropy Determined by ESR

For a detailed determination of $NdTa_7O_{19}$ anisotropy, a $NdTa_7O_{19}$ single crystal was analyzed by X-band ESR spectroscopy. The angular dependence of the g-factor and ESR linewidth were measured at 10 K in the direction $B \,||\, c$ (Figure A.1 a,b).

Experimental

The continuous wave (CW) electron spin resonance spectroscopy measurements were performed using a conventional Bruker E500 spectrometer, operating in the X-band at the resonant frequency ν_L of 9.40 GHz. The spectrometer was equipped with a Varian TEM104 dual cavity resonator, an Oxford Instruments ESR900 cryostat and an Oxford Instruments ITC503 temperature controller. A small, mm-sized single crystal was glued to a (type) sample holder, which was placed in a 4 mm Suprasil® quartz ESR tubes (Wilmad). The measurements were conducted at 10 K with the modulation amplitude of 5 G, modulation frequency of 100 kHz, and microwave power of 2 mW.

Results

To determine the anisotropy and extract g-factor eigenvalues, $g_{||}$ and $g_{\perp}$, the angular dependence of the g-factor was fitted using Eq. (A.1):

$$g = \sqrt{g_{||}^2 cos^2(\theta - \theta_0) + g_{\perp}^2 sin^2(\theta - \theta_0)}. \tag{A.1}$$

The fit yields $g_{||} = 3.266(6)$ and $g_{\perp} = 0.41(3)$ with an angular offset of $\theta_0 = -4.7(1)$. For comparison, the values extracted from CEF simulation in polycrystalline $NdTa_7O_{19}$, were $g_{||} = 2.49$ and $g_{\perp} = 1.24$ [32]. The values obtained from single-crystal measurements thus reveal a considerably more pronounced anisotropy compared to the polycrystalline sample, highlighting the importance of single crystals for accurate determination of anisotropic properties.

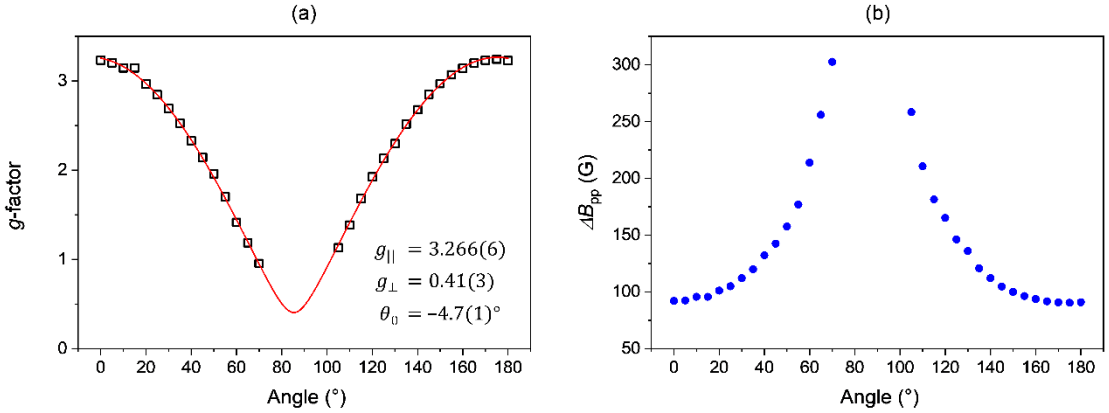


Figure A.1: The angular dependence of a) g-factor and b) ESR linewidth for the $NdTa_7O_{19}$ single crystal, confirming a pronounced anisotropy of this system with a considerable difference in $g_{||}$ and $g_{\perp}$values.

References

[1] S. B. Roy, "A Short History of Magnetism and Magnetic Materials," in *Experimental Techniques in Magnetism and Magnetic Materials*, Cambridge University Press, 2023, pp. 3–12.

[2] J. C. A. R. Needham, *The Shorter Science and Civilization in China*, 3rd Ed., UK: Cambridge Univ. Press., 1986.

[3] S. Blundell, *Magnetism in Condensed Matter*. New York: Oxford University Press Inc., 2001.

[4] J. E. Greedan, "Magnetic Oxides," in *Encyclopedia of Inorganic and Bioinorganic Chemistry*, John Wiley & Sons, Ltd., 2017, pp. 1–45. doi: 10.1002/9781119951438.eibc0116.pub2.

[5] V. Sechovský, "Magnetism in Solids: General Introduction," *Encycl. Mater. Sci. Technol.*, pp. 5018–5032, 2001, doi: 10.1016/b0-08-043152-6/00872-x.

[6] A. Vasiliev, O. Volkova, E. Zvereva, and M. Markina, *Low-Dimensional Magnetism*. Boca Raton, Florida, USA: CRC Press, Taylor & Francis Group, 2019.

[7] A. F. Orchard, *Magnetochemistry*. New York: Oxford University Press Inc., 2003.

[8] L.-P. Regnault, "Bulk Magnetic Materials: Low-dimensional Systems," *Encycl. Mater. Sci. Technol.*, no. October, pp. 856–864, 2001, doi: 10.1016/b0-08-043152-6/00164-9.

[9] L. J. De Jongh, "Introduction to Low-Dimensional Magnetic Systems," in *Magnetic Properties of Layered Transition Metal Compounds*, L. J. De Jongh, Ed. Dordrecht: Kluwer Academic Publishers, 1990, pp. 1–51. doi: 10.1007/978-94-009-1860-3.

[10] G. J. Nilsen, "Synthesis and Physical Properties of Low Dimensional Quantum Magnets," University of Edinburgh, 2010.

[11] C. Broholm, R. J. Cava, S. A. Kivelson, D. G. Nocera, M. R. Norman, and T. Senthil, "Quantum spin liquids," *Science*, vol. 367, no. 6475, 2020, doi: 10.1126/science.aay0668.

[12] C. E. Housecroft and A. G. Sharpe, *Inorganic Chemistry*, Second Ed. Essex, UK: Pearson Education Limited, 2005.

[13] M. Gibertini, M. Koperski, A. F. Morpurgo, and K. S. Novoselov, "Magnetic 2D materials and heterostructures," *Nat. Nanotechnol.*, vol. 14, no. 5, pp. 408–419, 2019, doi: 10.1038/s41565-019-0438-6.

[14] C. Lacroix, P. Mendels, and F. Mila., Eds., *Introduction to Frustrated Magnetism*. Berlin Heidelberg: Springer-Verlag, 2011.

[15] L. Balents, "Spin liquids in frustrated magnets," *Nature*, vol. 464, pp. 199–208, 2010, doi: 10.1038/nature08917.

[16] P. W. Anderson, "Resonating valence bonds: A new kind of insulator?," *Mater. Res. Bull.*, vol. 8, no. 2, pp. 153–160, 1973, doi: 10.1016/0025-5408(73)90167-0.

[17] P. W. Anderson, "The Resonating Valence Bond State in La_2CuO_4 and Superconductivity," *Science*, vol. 235, no. 1, pp. 1196–1198, 1986.

[18] L. E. Smart and E. A. Moore, *Solid State Chemistry: An Introduction*, 3rd Ed. Boca Raton, Florida, USA: CRC Press Taylor & Francis Group, 2005.

[19] J. R. Chamorro, T. M. McQueen, and T. T. Tran, "Chemistry of Quantum Spin Liquids," *Chem. Rev.*, vol. 121, no. 5, pp. 2898–2934, 2021, doi: 10.1021/acs.chemrev.0c00641.

[20] J. Paglione, N. P. Butch, and E. E. Rodriguez, Eds., *Fundamentals of Quantum Materials: A Practical Guide to Synthesis and Exploration*. Singapore: World Scientific Publishing Co. Pte. Ltd., 2020.

[21] M. Tachibana, *Beginner's Guide to Flux Crystal Growth*. Springer Tokyo, 2017. doi: 10.1007/978-4-431-56587-1.

[22] D. E. Bugaris and H. C. Zur Loye, "Materials discovery by flux crystal growth: Quaternary and higher order oxides," *Angew. Chemie - Int. Ed.*, vol. 51, no. 16, pp. 3780–3811, 2012, doi: 10.1002/anie.201102676.

[23] D. Elwell and H. J. Scheel, *Crystal Growth from High-Temperature Solutions*. Academic Press Inc. (London) Ltd, 1975.

[24] J. L. Schmehr and S. D. Wilson, "Active Crystal Growth Techniques for Quantum Materials," *Annu. Rev. Mater. Res.*, vol. 47, no. March, pp. 153–174, 2017, doi: 10.1146/annurev-matsci-070616-124006.

[25] H. A. Dabkowska and A. B. Dabkowski, "Crystal Growth of Oxides by Optical Floating Zone Technique," in *Springer Handbook of Crystal Growth*, G. Dhanaraj, K. Byrappa, V. Prasad, and M. Dudley, Eds. Berlin Heidelberg: Springer-Verlag, 2011, pp. 367–391.

[26] S. Miyahara and K. Ueda, "Exact Dimer Ground State of the Two Dimensional Heisenberg Spin System $SrCu_2(BO_3)_2$," pp. 3701–3704, 1999.

[27] B. Sriram Shastry and B. Sutherland, "Exact ground state of a quantum mechanical antiferromagnet," *Phys. B+C*, vol. 108, no. 1–3, pp. 1069–1070, 1981, doi: 10.1016/0378-4363(81)90838-X.

[28] H. Kageyama *et al.*, "Exact dimer ground state and quantized magnetization plateaus in the two-dimensional spin system $SrCu_2(BO_3)_2$," *Phys. Rev. Lett.*, vol. 82, no. 15, pp. 3168–3171, 1999, doi: 10.1103/PhysRevLett.82.3168.

[29] K. Onizuka, H. Kageyama, and Y. Narumi, "- Stripe Order of Excited Triplets -," vol. 69, no. 4, pp. 1016–1018, 2000.

[30] A. Koga and N. Kawakami, "Quantum Phase Transitions in the Shastry-Sutherland Model for $SrCu_2(BO_3)_2$," pp. 4461–4464, 2000.

[31] B. S. Shastry and B. Kumar, "$SrCu_2(BO_3)_2$: A Unique Mott Hubbard insulator," *Prog. Theor. Phys. Suppl.*, vol. 2, no. 145, pp. 1–16, 2002, doi: 10.1143/ptps.145.1.

[32] T. Arh *et al.*, "The Ising triangular-lattice antiferromagnet neodymium heptatantalate as a quantum spin liquid candidate," *Nat. Mater.*, vol. 21, no. 4, pp. 416–422, 2022, doi: 10.1038/s41563-021-01169-y.

[33] L. Ooi, *Principles of X–ray crystallography*. New York: Oxford University Press Inc., 2010.

[34] J. I. Goldstein *et al.*, *Scanning Electron Microscopy and X-Ray Microanalysis*, 3rd Ed. New York: Springer New York, 2003.

[35] C. P. Poole, *Electron Spin Resonance: A Comprehensive Treatise on Experimental Techniques*, 2nd Ed. Columbia, South Carolina, USA: John Wiley & Sons, Inc., 1983.

[36] R. W. Smith and D. A. Keszler, "Synthesis, structure, and properties of the orthoborate $SrCu_2(BO_3)_2$," *J. Solid State Chem.*, vol. 93, no. 2, pp. 430–435, 1991, doi: 10.1016/0022-4596(91)90316-A.

[37] M. E. Zayed *et al.*, "4-spin plaquette singlet state in the Shastry-Sutherland compound $SrCu_2(BO_3)_2$," *Nat. Phys.*, vol. 13, no. 10, pp. 962–966, 2017, doi: 10.1038/nphys4190.

[38] L. Šibav *et al.*, "Higher-Magnesium-Doping Effects on the Singlet Ground State of the Shastry-Sutherland $SrCu_2(BO_3)_2$," *Inorg. Chem.*, vol. 63, no. 43, pp. 20335–20346, 2024, doi: 10.1021/acs.inorgchem.4c02398.

[39] K. Kodama, J. Yamazaki, M. Takigawa, H. Kageyama, K. Onizuka, and Y. Ueda, "Cu nuclear spin-spin coupling in the dimer singlet state in $SrCu_2(BO_3)_2$," *J. Phys. Condens. Matter*, vol. 14, no. 17, 2002, doi: 10.1088/0953-8984/14/17/101.

[40] G. Liu, J. Luo, N. Wang, and D. Jin, "Doping effects on the two-dimensional spin dimer compound $SrCu_2(BO_3)_2$," *Phys. Rev. B*, vol. 71, no. 1, pp. 014441–014445, 2005, doi: 10.1103/PhysRevB.71.014441.

[41] H. A. Dabkowska *et al.*, "Crystal growth and magnetic behaviour of pure and doped $SrCu_2(^{11}BO_2)_2$," *J. Cryst. Growth*, vol. 306, no. 1, pp. 123–128, 2007, doi: 10.1016/j.jcrysgro.2007.04.040.

[42] A. A. Aczel *et al.*, "Impurity-induced singlet breaking in $SrCu_2(BO_3)_2$," *Phys. Rev. B*, vol. 76, no. 21, pp. 214427–214432, 2007, doi: 10.1103/PhysRevB.76.214427.

[43] B. H. Toby and R. B. Von Dreele, "GSAS-II : the genesis of a modern open-source all purpose crystallography software package," pp. 544–549, 2013, doi: 10.1107/S0021889813003531.

[44] I. G. Polyakova, "The criterion for the crystallization ability assessment as applied to borate glass powders and monoliths," *Entropy*, vol. 21, no. 10, 2019, doi: 10.3390/e21100994.

[45] A. Zorko, D. Arčon, A. Lappas, and J. Giapintzakis, "Near critical behavior in the two-dimensional spin-gap system $SrCu_2(BO_3)_2$," *Phys. Rev. B*, vol. 65, pp. 0244417–024422, 2001, doi: 10.1103/PhysRevB.65.024417.

[46] A. Zorko, D. Arčon, H. Kageyama, and A. Lappas, "Magnetic Anisotropy of the $SrCu_2(BO_3)_2$ System as Revealed by X-Band ESR," *Appl. Magn. Reson.*, vol. 27, no. 8, pp. 267–278, 2004.

[47] A. Zorko, D. Arčon, C. J. Nuttall, and A. Lappas, "X-band ESR study of the 2D spin-gap system $SrCu_2(BO_3)_2$," in *Journal of Magnetism and Magnetic Materials*, 2004, vol. 272–276, no. 1, pp. 2003–2005. doi: 10.1016/j.jmmm.2003.12.336.

[48] A. Zorko, D. Arčon, H. Van Tol, L. C. Brunel, and H. Kageyama, "X-band ESR determination of Dzyaloshinsky-Moriya interaction in the two-dimensional $SrCu_2(BO_3)_2$ system," *Phys. Rev. B - Condens. Matter Mater. Phys.*, vol. 69, no. 17, pp. 1–8, 2004, doi: 10.1103/PhysRevB.69.174420.

[49] Z. Shi *et al.*, "Emergent bound states and impurity pairs in chemically doped Shastry-Sutherland system," *Nat. Commun.*, vol. 10, no. 1, pp. 1–9, 2019, doi: 10.1038/s41467-019-10410-x.

[50] G. H. Wannier, "The Triangular Ising Net," *Phys. Rev.*, vol. 79, no. 2, pp. 357–364, 1950.

[51] L. Capriotti, A. E. Trumper, and S. Sorella, "Long-range néel order in the triangular heisenberg model," *Phys. Rev. Lett.*, vol. 82, no. 19, pp. 3899–3902, 1999, doi: 10.1103/PhysRevLett.82.3899.

[52] D. Hsieh *et al.*, "Unconventional spin order in the triangular lattice system $NaCrO_2$: A neutron scattering study," *Phys. B Condens. Matter*, vol. 403, no. 5–9, pp. 1341–1343, 2008, doi: 10.1016/j.physb.2007.10.295.

[53] A. Olariu *et al.*, "Spin dynamics in Heisenberg triangular antiferromagnets: A μSR study of $LiCrO_2$," *Phys. Rev. B - Condens. Matter Mater. Phys.*, vol. 79, no. 22, 2009, doi: 10.1103/PhysRevB.79.224401.

[54] Y. Shirata, H. Tanaka, A. Matsuo, and K. Kindo, "Experimental realization of a spin-1/2 triangular-lattice Heisenberg antiferromagnet," *Phys. Rev. Lett.*, vol. 108, no. 5, pp. 1–5, 2012, doi: 10.1103/PhysRevLett.108.057205.

[55] Y. D. Li, X. Wang, and G. Chen, "Anisotropic spin model of strong spin-orbit-coupled triangular antiferromagnets," *Phys. Rev. B*, vol. 94, no. 3, pp. 1–12, 2016, doi: 10.1103/PhysRevB.94.035107.

[56] J. Iaconis, C. Liu, G. B. Halász, and L. Balents, "Spin liquid versus spin orbit coupling on the triangular lattice," *SciPost Phys.*, vol. 4, no. 1, p. 1—23, 2018, doi: 10.21468/SciPostPhys.4.1.003.

[57] Z. Zhu, P. A. Maksimov, S. R. White, and A. L. Chernyshev, "Topography of Spin Liquids on a Triangular Lattice," *Phys. Rev. Lett.*, vol. 120, no. 20, pp. 207203—207207, 2018, doi: 10.1103/PhysRevLett.120.207203.

[58] S. T. Liddle and J. Van Slageren, "Improving f-element single molecule magnets," *Chem. Soc. Rev.*, vol. 44, no. 19, pp. 6655–6669, 2015, doi: 10.1039/c5cs00222b.

[59] E. Cavalli, L. I. Leonyuk, and N. I. Leonyuk, "Flux growth and optical spectra of $NdTa_7O_{19}$ crystals," *J. Cryst. Growth*, vol. 224, no. 1, pp. 67–73, 2001, doi: 10.1016/S0022-0248(01)00670-4.

[60] E. A. Volkova, V. V. Maltsev, and N. I. Leonyuk, "Phase formation in neodymium tantalate based flux systems," *J. Optoelectron. Adv. Mater.*, vol. 5, no. 4, pp. 881–885, 2003.

[61] E. A. Volkova, A. V. Alekseev, and N. I. Leonyuk, "Crystallization of neodymium heptatantalate from molybdate based flux systems," *J. Cryst. Growth*, vol. 270, no. 1–2, pp. 145–149, 2004, doi: 10.1016/j.jcrysgro.2004.06.011.

[62] N. I. Leonyuk *et al.*, "A new generation of nonlinear optical and laser crystals of rare earth borate and tantalate families," *J. Optoelectron. Adv. Mater.*, vol. 9, no. 5, pp. 1206–1214, 2007.

[63] L. Wang, Z. Ouyang, T. Xiao, Z. Li, and Z. Tian, "Synthesis, structure and magnetism of RTa_7O_{19} (R = Pr, Sm, Eu, Gd, Dy, Ho) with perfect triangular lattice," *J. Alloys Compd.*, vol. 937, p. 168390, 2023, doi: 10.1016/j.jallcom.2022.168390.

[64] F. Pan *et al.*, "Structural and magnetic characterization of $CeTa_7O_{19}$ and $YbTa_7O_{19}$ with a two-dimensional pseudospin-1/2 triangular lattice," *Phys. Rev. B*, vol. 110, no. 17, pp. 1–8, 2024, doi: 10.1103/PhysRevB.110.174448.

Bibliography

Publications Related to the Dissertation

Journal Articles

L. Šibav, Ž. Gosar, T. Knaflič, Z. Jagličić, G. King, H. Nojiri, D. Arčon and M. Dragomir, "Higher-Magnesium-Doping Effects on the Singlet Ground State of the Shastry-Sutherland $SrCu_2(BO_3)_2$," *Inorg. Chem.*, vol. 63, no. 43, pp. 20335−20346, 2024, DOI: 10.1021/acs.inorgchem.4c02398.

L. Šibav, M. Lozinšek, Z. Jagličić, T. Arh, P. Khuntia, A. Zorko and M. Dragomir, "Optimized Flux Single-Crystal Growth of the Quantum Spin Liquid Candidate $NdTa_7O_{19}$ and Other Rare-Earth Heptatantalates, $ErTa_7O_{19}$ and $GdTa_7O_{19}$," *Cryst. Growth Des.*, vol. 25, no. 12, pp. 4646−4654, 2025, DOI: 10.1021/acs.cgd.5c00624.

L. Šibav, T. Knaflič, G. King, Z. Jagličić, M. Koblar, K. Yu. Povarov, S. Zvyagin, D. Arčon and M. Dragomir, "Influence of La-doping on the magnetic properties of the two-dimensional spin gapped system $SrCu_2(BO_3)_2$," *Inorg. Chem.*, vol. 65, no. 1, pp. 291−302, 2026, DOI: 10.1021/acs.inorgchem.5c04249.

Published Scientific Conference Contributions – Abstracts (Invited Lecture)

L. Šibav, A. Zorko, M. Dragomir, "Optimization of single-crystal growth of the quantum spin liquid candidate $NdTa_7O_{19}$ by flux method", in *ICCGE20*: International Conference on Crystal Growth and Epitaxy: 30 July – 4 August 2023, Naples, Italy.

Published Scientific Conference Contributions – Abstracts (Contributed Lectures and Poster Presentations)

L. Šibav, M. Dragomir, "Tuning the magnetic and charge ground states of the Shastry-Sutherland compound $SrCu_2(BO_3)_2$ by chemical doping", in *Throughout knowledge towards a green new world: 13th Jožef Stefan International Postgraduate School Students' Conference and 15th Young Researchers' Day of Chemistry, material science, biochemistry and environment (CMBE day),* Ljubljana, Slovenija: Jožef Stefan International Postgraduate School, Jožef Stefan Institute, 2021.

L. Šibav, M. Lozinšek, D. Arčon, M. Dragomir, "Single-crystal growth of doped $SrCu_2(BO_3)_2$", in *Slovenian Chemistry Days 2021, 27th Annual Meeting of the Slovenian Chemical Society*, Portorož, Slovenia: Slovenian Chemical Society, 2021.

L. Šibav, D. Arčon, Z. Jagličić, G. King, M. Koblar, M. Otoničar, M. Dragomir, "Structural and magnetic studies of doped $SrCu_2(BO_3)_2$: from atomic to macroscopic scale", in *EPDIC17*, Šibenik, Croatia, 2022.

L. Šibav, D. Arčon, Z. Jagličić, G. King, M. Dragomir, "Doping effects on the structural and magnetic properties of $SrCu_2(BO_3)_2$", in *The Twenty-eighth Croatian-Slovenian Crystallographic Meeting, CSCM28,* Zagreb, Croatia: Croatian Academy of Sciences and Arts, Croatian Crystallographic Association; Ljubljana, Slovenia: Faculty of Chemistry and Chemical Technology, University of Ljubljana, 2022.

L. Šibav, G. King, Z. Jagličić, M. Koblar, M. Otoničar, D. Arčon, M. Dragomir, "Experimental investigation of magnetic dilution effect on the frustrated quantum antiferromagnet $SrCu_2(BO_3)_2$", in *18th European Conference on Solid State Chemistry*, Prague, Czechia: University of Pardubice, 2023.

L. Šibav, T. Knaflič, Z. Jagličić, G. King, M. Koblar, M. Otoničar, K. Povarov, S. A. Zvyagin, D. Arčon, M. Dragomir, "Effects of La-doping on the ground state of $SrCu_2(BO_3)_2$", in *Slovenian Chemistry Days 2023, 29th Annual Meeting of the Slovenian Chemical Society*, Portorož, Slovenia: Slovenian Chemical Society, 2023.

L. Šibav, M. Dragomir, "Recent advances in synthesis and crystal growth of doped $SrCu_2(BO_3)_2$", in *19th European Conference on Solid State Chemistry*, Málaga, Spain, 2025.

M. Dragomir, L. Šibav, G. King, Z. Jagličić, D. Arčon, "Structure and magnetism of doped-$SrCu_2(BO_3)_2$", in *IUCr 2023: 26th Congress and General Assembly of the International Union of Crystallography*, Melbourne, Australia, 2023.

M. Dragomir, M. Lozinšek, L. Šibav, T. Arh, Z. Jagličić, A. Zorko, "Single crystal growth and structural characterisation of new phases in the binary Er_2O_3–Ta_2O_5 system", in *Slovenian Chemistry Days 2023, 29th Annual Meeting of the Slovenian Chemical Society*, Portorož, Slovenia: Slovenian Chemical Society, 2023.

M. Dragomir, L. Šibav, M. Lozinšek, A. Zorko, "Crystal growth and magnetic properties of the quantum spin liquid candidate $NdTa_7O_{19}$ and other rare-earth heptatantalates", in *Thirty-first Slovenian-Croatian Crystallographic Meeting*, Ljubljana, Slovenia: Faculty of Chemistry and Chemical Technology, University of Ljubljana, 2025.

K. Jaksetič, M. Pregelj, M. Gomilšek, M. Dragomir, L. Šibav, M. Pascal, F. Orlandi, D. Khalyavin, A. Zorko, "Unconventional magnetic states in geometrically frustrated rare-earth heptatantalates", in *ÖPG-SPS Meeting Vienna 2025*, Vienna, Austria, 2025.

All the conference contributions were presented by the first author.

Workshops

Topas user meeting at *EPDIC17*, Šibenik, Croatia, 29th–31th May 2022.

European School on Magnetism 2022, Saarbrücken, Germany, 11th–23th September 2022 (mixed format onsite and online, attended online).

Fundamentals of Quantum Materials Winter School & Workshop 2023, University of Maryland, College Park, Maryland, USA, 16th–19th January 2023.

Biography

The author of the dissertation was born in Slovenia. Her interest in chemistry developed during her secondary education at Nova Gorica Grammar School, where she regularly participated in national chemistry competitions, earning three gold awards and one silver. Following graduation, she enrolled in the Bachelor's programme in Chemistry at the Faculty of Chemistry and Chemical Technology, University of Ljubljana, completing her degree in 2017 with a thesis entitled "X-ray structural analysis of certain nickel complexes with tridentate ligands" under the supervision of Asst. Prof. Andrej Pevec. She continued her education in the Master's degree programme in Chemistry at the same faculty, completing the studies in 2020 with a thesis entitled "Synthesis and characterization of mechanochemical synthesis products of light metal imidazolates and tetrahydridoborates" under the supervision of Prof. Anton Meden.

In October 2020, she enrolled in the PhD study programme Nanosciences and Nanotechnologies at the Jožef Stefan International Postgraduate School and started the position of Young Researcher at Electronic Ceramics Department (K5) at Jožef Stefan Institute under the supervision of Asst. Prof. Mirela Dragomir. Her doctoral research focused on synthesis and characterization of low-dimensional magnetic materials, with two main research subtopics: chemical doping of the Shastry-Sutherland system $SrCu_2(BO_3)_2$ and single-crystal growth of perfect triangular lattice rare-earth heptatantalates, $RETa_7O_{19}$.